Chemical Substructure of High Mass Star Forming Regions

Siyi Feng
Max-Planck-Institut für Astronomie

Heidelberg 2014

Dissertation in Astronomy
submitted to the
Combined Faculties of the Natural Sciences and Mathematics
of the Ruperto-Carola-University of Heidelberg, Germany,
for the degree of
Doctor of Natural Sciences

Put forward by
Siyi Feng
born in Nanchong, China

Oral examination: February 6, 2015

Chemical Substructure of High Mass Star Forming Regions

Referees: **Prof. Dr. Henrik Beuther**
Prof. Dr. Cornelis P. Dullemond

致天上的外公外婆
願繁星與共

To my beloved grandfather and grandmother
may you rest among the stars...

Abstract

High mass stars (stars with mass M $>$ 8 $M_{\odot}$) are one of the most fundamental building blocks in the Universe. Deeply embedded in the dense clouds at further distances than their low mass counterparts, the forming processes of these fast evolving objects are still unclear. In the earliest phases of the high mass star forming regions (HMSFRs), many complicated astrophysical processes, such as fragmentation, accretion, inflows and outflows are coexistent that dynamic studies are not enough to understand all the mysteries. Therefore, chemistry has developed into a powerful tool in probing the nature of them.

With the aim of understanding the chemical and physical processes in the very beginning of high mass star formation, I selected a series of HMSFRs at different evolutionary stages, and studied their chemical-physical properties via high spatial resolution observations at (sub)mm wavelengths.

The results can be summarised shortly as follows:

1. At a spatial resolution of $<$ 1 500 AU, fragmentation process is observed in the continuum maps of all the resolved sources. Above all, the fragments in 4 starless clumps are on average more massive (with M $>$ 10 $M_{\odot}$) than the Jeans mass of the large-scale clump, indicating that thermal motions is not the dominant support to against collapse, and high mass stars may form in a "scaled up" version similar to the low mass stars.
2. Observations at a spatial resolution of 1 000 AU resolve NGC 7538 S into at least 3 fragments, having comparable sizes and masses derived from continuum emissions. However, these fragments exhibit distinguishing spectral line emissions at 1.3 mm wavelength, revealing different evolutionary stages. Combing with a 1-D gas-grain model fitting, for the first time, this project suggests that these fragments may result from different warm-up paces after synchronised fragmentation, and that the warm-up processes from one stage to another is rapid.
3. Chemical variations at small scales may be caused by the evolutionary stage diversity of fragments, but may also come from chemical difference of molecular species. With the first complimentary data obtained from both interferometric and single-dish telescopes at 1.3 mm, I analysed the continuum and spectral line features at a spatial resolution of 1 200 AU in Orion-KL. From the central warmer condensations to the cooler outflow regions, gas temperatures and densities differ, leading to spatial distribution inhomogeneity and abundance diversity of nitrogen (N-) bearing, sulfur (S-) bearing and oxygen (O-) bearing molecules.
4. Even at a spatial resolution of 1 000 AU, NGC 7538 IRS1 remains unresolved. At 1.3 mm, this core has a unique spectrum at the continuum peak: a majority of the lines exhibit absorption feature, while at least 3 lines from CH_3OH and $HCOOCH_3$ exhibit strong, pure emission. I proposed several hypotheses, attempting to interpret this by source geometry and/or line excitation states.
5. Complex organic molecules (COMs) are ubiquitously detected in the hot molecular cores (HMCs). Thanks to the high sensitivity observations, I identified several low abundant COMs ($< 10^{-11}$ with respect to H_2) demonstrating complicated chemistry in my sources.
6. In addition to the fragmentation process, the high mass starless cores are not completely chemically quiescent. None line detection in 4 infrared dark clouds at 1.1 mm may indicate these regions are in the early, cold evolutionary stage. However, detection of several dense gas tracers ($> 5\sigma$ rms) especially at 3 mm, implies the presence of active gas phase chemistry.

From our study, chemistry is an efficient tool in diagnosing evolutionary events coexistent at the small scales of HMSFRs.

Zusammenfassung

Massereiche Sterne (Sterne mit einer Masse $M > 8\,M_{\odot}$) sind eine der wichtigsten Bausteine im Universum. Da sie nur in weit entfernten dichten Wolken tief eingebettet vorkommen, sind die Entstehungsprozesse dieser schnell entwickelnden Objekte immer noch unklar. In den frühesten Phasen der massereichen Stern Entstehungebieten (high mass star forming regions HMSFRs) finden viele komplizierte astrophysikalische Prozesse, wie Fragmentierung, Akkretion, In- und Ausflüsse statt und es hat sich gezeigt, dass dynamische Studien nicht ausreichen um alle Mysterien zu verstehen. Jedoch hat sich die Chemie als schlagkräftiges Werkzeug gezeigt, um die Eigenschaften dieser Objekte zu studieren.

Mit dem Ziel, die chemischen und physikalischen Prozesse am Anfang von massereicher Sternentstehung zu verstehen, habe ich eine Reihe von HMSFRs in unterschiedlichen evolutionären Stadien ausgewählt und ihre chemischen und physikalischen Eigenschaften mit Hilfe von räumlich hoch aufgelösten (sub)mm Beobachtungen studiert.

Die Ergebnisse können wie folgt kurz zusammengefasst werden:

1. Bei einer räumlichen Auflösung von $< 1\,500$ AU beobachten wir Fragmentierung für alle aufgelösten Quellen in den Kontinuums Karten. Darüber hinaus sind die Fragmente von 4 sternenlosen Klumpen im Schnitt massereicher ($M > 10\,M_{\odot}$) als die Jeans Masse des großräumigen Klumpen. Dies deutet darauf hin, dass massereiche Sterne in einer maßstäblich vergrößerten Form, ähnlich wie massearme Sterne entstehen.
2. Beobachtungen im Kontinuum mit einer räumlichen Auflösung von 1 000 AU lösen NGC 7538 S in 3 Fragmente auf, die ähnliche Größen und Massen haben. Jedoch zeigen diese Fragmente unterschiedliche Linien Emission bei einer Wellenlänge von 1.3 mm, die unterschiedliche evolutionäre Stadien andeuten. In Kombination mit einem 1-D Gas-Teilchen Modell, zeigt dieses Projekt zum ersten Mal, dass die Fragmente aus einer unterschiedlichen Erwärmungsphase nach der gleichzeitigen Fragmentierung hervorgehen könnten, und dass die Erwärmungsprozesse von einer zu der anderen Phase schnell sind.
3. Chemische Variationen auf kleinen Skalen kann durch die unterschiedlichen evolutionären Stadien der Fragmente ausgelöst werden, jedoch könnte es auch von den chemischen Unterschieden der Moleküle kommen. Mit dem ersten komplementären Datensatz bestehend aus Messungen mit einem Interferometer und einzelnen Antennen bei 1.3 mm, habe ich das Kontinuum und Linien Emission von Orion-KL mit einer räumlichen Auflösung von 1 200 AU studiert. Ausgehend von den warmen zentralen Kondensierungen zu den kälteren Ausflußregionen ändert sich die Gas Temperatur und Dichte. Dies führt zu einer räumlichen Inhomogenität und Häufigkeitsunterschiede von stickstoffhaltigen, schwefelhaltigen und sauerstoffhaltigen Molekülen.
4. Selbst eine räumlichen Auflösung von 1 000 AU löst NGC 7538 IRS1 nicht auf. Bei 1.3 mm zeigt dieser Kern ein einzigartiges Spektrum: Die Mehrheit der Linien zeigt sich in Absorption, wohingegen mindestens 3 Linien von CH_3OH und $HCOOCH_3$ starke, reine Emissionslinien zeigen. Ich schlage mehrere Hypothesen vor, um dies mit der Geometrie des Objektes oder der Linien Anregungszustände zu erklären.
5. Komplexe organische Moleküle (complex organic molecules COMs) sind überall in den heißen molekularen Kernen (hot molecular cores - HMCs) detektiert. Dank der hohen Sensitivität der Beobachtungen, identifizierte ich mehrere schwach vorkommende COMs ($< 10^{-11}$ im Vergleich zu H_2), welche die komplizierte Chemie in meinen Quellen demonstrieren.
6. Zusätzlich zu dem Fragmentierungsprozess, sind massereiche sternenlose Kerne chemisch nicht untätig. Vier Infrarot Dunkelwolken zeigen keine Linienemission bei 1.1 mm. Dies deutet an, dass diese Regionen in einem früheren, kälteren evolutionären Stadium sind. Jedoch deutet die Detektion von mehreren dichte Gas Indikatoren ($> 5\sigma$ rms) vor allem bei 3 mm, eine aktive Chemie in der Gasphase an.

Unsere Studie zeigt, dass die Chemie ein effektives Diagnosewerkzeug von evolutionären Abläufen ist, welche gleichzeitige auf der kleinen Skala von HMSFRs ablaufen.

Contents

1 Introduction **1**

1.1 Why High Mass Star Forming Regions (HMSFRs) . . . 1

1.1.1 The life cycle of stars . . . 1

1.1.2 Unique feathers of high mass stars . . . 2

1.1.3 Questions . . . 6

1.2 Why Chemistry . . . 7

1.2.1 Chemical composition of the HMSFRs . . . 8

1.2.2 Evolutionary stages of HMSFRs: from the chemistry perspective . . . 9

1.2.3 Chemical models . . . 11

1.2.4 Questions . . . 15

1.3 Observational Approach . . . 16

1.4 About This Work . . . 19

2 Resolving the chemical substructure of Orion-KL **23**

2.1 Motivation . . . 23

2.2 Observations and Data Reduction . . . 25

2.2.1 Submillimeter Array (SMA) . . . 25

2.2.2 Single-dish observations with the IRAM 30 m telescope . . . 26

2.2.3 Data merging . . . 26

2.3 Observational Results . . . 27

2.3.1 Continuum emission . . . 27

2.3.2 Spectral line emission . . . 29

2.4 Calculations . . . 43

2.4.1 Temperature estimates . . . 43

2.4.2 Column densities . . . 48

2.4.3 Molecular abundances . . . 53

2.4.4 Error budget . . . 55
2.5 Discussion . . . 58
2.5.1 Comparison with the other results . . . 58
2.5.2 Chemistry in the Hot Core . . . 60
2.5.3 Chemistry in the outflow . . . 62
2.5.4 Search for COMs . . . 65
2.6 Conclusions . . . 66
2.7 Appendix . . . 68

3 Inferring the evolutionary stages of NGC 7538 S and NGC 7538 IRS1 from chemistry 89
3.1 Motivation . . . 89
3.2 Targets . . . 90
3.3 Observations . . . 91
3.4 Observational Results . . . 92
3.4.1 Continuum emission . . . 92
3.4.2 Spectral line . . . 95
3.5 Calculation . . . 99
3.5.1 Temperature estimates . . . 99
3.5.2 Column densities . . . 101
3.5.3 Molecular abundances . . . 105
3.5.4 Error budget . . . 105
3.6 Model . . . 109
3.6.1 Physical model . . . 109
3.6.2 Chemical model . . . 110
3.6.3 Initial abundances . . . 111
3.6.4 Iterative fitting of the data . . . 111
3.6.5 Uncertainties of the fitting . . . 114
3.7 Discussion . . . 116
3.7.1 Comparison with the other results . . . 117
3.7.2 Hierarchical fragmentation in NGC 7538 S: synthesis of observations and models . . . 118
3.7.3 The absorption and emission feature in IRS1 . . . 119
3.8 Conclusions . . . 124
3.9 Appendix . . . 126

4 Are the Infrared Dark Clouds Really Quiescent? 137
4.1 Motivation . . . 137
4.2 Observations . . . 138

4.2.1 Submillimeter Array (SMA) . . . 138
4.2.2 Single-dish observations with the IRAM 30 m telescope . . . 139
4.3 Observational Results . . . 141
4.3.1 Fragmentation at small scale from SMA observations . . . 141
4.3.2 Line survey from IRAM 30 m at 1 mm & 3 mm . . . 141
4.4 Analysis and Discussion . . . 152
4.4.1 Fragmentation . . . 152
4.4.2 Molecular column density and abundance . . . 155
4.4.3 Chemical similarity and difference between HMSCs and low mass prestellar cores . . . 162
4.4.4 CO depletion . . . 163
4.4.5 Ionization . . . 164
4.5 Conclusions . . . 165
4.6 Appendix . . . 166

5 Remarks and Future Prospects **173**
5.1 Summary of the Main Results . . . 173
5.2 Prospects for the Future Work . . . 176
5.2.1 Feedback processes & shock chemistry . . . 178
5.2.2 Disk chemistry . . . 179
5.2.3 Chemical clocks: deuteration & S-bearing molecules . . . 180
5.2.4 Astrochemistry in the global scale . . . 182

Acknowledgments **183**

List of Figures

1.1 Life cycle of stars in the ISM . . . 3
1.2 Schematic representation of the COM formation from collapsing HMSC through HMPO to the HMC . . . 14
1.3 The most advanced submillimeter interferometers in use so far . . . 18

2.1 The amplitude in Jy versus the projected baseline from the combination of the interferometer (SMA) and single-dish (IRAM 30 m) data . . . 27
2.2 Continuum map of Orion-KL obtained from SMA at 1.3 mm . . . 30
2.3 Spectra taken toward substructures of Orion-KL . . . 32
2.4 Maps of the intensity distribution of molecules containing < 6 atoms, which are detected in the combined SMA-30 m data at 1.3 mm . . . 34
2.5 Maps of the intensity distribution of COMs detected in the combined SMA-30 m data at 1.3 mm . . . 35
2.6 Lines having only one transition with low specific intensity (≤ 10 Jy beam^{-1}) in Orion-KL data . . . 36
2.7 Gaussian fitting to the line profile of ^{13}CO, $C^{18}O$, HNCO, SO_2 and $^{34}SO_2$ extracted from NE of Orion-KL . . . 39
2.8 The rotation diagrams and LTE fittings of CH_3CN towards substructures in Orion-KL . . . 46
2.9 The rotation diagrams of O- and S-bearing species towards HC, mm2, mm3a and mm3b of Orion-KL . . . 49
2.10 Molecular column densities and abundances toward 8 positions in Orion-KL . . . 54
2.11 Comparing the observed SO_2/SO ratio to the chemical modelling result in Orion-KL . . . 64
A1 The spectrum from HC of Orion-KL . . . 78

A2 Synthetic spectrum fitting of Complex Organic Molecules (COMs) towards their emission peaks of Orion-KL . . . 79
A2 (continued) . . . 80
A2 (continued) . . . 81
A2 (continued) . . . 82
A3 The line profile of identified species from each continuum peak of Orion-KL . . 83
A3 (continued) . . . 84
A3 (continued) . . . 85
A3 (continued) . . . 86
A4 The line wing flux integration maps from the combined SMA-30 m data at 1.3 mm 87
A5 Channel maps of unblended CH_3OH lines show multiple velocity dependent emission peaks in Orion-KL . . . 88

3.1 Overview of the NGC 7538 complex (left) and colormaps of the continuum flux obtained with the PdBI at 1.3 mm (right) . . . 93
3.2 Spectra extracted from selected positions of NGC 7538 S and IRS1 after imaging the whole data cube . . . 97
3.3 Maps of the intensity distribution of molecules detected in PdBI data at 1.3 mm 98
3.4 The rotation diagrams and LTE fittings of CH_3CN and H_2CO towards substructures in NGC 7538 S and IRS1 . . . 100
3.5 Molecular column densities toward 5 positions in NGC 7538 S and 2 positions in IRS1 . . . 103
3.6 Best fit of molecular abundances in MM1-MM3 . . . 113
3.7 Synthetic spectrum fitting (upper) and spatial distribution maps (lowers) of CH_3OH lines in MM1 . . . 121
3.8 Synthetic spectrum fitting (upper) and spatial distribution maps (lower) of CH_3OH lines in mmS . . . 122
B1 Synthetic fitting of $HCOOCH_3$ in NGC 7538 IRS1 (mmS and continuum peak) and MM1 . . . 132
B1 (continued) . . . 133
B2 Line profiles of identified species toward the continuum substructures identified in NGC 7538 S and IRS1 . . . 134
B2 (continued) . . . 135
B2 (continued) . . . 136

4.1 Compilation of the continuum data from 70 μm to 1.2 mm wavelength for 4 G 28.34 S, IRDC 18530, IRDC 18306 and IRDC 18308 . . . 142
4.2 Averaged spectra of G 28.34 S, IRDC 18530, IRDC 18306 and IRDC 18308 from IRAM 30 m line survey at 1 mm & 3 mm . . . 144

4.3 Molecular spatial distribution in G 28.34 S, IRDC 18530, IRDC 18306 and IRDC 18308 . . . 145
4.3 (continued) . . . 146
4.3 (continued) . . . 147
4.3 (continued) . . . 148
4.4 Hyperfine structure fittings to the observed N_2H^+ (J = 1 → 0), C_2H (N = 1 → 0), HCN (J = 1 → 0) and $H^{13}CN$ (J = 1 → 0) from G 28.34 S, IRDC 18530, IRDC 18306 and IRDC 18308 . . . 158
4.4 (continued) . . . 159
C1 Line profiles of identified species toward G 28.34 S, IRDC 18530, IRDC 18306 and IRDC 18308 . . . 170
C1 (continued) . . . 171
C1 (continued) . . . 172

List of Tables

1.1 Types of gas-grain reactions used in the modern chemical networks 12

2.1 Properties of substructures in Orion-KL 31
2.2 Identification of saturated COMs and complex carbon chains in Orion-KL 44
2.3 Rotation temperature sets for each substructure derived from CH_3CN, $HCOOCH_3$, CH_3OH and $^{34}SO_2$ 50
2.4 Optical depth and abundance ratios for CO, ^{13}CO, OCS and CH_3CN with respect to their isotopologues in each substructure of Orion KL 57
A1 Identified emission lines from the SMA-30 m combined dataset. 68
A2 The intensity integrated over the width of each transitions of CH_3CN, CH_3OH, $HCOOCH_3$ and $^{34}SO_2$ 72
A2 (continued) 73
A2 (continued) 74
A3 The intensity integrated over the width of each line 75
A4 Column densities and abundances for molecules with respect to H_2 76
A4 (continued) 77

3.1 Properties of continuum substructures in NGC 7538 S and IRS1 94
3.2 Optical depth and abundance ratios for SO, ^{13}CO, OCS and CH_3CN with respect to their isotopologues in each substructure of NGC 7538 S and IRS1 mmS 107
3.3 Top 35 initial abundances with respect to H for the MM3 condensation. 112
3.4 Best fit physical parameters of NGC 7538 S-MM1–MM3 from 1-D gas-grain model. 114
3.5 Best fit results of NGC 7538 S-MM1–MM3 from 1-D gas-grain model 115
3.6 The detected CH_3OH lines in NGC 7538 IRS1 123

B1 Identified lines from PdBI dataset. . . . 126
B2 The intensity integrated over the width of each line of NGC 7538 S and IRS1 . . 129
B3 Column densities and abundances for molecules with respect to H_2 in NGC 7538 S substructures, IRS1 peak and mmS . . . 130
B3 (continued) . . . 131

4.1 SMA observations toward four IRDCs . . . 140
4.2 IRAM 30 m observations on the four IRDCs . . . 140
4.3 Identified lines from 30 m dataset . . . 149
4.4 Parameters of the fragments and two hypotheses of fragmentation . . . 154
4.5 T_{ex} derived from hyperfine fittings to N_2H^+, C_2H, HCN and $H^{13}CN$ multiplet in four IRDCs . . . 160
4.6 Optical depth τ and T_{ex} derived for CO ($1 \rightarrow 0$) isotopologues on four IRDCs . . 161
4.7 CO depletion, HNC/HCN ratio, lower limit of ionization and velocity asymmetric degree of $H^{13}CO^+$ in four IRDCs . . . 162
C1 The intensity integrated over the width of each line, and the optical depth of the main line in each IRDC . . . 167
C2 Average column densities and abundances for molecules with respect to H_2 in each IRDC . . . 168
C2 (continued) . . . 169

Acronyms

AGB Asymptotic Giant Branch

ALMA Atacama Large Millimeter/submillimeter Array

ASIC Application-Specific Integrated Circuit

ATLASGAL The APEX Telescope Large Area Survey of the Galaxy

CDMS Cologne Database for Molecular Spectroscopy catalogue

cm centimeter

COM Complex Organic Molecule

CRP Cosmic-ray particles

CSO Caltech Submillimeter Observatory

EMIR Eight MIxer Receiver

EPoS Earliest Phases of Star Formation

FUV Far Ultra Violet

GISMO Goddard-IRAM Superconducting 2 mm Observer

GMC Giant Molecular Clouds

HERA HEterodyne Receiver Array

HMC Hot Molecular Core

HMPO High Mass Protostellar Object

HMSC High Mass Starless Core

HMSFR High Mass Star Froming Region

HST Hubble Space Telescope

IRDC Infrared Dark Cloud

ISM Interstellar Medium

ISO Infrared Space Observatory

JCMT James Clerk Maxwell Telescope

JPL Jet Propulsion Laboratory

JWST James Webb Space Telescope

LTE Local Thermodynamic Equilibrium

MHD magnetohydrodynamics

mm millimeter

MSX Mid-course Space Experiment

MUSCLE MUlti Stage CLoud codE

MYSO Massive Young Stellar Object

NE northeast

NIKA New IRAM KIDs Array

NOEMA NOrthern Extended Millimeter Array

NW northwest

Orion-BN Becklin-Neugebauer Nebula in Orion

Orion-KL Kleinmann-Low Nebula in Orion

PAH Polycyclic Aromatic Hydrocarbon

PdBI Plateau de Bure Interferometer

PDR photo-dissociation region

SE southeast

SED Spectral Energy Distribution

SMA Submillimeter Array

SST Spitzer Space Telescope

SW southwest

SWARM SMA Wideband Astronomical ROACH2 Machine

UCHII Ultra Compact HII

UV ultraviolet

VLA Very Large Array

YSO Young Stellar Object

1 Introduction

I hail from the explosive jetsam of a multitude of high-mass stars that died more than 5 billion years ago.

– Neil deGrasse Tyson (2007), *Death by Black Hole*

Ever since the dawn of civilisation, mankind's curiosity on the origin of life never stops. Where do we come from? What are we? Where are we going? They are the most essential questions we ask ourselves. We made telescopes, gazed at the immense sky, and seek for answers by peering behind the gas and dust.

1.1 Why High Mass Star Forming Regions (HMSFRs)

1.1.1 The life cycle of stars

In between the enormous, twinkling stars, the vast interstellar space is not empty, but full of gas and dust (interstellar medium, ISM). It is the nurseries of our life seed, where the stars have been through their life cycles, while the dust and gas reincarnate (Figure 1.1).

Theoretically, the ISM contains various phases of clouds (McKee & Ostriker 1977; Snow & McCall 2006). Initially, the most tenuous clouds (n $\sim$ 10 particles cm^{-3}) are fully exposed to interstellar radiation field, and hence photodissociation destroys almost all the molecules, leading the diffuse clouds to be dominated by neutral atomic (HI) and ionized gas (e.g., C^+). Then, surrounded by the diffuse atomic gas, the ultraviolet (UV) regime of interstellar radiation field is sufficiently attenuated in the cloud center for H_2 to survive, and these diffuse molecular clouds (T $\sim$ 30–100 K) are characterised by low density (n $\sim$ 10^2 cm^{-3}) and high ionization fraction. Subsequently, large scale diffuse molecular clouds collapse due to turbulence and self-gravity/magnetic field (Heiles & Crutcher 2005), and efficiently UV shielding (e.g., $C^+ \rightarrow C \rightarrow CO$) helps to form the giant molecular clouds (GMC). The GMCs fragment into

several cold dense clouds ($T \leq 10$ K, $n \sim 10^6\,cm^{-3}$), which are the precursors of star forming regions. Protostars are formed within these regions. In particular, some of them are gradually surrounded by disks of gas and dust, which eventually assemble some solar-like systems of planets. Although the formation of stars with different masses are still an open issue, all of them evolve along the main sequence, during which they radiate heat by nucleosynthesis and mass loss. Taking advantage of the radiation from the central star, and by preserving the organic materials from the interstellar clouds, life may be supported in the planets. When the central star slowly burns up all the nuclear fuels, its ultimate fate is mass-depended. For a low mass star ($M < 8\ M_\odot$[1] when hydrogen fusion starts), it burns out[2] ultimately and ejects its gas shell as planetary nebula (HII region), while the central core may become a white dwarf. At the end stage of a high mass star, Type II supernovae eject several heavy nuclei (e.g., Si, S, Cl, Ar, Na, K, Ca, Sc, Ti) by violent explosions, which could further trigger star formation in the nearby GMCs. These elements refill the gas and some attach on the grain surface, which will be incorporated in future generations of stars and planets.

The effect of high mass stars on ISM is significant. On one hand, they introduce most[3] of the the heavy elements to the Universe by nucleosynthesis, and thus change the star formation efficiency via cooling process (which depends on the abundance of heavy elements). On the other hand, they are the only stars whose formation activities are observable in extragalactic system so far. Therefore, understanding their formation processes will help us to explore the initial condition of ISM in general.

1.1.2 Unique feathers of high mass stars

Compared to their low mass counterparts, formation of high mass stars is still not yet well studied because of their complicated and mysterious features.

From a observational perspective, high mass stars are deeply embedded in the cores of dense molecular clouds, which are on average further away (at a distance >1 kpc) than the low mass star forming regions (with distance on the order of $\sim 10^2$ pc), and are heavily obscured by circumstellar dust (with extinction $A_V > 100$). Moreover, they are fewer than the low mass stars, but they dominate the total luminosity. In addition, within the low temperature, high gas and dust column densities environment, the formation of high mass stars occurs in a clustered mode (e.g.,

[1] A star with mass $2.3\ M_\odot < M < 8\ M_\odot$ is also named as a"intermediate mass star". For convenience, we name all the stars with mass $M < 8\ M_\odot$ as "low mass star" in this thesis.

[2] Very low mass star ($M < 0.2\ M_\odot$) burns up all the H; sun-like mass star burns up He to C via triple alpha process (He flash); and high mass star $M \geq 8\ M_\odot$ evolves along the main sequence via CNO cycle.

[3] Another rare case is Type Ia supernovae, which is from a nuclear based explosion after a white dwarf reaches its Chandrasekhar limit by accreting mass from a neighbouring star (usually a red giant).

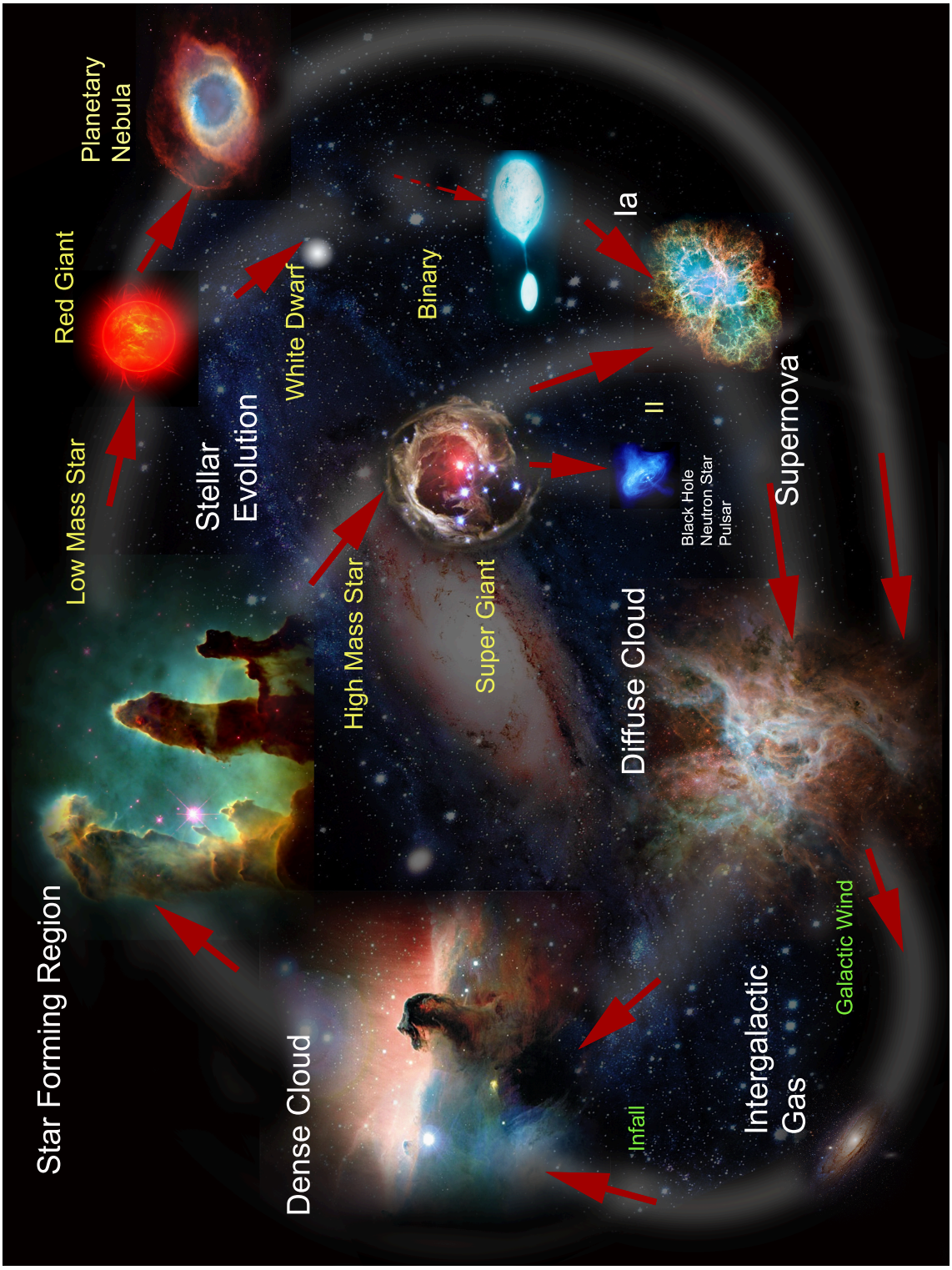

Figure 1.1: Life cycle of stars in the ISM. The represented astronomic objects are: Diffuse cloud (Tarantula Nebula image from HST, credit: ESA/NASA), Dense cloud (Horsehead Nebula, credit: ESO), Star forming region (Eagle Nebula, credit: NASA/ESA/STScI), Super giant (V838, credit: NASA/ESA/STScI/AURA), Planetary nebula (NGC7293 from HST, credit: NASA/ESA), Pulsar (X-ray of Crab pulsar from Chandra, credit: NASA/CXC/SAO), Supernova (supernova remnant of Crab nebula from HST, credit: NASA/ESA).

Bonnell et al. 1998; Stahler & Palla 2005; Bonnell et al. 2007), so it is hard to spatially resolve them. Furthermore, due to their high mass, their formation is fast before approaching the main sequence, making the identification of their initial conditions more difficult.

From a theoretical perspective, the classic scenario in which "accretion ceases before the initiation of hydrogen fusion" does not apply to the formation of high mass stars. Traditionally, enlightened by Immanuel Kant (1775)[4] and Pierre-Simon Laplace (1796)[5], the general accepted picture on the forming process of stars was founded by Larson (1969) and Shu et al. (1987). For low mass stars, Lada (1991) and André (1995) described the evolutionary sequence based on the spectral energy distribution (SED) as follows: Deeply embedded in a dense GMC, gas becomes gravitationally unstable, probably due to turbulent motions and/or magnetic fields, fragments into prestellar clouds, and then collapses into protostellar cores with mass on the order of Jeans mass (Larson 2005). Surrounding each core is a dense ($n \sim 10^5\,cm^{-3}$), optically thick envelope, which traps the radiation exerted from the isothermally collapsing core, resulting in the central heating (up to $T \sim 2\,000\,K$) and H_2 dissociation, exhibiting a cold SED with peak in the far-infrared or sub millimeter (mm) regime (Class 0). The protostar forms when all H_2 is endothermic dissociated, leaving nothing else to cool the center down. Its mass increases by accreting gas from the surrounding envelope through a flattened accretion disk Hartmann (1998). At this stage, accretion also drives bipolar jets, which may sweep up the surrounding gas and form an extended outflow (e,g. Richer et al. 2000; Arce et al. 2007). The flattening envelope and the cavity penetrated by the outflow decrease the opacity, and the central hot protostar exhibits a SED peak in the mid-infrared regime (Class I). When the envelope is completely removed, the protostar stops accretion. During this stage, the central protostar with the circumstellar disk (namely "protoplanetary disk") forms the Class II object, and its SED peaks in near-infrared and becomes visible in optical regime. The contraction of the protostar (Class III) and the increase of the central energy finally ignite hydrogen fusion, revealing a new born star which evolves along the main sequence (e.g., Hayashi 1961; Palla & Stahler 1993). The object in the period after cease of contraction but before hydrogen fusion is named as a "pre-main sequence star", and objects evolve form Class 0 till the initiation of main sequence evolution are named as young stellar objects (YSO).

However, high mass stars already start hydrogen fusion with $M > 8\,M_\odot$ before the cease of accretion process, i.e., they still accrete gas even after reaching the main sequence. Therefore, compared to the radiation pressure which halts the ongoing accretion of low mass protostar in the above classical 1-D picture, the radiation pressure from the high mass central object is much

[4] *"Universal Natural History and Theory of the Heavens"*
[5] *"Exposition du systeme du monde"*

higher than expectation. Several hypothesis have been proposed to reconcile this contradictory, among them two main schools of thoughts are popular (summarised in the reviews of Beuther et al. 2007; Krumholz & Bonnell 2007; Tan et al. 2014 in detail).

One of the most common paradigm is the "core accretion" scenario. In this view, a dense cloud contains several initial fragments (namely, "prestellar cores"), which accumulate gas before their core collapse. Noting that with the assumptions on the geometry of protostars (i.e., 1-D spherical model) and the dust properties of ISM (i.e., steady and homogeneous grain model) in the traditional picture, the gas and dust infall can not compete against the radiation pressure from a star with $M < M_{\odot}$. Some theoretical works extend the "concentrate fragmenting clump" view by changing these assumptions quantitatively (Kahn 1974; Yorke 1986; Wolfire & Cassinelli 1987). These works include modifications, such as a cavity which is created by jet/outflow and channels away radiation to keep accretion (e.g., Wolfire & Cassinelli 1987; Tan & McKee 2002; Yorke & Sonnhalter 2002; Krumholz et al. 2005; Cunningham et al. 2011), reduction of dust opacity and introduction of very high accretion rates of 10^{-4}–10^{-3} $M_{\odot}yr^{-1}$ (e.g., Osorio et al. 1999; Norberg & Maeder 2000; Edgar & Clarke 2003; McKee & Tan 2003), accretion through the evolving hypercompact HII region (e.g., Keto 2003; Keto & Wood 2006), the effect of turbulence (e.g., Padoan & Nordlund 2002; Gong & Ostriker 2011), Rayleigh Taylor instability (Krumholz & Bonnell 2007), and the effect from the magnetic field. In the past years, several observations on highly collimated jet and outflows (e.g., Marti et al. 1993; Beuther & Shepherd 2005; Wu et al. 2005; Garay et al. 2007; López-Sepulcre et al. 2009) and rotating structures (e.g.,Cesaroni et al. 2005; Patel et al. 2005; Beltrán et al. 2006; Wang et al. 2012; Beuther et al. 2013a) around some massive protostars support this "scaled-up" model, and 3D simulations based on this picture are able to be performed self-consistently by including multiple physical effects (e.g., Krumholz et al. 2009; Kuiper et al. 2011; Kuiper & Klessen 2013).

Based on the fact that high mass stars are mostly observed in the clustered mode, some other theoretical works suggest the "coalescence and competitive accretion" view. In this scenario, several protostellar seeds (with mass on the order of 0.5–1 Jeans mass, Bonnell et al. 2001, 2007) are in the same cluster, and it is their masses and locations within the gravitational potential well that determines their accretion rates and final masses, i.e., the deeper a protostellar seed is embedded in the potential well (e.g., at the cluster center), the more mass it can gather (Bonnell et al. 2004). In the extreme case, a more massive star may be formed by the merge of two or more low-mass stars in high protostellar density environment (with a rate $> 10^6$ protostellar seeds pc^{-3}, e.g., Bonnell et al. 1998; Bally & Zinnecker 2005). Although such extreme circumstance is not usually found in the protostellar cluster, this picture avoids the problem brought from the radiation pressure.

1.1.3 Questions

Thanks to the improvement of new generations of (sub)mm telescopes, our knowledge about high mass star formation has increased (e.g., Beuther et al. 2007; Krumholz & Bonnell 2007; André et al. 2013; Dobbs et al. 2013; Dunham et al. 2014; Frank et al. 2014; Tan et al. 2014). However, the mysteries of high mass star formation are still unveiling, and hypotheses need large samples of observations to be verified. Two major areas which need investigation are:

- **The initial conditions of HMSFRs**
  To date no dynamic simulations have been performed self-consistently in depicting all the complex features observed in the very initial stages of HMSFRs. Therefore, to test the theoretical distinctions, observing the very beginning of HMSFRs is crucial. For example, the essential difference between the aforementioned two high mass forming views is the origin of the final stellar mass. In the "core accretion" paradigm, clouds fragment into high-mass prestellar cores (with mass on the order of $\sim 10^2$ $M_\odot$ each) at the very beginning. In contrast, the "competitive accretion" model suggests the merge of the low mass protostellar seeds afterward. Another example is the measurement of the fragments velocity dispersion, which can indicate the degree of supersonic turbulence (e.g., Sakai et al. 2008; Wang et al. 2008; Fontani et al. 2011) and the fragments (prestellar cores/protostars) bounding condition within that cloud (e.g., Pillai et al. 2011; Sánchez-Monge et al. 2013; Tan et al. 2013). However, the timescale prior to the prestellar collapse is very short (on the order of 5×10^4 yrs, e.g., Russeil et al. 2010; Tackenberg et al. 2012), so the conditions are still poorly characterised from limited observations. Are the initial clouds dominated by a single core or do we witness already strong fragmentation in this very beginning (e.g., Bontemps et al. 2010)? Are these fragments Virial bounded or gravitational unbounded? What are the dynamic and chemical properties of the fragments? Are these environments similar to or different from prestellar phase of low mass star forming regions? Do we see streaming motions indicating of turbulent flows (e.g., Bergin et al. 2004; Vázquez-Semadeni et al. 2006; Heitsch et al. 2008; Banerjee et al. 2009)?

- **The evolutionary sequence of high mass stars**
  Although high mass stars evolve rapidly, the birth sites of their forming regions are highly complex structures, consisting of several gas and dust cores in different evolutionary stages. Based on (sub)mm observations performed on telescopes with high spatial resolutions, these distant and deeply embedded cores are able to be resolved. Beuther et al. (2007) and Zinnecker & Yorke (2007) summarised the physical differentiations from several observations, and described the evolutionary sequence of high mass stars qualitatively:

Initially, dense and cold gas assemble into cores with mass on the order of 10^2–10^3 $M_\odot$, where no protostellar objects are embedded (High mass starless core, HMSC). Later, accretion leads to the forming of high mass protostellar objects (HMPOs), whose temperatures and densities are higher than HMSCs, while violent activities (e.g., outflow, inflow) may occur in this phase. Finally, envelopes of many protostars disperse and hence accretions cease, so that supersonic winds and strong UV-radiation ionise their surrounding gas, creating ultra compact HII (UCHII) regions and giving birth to the new stars. In some extreme cases, protostars reach the main sequence so fast that their hydrogen fusion have already started even when they are deeply embedded and continuing accret envelopes.

This framework characterises well the evolutionary physical properties of the HMSFRs. However, without clear distinction in between phases, questions remain: What are the the chemical properties of these different phases? Can we quantify and diagnose the evolutionary stage of a particular region?

1.2 Why Chemistry

Accompanied with complicated dynamic processes, stellar embryos in the interstellar clouds contain a rich chemistry. The interstellar chemical components not only play an essential role in the life cycle of stars, but more importantly, their abundances and spatial distributions are sensitive to the physical parameters in their local environments, such as temperature, density and ionization rate. Therefore, they offer clues on the dynamical-chemical processes which are occurring during the star formation, e.g., the growth of the grains, the shocks or the impacts of the cosmic-rays.

For HMSFRs, the only way to probe the fundamental processes deep in a distant GMC is through observations of molecular lines and dust continuum at infrared and (sub)mm wavelengths. In addition, compared to the short timescale that prestellar clouds collapsing into protostellar objects, chemical properties often take significant time to respond to the violent dynamic changes. Therefore, chemical features within a HMSFR can be used to retrace its present structure and the past physical conditions (e.g., Schilke et al. 1997; Charnley et al. 1997; Bachiller et al. 2001; Viti et al. 2004; Favre et al. 2011a; Bisschop et al. 2013; Garrod 2013). Moreover, since the chemical compositions are strongly time dependent, the chemical age of a particular region can be estimated by comparing the observed physical parameters (temperature, abundance) to the modelling predictions. Furthermore, chemical characters can be used for diagnosing the evolutionary stage of that region quantitatively. Clearly, the interpretations of infrared and (sub)mm observations require a basic knowledge of astrochemistry.

In general, astrochemistry is a growing interdisciplinary field. Starting in the late 1960s, development of radio astronomy brought a flood of new detections in interstellar lines (first OH, NH_3, H_2O, H_2CO, and CO, with more than 170 species so far, and on average 3 new molecules are detected per year), which breaks the ice of astrochemistry. Over the past decade, the close collaborations among observers, chemists, and modellers keep refreshing our understanding of the molecular universe (a comprehensive review of Tielens 2013). Among all the branches of astrochemistry, the observational side is all about lines. To probe the kinetics (derived from the line profiles) from molecular abundances (line strength) and temperatures (line ratios), a large numbers of observations are performed from (sub)mm (probing rotational transitions of simple molecules) through infrared (ro-vibrational transitions) to ultraviolet and visible (electronic transitions) wavelength. The main topic most observational astrochemists are concerning with is which molecules (specifically which lines) are good diagnostics for various physical conditions and dynamic processes (e.g., collapse, outflow, coolants to disperse energy by collision).

1.2.1 Chemical composition of the HMSFRs

High mass stars are born in warm (T $>$ 100 K) and dense (n $>$ 10^4 cm^{-2}) interstellar clouds, where 99% of the molecules are in the gas phase. While H_2 is the dominant species under these conditions, the second most abundant species CO locks up nearly all the gas-phase carbon (van Dishoeck & Black 1988). Although the major reservoir of the remaining oxygen is still an open issue (e.g., Hollenbach et al. 2009; Liseau et al. 2012), and the main nitrogen carrier is still uncertain in dense clouds (e.g., Daranlot et al. 2012), more than 100 other molecules are detected in the gas phase from emission lines at (sub)mm wavelength (see the molecular database at "Splatalogue"[6], which is a compilation of the Jet Propulsion Laboratory (JPL[7]), Cologne Database for Molecular Spectroscopy catalogue (CDMS[8]), and Lovas/NIST catalogues, Pickett et al. 1998; Lovas 2004; Müller et al. 2005).

Given that the dense and cold (T $\sim$ 10 K) initial environment of star formation, some atoms are locked up in dust grain (depletion). The grains, with typical radius of 0.1 μm and abundance of $\sim$ 1% by mass (10^{-12} with respect to H by number), are particles consisting of amorphous C and Si, locking up 100% of Mg, Fe, $\sim$ 70% of C and 30% of O (Draine 2003, 2011). Absorbing and scattering UV radiation, they shield molecules deeper into the cloud from dissociation. Layers of volatile materials ("icy mantle", including a H_2O-dominated polar and a CO-dominated non-polar layer, e.g., Öberg et al. 2011) cover these silicate or carbonaceous cores, and they can be observed through broad absorption features in the mid-infrared spectra of these environments.

[6] www.splatalogue.net
[7] http://spec.jpl.nasa.gov
[8] http://www.astro.uni-koeln.de/cdms/catalog

Of all the gas and solid phase species, complex organic molecules (organics containing more than 6 atoms, COMs) are of great importance. Although having low abundances in massive young stellar objects (MYSOs, including high mass protostars and pre-main sequence stars) like Orion-KL, SgrB2, G34.3+0.15, W3(H2O), larger COMs, e.g., CH_3CH_2OH (ethanol, Rizzo et al. 2001), CH_3COCH_3 (acetone, Snyder et al. 2002), CH_3CHO (acetaldehyde, Nummelin et al. 2000), $(CH_2OH)_2$ (ethylene glycol, Hollis et al. 2002), CH_2OHCHO (glycolaldehyde, Hollis et al. 2000, 2004; Jørgensen et al. 2012) have been previously detected solely in dense clouds. Because of their high degree of chemical and structural complexity, the precise origins and formation mechanisms of these COMs is still a subject of debate. Nevertheless, understanding these topics is particularly important for understanding the chemical evolution of the ISM and further the understanding of prebiotic origin of life (e.g., Garrod et al. 2008; Herbst & van Dishoeck 2009; Garrod & Widicus Weaver 2013) .

1.2.2 Evolutionary stages of HMSFRs: from the chemistry perspective

The basic evolutionary sequence of high mass protostellar objects outlined in Section 1.1.3 (HMSC → HMPO → UCHII) is mainly derived from large studies of the physical processes. On top of this, given the chemical differentiations of various HMPOs at a scale on the order 10″–30″ (0.05–1.2 pc at a distance ranging 1–8 kpc, Gerner et al. 2014), sources as HMPOs are further split into two substages: one is warmer, chemically richer and more evolved than the other. Chemically, the more evolved sources are classified as in the "hot molecular core" (HMC) phase (e.g., Kurtz et al. 2000; Cesaroni 2005). Hence, the evolutionary sequence of HMSFRs can be described as four chemical-dynamic stages: HMSC → HMPO → HMC → UCHII. Although there is no quantitative parameters to precisely discrete these stages so far, sources in the HMSC and HMC phases have no overlap, exhibiting distinctive chemical-dynamic properties.

- HMSCs: They are usually observed in the infrared dark clouds (IRDCs). IRDCs are cold ($T < 20$ K, Carey et al. 1998; Pillai et al. 2006), dense ($n \geq 10^3$–10^5 cm^3, Teyssier et al. 2002; Rathborne et al. 2006; Butler & Tan 2009; Vasyunina et al. 2009; Ragan et al. 2009) and highly filamentary clouds (ranging from $\sim$ 1 pc to several tens of pc, e.g., Jackson et al. 2010; Beuther et al. 2011; Wang et al. 2014), absorbing mid-infrared emission from galactic background, and emitting at (sub)mm wavelength. Ever since the first identifications by the mid-infrared space observatories Infrared Space Observatory (ISO, Perault et al. 1996) and Mid-course Space Experiment (MSX, Egan et al. 1998), IRDCs are widely believed to be the birthplace of high mass stars (Bergin & Tafalla 2007). In addition to a majority of mid-infrared dark high mass cores, IRDCs may also harbour a few low mass prestellar cores (median mass of the cores $\sim$ 120 $M_\odot$, Rathborne et al. 2006). Being in the low temperature environment, the molecular composition of IRDCs is far from thermodynamic equilibrium. Recent observations (e.g., Vasyunina et al. 2009; Miettinen et al.

2011; Beuther et al. 2013b; Sanhueza et al. 2013) reveal that IRDCs are characterised by high depletion factors, bright emission in N-bearing molecules such as NH_3 and N_2H^+ (e.g., Zhang et al. 2009; Henshaw et al. 2013), and high deuterium fractionation (e.g., Pillai et al. 2006; Fontani et al. 2011; Vasyunina et al. 2011). These chemical properties are similar to their low mass counterparts.

- HMPOs: With a thick envelope surrounding the center protostar, these regions are observable in the infrared regime but still dark in the centimeter (cm) observations. They are physically (e.g., mass, size) similar to but chemically different from (e.g., richer gas phase molecules) HMSCs (Sridharan et al. 2002; Beuther et al. 2002; Gerner et al. 2014). Gravitational collapse and gas accretion increase the gas temperatures and densities, and hence the central regions gradually evolve from isothermality to hydrostatic equilibrium in this phase.

- HMCs: They are compact objects (with the source size ≤ 0.05 pc), exhibiting high temperatures ($T > 100$ K), high densities ($n > 10^6$ cm^{-3}, Palau et al. 2011), and rich gas phase chemistry (Kurtz et al. 2000). Numerous spectral surveys (see, e.g., Blake et al. 1987; Turner 1989; Wright et al. 1996; Schilke et al. 2001; Belloche et al. 2009; Tercero et al. 2010 and summarised by Herbst & van Dishoeck 2009) have revealed that hot cores are characterised by a large abundance of simple organic molecules, including H_2CO (formaldehyde), HCOOH (formic acid), and highly saturated[9] COMs such as CH_3OH (methanol), $HCOOCH_3$ (methyl formate) and CH_3OCH_3 (dimethyl ether). Because of their high excitation temperature and similar abundance to solid envelopes of YSO, these COMs may come from sublimation of the hydride-rich ices which coat the dust grains (e.g., Charnley et al. 1992; Caselli et al. 1993). Moreover, outflows driven in this phase may shock the gas, enabling some reactions with activation energies and endothermicities to proceed (e.g., Neufeld & Dalgarno 1989a,b).

- UCHII: They are the regions where compact (with the source size 0.01–0.1 pc and density $n > 10^4$ cm^{-3}) UV ionized gas surrounds several newly formed B-/O-type stars. Detected via cm free-free emission and far-infrared emission (Wood & Churchwell 1989; Becker et al. 1990; Giveon et al. 2005; Hoare et al. 2012; Urquhart et al. 2013), these regions harbour rich dynamics (e.g., infall, outflow, stellar winds, shocks and accretion disk rotations, Kurtz et al. 2000; Churchwell 2002; Churchwell et al. 2010), owing to the coexistence of stellar evolution and accretion. Around them are extended, warm ($T < 300$ K) and neutral gas (e.g., HI, H_2) dominated photo-dissociation regions (PDRs), where the thermal

[9] A type of COM which has a chain of carbon atoms linked together by single bonds and hydrogen atoms filling all of the other bonding orbitals of the carbon atoms.

balance, chemistry and ionization balance are driven by UV photons. Therefore, PDRs associated with UCHIIs are studied for investigating the impacts the UV field on the gas and grain surface (e.g., photoionization, photodissociation, Guzmán et al. 2012; Pety et al. 2012; Guzmán et al. 2013; Gratier et al. 2013).

1.2.3 Chemical models

The initial dense star forming regions are not in thermodynamic equilibrium because of the low temperature. Therefore, chemistry is controlled by two body reactions[10], and abundances of species in a region depend on the physical conditions of the environment such as temperature, density, radiation field, etc. Developed by Herbst & Klemperer (1973); Dalgarno & Black (1976); Watson (1976); Prasad & Huntress (1980) and Millar et al. (1991), basic dark cloud gas-phase ion-molecule chemistry (pseudo time-dependent) produces adequate results for many protostellar environment (e,g., TMC-1, OMC-1, SgrB2, Blake et al. 1987). However, gas-phase simulations alone are insufficient to reproduce new observational results from sources in more evolved stages, e.g., the elevated abundances of highly saturated organic molecules like H_2CO and COMs in HMC and its low mass counterpart the hot corino (e.g., Herbst & van Dishoeck 2009). By taking account of photon-processes and surface reactions at low temperature ($T_{dust} \sim 10\,K$), grain-surface chemistry was gradually introduced by Allen & Robinson (1977); Tielens & Hagen (1982); D'Hendecourt et al. (1985) and Hasegawa & Herbst (1993).

Aside from the shock chemistry, gas-grain modelling is widely accepted nowadays, with a general consensus that that hydrogenation and oxidation dominate reactions on the surface, and sublimation of molecules return to gas when warmed-up (Viti et al. 2004; Garrod & Herbst 2006). Treating chemistry as a function of both time and location, this view has been adapted to simulate the chemical processes in all evolutionary stages of forming both high mass and low mass stars (Figure 1.2). Although further study is needed in modelling particular cases, the gas-grain networks (e.g., UMIST, Woodall et al. 2007; OSU, Garrod et al. 2008; KIDA, Wakelam et al. 2012, with basic reactions summarised in Table 1.1) are expected to be used for estimating the chemical age of a particular region, and exploring the origin of COMs through a bottom-up approach[11] (van der Tak 2005; Garrod et al. 2008; Herbst & van Dishoeck 2009; Tielens 2013).

[10]Three body reactions are not important until density $> 10^{13}\,cm^{-3}$, e.g., in the atmosphere of Asymptotic giant branch (AGB) stars, the inner midplanes of protoplanetary disks, and the formation of the first stars in the Universe (Rohlfs & Wilson 2004; van Dishoeck 2014)

[11]The COMs in the ISM are believed to be formed from two approaches. The "bottom-up" approach happens in star forming regions, which starts from CO, and small species keep reacting to produce more complex species. Another is the "top-down" route, which injects some COMs in diffuse ISM by break downing the very complex species like Polycyclic aromatic hydrocarbon (PAH) into small pieces, see Tielens (2013) for the review.

Table 1.1: Types of gas-grain reactions used in the modern chemical networks

A. Gas Phase Reactions

Reaction type	Example			Rate	Note
Ion-Neutral	$H_3^+ + CO$	$\rightarrow$	$HCO^+ + H_2$	κ	dominant reaction type
Neutral-Neutral	$O + CH_3$	$\rightarrow$	$H_2CO + H$	κ	many having high barrier
Charge Exchange	$H + H_2^+$	$\rightarrow$	$H_2 + H^+$	κ	mostly barrierless
Atomic Ion-Ion Neutralization	$C^- + O^+$	$\rightarrow$	$C + O$	κ	barrierless
Ion-Molecular Ion Neutralization	$H^- + NH_4^+$	$\rightarrow$	$NH_3 + H_2$	κ	barrierless
Dissociative Recombination	$H_3^+ + CO^-$	$\rightarrow$	$HCO^+ + H_2$	κ	barrierless
Radiative Recombination	$H_2CO^+ + e^-$	$\rightarrow$	$H_2CO + h\nu$	κ	mostly barrierless
Radiative Attachment[a]	$C_6H + e^-$	$\rightarrow$	$C_6H^- + h\nu$	κ	less efficient for small molecules
Associative Detachment	$H^- + CH_3$	$\rightarrow$	$CH_4 + e^-$	κ	barrierless
Radiative Association	$C^+ + H_2$	$\rightarrow$	$CH_2^+ + h\nu$	κ	mostly barrierless
Chemical Ionization	$CH + O$	$\rightarrow$	$HCO^+ + e^-$	κ	
Photodissociation	$CO + h\nu$	$\rightarrow$	$C + O$	$\kappa_{h\nu}$	
Photoionization	$H + h\nu$	$\rightarrow$	$H^+ + e^-$	$\kappa_{h\nu}$	
Cosmic-Ray Proton (CRP)					
CRP dissociation	$CO + \zeta_{CRP}$	$\rightarrow$	$C + O$	κ_{CRP}	
CRP ionization	$H_2 + \zeta_{CRP}$	$\rightarrow$	$H_2^+ + e^-$	κ_{CRP}	
Cosmic-Ray Photon (CRν)					
CRν dissociation	$CO + \zeta_{CR\nu}$	$\rightarrow$	$C + O$	$\kappa_{CR\nu}$	
CRν ionization	$C + \zeta_{CR\nu}$	$\rightarrow$	$C^+ + e^-$	$\kappa_{CR\nu}$	
Collisional Dissociation	$H + H_2$	$\rightarrow$	$H + H + H$	κ	most having high barrier (> 1 eV)
Three Body reactions[b]	$H + H + H$	$\rightarrow$	$H + H_2$	κ_{3body}	

Types are taken from Woodall et al. (2007), except for *a.* from Herbst (1981) and *b.* from Anicich (1993).
κ [cm^3s^{-1}] = $\alpha(T/300)^\beta e^{-\gamma/T}$, with α, β, γ as laboratory rate coefficients.
$\kappa_{h\nu}$ [s^{-1}] = $\alpha e^{-\gamma A_v}$, with A_v as visual extinction.
κ_{CRP} [s^{-1}] = $\alpha\zeta$, with ζ as H_2 cosmic-ray ionization rate.
$\kappa_{CR\nu}$ [s^{-1}] = $\alpha(T/300)^\beta\gamma/(1-\omega)$, with $\alpha = 1.3 \times 10^{-17}$ and ω as dust grain albedo in the far ultraviolet.
κ_{3body} [cm^6s^{-1}/cm^3s^{-1}].

B. Grain Surface Reactions

Reaction type	Example			Rate
Adsorption	H_2O	$\rightarrow$	H_2O (ice)	κ_{ads}
Desorption	H_2O (ice)	$\rightarrow$	H_2O	κ_{des}
Grain-surface Hydrogenation	O (ice) + H (ice)	$\rightarrow$	OH (ice)	κ_{sur}
Grain-surface Radical-radical	OH (ice) + H (ice)	$\rightarrow$	H_2O (ice)	κ_{sur}

$\kappa_{ads} = \sigma_d\langle v_{th}(i)\rangle n_d$, with σ_d as dust cross-section, v_{th} as species thermal velocity, and n_d as grain density.
κ_{des}, e.g., Leger et al. (1985) and Semenov et al. (2010).
κ_{sur}, e.g., Hasegawa et al. (1992).

(1) HMSC: In the dense cloud ($n > 10^4\,cm^{-3}$), at low dust temperature (10–20 K), a few gas phase atoms land (freeze out), and all of them except for He adsorb on the icy surface. If sufficiently light, these atoms (e.g., H, O, C, N) can migrate, and reactions may occur over the surface by tunnelling or thermal hopping (Tielens & Hagen 1982), predominately producing H_2 and probably partial hydrogenations/deuterations (e.g., CH, NH, OH, NH_2, CH_2, CH_3). Gas phase CO may also freeze out to the grain surface, and some of them produce HCO $\rightarrow$ H_2CO $\rightarrow$ CH_2OH/CH_3O $\rightarrow$ CH_3OH (Woon 2002) or other COMs (e.g., zero generation COM, Aikawa et al. 2012; Garrod 2013) subsequently, while some other species are triggered by small UV irradiation at elevated temperatures (20–40 K, Bacmann et al. 2012), and produce radicals (e.g., CH_3O^+, HCO^+, N_2H^+) in the warm-up period. Sublimation back into the gas phase is slow at such temperatures compared to the accretion of new materials, while the diffusion of atomic hydrogen appears to be relatively fast. At this stage, an icy mantle is formed with large amounts of H_2O, followed by CO, CO_2, some CH_4 and NH_3 (Öberg et al. 2011).

(2) HMPO: In the process of prestellar collapsing, compression, accretion luminosity and potentially already hydrogen burning heat the gas and dust, leading to radicals association forms larger molecules such as $HCOOCH_3$ (first generation COM) in a HMPO stage. From this stage on, the central core of the protostellar object progressively reaches the hydrostatic equilibrium, and molecules (e.g., radicals like HCO^+, simple organics like H_2CO, and zero generation COMs like CH_3OH) on the grain surface start to be evaporated back to the gas, mainly due to thermal heating (Gerner et al. 2014).

(3) HMC: No critical point has been defined yet in the continuous evolution from HMPO to the HMC phase, but the process of sublimation becomes intense as gas and dust temperature increase via several mechanisms, e.g., thermal evaporation, cosmic-ray spot heating, explosive desorption, liberation by reaction, grain-grain collision in turbulent layers (D'Hendecourt et al. 1985; Hasegawa & Herbst 1993; Shalabiea & Greenberg 1994; Aikawa et al. 2005, 2008; Garrod et al. 2008). When the envelope reaches a temperature $T > 100$ K, evaporated CH_3OH, H_2CO and radicals rapidly become protonated, and produce more COMs or even Polycyclic aromatic hydrocarbons (PAHs) (second generation COM) through ion-neutral and neutral-neutral reactions in the warm dense gas of the HMC (van der Tak et al. 2007). In addition, violent dynamic processes (e.g., outflows interacting with the envelope) can even destroy the grain core, bringing SiO to the gas.

(4) UCHII: Envelope may still be accreted even after hydrogen fusion initiates in the central star. The UV photons from the burning star and the interstellar comic rays dissociate the COMs and ionise the diluted envelope, forming a thin layer of PDR, which consist of ionized carbon (CII), neutral hydrogen (HI) and oxygen (OI), as well as cascade products of recombination lines (Kim & Koo 2001; Jeyakumar & Roshi 2013; Krumholz et al. 2014).

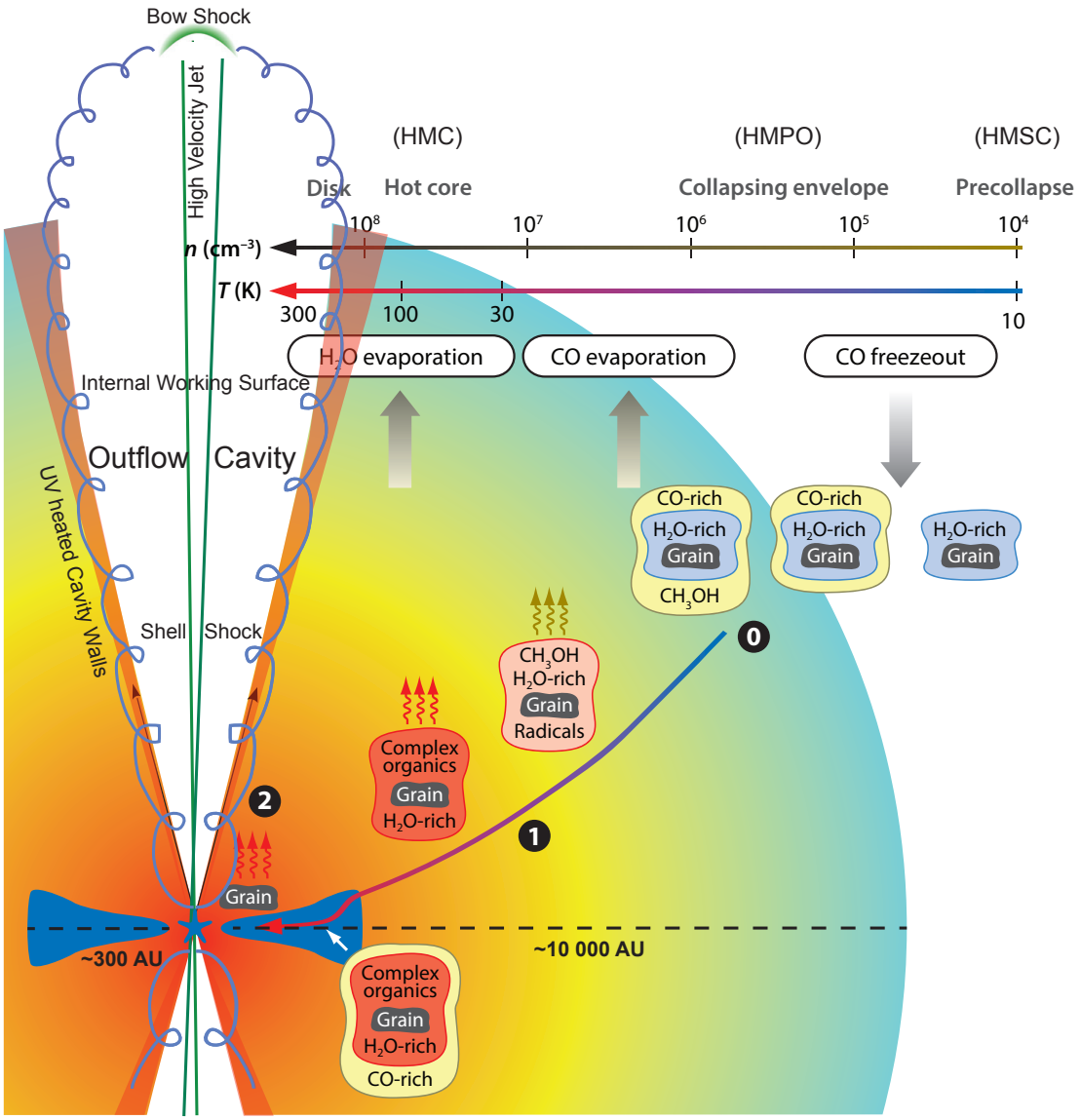

Figure 1.2: Schematic representation of the COM formation from collapsing HMSC through HMPO to the HMC. This cartoon used to suggest the molecular evolution, feedback processes in the low mass star forming region in Herbst & van Dishoeck (2009); van Dishoeck et al. (2011) and early ice formation in Öberg et al. (2010), and is adopted in this thesis (with some modifications), suggesting similar chemical evolution route of COMs in the high mass star forming process: CO freezes out on the grain surface in the HMSCs, and may be partially hydrogenated into $H_2CO \rightarrow CH_3OH$ (point 0); association of radicals forms some COMs in the warm-up HMPO period (point 1), and eventually larger COMs are produced from evaporated CH_3OH and H_2CO in the HMC phase (point 2).

1.2.4 Questions

Ever since the foundation of astrochemistry, there are a lot of studies focusing on star forming regions, which aim at using observations to set the boundary conditions for models (e.g., Charnley et al. 2001; Tafalla 2011; Gerner et al. 2014). However, most of them focus on the low mass star forming regions, while HMSFRs still have poorly characterised chemistry. Moreover, some contradictions exist when comparing the observational results to the model predictions (e.g., Neill et al. 2013; Emprechtinger et al. 2013). A more adequate chemical model requires a large sample of observations and to focus on the following topics:

- **Chemical differentiations at the small scales of HMSFRs**
  Molecular clouds are not homogeneous but highly structured with large variations in dynamics and chemistry, especially for the embedded regions of high mass protostellar objects. Several neighbouring regions with similar masses and luminosities may have completely different molecular components, e.g., Orion-KL and Orion S ($1.5' \sim 0.18$ pc apart at a distance of 450 pc, Sutton & Sandell 1996), NGC 6334 I and I (N) ($1.5' \sim 0.8$ pc apart at a distance of 1.7 kpc , Beuther et al. 2005a). Is this an evolutionary effect? Or are there any unknown "enzymes" in these clusters? If initial fragmentation is universally detected in the very early phase of HMSFRs, do they also show similar chemical differentiation at even smaller scales (on the order of 1 000 AU[12])?

- **Chemical properties in IRDCs**
  Although some cores in IRDCs show chemical similarities to low mass prestellar objects (e.g., high depletion factor, high deuterium fraction and large abundant of N-bearing molecules), the number of studied regions is limited. Moreover, other questions on the initial chemical condition of HMSFRs still remain: Is there any spatial correlation between the highly depleted molecules (e.g., CO) and N-bearing radicals (e.g., N_2H^+), suggesting that CO is the predominant destruction agent for N_2H^+ (Jørgensen et al. 2004)? What is the abundance of carbon chains (early time indicator, e.g., Hirota et al. 2009)? What is the ionization rate and can it be used to constrain the rate of YSO contraction? Are the IRDCs really quiescent or are there any chemical difference indicating hierarchic fragmentation within these filamentary structures?

- **The COMs**
  Gas phase COMs from several observations have comparable abundance to those detected in the icy envelopes of some YSOs, which indicates that the COMs are sublimated from icy grain mantles. However, this hypothesis was recently contested, owing to the fact that

[12] 1 AU $\sim 4.8 \times 10^{-6}$ pc

observed abundance of COMs are several orders of magnitude lower than the model prediction (Peeters et al. 2006). Since both the surface physics and dust grains chemistry are poorly defined, especially when the low temperatures effect is considered, whether the COMs are from grains or produced by simpler species in the gas is still uncertain. In addition, how far does the chemical complexity go, and are they the precursor of prebiotic molecules are still open questions.

- **Quantitative astrochemistry**
  We have tremendous amounts of ice and gas phase data so far, in both low and high mass star forming regions. Do they show systematic trends? Independent of the physical framework, do the forming processes for both low and high mass stars show similar chemical trends? Can chemistry constrain the timescale of a certain region? These are the essential questions we are looking forward to the answers.

1.3 Observational Approach

Our knowledge of chemistry in HMSFRs depends on spectral line studies from a large sample of observations. Due to the source geometry, lines at both near-mid-infrared (from molecular ro-vibration) and (sub)mm wavelengths (from molecular rotation) may appear as emission or absorption features. However, lines from rotational transitions are preferred for studies of the complicated environment of HMSFRs, because they are sensitive to both cool and warm gas (E_u/k_B ranges from 10 K to 1 000 K, compared to ro-vibration $E_u/k_B > 1\,000$ K), and do not suffer from extinction.

Given that HMSFRs are on average further away than the low mass star forming regions, and that they are forming in a clustered mode, to disentangle the cores at different evolutionary stages challenges the spatial resolution of modern (sub)mm telescopes. For example, at a spatial resolution of 7″, a telescope is able to obtain information from the envelope of YSO (size of 1 000 AU) in Taurus (at a distance of $\sim$ 140 pc), or to pierce the outer disk of this source at 0.7″ (size of 100 AU), or to explore its inner disk at 0.04″ (size of 5 AU). In contrast, we need at least 3 times higher spatial resolution if we want to resolve the structures on the above scales in the nearest HMSFR Orion (at a distance of $\sim$ 450 pc) or further. Moreover, many gas-phase molecules (especially COMs) have low abundances (e.g., 10^{-11}–10^{-12} with respect to H_2), and some species have extended distributions which may be "filtered out" (Bajaja & van Albada 1979) by interferometric telescopes. Therefore, to unveil the chemical complexity of HMSFRs and associated shocks requires instruments to perform observations at high spectral and spatial resolution, with high sensitivity and complete information on all scales.

Below I summarise the capabilities of (sub)mm instruments which I have used to obtain data in this thesis, and the most powerful radio instruments for the upcoming 1–2 decades (Figure 1.3).

- Submillimeter Array (SMA)
  Located on Mauna Kea, Hawaii, the SMA[13] has already served for observations at around 230, 345, 400/690 GHz (1.3 mm, 870 μm, 750/435 μm) with 2 polarisations since 2003. Recently, in parallel to the SMA legacy ASIC (Application-Specific Integrated Circuit) correlators, new SWARM correlators (SMA Wideband Astronomical ROACH2 Machine) started to come into operation, which provide a total observational band as wide as 6 GHz (4 GHz ASIC+2 GHz SWARM) from each of 2 receivers. Eight 6 m antennas are in the array, from which 4 configurations, with a maximum baseline of 500 m, are available: subcompact, compact, extended and very extended. During the past decade, it has revealed to us various interesting features ranging from dense prestellar cores in IRDCs to the magnetic field structure of high mass outflows, at the scale from galactic center to the extragalactic HMSFRs at high spatial resolution[14].

- IRAM telescopes & NOrthern Extended Millimeter Array (NOEMA)
  IRAM[15] operates two sub (mm) instruments: a 30 m diameter single-dish telescope and a six-antenna array with 15 m diameter dishes (Plateau de Bure Interferometer, PdBI). The 30 m telescope is located on Pico Veleta, Spain. With dual polarisation HERA (HEterodyne Receiver Array)/EMIR (Eight MIxer Receiver) and NIKA (New IRAM KIDs Array)/GISMO (Goddard-IRAM Superconducting 2 mm Observer) receivers, it is able to map the extended emissions from gas and dust at 3, 2, 1 and 0.8 mm wavelengths. Located in the French Alps, the PdBI array can be arranged in four (ABCD) configurations, with a maximum baseline of 760 m. Observations can be performed with PdBI at the same bands as the 30 m. Although PdBI covers a narrower bandwidth (4 GHz) than the 30 m (8 GHz) so far, data from both telescopes can be combined to obtain complete spatial information in the whole field of view. The successor to the PdBI is NOEMA. By doubling the number of PdBI antennas, it will reach a maximum 2 000 m baseline in the near future. It has the aims of exploring some of the most fundamental fields of modern astronomy, e.g., detecting COMs while searching for the key elements of life, following various stages of star formation and stellar evolution, this telescope will be the most powerful (sub)mm radio telescope of the northern hemisphere.

[13] http://sma1.sma.hawaii.edu/status.html
[14] http://www.cfa.harvard.edu/sma/events/smaConf
[15] http://iram-institute.org

Figure 1.3: The most advanced submillimeter interferometers in use so far. Top: SMA (credit: SMA); middle: PdBI (credit: MPG); bottom: ALMA under construction (credit: ALMA/ESO/NRAO/NAOJ).

- Atacama Large Millimeter/submillimeter Array (ALMA)
  One of the most powerful (sub)mm arrays in existence by far is ALMA[16], which is located at the Chajnantor plateau, Chile, and is expected to cover the spectral window from 30 to 950 GHz. With fifty 12 m-antennas in the long baseline configurations (maximum baseline of 15 km) in use, observations are able to reach at a maximal resolution of 0.01″. Additionally, the ACA (Atacama Compact Array, twelve 7-m antennas) and the TP (Total Power array, four 12 m antennas) will complement the short baseline simultaneously. Although it has not been fully constructed, the early science carried on in Cycle 0–2 has reached high sensitivity, and revealed to us intriguing results ranging from outflow, jets, protoplanetary disks and ionized winds to the identification of prebiotic lines, and chemical properties in the very early phase of star forming regions (e.g., rings in the HLTau disk, and Jørgensen et al. 2012; Arce et al. 2013; Peretto et al. 2013). Therefore, we are expecting ALMA to push the limits of the exploration of our universe in the near future.

1.4 About This Work

Line surveys of HMSFRs in the mm/sub-mm atmospheric windows allow us to observe evolutionary differences in molecular emission spectra (see Herbst & van Dishoeck 2009 for a comprehensive review, Foster et al. 2011; Sanhueza et al. 2012; Hoq et al. 2013; Jackson et al. 2013; Gerner et al. 2014). The multitude of detected lines allow for an unbiased statistical analysis of the evolution of the chemical compositions on large scales ($> 10^5$ AU). However, what are the chemical properties within a particular region? Can we witness any fragmentation in a HMSFR in the very early stage? Do the fragments display homogeneity in their chemistry or are there large variations? Can we use certain lines as a diagnostic to indicate the dynamical properties of that region? With the advancement of the high spatial resolution capabilities of modern facilities, we aim to provide direct observational constraints on detailed aspects of formation theories such as hierarchical fragmentation, and shocks, which are expected to lead to chemical variation on small scales ($< 2\,000$ AU) in HMSFRs. Recently, a few studies have been undertaken (e.g., AFGL 2591, Jiménez-Serra et al. 2012; IRDC G11.11-0.12, Wang et al. 2014; IRDC G11.92-0.61-MM2, Cyganowski et al. 2014), but only by observing the chemical composition of a larger number of HMSFRs at the high resolutions can these formation theories be rigorously tested. To explore this question, in this thesis I focus on studying the chemistry of several HMSFRs on small scales, in the phases ranging from HMSC to HMC.

[16] http://www.almaobservatory.org/

To make clear the definition of different spatial structures, I adopted the nomenclature from Zhang et al. (2009): a structure with a typical size of ~ 1 pc is named as a "clump", which is capable of forming a cluster of stars; a "core", with a size of ~ 0.1 pc, contains a group of prestellar objects or protostars; and a "condensation" is a ~ 0.01 pc substructure within the core, which can form a star or multiple-star system later.

This thesis is structured as the follows. First, we turn our attention to the nearest HMSFR Kleinmann-Low Nebula in Orion (Orion-KL). In Chapter 2[17] I present a line survey of Orion-KL at 1.3 mm obtained from combined SMA interferometric and IRAM 30 m single-dish observations. The observations resolve Orion-KL into several individual substructures in the continuum map at a spatial resolution of 3″ (1 200 AU at a distance of 414 pc). Spectra extracted from each substructures reveal chemical variations internal of this HMC source. Thanks to the high sensitivity of the combined data for the first time, I identify more than 160 emission lines from 19 species (24 isotopologues), including 11 complex organic molecules (COMs). By analysing the spatial distribution and chemical properties (molecular abundance) of the associated (N-, O-, S-bearing) gas, I characterise the physical environment (temperature, dust density) of Orion-KL, from the central hot core to the ambient outflow regions.

Orion-KL provides us an important template for interpreting the chemistry of more distant HMSFRs. Therefore, in Chapter 3[18] I present continuum images and spatial distribution maps of 15 species (including 21 isotopologues) in two neighbouring HMSFRs, NGC 7538 S and NGC 7538 IRS1, which are obtained from PdBI at 1.3 mm. Although separated by only 80″ (1 pc at a distance of 2.65 kpc), these two sources exhibit distinct features for both continuums and spectral lines at a spatial resolution of 0.4″ (1 000 AU). On one hand, chemical and physical analysis of the observational results are combined with gas-grain modelling, with the aim of interpreting the "hierarchical fragmentation" within NGC 7538 S at the scale of 5 000 AU (i.e., NGC 7538 S fragments into 3 condensations with similar continuum intensities but different spectral line emissions). On the other hand, chemical and dynamic hypothesis are given to interpret the atypical "absorption mixed with pure emission" spectrum at mm wavelength in the unresolved central of core IRS1. This is the first case study combining observational results to modelling in this region[19], which reveals the chemical complexity within a small scale of HMSFR, and illustrates the strength of chemical diagnostics in constraining the evolutionary stages.

[17] based on a paper submitted to A&A

[18] based on a paper submitted to A&A

[19] I focus on the observation analysis, while the chemical network and fitting in this thesis was contributed by my collaborator Dmitry Semenov.

Fragmentation is clearly observed in the above HMC sources. Now, our curiosity on the very initial stages of HMSFRs drive us to observe more IRDCs with high spatial resolution. In Chapter 4[20], I present the observational results of four IRDCs obtained from both SMA and IRAM 30 m telescopes. At a spatial resolution of 2″ (∼ 0.05 pc at a distance of 3.6–4.8 kpc), the fragments have on average mass > 10 $M_{\odot}$, exceeding the Jeans mass of the large-scale clump and supporting the "core accretion" scenario, while no line detection at 1.1 mm at this scale indicate that these regions are in the very cold environments (T < 20 K). In contrast, line surveys at 1 mm and 3 mm reveal that these regions at a larger scale (1.5′∼ 2 pc) are not completely chemically quiescent. Instead, high depletion of CO, high ionization factor, a large number of N-bearing molecules, the appearance of carbon rings, and anti-correlated spatial distribution between N_2H^+, NH_2D and CO are similar properties to low mass protostellar regions. In addition, an asymmetric line profile of HCO^+ implies infall motion, while a > 5σ detection of shock tracer (SiO) indicates protostellar objects may already exist in some regions.

Finally in Chapter 5 I summarise the work presented in this thesis and highlight what I made to improve our understanding of chemistry in the HMSFRs. Last but not least, I list the ongoing and potential works in the framework of this thesis.

[20]based on a paper in preparation

2 Resolving the chemical substructure of Orion-KL

2.1 Motivation

The Becklin-Neugebauer and Kleinmann-Low Nebula in Orion (Orion BN/KL), at a distance of 414 ± 7 pc (Sandstrom et al. 2007; Menten et al. 2007), is ideal for studies of the physical and chemical properties of HMSFRs. As the nearest HMSFR, Orion-KL has been characterised as a typical HMC source via extensively observations at both far-infrared to (sub)mm wavelengths accessible from space (e.g., Olofsson et al. 2007; Bergin et al. 2010; Crockett et al. 2014) and radio, mm and submm wavelengths accessible from the ground.

Previously, a broad range of studies on Orion-KL have been conducted either with single-dish telescopes (e.g., Johansson et al. 1984; Sutton et al. 1985; Blake et al. 1987; Turner 1989; Greaves & White 1991; Schilke et al. 1997, 2001; Lee & Cho 2002; Comito et al. 2005; Remijan et al. 2008; Tercero et al. 2010) or interferometers (e.g., Wright et al. 1996; Blake et al. 1996; Beuther et al. 2005b, 2006; Friedel & Snyder 2008; Guélin et al. 2008). Strong emission lines in these observations have revealed complex dynamics (e.g., Sutton et al. 1985; Blake et al. 1987; Turner 1989; Beuther & Nissen 2008; Beuther et al. 2010b) and chemistry (e.g., Wright et al. 1996; Blake et al. 1996; Beuther et al. 2005b, 2006; Friedel & Snyder 2008; Guélin et al. 2008; Widicus Weaver & Friedel 2012; Friedel & Widicus Weaver 2012). However, both single-dish-only and interferometer-only observations have limitations. Single-dish observations have low spatial resolution, making it difficult to detect spatial variations of chemistry on small scales. In contrast, interferometric observations can probe spatial variations on small scales, but suffer from filtering-out to large scale structures (the "missing short spacing" problem, Bajaja & van Albada 1979), making measurements of the chemistry of more extended features unreliable. Therefore, to study the chemistry at small scales of Orion-KL with a full spatial coverage, we need to obtain a combined dataset from both interferometric and single-dish telescopes.

A typical HMC source is a compact object (hot core) characterised by high temperature and high density gas, including a large number of gas-phase COMs. Recently, several interferometric observations of COMs in Orion-KL (e.g., Friedel et al. 2005; Friedel & Snyder 2008; Guélin et al. 2008; Favre et al. 2011a,b; Widicus Weaver & Friedel 2012) have shown spatial-related chemical differentiation. However, the relatively low sensitivity of these observations means that the lowest abundance COMs (e.g., CH_2OHCHO, CH_3CH_2OH and CH_3CHO) are below the 3σ detection limit, or are blended by strong neighbourly lines. With our high sensitivity and high spatial resolution data, one goal of this study is to search for more COMs, and to investigate their chemistry by comparing their spatial distributions and abundances.

In the HMC sources, outflow is an important mechanism, because it can sputter mantle/core grains, produce shocks, heat the surrounding ISM and shape the parent molecular clouds (e.g., Offner et al. 2013; Bate et al. 2014; Krumholz et al. 2014). The region in Orion-KL which is most affected by outflow and shock events is call the "plateau" (Blake et al. 1987; Wright et al. 1996; Lerate et al. 2008; Esplugues et al. 2013), and is characterized by spectra with broad line wings. Two roughly perpendicular outflows are seen in Orion-KL, traced by the proper motion of H_2O masers at 22 GHz (Genzel et al. 1981). One is a high-velocity outflow (30–100 km s^{-1}, along the northwest-southeast (NW–SE) axis); this outflow is also detected in OH (hydroxyl) masers (Norris 1984; Cohen et al. 2006), broad bipolar CO line wings (Zuckerman et al. 1976; Kwan & Scoville 1976; Erickson et al. 1982; Masson et al. 1987; Chernin & Wright 1996; Beuther & Nissen 2008; Zapata et al. 2009), and lobes of poorly collimated shock-excited H_2 (Beckwith et al. 1978; Scoville et al. 1982; Taylor et al. 1984; Allen & Burton 1993; Sugai et al. 1994). Although the source responsible for driving the outflow is still uncertain, the outflow is suggested to be only about 500–700 years old (Lee & Burton 2000; Doi et al. 2002; Gómez et al. 2005; Nissen et al. 2007; Gómez et al. 2008; Beuther & Nissen 2008; Bally et al. 2011; Goddi et al. 2011; Nissen et al. 2012). The other is a low-velocity ($\sim$ 18 km s, $\triangle$V $\sim$ 35 km s^{-1}, along the northeast-southwest (NE–SW) axis) outflow (Genzel et al. 1981; Gaume et al. 1998), which is also detected in SO (Plambeck et al. 1982) and SiO masers (Wright & Plambeck 1983; Plambeck et al. 2009). This outflow is believed to be closely associated with an expanding gas shell or torus around Source I, but whether its age is $>$ 3 000 years (Menten & Reid 1995; Greenhill et al. 1998; Doeleman et al. 1999; Reid et al. 2007) or much younger (Plambeck et al. 2009) is still not clear. Another goal of this study is to look for additional chemical signposts of these outflows, apart from the known masers, in order to better understand their physical and chemical properties.

In this chapter, we present the first combined interferometric (SMA) and single-dish (IRAM 30 m) line survey at 1.3 mm toward Orion-KL. These combined data, which resolve small-scale substructure at a linear resolution of 1 200 AU and are sensitive to more extended components, allow us to accurately map the distribution of molecular species, to determine their abundances and ultimately to analyse spatial variations in the chemistry. In Section 2.2, we describe the

observations and their combination. In Section 2.3, we present a continuum map and maps of the distribution of different molecules, including simple molecules and COMs; where the presence of COMs is identified by synthetic spectrum fitting. The spatial distribution of column densities and abundances for all the detected species are derived in Section 2.4, and a discussion of the chemistry in the hot core and outflows of Orion-KL can be found in Section 2.5.

2.2 Observations and Data Reduction

2.2.1 Submillimeter Array (SMA)

We carried out observations of Orion-KL with the SMA on Feb 15th, 2005 and Feb 19th, 2005. At 1.3 mm (220/230 GHz) in the compact configuration with 7 antennas, the baselines rang between 16 and 69 m. The short baseline cutoff causes source structures $\geq 20''$ to be filtered out. The primary beam is $52''$, and the phase center of the observations is $\alpha_{2000} = 05^{h}35^{m}14.5^{s}$ and δ_{2000}=−5°22′30.45″ with $V_{lsr} \sim 7$ km s^{-1}. Bandpass calibration was done with Callisto, and the flux calibration is estimated to be accurate within 15%, based on the SMA monitoring of quasars. Phase and amplitude calibration was performed via frequent observations of the quasar 0607-157. The zenith opacities, measured with the NRAO tipping radiometer located at the Caltech Submillimeter Observatory, were exceptionally good during both tracks with $\tau(1.3\text{ mm}) \sim 0.03 - 0.04$, because the 1.3 mm data were observed simultaneously with 440 μm data (Beuther et al. 2006). Further technical descriptions of the SMA and its calibration schemes can be found in Ho et al. (2004). The receiver operated in a double-side band mode with an intermediate frequency of 4–6 GHz so that the upper and lower side band were separated by 10 GHz. The correlator had a bandwidth of 2 GHz and the channel separation was 0.8125 MHz, corresponding to a velocity resolution of 1.2 km s^{-1}. Measured double-side band system temperatures corrected for the atmosphere were between 150 and 300 K (depending on the elevation of the source).

The initial flagging and calibration was done with the IDL superset MIR, which was originally developed for the Owens Valley Radio Observatory and adapted for the SMA[1]. The imaging and data analysis was conducted in MIRIAD (Sault et al. 1995) and CASA[2]. Between the two observations, the frequency setups were shifted by 0.4 GHz, yielding a slightly larger total bandwidth for the combined dataset (218.870–221.234 GHz for the lower sideband, and 228.870–231.234 GHz for the upper sideband). The synthesised beams of the combined data are $3.49'' \times 2.57''$ for the lower sideband and $3.68'' \times 2.69''$ for the upper sideband, respectively.

[1] http://cfa-www.harvard.edu/~cqi/mircook.html.
[2] http://casa.nrao.edu

2.2.2 Single-dish observations with the IRAM 30 m telescope

In addition to the high spatial resolution data from the SMA, we mapped an area of $1' \times 1'$, with the IRAM 30 m telescope, to complement the short-spacing information missing from the interferometric observations. Observations were performed in the on-the-fly mode on 30th November 2012, covering a broad bandpass (8 GHz bandwidth for each sideband) of EMIR at 220/230 GHz. Observations were conducted under excellent weather conditions (T_{sys} = 266 K, $\tau \sim 0.152$ at 220 GHz). The focus was on Uranus and pointing was checked on Uranus and 0420-014. Using a forward efficiency of 92% and a main beam efficiency of 58%, we converted the data from antenna temperature (K) to flux (Jy) by using an efficiency[3] of 7.8. The beam of the 30 m telescope at 230 GHz is $\sim 11.3''$ in the upper band side and $\sim 11.8''$ in the lower band side. The observations cover frequencies 213.4–221.2 GHz and 229.2–236.8 GHz, with a velocity resolution of 0.255 km s^{-1}. We used the Gildas[4] software for data reduction, and then converted the 30 m data to the MIRIAD data format.

2.2.3 Data merging

The 30 m single-dish spectral line data were first converted to visibilities, and then combined with the SMA data using the MIRIAD package task UVMODEL. To recover large-scale emission, while simultaneously maintaing high spatial resolutions for resolving small scale structure, we chose an intermediate weighting between natural and uniform ("robust"= −0.5 value in MIRIAD). However, as continuum information is not available from the 30 m observations, only the spectral-line data can be corrected in this way.

The combined data have a field of view of 52″, and a beam of $5.55'' \times 4.35''$ with position angle P.A. = +8° in the lower sideband and $5.44'' \times 4.43''$ with P.A. = +2° in the upper sideband. The frequency overlap between the SMA and 30 m data results in the combined data having a frequency range 218.870–221.150 GHz and 229.052–231.234 GHz. Figure 2.1 presents amplitude versus projected uv distance plot, showing the good combination of the single-dish and interferometer data. Missing projected baselines shortward of 10 kλ from the SMA have hereafter been complemented by using the 30 m data. After combination, the 1σ rms per 1.2 km s^{-1} channel is measured to be 80 mJy beam^{-1} for the lower sideband, and 70 mJy beam^{-1} for the upper sideband.

[3] http://www.iram.es/IRAMES/mainWiki/Iram30mEfficiencies
[4] http://www.iram.fr/IRAMFR/GILDAS

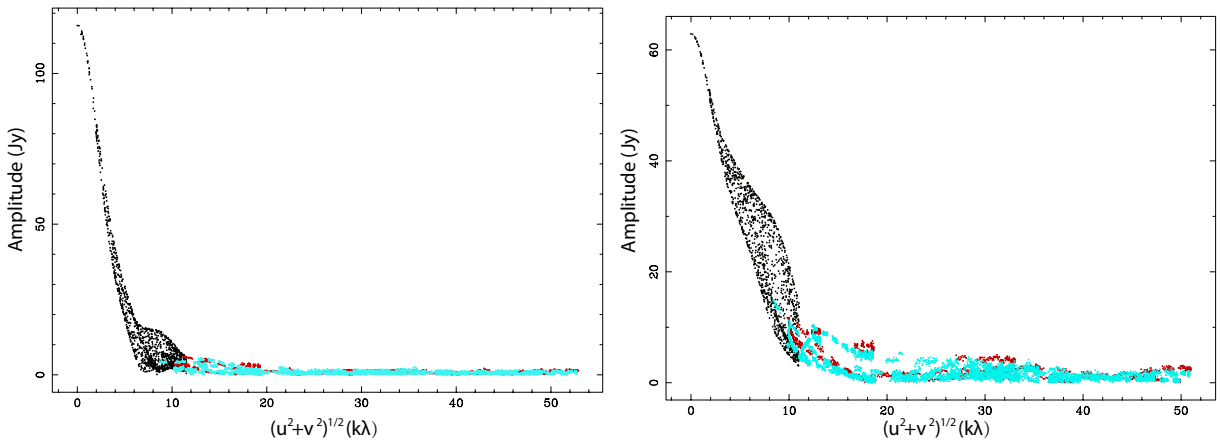

Figure 2.1: The amplitude in Jy versus the projected baseline shows the combination of the interferometer and single-dish data, from the upper side-band (top) to lower side-band (bottom). Red and blue dots present data from SMA on Feb. 15, 2005 and Feb. 19, 2005, respectively, showing the lack of baselines shorter than 10kλ. Black dots are data converted from 30 m single-dish observations, which fill in the missing short spacing information.

2.3 Observational Results

2.3.1 Continuum emission

Orion-KL has a rich spectrum of molecular emission lines, so extracting the continuum requires some care. To construct our continuum map, we average the line-free parts of the upper and lower sideband from the SMA-only data , and present the resulting 1.3 mm continuum image as contours overlaid on a map of the outflow traced by shock-excited H_2 (Nissen et al. 2007) in Figure 2.2. We detect the previously known compact continuum substructures of this region, and resolve some of these substructures into multiple distinct sources. We list the following resolved condensations in Table 2.1:

- The brightest Hot Core (HC): located close to a well-studied infrared source IRc2 (Downes et al. 1981; Wynn-Williams et al. 1984), it is the first condensation in Orion-KL detected by the high spatial resolution mm observations (Masson et al. 1985; Mundy et al. 1986; Woody et al. 1989; Wright et al. 1992), and it exhibits the largest peak specific intensity (Jy beam^{-1}) in the 1.3 mm SMA continuum map. With the temperature estimated to be 100-300 K (e.g., Wilner et al. 1994; Wilson et al. 2000; Beuther et al. 2005b), this source has been found to be abundant in hydrogenated species and nitrogen (N-) bearing molecules (Sutton et al. 1995; Blake et al. 1996; Wright et al. 1996; Wilson et al. 2000). With even higher resolution (0.7″, $\sim$ 300 AU), observations from SMA at 865 μm/348 GHz expose additional substructure within the HC (Beuther et al. 2004). Presented as black contours overlaid on the 1.3 mm colormap in the inner panel of Figure 2.2,

these structures are: hotcore (hereafter we use "HC" to denote the whole region from 1.3 mm continuum, and "hotcore" to denote the position from 865 μm continuum), SMA1 (a high-mass protostellar source, suggested to be the driving source of the high-velocity outflow, Beuther & Nissen 2008), Source I (located at the center of the SiO masers, and believed to drive the bipolar low-velocity outflow; Menten & Reid 1995) and Source N (a Herbig Ae/Be or mid-B star with a luminosity of $\sim 2\,000\,L_{\odot}$, Menten & Reid 1995; Greenhill et al. 2004; Gómez et al. 2005; Rodríguez et al. 2005; Goddi et al. 2011; Nissen et al. 2012).

- mm2: located $\sim 7''$ west of the HC, and $\sim 5''$ south of the BN object. Coincident with infrared source IRc3, IRc6 and IRc20 (Dougados et al. 1993), this condensation is also known as the western clump (WC; Wright et al. 1992), or the northwest clump (NWC, Blake et al. 1996; Tang et al. 2010; Favre et al. 2011a). The mass (2–3$M_{\odot}$), H_2 column density, and high temperature (a few hundred K) in this source suggest that it may be the site of ongoing low-mass star formation there (Schreyer & Henning 1999).

- mm3a & mm3b: These two condensations are located southwest of the HC. Coincident with infrared IRc5 (Dougados et al. 1993), they were previously considered to be a single clump called the southwest clump (SWC, Tang et al. 2010), or CntC (Murata et al. 1992), situated at the compact ridge (CR, Blake et al. 1996; Wright et al. 1996; Tang et al. 2010). Similar dual continuum peaks have been detected in other high spatial resolution observations of HMSFRs (Tang et al. 2010; Favre et al. 2011a; Friedel & Widicus Weaver 2011), and so we consider them to be separate sources. The CR is known to have different kinematics and chemistry compared to the HC: it is a vast region ($\sim$ 15–25$''$, Plume et al. 2012; Esplugues et al. 2013) with a lower temperature (Genzel & Stutzki 1989), is dominated by O-bearing molecules (Blake et al. 1987; Wright et al. 1996; Liu et al. 2002), and is believed to be the region where two outflows interact with the dense ambient material (Blake et al. 1987; Liu et al. 2002). Therefore, to ensure that we fully characterise its chemical properties, the following study focuses separately on mm3a & mm3b, instead of considering CR as a whole.

- The southern ridge (S): the southernmost condensation detected in the 1.3 mm continuum map. Although it has been detected in other observations (Eisner et al. 2008; Favre et al. 2011a), it has not been characterized in detail.

- The northeast condensation (NE): a strong continuum emission peak which is adjacent the HC and the north extended ridge (ER, Sutton et al. 1985; Blake et al. 1987). This condensation is usually filtered out in high spatial resolution observations, but can be clearly detected in interferometric observations made with large scale configurations (Murata et al. 1992; Tang et al. 2010). Comparison with the existing single-dish maps suggests it is as

part of a large-scale dusty filament along the NE–SW direction (e.g., detected by JCMT at 450 μm, Wright et al. 1992; SCUBA at 450 μm and 850 μm, Di Francesco et al. 2008). In addition, this condensation is in the plateau of the low-velocity outflow, so its chemistry may be affected by shocks (Section 2.5.3).

Because of the limited UV coverage and field of view, the high velocity outflow and the BN object are not detected above 5σ in the SMA-only continuum map. To study the chemistry in these regions from the combined data, we take the positions of the high-velocity plateau ($V_{lsr} \sim 11$ km s^{-1}) and BN object from Beckwith et al. (1978), and mark them as OF1N, OF1S, and BN in Figure 2.2.

Table 2.1 lists the nominal absolute positions of these substructures, as well as the peak specific intensity (Jy beam^{-1}) for each continuum substructure, obtained from the SMA-only 1.3 mm continuum map (Figure 2.2, for more detail about this table, see Section 2.4.2). The HC is the brightest condensation, mm2, mm3a and mm3b are fainter, while NE, S, OF1N and OF1S are even weaker.

2.3.2 Spectral line emission

Line identification

After imaging the whole 30 m-SMA combined data cube, we extracted the double sideband spectrum from each substructure marked with red circle in Figure 2.2, and shown these in Figure 2.3. The majority of lines are strongest toward the HC, so we use the spectrum from HC to identify lines. However, line identification is not always unambiguous in a region such as the Orion-KL HC, both because of a high density of lines (that can have different line-width according the species) and because the ~ 1.2 km s^{-1} spectral resolution of the observations does not allow us to separate all the blending. For strong lines, we first compare their rest frequency with an existing single-dish survey catalogue of Orion-KL by Sutton et al. (1985). Next, we cross-check their rest frequencies with the molecular database at "Splatalogue" (Section 1.2.1), and confirm the identification if the CDMS/JPL intensity is $> 10^{-6}$ nm^2 MHz.

In addition to the detection of strong lines marked in Figure A1 using the above method, we can also detect multiple transitions of low abundant COMs in Orion-KL, owing to the high sensitivity and recovering the full intensity for spatially extended molecular emission from the combined dataset. We use a synthetic spectrum fitting program (Sanchez-Monge 2011; Palau et al. 2011) in conjunction with molecular data from the JPL and CDMS catalogs, to simultaneously fit multiple COM lines under the assumption that all transitions are optically-thin, in Local

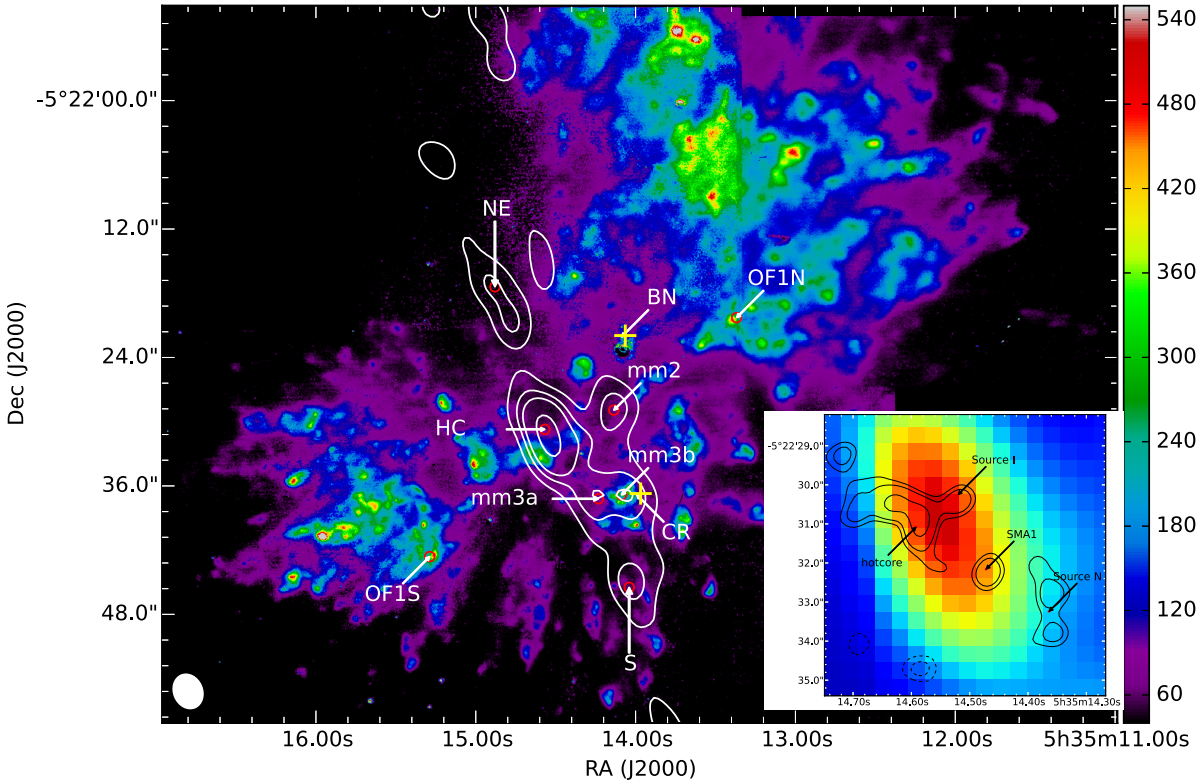

Figure 2.2: The colormap shows the brightness (in counts per 400 s) of shocked H_2 emission (Nissen et al. 2007), and the white contours show the SMA-only 1.3 mm continuum emission at -5σ, 5σ, 10σ, 15σ, 20σ, 30σ and 60σ levels with the rms= 0.04 Jy beam^{-1}. Red circles mark the peaks of Hot Core (HC), mm2, mm3a, mm3b, the southern region (S), northeast condensation (NE), NW and SE parts of the high-velocity outflow (OF1N, OF1S). Yellow crosses mark the BN object and the compact ridge (CR). The beam at the bottom left corner is from the SMA-only data. The insert panel shows the HC region in detail, with black contours of the 865 μm continuum from Beuther et al. (2004) overlaid on the SMA continuum colour map.

Table 2.1: Properties of substructures, which are marked on the continuum image obtained from SMA observations at 1.3 mm (Figure 2.2). Positions with upper case are from the references listed in the footnotes; without are from 1.3 mm SMA continuum observations.

Source		R. A. (α) [J2000] 5h35m ~	Dec. (δ) [J2000] $-5^{o}22^{'}$ ~	I_ν[a] (Jy/beam)	T_{rot} (K)	$N^{d}_{H_2,1}$ (10^{23}cm^{-2}) 3.49"×2.57"	$N^{e}_{H_2,2}$ (10^{23}cm^{-2}) 5.55"×4.35"	Alternative Designations
HC		14.6s	31.0"	2.75 ± 0.3	156 ± 10[b_1] 124 ± 7[b_2] 123 ± 11[b_3] 155 ± 15[b_4] 141 ± 28[b_5]	23.7 ± 3.9 30.1 ± 4.8 30.4 ± 5.6 23.9 ± 4.5 26.3 ± 6.9	11.7 ± 0.5	Ca[j], SMM3[l], CntB[k]
	hotcore[f]	14.58s	30.97"					
	SMA1[f]	14.46s	32.36"					
	Source I[g]	14.51s	30.53					
	Source N[g]	14.35s	33.49					
mm2		14.1s	27.1"	0.87 ± 0.10	110 ± 10[b_1] 110 ± 7[b_3] 129 ± 11[b_4] 126 ± 32[b_5]	10.8 ± 2.1 10.8 ± 1.8 9.1 ± 1.7 9.4 ± 2.8	9.1 ± 0.1	NWC[h,i], Cc[j], SMM2[l], WC[n], CntD[k]
CR[l]		14.0s	36.9"					SWC[i], SMM1[l]
	mm3a	14.3s	37.9"	0.96 ± 0.09	103 ± 5[b_1] 103 ± 5[b_3] 120 ± 9[b_4] 62 ± 16[b_5]	12.8 ± 1.8 12.8 ± 1.8 10.9 ± 1.7 22.0 ± 6.4	6.3 ± 0.1	Cb1[j], CntC[k]
	mm3b	14.1s	36.4"	1.01 ± 0.11	88 ± 5[b_1] 105 ± 5[b_3] 121 ± 11[b_4] 57 ± 14[b_5]	15.9 ± 2.5 13.2 ± 2.0 11.3 ± 2.1 25.4 ± 7.6	6.8 ± 0.05	Cb2[j], CntC[k]
NE		14.8s	19.1"	0.38 ± 0.09	45 ± 2[b_1]	18.9 ± 3.7	3.4 ± 0.03	CntH[k]
S		14.0s	45.4"	0.41 ± 0.06	45 ± 2[c]	13.4 ± 2.5	1.1 ± 0.01	Cd[j], MM23[m]
OF1N		13.4s	20.5"	σ = 0.04	45 ± 2[c]	< 4.0	~ 1.1	PK1[o]
OF1S		15.3s	42.5"	σ = 0.03	45 ± 2[c]	< 3.0	~ 0.6	PK2[o]
BN[o]		14.11s	22.7"					

a. Peak specific intensity I_ν is obtained from each substructure of SMA-only continuum.

b_1. Excitation temperature is from CH_3CN rotation map fitting in Figure 2.8.

b_2. Excitation temperature is from $CH_3^{13}CN$ rotation map fitting in Figure 2.8.

b_3. Excitation temperature is from $HCOOCH_3$ rotation map fitting in Figure 2.9.

b_4. Excitation temperature is from CH_3OH rotation map fitting in Figure 2.9.

b_5. Excitation temperature is from $^{34}SO_2$ rotation map fitting in Figure 2.9.

c. Excitation temperature is assumed the same as that in NE from CH_3CN.

d. H_2 column density is calculated from the SMA-only continuum at substructure peak using Eq. 2.10, performed in Section 2.4.2.

e. H_2 column density is calculated from the conversion of combined SMA-30 m $C^{18}O$ at temperatures derived from $HCOOCH_3$, performed in Section 2.4.2.

References. *f*.Beuther et al. (2004);

g.Menten & Reid (1995);

h.Blake et al. (1996);

i.Tang et al. (2010);

j.Favre et al. (2011a);

k. Murata et al. (1992);

l.Zapata et al. (2011);

m.Eisner et al. (2008);

n.Wright et al. (1992);

o.Beckwith et al. (1978)

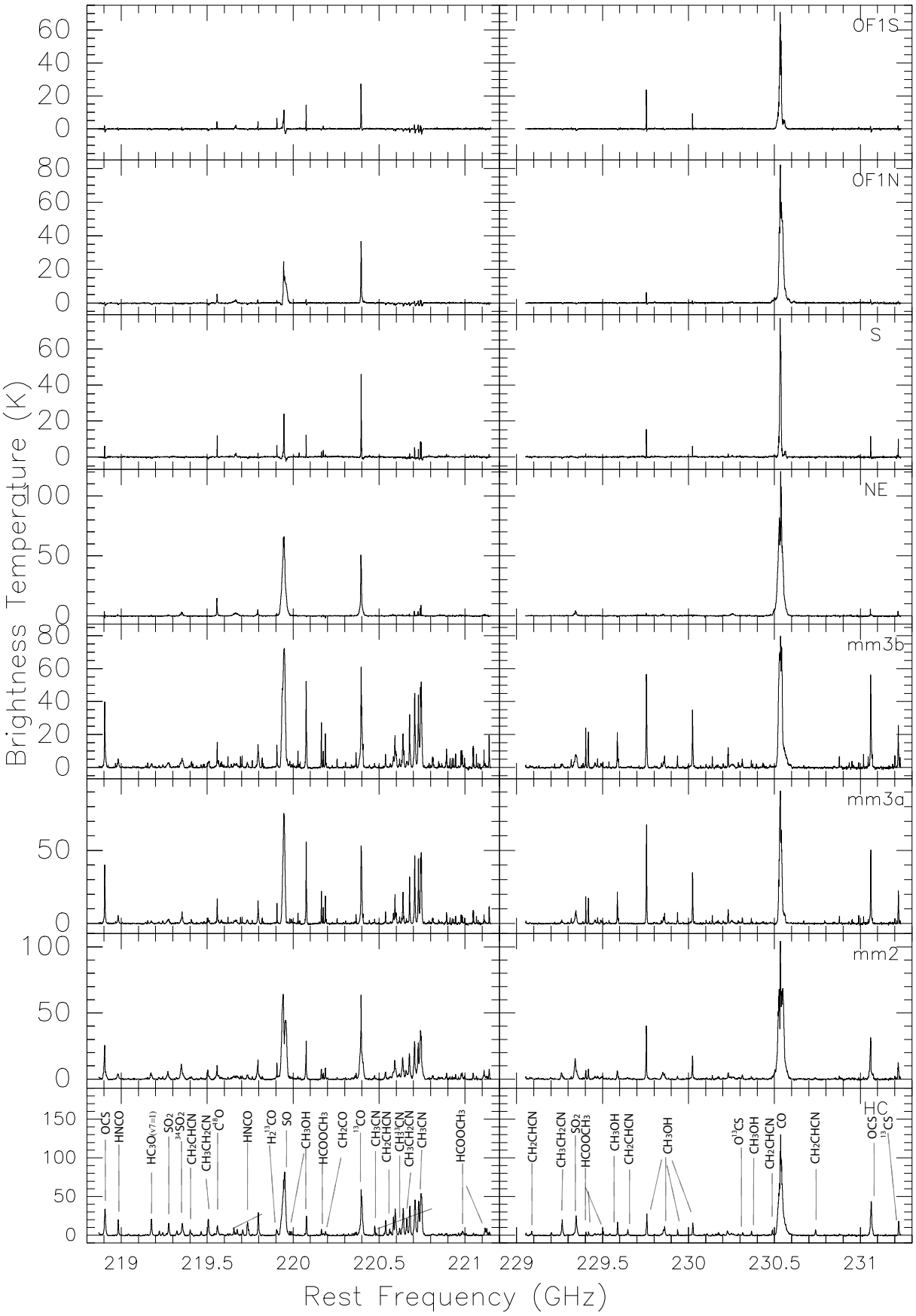

Figure 2.3: Spectra taken toward selected positions (marked with red circles in Figure 2.2) after imaging the whole data cube. The spectral resolution is smoothed to 1.2 km s^{-1} after the combination of SMA and 30 m data, and strong emission lines are labeled. A blow-up figure of the spectrum in the HC is Figure A1.

Thermodynamic equilibrium (LTE), and have the same line width[5]. Given these assumptions, the fitted flux densities are not always a perfect match to the observed spectra. However, in many cases we are able to robustly identify multiple transitions of a COM (Figure A2). We discuss the properties of the identified COM species further in Section 2.3.2.

Employing the above two approaches, we identified more than 160 lines that we have assigned to 24 molecules over the entire band; we label the unblended strong emissions in Figure 2.3, and list all the lines in Table A1. This table includes the rest frequencies, quantum numbers, symmetry label, and upper state energy for each transition. Lines marked with "†" are from molecules containing < 6 atoms shown in Figure 2.4, and those marked with "‡" are from molecules we designate as COMs shown in Figure 2.5. Comparing to the laboratory measured rest frequencies recorded in the "Splatalogue" database, a line from our observations having a frequency resolution of 0.8125 MHz ($\sim$ 1.2 km s^{-1} at 1.3 mm) can be attributed to multiple species. Therefore, the present observations do not allow us to identify those broad-width lines, and we marked these potentially blended lines with "*" in Table A1.

Line imaging

In total, all the lines listed in Table A1 can be attributed to 19 different species (including 24 isotopologues). All of them show different spatial distributions, velocity widths and velocity at line center in each substructure (see Figure A3, on average, centered at V_{lsr} $\sim$ 6–7 km s^{-1} in the HC, V_{lsr} $\sim$ 8–10 km s^{-1} in mm2, mm3a & mm3b, and V_{lsr} $\sim$ 10–12 km s^{-1} in NE). Choosing one of the strongest unblended transitions from each species, we produce their distribution maps from the SMA-30 m combined data. In avoiding contamination from other strong lines, we integrate the intensity of each line through 40%–60% of their profile range in Figure A3 (the chosen velocity ranges are slightly larger than the FWHM of the lines, in order to account for the small variation in the peak velocity between different substructures).

The combined data at 230 GHz covers a field of view of 52″, which is larger than the extent of the source (not including the outflows), so our maps exhibit negligible artifacts caused by residual missing flux. The high quality of our data allows us to map molecules such as $^{34}SO_2$, $O^{13}CS$, HNCO, $H_2^{13}CO$, ^{13}CO and CH_2CO for the first time with both high resolution and sensitivity to spatial information on all scales. Sorted by different groups, we present the flux integration map

[5]The synthetic fitting program we use here is for line detection, but not finding the best fit of column density and temperature to the observations. Because the synthetic fitting is performed with optically thin assumption, it can also be used to indicate whether a particular line is optically thin or not.

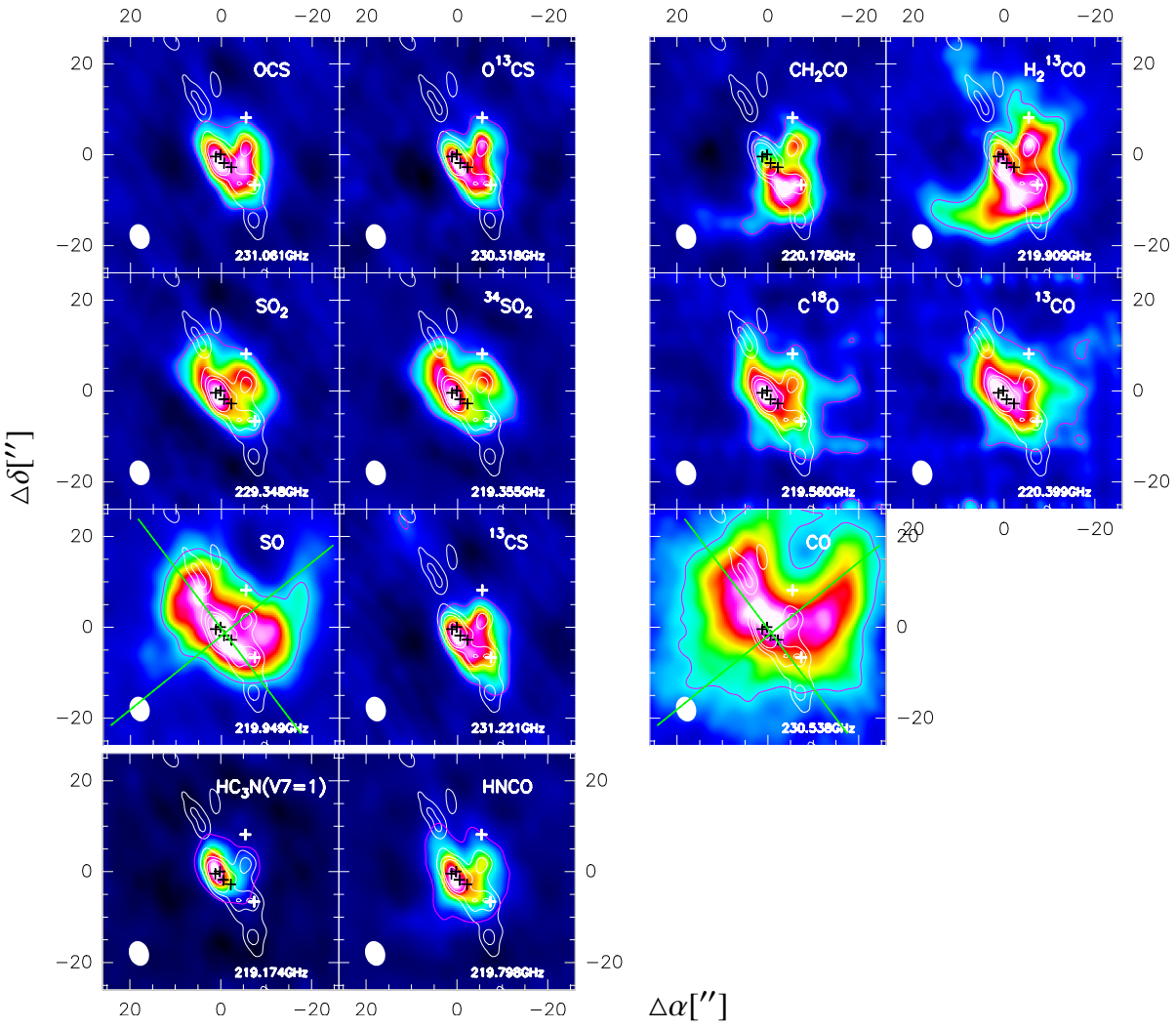

Figure 2.4: Maps of the intensity distribution of molecules containing < 6 atoms, which are detected in the combined SMA-30 m data at 1.3 mm (corresponding transitions are marked with "†" in Table A1). The intensities have been derived by integrating the line emission over the velocity range shown in Figure A3. The filled beam at the bottom left corner is from SMA-30 m data. White contours show the continuum from the SMA-only data (at -5σ, 5σ, 15σ, 25σ, and 60σ levels). Purple contours show $\pm 1\sigma$ levels of the molecular emission (solid contours indicate positive flux and dashed contours indicate negative flux). Green lines in the SO and CO maps sketch the outflow directions. The white crosses mark the BN object and the CR, and the black crosses mark the positions of the hotcore, Source I, Source N and SMA1, as in Figure 2.2. All images have different color scales (in Jy beam^{-1}kms^{-1}), increasing from black to white, which are optimised to emphasise the features in the distribution of each molecules.

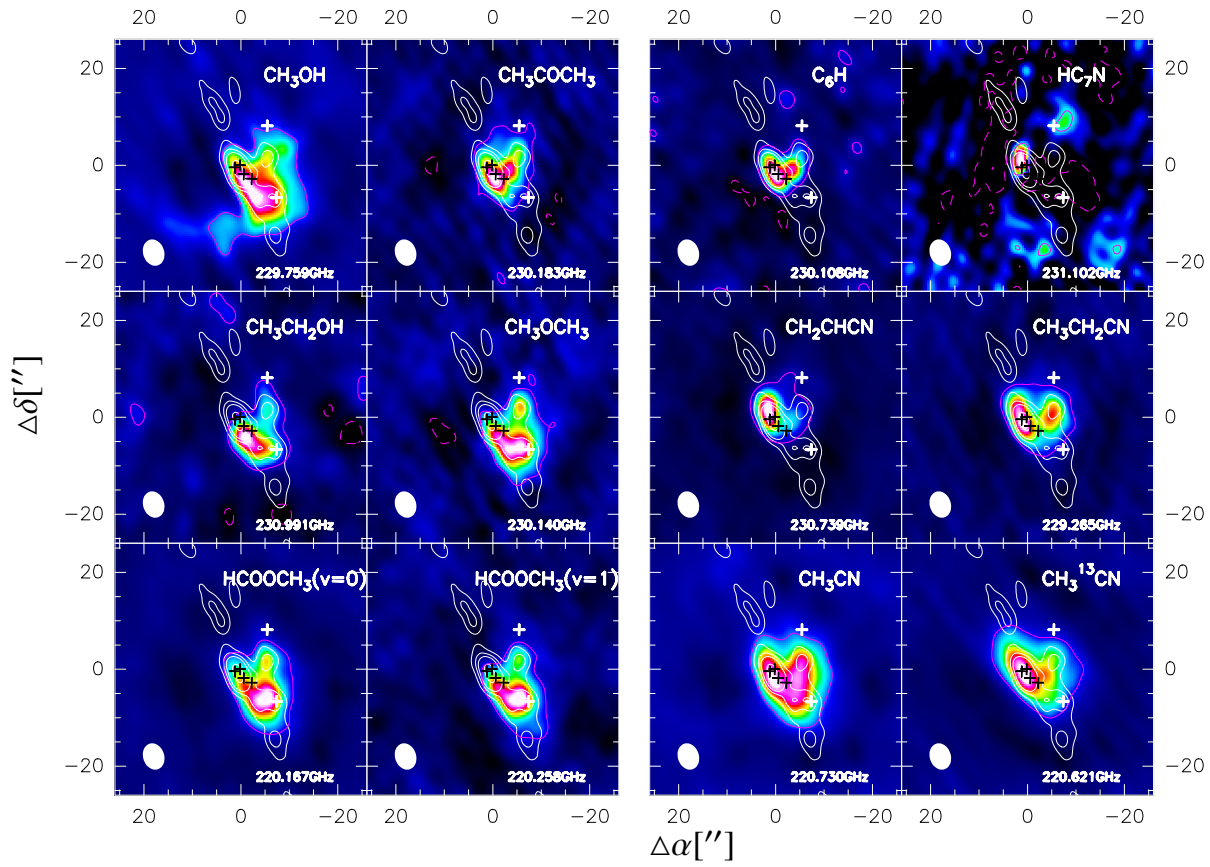

* Channel maps of more CH_3OH lines are shown in Figure A5.

Figure 2.5: Maps of the intensity distribution of COMs detected in the combined SMA-30 m data at 1.3 mm (corresponding transitions are marked with "‡" in Table A1). The intensities have been derived by integrating the line emission over the velocity range shown in Figure A3. The filled beam at the bottom left corner is from SMA-30 m data. White contours show the continuum from the SMA-only data (at -5σ, 5σ, 15σ, 25σ, and 60σ levels). Purple contours show $\pm1\sigma$ levels of the molecular emission (solid contours indicate positive flux and dashed contours indicate negative flux). The white crosses mark the BN object and the CR, and the black crosses mark the positions of the hotcore, Source I, Source N and SMA1, as in Figure 2.2. All images have different color scales (in Jy beam^{-1}kms^{-1}), increasing from black to white, which are optimised to monosulfide the features in the distribution of each molecules.

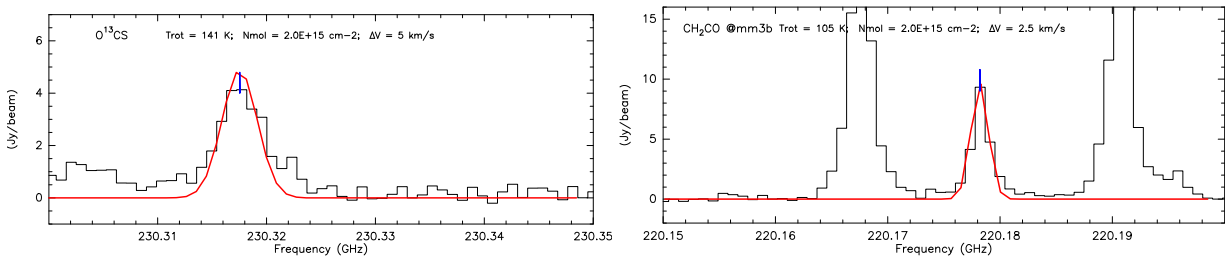

Figure 2.6: Lines having only one transition with low specific intensity ($\leq$ 10 Jy beam^{-1}) in Orion-KL data, fitted with synthetic spectrum from their emission peaks.

for each identified species in Figure 2.4 and Figure 2.5. Compared to previous submm and mm (especially interferometric) observations in Orion-KL (listed in the following paragraphs), the main features of our molecular distribution maps are:

1. All the identified S-bearing species in our dataset are diatomic/triatomic containing no H. Most of them have extended distributions (except for SO_2 and $^{34}SO_2$), exhibiting a "V" shaped morphology that extends from the HC peak, through mm3a, mm3b to mm2. Their velocities at line center also vary among substructures, from 6 km s^{-1} (HC) through 8 km s^{-1} (mm2, mm3a & mm3b, S) to 11–12 km s^{-1} (NE).

   - OCS and $O^{13}CS$ (carbonyl sulfide) peak at SMA1, and have emission that extends to the CR. In addition, OCS is also detected in NE and S. Although only one line of $O^{13}CS$ is detected in our data (19 $\rightarrow$ 18, Figure 2.6), other lines of this isotopologue have been previously confirmed and imaged by single-dish observations (e.g., Sutton et al. 1985; Ziurys & McGonagle 1993; Tercero et al. 2010). In addition to the detections by single-dish surveys (e.g., Sutton et al. 1985; Turner 1991; Schilke et al. 1997; Tercero et al. 2010), previous interferometric surveys of OCS also reproduce the same "V" shape widespread intensity distribution of this molecule, peaking at the HC (e.g., Wright et al. 1996; Friedel & Snyder 2008).
   - SO_2 and $^{34}SO_2$ (sulfur dioxide) peak at the hotcore and SMA1, and exhibit extended emission in the NE direction, with $V_{lsr} \sim 11$ km s^{-1}. Unlike the other S-bearing species, no emission has been detected from these species in S, and they do not display clear V-shaped feature. However, there is a clear second velocity component in the line profile of $^{34}SO_2$ (at $\sim$ 22.7 km s^{-1}, Figure 2.7) and SO_2 (at 22.1 km s^{-1}, Figure 2.7). In addition, red- and blue- shifted $^{34}SO_2$ trace outflows in the NW–SE direction (Figure A4). Single-dish studies (e.g., SO_2, Blake et al. 1987; Persson et al. 2007; Esplugues et al. 2013; $^{34}SO_2$, Esplugues et al. 2013) conclude that these molecules are good tracers not only for the warm dense gas, but also for regions affected by

shocks. They suggest the second velocity component[6] is related to shocks associated with the BN object. On small scales, interferometric observations of Orion-KL also detect a compact SO_2 peak (Wright et al. 1996; Zapata et al. 2011) and strong extended emission of $^{34}SO_2$ to mm2 (Beuther et al. 2005b).

- SO (sulfur monoxide) has multiple strong emission peaks towards HC, NE, mm3a and mm3b, and exhibits strong self-absorption in mm2 (Figure A3). There is also significant emission extending along both the plateau of high ($V_{lsr} \sim 11$ km s^{-1}) and low velocity ($V_{lsr} \sim 6.5$ km s^{-1}) outflows. Similar to $^{34}SO_2$, its line wings are broad (FWHM $\triangle V \sim 30$ km s^{-1}), and a second velocity component is clear in the line profile at ~ 21 km s^{-1} (see Figure A3 mm3b), which may be associated with shock events. These morphological features (elongated emission peak(s) and broad line wings of SO) have also been detected by both single-dish (Persson et al. 2007; Esplugues et al. 2013) and interferometric (Wright et al. 1996) line studies.

- ^{13}CS (carbon monosulfide) has only 1 transition in our data set, but it is very strong, peaking at SMA1, with a similar distribution to $O^{13}CS$ –extended emission from NE through HC to the CR. Due to its high dipole moment, this molecule is considered a dense gas tracer (e.g., Bronfman et al. 1996), and its detection in both CR and NE is confirmed by Persson et al. (2007) and Tercero et al. (2010).

2. The distribution of simple $C_xH_yO_z$ (x,z=1,2..;y=0,1,2...;$x + y + z \leq 5$) molecules are co-spatially extended.

- CO, $C^{18}O$ and ^{13}CO (carbon monoxide) have a common morphological peak at the HC (though the integrated intensity of CO peaks north of the HC due to its strong self-absorption in this source, see Figure A3). Velocity at line center V_{lsr} ranges from 6 km s^{-1} (HC) through 8 km s^{-1} (mm2, mm3a, mm3b, S) to 10 km s^{-1} (NE, OF1N, OF1S), and broad red shifted and blue shifted line wings trace both high-velocity (CO, ^{13}CO) and low-velocity ($C^{18}O$) outflows (Figure A4). As the second most abundant species in the ISM, this species has been detected in numerous other observations of Orion-KL ($C^{18}O$, Beuther & Nissen 2008; Plume et al. 2012; CO, Kwan & Scoville 1976; Zuckerman et al. 1976; Erickson et al. 1982; Blake et al. 1987 (single-dish), Masson et al. 1987; Chernin & Wright 1996; Zapata et al. 2009;

[6] $V_{lsr} = 20.5$ km s^{-1} in Esplugues et al. (2013)

Peng et al. 2012b (interferometry), ^{13}CO, Wilson et al. 2011 (single-dish)), which found the same morphology we see: extended structure, with bipolar line wings covering from the NE through HC to the CR, and tracing outflows.

- CH_2CO (ketene) has a single transition detected ($11_{1,11} \rightarrow 10_{1,10}$, Figure 2.6), peaking at mm3a and mm3b, with strong emission extending to OF1S and NE filament. With $V_{lsr} = 8\,km\,s^{-1}$ and $\triangle V = 2.5\,km\,s^{-1}$ in mm2, mm3a & mm3b, this line has also been confirmed by Sutton et al. (1985), and this species has also been detected in Orion-KL by Lee & Cho (2002).
- $H_2^{13}CO$ (formaldehyde) exhibits an elongated peak stretching from SMA1 towards mm3a. Similar to the simple organic CH_2CO, it also shows extended structure along the southeastern lobe of the high velocity outflow and NE. Single-dish detections (e.g., Persson et al. 2007) confirm that this molecule is a present in both the CR and the outflows.

3. HNCO (isocyanic acid) is the simplest organic molecule containing C, H, O and N. Peaking at SMA1, it shows extended emission toward all the substructures, with V_{lsr} ranging from 6 $km\,s^{-1}$ (HC) through 8 $km\,s^{-1}$ (mm2, mm3a, mm3b, S, OF1S) to 12 $km\,s^{-1}$ (NE, OF1S), and a second velocity component at $\sim$ 19.8 $km\,s^{-1}$ (Figure 2.7). Although the formation pathway of HNCO is still not clear (Hasegawa & Herbst 1993; Turner et al. 1999; Garrod et al. 2008; Tideswell et al. 2010), its distribution is observed to be correlated with shock tracing molecules SiO (e.g., Zinchenko et al. 2000) and CH_3OH (e.g., Meier & Turner 2005), suggesting it is also produced in shocks.

4. In contrast, large C-C single bond COMs are the typical COMs detected in HMSFRs, and they exhibit a variety of morphological structures in Orion-KL. In general, N-bearing COMs have a similar peak as HNCO–at or near HC; while most of the O-bearing COMs are co-spatial with CH_2CO–peaking at mm3a and mm3b, and extending even to southern CR (e.g., $HCOOCH_3$, CH_3OCH_3). This spatial segregation of the N- and O-bearing COM peaks has also been reported by other single-dish (Blake et al. 1987; Persson et al. 2007) and interferometric studies with high spatial resolution (e.g., Wright et al. 1996; Beuther et al. 2005b; Favre et al. 2011a; Friedel & Widicus Weaver 2012). In addition, there are several other O-bearing COMs we identified in this study, which have unique morphologies. To understand the spatial differentiation of COMs at small scales (Figure 2.5), we focus the comparison between our observations to other recent interferometric studies of these molecules (Table 2.2).

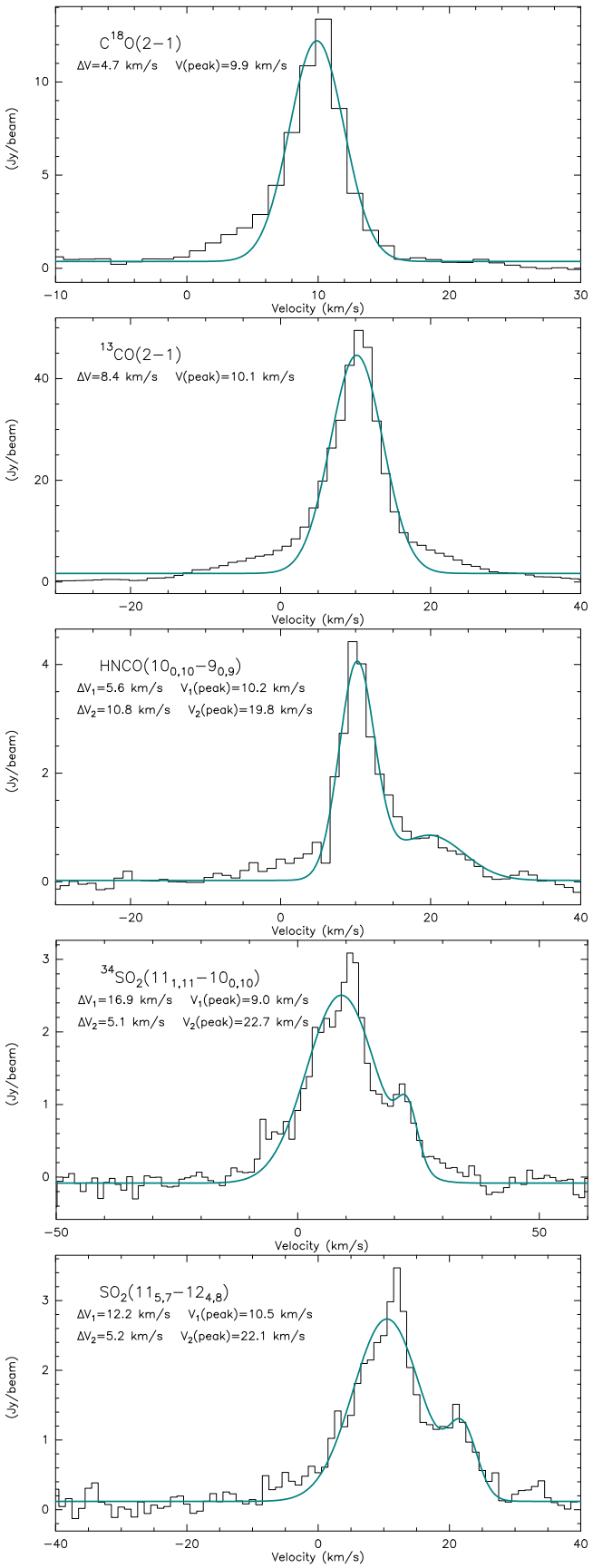

Figure 2.7: Gaussian fitting to the line profile of ^{13}CO, $C^{18}O$, HNCO, SO_2 and $^{34}SO_2$ extracted from NE of Orion-KL. Outflow signatures are seen in the broad line wings and the second velocity component in the HNCO, SO_2 and $^{34}SO_2$ line profile.

- CH_3CN and $CH_3^{13}CN$ (methyl cyanide) are two abundant N-bearing COMs. In our dataset, we detect the J = 12 → 11 ladder of both molecules around 220 GHz. Most of the $CH_3^{13}CN$ lines are blended, but lines with K = 2, 4, 5, 6 are clearly detected in the HC (Figure 2.8). In particular, K = 2 line of $CH_3^{13}CN$ is clearly co-spatial with CH_3CN (Figure A3)–peaking at SMA1 (V_{lsr} = 6 km s^{-1}), and extending to mm2, mm3a, mm3b (V_{lsr} = 8 km s^{-1}), and NE (V_{lsr} = 10 km s^{-1}), exhibiting a "V"-shape morphology. Neither CH_3CN nor $CH_3^{13}CN$ are detected in OF1N (S), but CH_3CN is detected toward S (V_{lsr} = 8 km s^{-1}). This "V"-shape morphology of CH_3CN has also been detected in e.g., Beuther et al. (2005b); Zapata et al. (2011); Widicus Weaver & Friedel (2012); Bell et al. (2014), as well as the NE extension in Wright et al. (1996). This species is considered to be warm and dense gas tracer (e.g., Kalenskii et al. 2000; Araya et al. 2005), with gas phase and grain surface chemical models predicting that it is only detected in an environment with elevated temperatures (e.g., Purcell et al. 2006). We use the CH_3CN ladder and the $CH_3^{13}CN$ ($12_2 \rightarrow 11_2$) line to estimate the temperature of the substructures where these molecules are detected (see Section 2.4.1).

- CH_2CHCN (vinyl cyanide) exhibits strong compact emission north of the hotcore, with $V_{lsr} \sim 6$ km s^{-1}, and a slight extension toward mm2. The northern peak is also coincident with that in higher resolution maps of this species from CARMA at 1 mm (Friedel & Snyder 2008), SMA at 865 μm (Beuther et al. 2005b) and PdBI at 3 mm (Guélin et al. 2008).

- CH_3CH_2CN (ethyl cyanide) emission also makes a "V"-shaped structure. Unlike the single-peaked structure of CH_2CHCN, CH_3CH_2CN exhibits a dual-peaked structure, with a first emission peak at the hotcore (6 km s^{-1}), and a second peak at mm2 (10 km s^{-1}). Although there are two velocity component in mm3a and mm3b (6 km s^{-1}, 10 km s^{-1}), there is no detection in southern CR, which is consistent with Blake et al. (1987). This observed morphology is consistent with that from other interferometric observations with high spatial resolution (Wright et al. 1996; Beuther et al. 2005b; Friedel & Snyder 2008; Guélin et al. 2008; Widicus Weaver & Friedel 2012; Peng et al. 2013).

- CH_3OH (methanol) has multiple transitions in our data (Figure A2). We obtained the channel maps of all the unblended strong CH_3OH transitions in our dataset, and found two types of spatial distributions (Figure A5). One type of lines clearly shows extended emission from mm2 and S (7.2–8.4 km s^{-1}, e.g., lines of $8_{0,8} \rightarrow 7_{1,6}$E, $8_{-1} \rightarrow 7_0$E, $3_{-2,2} \rightarrow 4_{-1,4}$E) towards the high velocity outflow OF1N(S), exhibit-

ing a similar SE tail as $H_2^{13}CO$ at 7–10 km s^{-1}, which has not been detected before; whereas the other type of lines (e.g., lines of $15_{4,11} \rightarrow 16_{3,13}$E, $22_{4,18} \rightarrow 21_{5,17}$E, $19_{5,14} \rightarrow 24_{4,17}A--$) does not show such SE tail. However, both of them show multiple velocity dependent emission peaks: toward SMA1 at 4 km s^{-1}, mm3a at 8 km s^{-1}, and mm3b at 10 km s^{-1}. The multiple peak structure is different from the traditional segregated dichotomous distribution of COMs in Orion-KL (main emission peak is either at HC or mm3a (b)), though it has also been observed in other interferometric surveys (Wright et al. 1996; Beuther et al. 2005b; Friedel & Snyder 2008; Guélin et al. 2008; Friedel & Widicus Weaver 2012; Peng et al. 2012a). Methanol has previously been detected in the Orion outflow (Wang et al. 2011b), and furthermore line $8_{-1} \rightarrow 7_0$E is known to be a potential Class I maser, tracing shocks (Fish et al. 2011). As a result, the SE tail can be reasonably explained as a feature of the outflow. In addition, the SMA1-Source N area is also suggested to be the launching point of the Orion-KL outflows (e.g., Menten & Reid 1995; Beuther & Nissen 2008), which may explain CH_3OH and $H_2^{13}CO$ peaking in this area.

- $HCOOCH_3$ (methyl formate) has the largest number of detected lines in our data (Figure A2). There are two types of $HCOOCH_3$ in the whole observational band, torsionally excited lines ($\nu = 1$) and lines in ground state ($\nu = 0$). Both of them have identical distribution (Figure 2.5)–peaking at mm3a and mm3b, with a clear detection in the southern CR, which is similar to CH_2CO. This morphology has also been reported by Wright et al. (1996); Beuther et al. (2005b); Guélin et al. (2008); Friedel & Snyder (2008); Favre et al. (2011a); Widicus Weaver & Friedel (2012), indicating that these molecules arise in a cooler and less dense environment than the hot core.

- CH_3OCH_3 (dimethyl ether) peaks toward mm3a and mm3b, and is co-spatial with $HCOOCH_3$ extending to the southern CR. Unlike the other COMs, its emission in mm2 is considerably stronger than toward the HC. This morphology has also been imaged with other interferometric studies (Liu et al. 2002; Beuther et al. 2005b; Guélin et al. 2008; Friedel & Snyder 2008; Favre et al. 2011b; Brouillet et al. 2013).

- CH_3CH_2OH (ethanol), the functional isomer of CH_3OCH_3, exhibiting extended emission from the vicinity of HC to mm2, mm3a, and mm3b, indicating the same distinctive V-shaped molecular emission as the N-bearing COMs. However, unlike CH_3OCH_3 and the other COMs, it peaks in-between the hot core and mm3a. The difference in the location of their peaks is exactly the same as reported by Guélin et al. (2008); Brouillet et al. (2013) from PdBI and Friedel & Snyder (2008) with the EVLA and CARMA at high spatial resolution. In the grain mantle chemistry models,

both isomers are produced from two radicals involved in the synthesis of CH_3OH ice (Garrod et al. 2008). Therefore, their spatial differentiation may result from the chemical differences between the CH_2OH- and CH_3O- radicals across Orion-KL, e.g., variations in production rates or chemical evolution (Brouillet et al. 2013).

- CH_3COCH_3 (acetone) is an O-bearing COM, though, it has a similar distribution as CH_3CH_2CN–peaking at SMA1, extending to mm2, and no detection in the southern CR. Although its nature as a hot core tracer has been confirmed by detections both in Orion-KL (Friedel et al. 2005; Friedel & Snyder 2008; Widicus Weaver & Friedel 2012; Peng et al. 2013) and Sagittarius B2 (N-LHM) (Snyder et al. 2002), whether this species mainly forms on dust grains or in the gas phase is still not clear.

- There are also several other COMs, e.g., CH_3CHO (acetaldehyde), CH_2OHCHO (glycolaldehyde), $(CH_2OH)_2$ (ethylene glycol), and HCOOH (formic acid), which we do not detect in Orion-KL at 1.3 mm in the 30 m-SMA combined data. Of the first three, although there are some candidate detections from our synthetic fitting, they are blended with other nearby lines, and so cannot be confirmed. Although Liu et al. (2002) claimed to detect HCOOH in the CR, in their data the line at 1 mm is only a 2σ feature. Widicus Weaver & Friedel (2012) also did not detect any compact concentrations of HCOOH in our studied region neither, and conclude that the HCOOH emission must be extended on $> 1\,700$ AU scales.

In brief, from our detections, N-/O- bearing COMs do not just show two segregated peaks, but also exhibit more complicated spatial distributions. Most of the N-bearing species (except CH_2CHCN) are co-spatial and peak at the hotcore, while some O-bearing species ($HCOOCH_3$ and CH_3OCH_3) peak at mm3a and mm3b, and others present more unusual features (CH_3OH has velocity dependent peaks at both hotcore and mm3a/mm3b; CH_3CH_2OH peaks in between mm3a and hotcore; and CH_3COCH_3 peaks in a similar location as N-bearing COMs). This challenges the traditional hypothesis that all of these molecules are forming under the same chemical and physical conditions (Garrod et al. 2008; Laas et al. 2011).

5. Unlike the saturated COMs[7], long carbon chain (organics with carbon-carbon multiple bonds) molecules are less likely to be detected in star-forming regions (Thorwirth 2001; Rice & Maier 2013).

[7] A COM that has a chain of carbon atoms linked together by single bonds and has hydrogen atoms filling all of the other bonding orbitals of the carbon atoms.

- C_6H is the parent radical of C_6H^- (the first molecular anion been identified in the gas phase interstellar and circumstellar media (McCarthy et al. 2006), after its presence been predicted by Herbst (1981), and it has not been detected in Orion-KL before. In our dataset, we tentatively detect several weak and blended transitions of C_6H. Emission from this species appears to be confined to the HC.

- HC_3N and HC_7N are two cyanopolyynes ($HC_{2n+1}N$, n is an integer). We confirmed the detection of $HC_3N(v_7 = 1)$ to the north of the hotcore, and the two tentatively identified lines of HC_7N have the same distribution. The excited-vibrational state ($v_7 = 1$) of HC_3N shows a similar confined structure northeast of the HC in Wright et al. (1996); Beuther et al. (2005b) and Zapata et al. (2011), where it is suggested to form a shell around the HC. HC_3N is an especially useful dense gas tracer due to its relatively low optical depth transitions, large dipole moment, and simple linear structure (Bergin et al. 1996), and the $HC_3N(v_7 = 1)$ lines are believed to be primarily excited by a strong mid-infrared radiation field (e.g., Goldsmith et al. 1982). A gas-phase chemical model of a hot core with high but transitory abundances of cyanopolyynes has been presented in Chapman et al. (2009), where these species are formed from reactions between the precursor $C_{2n}H_2$ (e.g., C_2H_2, acetylene) and N-bearing species via gas phase chemistry (e.g., $C_{2n}H_2 + CN \rightarrow HC_{2n+1}N + H$).

2.4 Calculations

To study the chemical variations in the above mentioned substructures, a more precise approach than our above qualitative comparison of the morphology of different species is to measure the quantitative differentiations in chemical parameters toward individual substructures, i.e., the temperatures, molecular column densities and abundances.

2.4.1 Temperature estimates

Temperature is commonly used as a benchmark for comparison between model results and observations. Since N-, O- and S- bearing species show different spatial distributions, we estimate their temperatures in each substructure separately.

Species	Identification	Peak	Column density @Peak (cm^{-2})	Other Interferometric detections
CH_3CN, $CH_3^{13}CN$	√	SMA1	1.2(17), 1.3(15)	a, b, e, i
CH_2CHCN	√	North to hotcore	≥3.5(15)	b, d, e
CH_3CH_2CN	√	hotcore	≥1.3(16)	a, b, d, e, i, k
CH_3OH	√	SMA1 & mm3a	≥8.2(17)	a, b, d, e, f, i, m
$HCOOCH_3$	√	mm3a & mm3b	≥1.2(17)	b, d, e, g, i, k
CH_3COCH_3	√	SMA1	≥1.5(16)	c, i, k
CH_3OCH_3	√	mm3a & mm3b	≥1.6(17)	b, d, e, h, i, j
CH_3CH_2OH	√	near SMA1 & mm3a	≥ 2.0(16)	d (×), e & j(only 1 line)
$(CH_2OH)_2$	×	–	–	–
CH_3CHO	×	–	–	d (×), i(×), n (ALMA)
CH_2OHCHO	×	–	–	g. (some lines < 3σ)
HCOOH	×	–	–	d (×), l (< 3σ), i(only from the extended configuration)
C_6H	*	SMA1	≥3.3(15)	–
HC_7N	*	North to hotcore	≥5.5(16)	–

References. a. Wright et al. (1996); b. Beuther et al. (2005b); c. Friedel et al. (2005); d. Friedel & Snyder (2008); e. (Guélin et al. 2008); f. Zapata et al. (2011); g. Favre et al. (2011a); h. Favre et al. (2011b); i. Widicus Weaver & Friedel (2012); j. Brouillet et al. (2013); k. Peng et al. (2013); l.Liu et al. (2002); m. Peng et al. (2012a); n. Loomis et al. VSGC conference

Table 2.2: Identification of saturated COMs and complex carbon chains in Orion-KL. Confirmed COMs are marked with "√", tentative detections with "*", and non-detections with "×". At each of their main emission peak (Figure 2.5), column density of CH_3CN is obtained with optical depth correction, while column densities of the rest molecules are obtained at the temperature of an adjacent substructure, with an assumption that the species lines are optically thin (we mark them with "≥"), $x(y) = x \times 10^y$.

CH_3CN:

A good tracer of temperature in high-density gas ($n \gtrsim 10^5$ cm^{-3}) is CH_3CN, which is a symmetric-top molecule with no dipole moment perpendicular to the molecular axis, and whose K-ladders in rotational levels are excited solely by collisions. Provided that the collision rate is sufficient to thermalize the rotational levels within each K-ladder, the rotational excitation temperature of CH_3CN is equal to the gas kinetic temperature (Boucher et al. 1980; Wright et al. 1995). Our observation band covers the J = 12 → 11 transitions of CH_3CN around 220 GHz, with upper state energy levels from ~ 70 K to ~ 500 K, yielding a large range for determining temperatures. If we assume that the emission from all of these transitions originate from the same parcels of gas along the line of sight, in Local Thermodynamic Equilibrium (LTE), having the same size, velocity, and a single temperature, then rotational temperatures can be derived from the rotational diagrams (Hollis 1982; Loren & Mundy 1984; Olmi et al. 1993; Goldsmith & Langer 1999). Traditionally, in the optically thin limit, the level populations, are then directly proportional to the line intensities of the K components, The parameters used to estimate the level populations of CH_3CN transitions (the line strength $S\mu^2$ (D^2), the lower state energy E_L (cm^{-1}) and upper state degeneracy g_u) in our data are listed in Table A2I(a).

The K = 3, 6 lines are from ortho (o-) transitions, which have a statistical weight twice as large as those of the other para (p-) lines. Radiative transitions between these two types are prohibited, so we exclude these lines in the optically thin rotation diagram fitting (shown in black lines in Figure 2.8, also see Andersson et al. 1984).

Dashed lines in panel 1 of Figure 2.8 show the synthesised fitting under the assumption of optically thin emission in LTE for the HC. To reduce the number of free parameters, we also assume that all the K = 0–8 components have the same line width[8]. A satisfactory fit is obtained to all lines except K = 0, 1, 2. Since all transitions were observed simultaneously, calibration errors due to poor pointing or amplitude scaling are not responsible, and remaining explanations for the deviations are as follows: (1). The K = 0, 1 lines are so close in frequency that they are blended in our fitting due to the uniform line width we assumed. (2). It is also likely that lines at K = 2 are more optically thick.

Compared to CH_3CN, lines of its rare isotopologue $CH_3^{13}CN$ should be optically thin. However, $CH_3^{13}CN$ ($12_2 \rightarrow 11_2$) is the only transition which is not blended with the broad line wings of CH_3CN in substructures other than HC. Even in the HC, only the K = 2, 6, 7 lines are unblended (panel 7 of Figure 2.8). Excluding the o- type lines (K=3, 6), the rotation temperatures in HC we derive from the main and rare isotopologues of CH_3CN have large difference (black dots with fittings in panel 2 and 8 of Figure 2.8). Optical depth seems to be the most likely reason

[8]The K = 9 line is blended by strong ^{13}CO

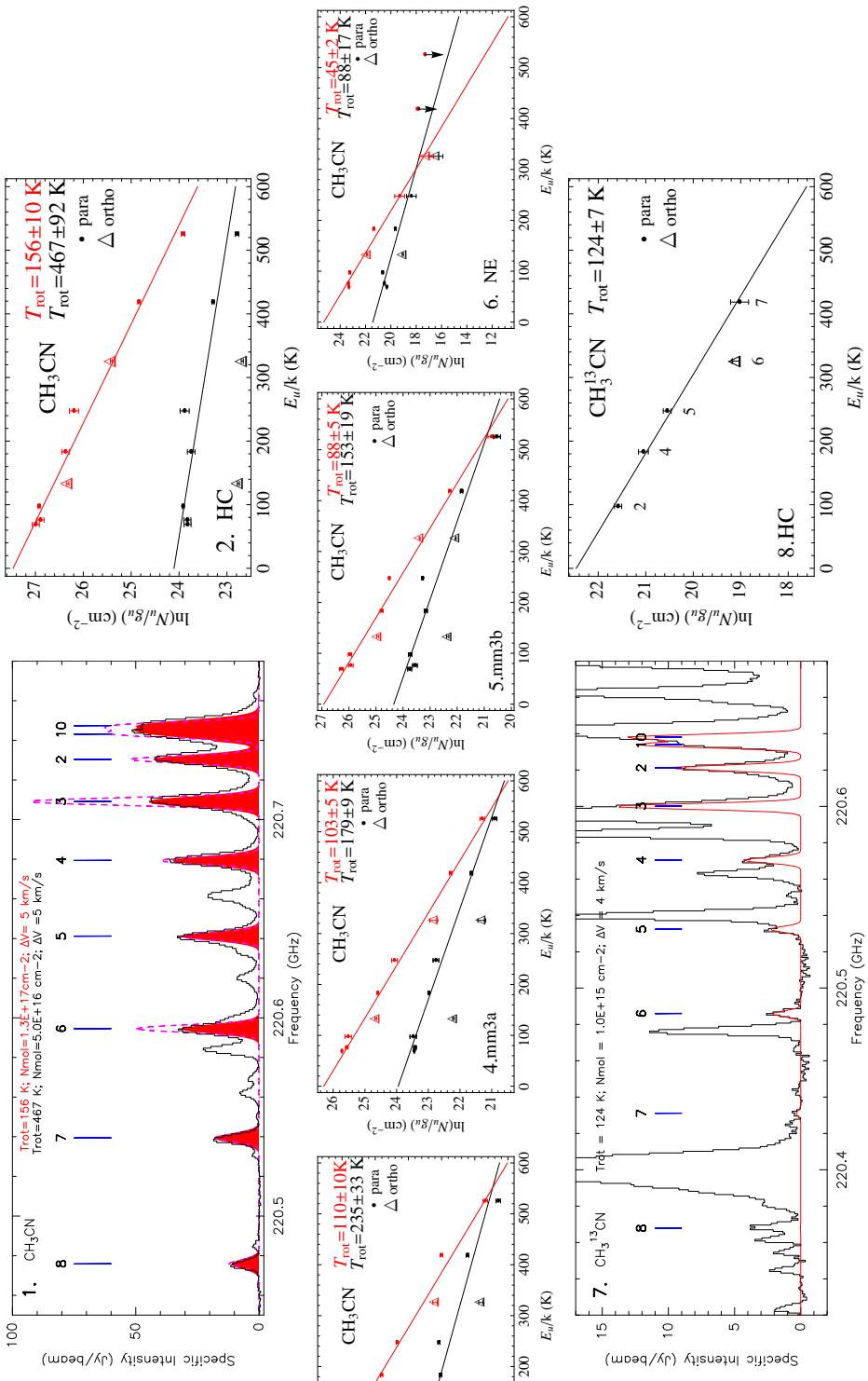

Figure 2.8: Panel 1 presents the CH_3CN spectrum towards the HC in black, LTE model fit in dashed purple, and fitting with optical depth correction in filled red. Panels 2-6 show the rotation diagram of CH_3CN derived for each substructure, with dots for p-CH_3CN, and triangles for o-CH_3CN. Black fittings are in optically thin assumption only to the p- lines, and red fittings are to both o- and p- lines by optical depth correction. Panel 7 presents the $CH_3^{13}CN$ spectrum towards the HC in black and the LTE model fit in red. Panels 8 shows the rotation diagram of $CH_3^{13}CN$ in HC with black dots (p-) and triangles (o-) from observation, and fitting is o- excluded with optically thin assumption. For lines without detection, an upper limit equal to the 3σ rms is given as arrow mark. The estimated rotation temperature from each rotation diagram is indicated in each panel. Error bars reflect only the uncertainties in the Gaussian fit of integrated intensities $\int T_B(\upsilon)d\upsilon$.

for such inconsistency, so to investigate this hypothesis, we use the following iterative approach to correct the optical depth of CH_3CN lines and derive the opacity corrected rotation temperature $T_{rot,p}$ (p=HC, mm2, mm3a, mm3b, NE) of each substructure (red dots with fittings in panel 2-6 of Figure 2.8):

(1) Obtain the rotation temperature $T_{1,p}$ from weighted least squares fit to Boltzmann diagram, assuming all the p-CH_3CN lines are optically thin (see fit to the black dots in Figure 2.8, panel 2-6);
(2) Estimate the optical depth of CH_3CN ($12_2 \rightarrow 11_2$) $\tau_{K,1\ (K=2)}$ by comparing its main beam temperature with that of $CH_3^{13}CN$ ($12_2 \rightarrow 11_2$), and calculate the column density of line $12_2 \rightarrow 11_2$ at $T_{1,p}$ with the optical depth correction. Then, estimate the total column density of CH_3CN as $N_{1,p}$ assuming LTE (see Section 2.4.2 for more details about the correction);
(3) With $T_{1,p}$ and $N_{1,p}$ as trial input parameters, estimate the optical depth for the remaining transitions in the CH_3CN ladder $\tau_{K,1\ (K=0-8)}$ with the RADEX code package[9] (van der Tak et al. 2007), then correct their column densities line by line (dots and triangle in red in Figure 2.8), and obtain a new rotation temperature $T_{2,p}$;
(4) Repeat step (3) until $(|T_{n,p} - T_{n-1,p}|)/T_{n-1,p} \leq 10\%$ (n=2,3,...; see fittings in red in Figure 2.8).

The above approach[10] can be applied to sources HC, mm2 mm3a, mm3b and NE, where the CH_3CN ladders can be clearly detected. In S and OF1N(S), the CH_3CN lines are below the 3σ detection threshold, so we assume the rotation temperature in these positions to be the same as that at NE.

For the other N-bearing species, since we do not have their rare isotopologues to estimate their optical depths, we do not use them to derive T_{rot}.

[9]RADEX is a one-dimensional non-LTE radiative transfer code, providing an alternative to the widely used rotation diagram method. Without requiring the observation of many optically thin emission lines, it can be used to roughly constraining the excitation temperature in addition to the column density.

[10]In reality, molecules do not distribute homogeneously in the clouds, and that they are far from being homogeneous in densities and temperatures. The ultimate best-fit requires a sophisticated, fully 3D physico-chemo-LRT modelling, which is beyond the scopes of our chapter. Our iterative approach is between realism and feasibility of the modelling, which fits both o-/p- CH_3CN well.

$HCOOCH_3$, CH_3OH and $^{34}SO_2$:

$HCOOCH_3$ has the largest number of lines in our dataset, and from satisfactory synthetic fitting (especially for lines in the torsionally excited state $v = 1$, Figure A2), we can reasonably assume that most of its lines are optically thin. Line emissions from this species are not contaminated by N-bearing species due to their different spatial distribution, so we use them to derive a second set of temperatures for estimating column densities of all the O-bearing species (including simple molecules and COMs).

On the other hand, CH_3OH and $H_2^{13}CO$ have an unusual spatial distribution (dual peaks and/or extended emissions at both HC and mm3a (b), and tail towards SE), which may be affected by their different temperatures. Since multiple transitions of CH_3OH are available in our data, we can also use them to derive a third temperature set.

For S-bearing species, since they may be sensitive to the ambient shock environment, their temperature in each substructure may be different from the other species. However, in our data, some of the S-bearing species have only a single transition ($O^{13}CS$, ^{13}CS), and other lines may not be optically thin (SO_2, SO, OCS). As $^{34}SO_2$ is the only S-bearing rare isotopologue which has multiple transitions in our observations, we apply temperatures derived from transitions of $^{34}SO_2$ to the other S-bearing species.

Using the lines list in Table A2, we derived the rotation temperatures in each substructure from $HCOOCH_3$, CH_3OH and $^{34}SO_2$ (Figure 2.9), and list these temperature sets in Table 2.3. Temperatures derived from $HCOOCH_3$ lines in the ground and torsionally excited states separately have some differences, but they do not deviate significantly from temperatures derived from all lines, therefore, we use the "mixed" temperatures in the end. Although temperatures derived from different species at the same substructure vary, HC is consistently the warmest substructure, while mm2, mm3a and mm3b are slightly cooler. In the outflow regions, there are not sufficiently strong lines for species other than CH_3CN to derive the temperature, which may suggest these regions are cooler, exhibiting similar chemical properties.

2.4.2 Column densities

Molecular column densities

For all the isotopologues we detect, we calculate their column densities from the integrated spectral line intensities as below.

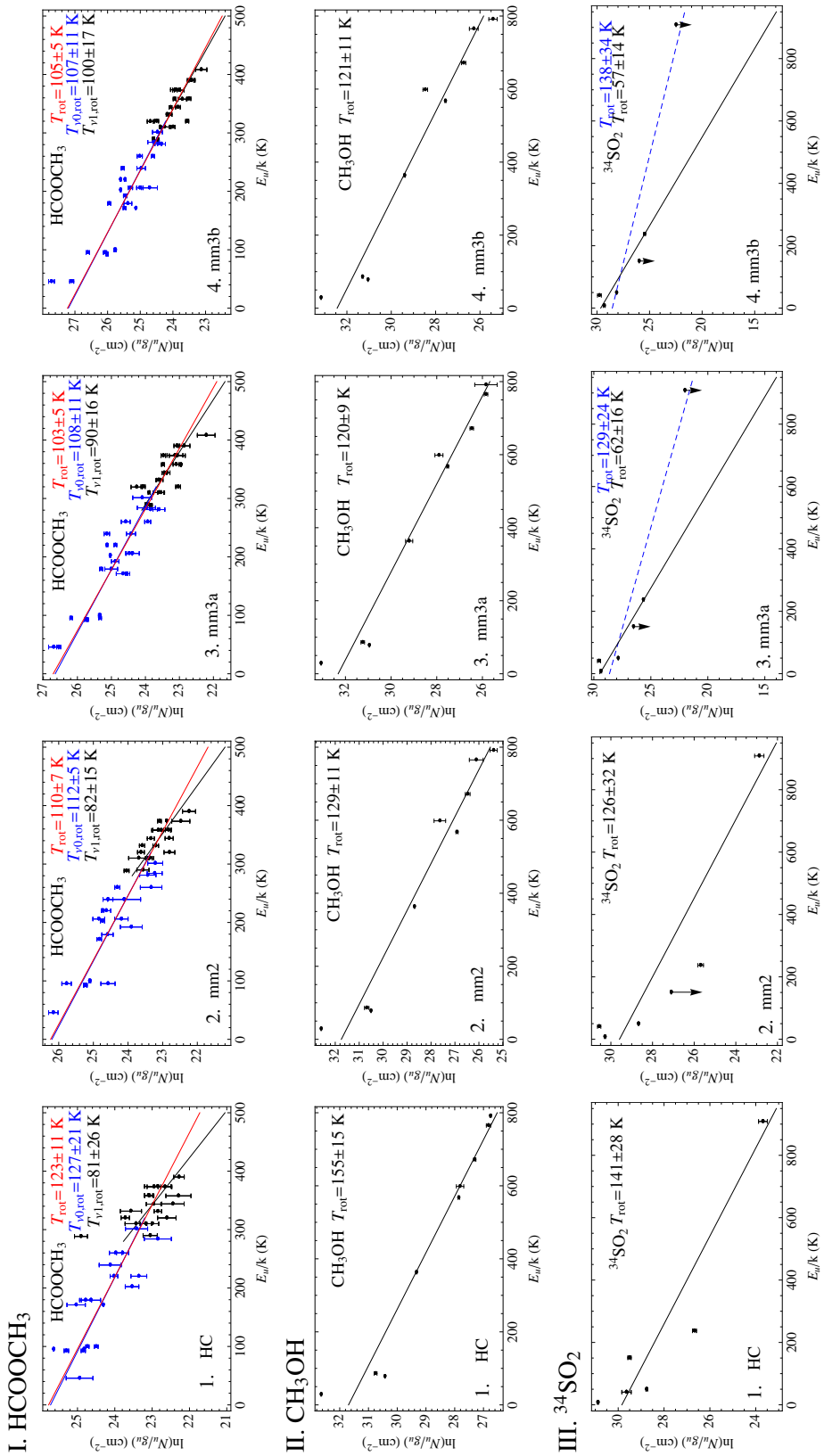

Figure 2.9: The rotation diagrams of O- and S-bearing species towards HC, mm2, mm3a and mm3b of Orion-KL. Panels in row I show two states of $HCOOCH_3$ lines, with the blue and black dots from observation of ground state ($v = 0$) and torsionally excited state ($v = 1$) lines, respectively. In the optically thin assumption, fittings for each state are plotted in blue or black, respectively, and fittings for all the transitions are plotted in red. Non-detection of $HCOOCH_3$ lines are not shown. Panels in row II and III show fittings on the optically thin assumption, with 3σ upper limits from non-detections plotted as arrow marks. Blue dashed lines in row III are fittings with upper limits included. The estimated temperature from each fitting is indicated in each panel. Error bars reflect only the uncertainties in the Gaussian fit of integrated intensities $\int T_B(\nu)d\nu$.

Species	HC (K)	mm2 (K)	mm3a (K)	mm3b (K)	NE (K)
CH_3CN	156 ± 10	110 ± 10	103 ± 5	88 ± 5	45 ± 2
$CH_3^{13}CN$	124 ± 7	–	–	–	–
$HCOOCH_3$	123 ± 11	110 ± 7	103 ± 5	105 ± 5	–
CH_3OH	155 ± 15	129 ± 11	120 ± 9	121 ± 11	–
$^{34}SO_2$	141 ± 28	126 ± 32	62 ± 16	57 ± 14	–

Table 2.3: Rotation temperature sets for each substructure derived from CH_3CN, $HCOOCH_3$, CH_3OH and $^{34}SO_2$. The substructures where no sufficient lines to derive the rotation temperature are marked with "–".

The optical depth τ_υ along the line of sight is (Zeng et al. 2006, Eq. A.25):

$$\tau_\upsilon = \frac{c^3}{8\pi\nu^3} A_{ul} N_u (e^{\frac{h\nu}{k_B T_{rot}}} - 1)\Phi(\upsilon). \tag{2.1}$$

where c is the speed of light, k_B is the Boltzmann constant, h is the Planck constant, ν is the line rest frequency, A_{ul} is the average spontaneous emission rate from the upper state E_u into the lower state E_l and $\Phi(\upsilon)$ is the distribution function of the line shape.

Integrating the optical depth over the observed linewidth (in velocity), $\int \Phi(\upsilon)d\upsilon = 1$, and the column density N_u of the line at ν Hz is,

$$N_u = \frac{8\pi\nu^3}{c^3 A_{ul}} \frac{1}{\exp(\frac{h\nu}{k_B T_{rot}}) - 1} \int \tau_\upsilon d\upsilon. \quad (cm^{-2}) \tag{2.2}$$

Assuming LTE, the total column density of all transitions for a molecule α is,

$$N_{T,\alpha} = \frac{N_u}{g_u} Q(T_{rot}) e^{\frac{E_u}{k_B T_{rot}}} \quad (cm^{-2}) \tag{2.3}$$

where $Q(T_{rot})$ is the partition function for the given excitation temperature of each sources, which is interpolated from a table of partition functions for fixed temperatures, obtained from CDMS/JPL.

Here, the CDMS/JPL line intensity $\ell(T_{rot})$ and the spontaneous emission rate A_{ul} are calculated as in Pickett et al. (1998), where η is a constant factor 2.7964×10^{-16},

$$\ell(T_{rot}) = \ell(300K)\frac{Q(300K)}{Q(T_{rot})}\frac{e^{-\frac{E_l}{k_B T_{rot}}} - e^{-\frac{E_u}{k_B T_{rot}}}}{e^{-\frac{E_l}{300K}} - e^{-\frac{E_u}{300K}}} \qquad (nm^2 MHz) \tag{2.4}$$

$$A_{ul} = \eta\ell(T_{rot})\nu^2\frac{Q(T_{rot})}{g_u}(e^{-\frac{E_l}{k_B T_{rot}}} - e^{-\frac{E_u}{k_B T_{rot}}})^{-1} \qquad (s^{-1}) \tag{2.5}$$

For the emission lines, we assume the Rayleigh-Jeans approximation ($\frac{h\nu}{k_B T_{rot}} \ll 1$) is valid, therefore Eq. 2.2 and Eq. 2.3 can be simplified as (Zeng et al. 2006, Eq. 4.26, also see Wilson et al. 2009),

$$N_u \cong \frac{8\pi k_B \nu^2}{hc^3 A_{ul}} T_{rot} \int \tau_\upsilon d\upsilon \qquad (cm^{-2}) \tag{2.6}$$

$$N_{T,\alpha} = \frac{8\pi k_B}{hc^3}\frac{(e^{\frac{h\nu}{k_B T_{rot}}} - 1)}{\ell(T_{rot})\eta} T_{rot} \int \tau_\upsilon d\upsilon \qquad (cm^{-2}) \tag{2.7}$$

Assuming that the observed emission in each substructure is homogeneous and fills the combined beam, the integration of measured main beam brightness temperature within the velocity range $\int T_B(\upsilon)d\upsilon$ can be substituted for the last term in the above equation:

$$T_{rot} \int \tau_\upsilon d\upsilon \cong \frac{\tau_{\alpha,0}}{1 - e^{-\tau_{\alpha,0}}} \int T_B(\upsilon)d\upsilon \qquad (K\ km\ s^{-1}) \tag{2.8}$$

Here $\tau_{\alpha,0}$ is the optical depth at line center.

We assume that related species have similar T_{rot}. In such case, we calculate the column density of N-bearing species at the optical depth corrected temperature set derived from CH_3CN, and S-bearing species at temperatures given by $^{34}SO_2$ rotation diagrams. For O-bearing species, we first estimate their column densities at temperatures derived from $HCOOCH_3$. Given the similarly unusual spatial distribution between $H_2^{13}CO$ and CH_3OH, we also estimate the column densities of both species at temperatures derived from CH_3OH. On top of that, two lines of CH_3OH are used to estimate the total column density of this species, due to their different morphological features (with or without SE tail).

In general, we assume that the observed transitions are optically thin ($\tau_{\alpha,0} \leq 1$, $\frac{\tau_{\alpha,0}}{1-e^{-\tau_{\alpha,0}}} \approx 1$). However, for several molecules with large abundances, we also observe the corresponding transition of their rare isotopologues, e.g., OCS (19 $\rightarrow$ 18)- $O^{13}CS$ (19 $\rightarrow$ 18), ^{13}CO (2 $\rightarrow$ 1)-CO (2 $\rightarrow$ 1)-$C^{18}O$ (2 $\rightarrow$ 1) and $CH_3^{13}CN$ ($12_2 \rightarrow 11_2$)- CH_3CN ($12_2 \rightarrow 11_2$). By measuring

the ratio between main beam brightness temperature of the main line $T_{B,\,\alpha,0}$ and its isotopologue $T_{B,\,\beta,0}$, we can estimate the optical depth at line center of a given transition $\tau_{\alpha,0}$ (Myers et al. 1983), given in Table 2.4.

$$\frac{1-\exp(-\tau_{\alpha,0}/\mathfrak{R}^{\alpha})}{1-\exp(-\tau_{\alpha,0})} \approx \frac{T_{B,\,\beta,0}}{T_{B,\,\alpha,0}} \tag{2.9}$$

Here $\mathfrak{R}_{\alpha}$ is the intrinsic abundance of the main isotope (e.g., ^{12}C) compared to its rare isotope (e.g., ^{13}C) in the ISM (Table 2.4, e.g., Wilson & Rood 1994; Chin et al. 1996). The remaining molecule lines, for which we cannot calculate the optical depth, are assumed to be optically thin.

Using the above method, we calculate the column densities of 22 isotopologues (for both optically thin and thick cases) in each substructure, and present them in Table A4I. In Table 2.4, we list the transitions for which we corrected their optical depths. We found that CO ($2 \rightarrow 1$), OCS ($19 \rightarrow 18$) and CH_3CN ($12_2 \rightarrow 11_2$) are significantly optically thick ($\tau = 6-117$) in all sources where they are detected. The validity of the assumption that the remaining molecular lines are optically thin will be discussed in Section 2.4.4.

In addition, since the main emission peak(s) of some COMs (CH_3COCH_3, CH_3CH_2OH, CH_2CHCN, C_6H, HC_7N) do not strictly coincide with either of the continuum peaks, we use the temperature from an adjacent substructure and determine their lower limits of column densities at their main emission peaks (Table 2.2, from transitions shown in Figure 2.5). Lines are assumed to be optically thin, so molecular column densities could be underestimated if this assumption is incorrect.

H_2 column densities

In Orion-KL, at 1.3 mm wavelength, the continuum emission is dominated by dust-neutral gas emission (Beuther et al. 2004). Assuming the dust emission at mm wavelengths is optically thin and has a single excitation temperature, namely, $T_{ex} \equiv T_{rot} = T_{dust}$ (Hildebrand 1983), we use the SMA-only data to calculate the H_2 column densities for different substructures, according to Schuller et al. (2009) :

$$N_{H_2} = \frac{I_{\nu} R}{B_{\nu}(T_{dust})\Omega_a \kappa_{\nu} \mu m_H} \qquad (cm^{-2}) \tag{2.10}$$

where I_{ν} is the peak specific intensity for each substructure on the continuum (in Jy beam^{-1}, taken to be the 3σ upper limit in the outflow regions), R is the isothermal gas to dust mass ratio (taken to be 150, from Draine 2011), $B_{\nu}(T_{dust})$ is the Planck function for a dust temperature T_{dust}, Ω_a is the solid angle of the SMA beam (in rad^2), $\kappa_{\nu} = 1.0$ cm^{2}g^{-1} is the dust absorption coefficient at 1.3 mm (assuming a model of agglomerated grains with thin ice mantles for densi-

ties 10^7 cm^{-3} (Blake et al. 1987), extrapolated from Ossenkopf & Henning 1994), μ is the mean molecular weight of the ISM, which is assumed to be 2.33, and m_H is the mass of an hydrogen atom (1.67×10^{-24} g). The results are reported in column $N_{H_2,1}$ of Table 2.1.

From the SMA-only observations, the total continuum flux at 1.3 mm is 13.3 Jy. However, extrapolating the flux from existing SCUBA (Submillimeter Common-User Bolometric Array) data at 450 μm (490 Jy, Johnstone & Bally 1999) to 1.3 mm, the total flux should be closer to $\sim$ 170 Jy at 1.3 mm. The difference implies that > 90% of the flux has been filtered out by the SMA observations. In contrast, $C^{18}O$ from a combination of 30 m and SMA observations is detected toward all the substructures, and should not suffer from the same spatial filtering as the SMA-only continuum data. As a result, it is a more reliable probe of the total column density of gas in the cloud at all spatial scales. Moreover, as a rare isotopologue line, it can be reasonably assumed to be optically thin, so we use it to make a second, independent estimation of the H_2 column density in all the substructures. By assuming a constant abundance in all substructures $\frac{N_{C^{18}O}}{N_{H_2}} = \frac{N_{C^{18}O}}{N_{CO}}\frac{N_{CO}}{N_{H_2}} \sim \frac{10^{-4}}{560} \sim 1.79 \times 10^{-7}$ (Wilson & Rood 1994), H_2 column densities can be calculated from the column densities of optically thin $C^{18}O$ emission (reported in the column $N_{H_2,2}$ of Table 2.1).

2.4.3 Molecular abundances

Subsequently, to study the chemical properties within the small scale of Orion-KL, we derive the molecular abundances with respect to H_2 (converted from $C^{18}O$) in each substructure (Table A4II).

Figure 2.10 presents the molecular column densities, and the abundance of each species with respect to $N_{H_2,2}$. Generally, all the molecules have higher column densities in the central regions (HC, mm2, mm3a and mm3b) than regions on the periphery (NE, S, OF1N and OF1S). While the abundances of some species have relatively small variations among the substructures (e.g., SO, CO, $C^{18}O$, ^{13}CO), some vary substantially: for example, N-bearing species are significantly under-abundant in the southern ridge and the outflow regions. O-bearing organic molecules containing $\leq$ 6 atoms (e.g., $H_2^{13}CO$, CH_2CO, CH_3OH) have more extended emission across all the substructures, with nearly constant large abundances in all the substructures except for NE. The S-bearing molecules are an intermediate case: most of them are not detected in the high-velocity outflow, but are clearly detected in NE (OCS, SO_2, $^{34}SO_2$, ^{13}CS) and (or) the southern ridge ($O^{13}CS$), with lower abundance. Such abundance differentiation among species is consistent with the spatial differentiation shown in Figure 2.4.

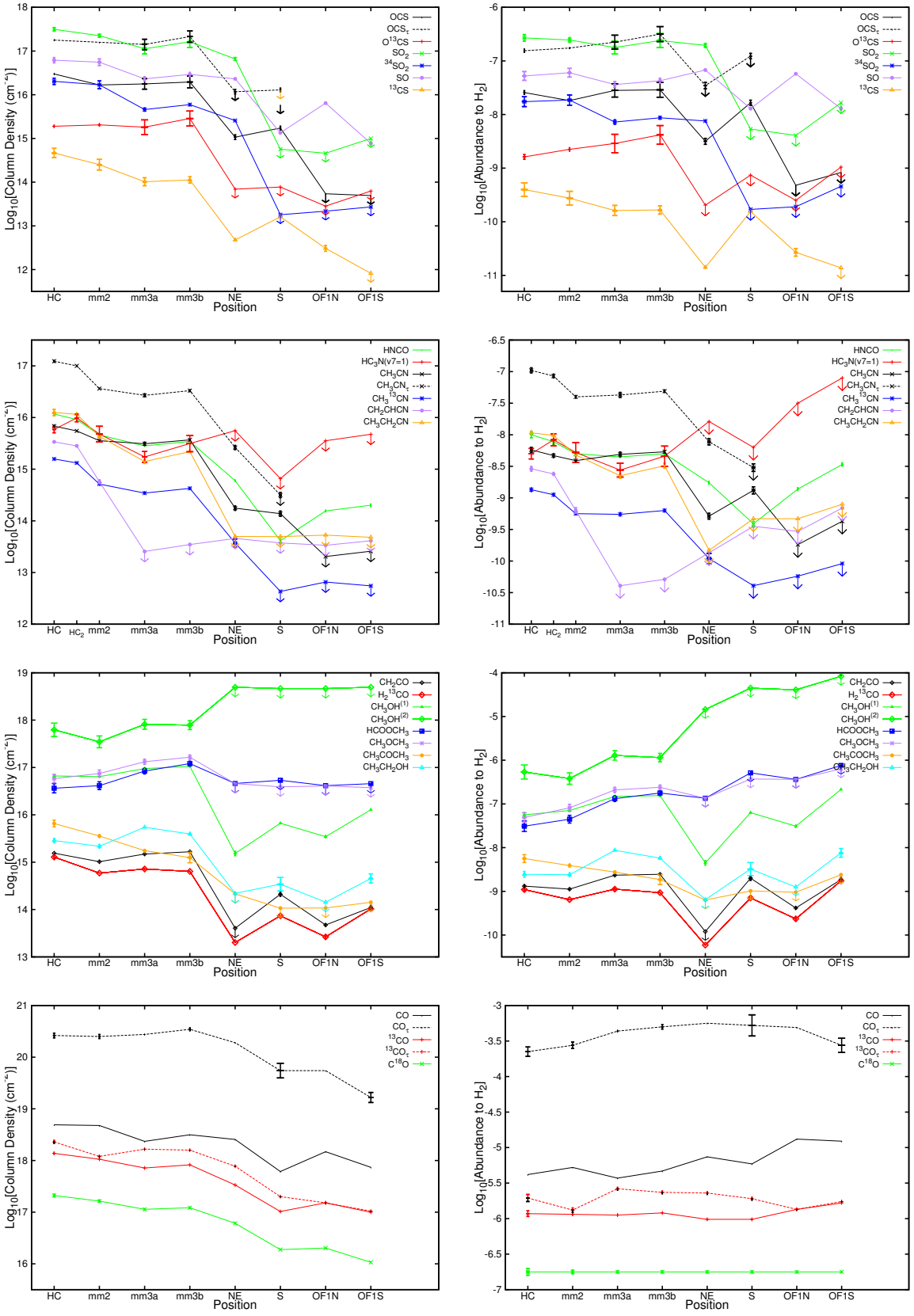

Figure 2.10: Panels in the left column show the molecular column densities toward 8 positions in Orion-KL. Panels in the right column show the corresponding molecular abundances of each species with H_2, which are converted from $C^{18}O$ assuming a constant $N_{C^{18}O}/N_{H_2} \sim 1.79 \times 10^{-7}$ ratio. See Section 2.4.2 and Section 2.4.4 for the calculation method and error budget.

2.4.4 Error budget

In this section, we consider the effect that the various assumptions we made in our quantitative analysis have on the results presented in this chapter.

1. T_{rot} (rotation temperature): The traditional rotation diagram method is subject to a number of uncertainties due to various assumptions (the emission is assumed to be optically thin and LTE is assumed to apply; see discussion in Snyder et al. 2005; Herbst & van Dishoeck 2009). If these assumptions are valid, the points on the population diagram will be well-fit by a straight line, with the slope proportional to the negative reciprocal of the temperature. However, this is not the case (see Figure 2.8). According to Table 2.2, the volume density is $\sim 10^7$ cm^{-3} (assuming a source size $\sim$ 10 times of the beam size, see also Blake et al. 1987; Plume et al. 2012), so LTE can be a reasonable assumption (except for such extreme cases as masering, and sub-/super thermal excited conditions), and the main reason for the fittings with uncertainties is the optical depth of the used lines.

   (1) In Section 2.4.1, we obtain the optical depth of CH_3CN ($12_2 \rightarrow 11_2$) by comparing its observed main beam brightness temperature to that of $CH_3^{13}CN$ ($12_2 \rightarrow 11_2$). Then, we use this optical depth as a standard in non-LTE radiative transfer fitting and derive a lower T_{rot} in each substructure. In the HC, the rotational temperatures derived from CH_3CN (156 ± 10 K) and $CH_3^{13}CN$ (124 ± 7 K) have some difference, however the molecular column densities are insensitive to temperature uncertainties of this magnitude, so our approach should still be applicable (Table A4). Uncertainties of T_{rot} in all substructures from linear fittings are 5%-10%.

   (2) In Section 2.4.1, T_{rot} for O-bearing species are derived from $HCOOCH_3$. In general, the temperatures derived from two different states of $HCOOCH_3$ lines are consistent, while the torsionally excited $HCOOCH_3$ ($\nu = 1$) lines appear to trace lower temperatures than lines in the ground state ($\nu = 0$), for the reason that LTE assumption may not be applied for the sub-thermal conditions (see also Demyk et al. 2008). In addition, we derived a third temperature set from CH_3OH. Although the difference of molecular column densities calculated for these two temperature sets are within the uncertainties, synthetic spectrum fitting (Figure A2) indicates that some lines of CH_3OH may be optically thick, which may explain why T_{rot} from CH_3OH is slightly higher than from $HCOOCH_3$.

   (3) For S-bearing species, T_{rot} derived from $^{34}SO_2$ varies from HC through mm2 to mm3a and mm3b. However, fitting uncertainties for temperatures in mm3a (62 ± 16 K) and mm3b (57 ± 14 K) are of 10%-30%, because we loose the constraint of fittings from the non-detection line with high E_u/k_B at 229.987 GHz. In Figure 2.9. We estimate the

temperature upper limits for both substructures by including the non-detected lines (in dashed blue line), and find the differences for column densities derived at temperatures from 57-62 K (non-detection are excluded in fittings) to 129-138 K (upper limits, column in blue in Table A4) are by a factor of < 3.

2. N_T (molecular column density): In Section 2.4.2, we first assume that all the identified molecular lines are optically thin, then we use Eq. 2.9 to obtain the optical depth of those main isotopologue lines whose rare isotopologues with the same transition are detected, and use Eq. 2.8 to correct the column density of the main isotopologue. In this approach, we assume the rare isotopologue lines are optically thin, and list the optical depths and abundance ratios for ^{13}CO (2 → 1), CO (2 → 1), OCS (19 → 18) and CH_3CN ($12_2 \rightarrow 11_2$) with respect to their rare isotopologue lines with and without optical depth correction in Table 2.4.

   However, equation 2.8 is based on the assumption that the molecule and its isotopologue have the same excitation temperature, which is often not the case. Therefore, a more accurate calculation requires LVG + proper chemical modelling. But nevertheless, our analytic calculations suggest that, the optical depth is the main issue which drives the error in the estimated molecular column density. For abundant molecules such as CH_3OH, HNCO, SO and SO_2, which we do not observe a corresponding transition of a rare isotopologue, our assumption that their lines are optically thin may result in the underestimation of their column density by a factor of 7-10 (coming from the average differences for OCS, CO and CH_3CN column density values before and after optical depth correction in Figure 2.10, and also from differences of column densities derived from two spatially different CH_3OH lines, Table A4).

   Aside from the optical depth, errors to the molecular column density based on T_{rot} and $\int T_B(\upsilon)d\upsilon$ are negligible compared to the chemical differentiation among the substructures (Table A4, on average < 5%).

3. N_{H_2} & Molecular abundance: Because no continuum information is available in the combined data, we use two methods to calculate the column density of H_2 (Table 2.1): from SMA-only continuum ($N_{H_2,1}$) and from SMA-30 m $C^{18}O$ ($N_{H_2,2}$), and derive the molecular abundances with respect to $H_{2,2}$. Comparing the column density of $H_{2,1}$ and $H_{2,2}$, We found $N_{H_2,2}/N_{H_2,1}$ is ∼ 0.8 in mm2, ∼ 0.5 in mm3a and mm3b, ∼ 0.4 in HC, ∼ 0.2 in NE, but 0.1 in S. Several reasons may lead to such difference: (1) the specific intensity (Jy beam^{-1}) used to calculate the column density is beam depended. The combined beam is larger than the SMA-only beam by a factor of ∼ 2.5, so it is reasonable that for larger beam size we obtain smaller H_2 column density (similar case in Beuther et al. 2007). (2) In producing the continuum, we select the "line-free" part, but there are still lines with low

Species		$\mathfrak{R}_\alpha$	HC	mm2	mm3a	mm3b	NE	S	OF1N	OF1S
$\tau_{CO\ (2\rightarrow1)}$			54	53	117	109	74.5	90	37	22.5
$N_{CO_\tau}/N_{C^{18}O}$	†	560 ± 25	1263 ± 21	1539 ± 58	2416 ± 45	2815 ± 72	3120 ± 51	2926 ± 20	2711 ± 31	1549 ± 18
$N_{CO}/N_{C^{18}O}$	⋆		23.4 ± 0.4	29.0 ± 1.1	20.7 ± 0.4	25.8 ± 0.7	41.9 ± 0.7	32.5 ± 0.2	73.3 ± 0.8	68.9 ± 0.8
$\tau_{^{13}CO\ (2\rightarrow1)}$			1.1	0.25	2	1.5	2	1.5	0.02	0.08
$N_{^{13}CO_\tau}/N_{C^{18}O}$	†	7.2 ± 0.9	10.8 ± 0.2	7.3 ± 0.2	14.6 ± 0.2	13.1 ± 0.2	12.7 ± 0.0	10.6 ± 0.0	7.6 ± 0.0	9.7 ± 0.2
$N_{^{13}CO}/N_{C^{18}O}$	⋆		6.5 ± 0.1	6.5 ± 0.2	6.3 ± 0.1	6.8 ± 0.1	5.5 ± -0.0	5.5 ± 0.0	7.5 ± 0.0	9.3 ± 0.2
$\tau_{OCS\ (19\rightarrow18)}$			6	9.5	8	11	≤11	≤7.5	−−	−−
$N_{OCS_\tau}/N_{O^{13}CS}$	†	77 ± 7	94.2 ± 2.1	77.8 ± 4.3	78.2 ± 8.0	75.2 ± 6.1	≤ 170.0	≤ 168.4	−−	−−
$N_{OCS}/N_{O^{13}CS}$	⋆		15.7 ± 0.4	8.2 ± 0.5	9.8 ± 1.0	6.8 ± 0.6	≥ 15.5	≥ 22.4	−−	−−
$\tau_{CH_3CN\ (12_2\rightarrow11_2)}$			18	10.2	8.7	9	15	≤2	−−	−−
$N_{CH_3CN_\tau}/N_{CH_3^{13}CN}$	†	77 ± 7	$77.9\pm2.4(75.0\pm1.7)^*$	70.6 ± 0.5	78.3 ± 2.0	78.0 ± 0.4	71.1 ± 5.7	≤ 74.0	−−	−−
$N_{CH_3CN}/N_{CH_3^{13}CN}$	⋆		$4.3\pm0.1\ (4.2\pm0.1)^*$	6.9 ± 0.0	9.0 ± 0.2	8.7 ± 0.0	4.7 ± 0.4	≥ 32.0	−−	−−

* Ratio at temperature derived from $CH_3^{13}CN$.

Table 2.4: Optical depth and abundance ratios for CO, ^{13}CO, OCS and CH_3CN with respect to their isotopologues in each substructure of Orion KL. † or ⋆ mark the estimations with or without optical depth correction. ≥ (≤) come from the 3σ limit of the non-detection of $O^{13}CS$ (OCS) and CH_3CN ($CH_3^{13}CN$) . The ratio between isotopologues $\mathfrak{R}_\alpha$ of $^{12}C/^{13}C$ and $^{16}O/^{18}O$ is provided from the local ISM ratio measured in Wilson & Rood (1994).Uncertainties on the measured values are typically ≤ 10%, as determined from T_{rot}, partition function $Q(T_{rot})$, and Gaussian fitting to $\int T_B(\upsilon)d\upsilon$.

emission (Figure A2), which may contaminate the continuum; (3) we simply assume that the volume densities in all substructures are the same (10^7 cm^{-3}), therefore so does the gas-to-dust ratio and the dust opacity. Since we do not know the size of each substructure, gas is possibly much denser in warmer source (HC, mm2, mm3a and mm3b) than it in the other cooler substructures (NE, S), so the homogeneous volume density assumption may be not accurate in the whole region. (4) Grain growth in the envelopes can be also a reason for difference in dust emissivity from center to periphery substructures at (sub-)mm (Miotello et al. 2014). (5) We also note that the difference for $C^{18}O$ column density in the central region is a factor of 30 higher than that in the outflow. Judging that $N_{H_2,2}$ is derived with the assumption that $N_{C^{18}O}/N_{H_2}$ = const in all the studied substructures, the fractional variation of $N_{C^{18}O}/N_{H_2}$ ratio in different substructures (e.g., CO freezing out onto dust grains in cooler region, Caselli et al. 1993) can be another factor that brings error in our estimation.

4. In addition, another simplification in our calculation is an assumed constant beam filing factor. Determination of molecular abundances in Orion-KL substructures relies upon an accurate source structure model for each molecule. When the source is smaller than the beam size, the main beam brightness temperature is diluted, leading to an underestimated brightness temperature for more compact structures. To correct this, an appropriate correction factor need to be applied. Since we do not know the accurate source sizes, we simply assume that the filling factor is unity in all the calculations.

2.5 Discussion

The presented observations comprise a large set of molecular lines (over 160 lines from 19 species, including 24 isotopologues) from combined SMA and IRAM 30 m data toward Orion-KL. Resolving Orion-KL into eight substructures and comparing S-, N-, and O-bearing molecules, we find complicated spatial morphologies for COMs, and strong chemical differentiation over the observed substructures.

2.5.1 Comparison with the other results

Previous quantitative studies of Orion-KL mainly focused on the HC, CR (with mm3a & mm3b treated as a single substructure in the periphery of CR) and plateau (OF1N, OF1S), therefore comparison of our estimated molecular abundance with previous results is limited to these substructures.

1. Since different molecules have different chemistries, the rotation temperatures derived using different tracers in the same substructure vary. Comparing with the results of others studies, our opacity corrected temperature in HC derived from CH_3CN is 120–160 K, which is a factor of 1.5 lower than that reported by Goddi et al. (2011) from NH_3. Our HC temperature probed by CH_3OH (~150 K) is a factor of 2 lower than that derived by Beuther et al. (2005b) and Friedel & Widicus Weaver (2012), probably because their higher spatial resolution observations probe the warmer inner region of the HC. However, temperatures for both species in mm2 (110–130 K), mm3a and mm3b (80–120 K) are consistent with the aforementioned studies within uncertainties. In particular, temperatures from CH_3OH in the HC and CR generally agree with those from large velocity gradient (LVG) modelling of $C^{18}O$ by Plume et al. (2012). In addition, although our adopted temperatures from $HCOOCH_3$ are slightly lower than those derived from the other species in this study, they well agree with the temperatures estimated by Favre et al. (2011a) from observations of this species at similar spatial resolution[11]. We note that S-bearing species may be affected by shocks in the environment. Although they were not often derived previously, and the high E_u/k_B transition brings large uncertainties in the rotation temperatures derived from $^{34}SO_2$, our estimated temperatures are within uncertainty of those derived by (Esplugues et al. 2013) from SO_2 in HC (190 ± 60 K) and CR (80 ± 30 K).

2. Due to the compactness of the detected substructures, column densities of CO, ^{13}CO and $C^{18}O$ are 10 times higher than those from lower-resolution observations in single-dish observations of Wilson et al. (2011) (FWHP ~ 13″) and in Plume et al. (2012) (Herschel/HIFI beam ranges from 13″ to 40″). Taking the beam ratio into account, our results are consistent with previous measurement.

3. In both HC and CR, the abundances of SO, SO_2, HNCO, HC_3N, CH_3OH (with SE tail), CH_2CHCN, CH_3CH_2CN and CO are comparable to the values in Blake et al. (1987); Wright et al. (1996) and Esplugues et al. (2013), within our factor of 1.5–2 uncertainties. $H_2^{13}CO$ is lower than the value derived from H_2CO in (Blake et al. 1987), assuming a standard $^{12}C/^{13}C$ ratio, but is comparable to that in Wright et al. (1996). After the optical depth correction, our OCS and CH_3CN abundances are 10 times higher than those in Blake et al. (1987), because the latter estimation was made assuming lines of these species to be optically thin. However, our abundances of OCS and ^{13}CS are comparable to those in Tercero et al. (2010), within our factor of 2 uncertainty.

[11] MF1-5 are the $HCOOCH_3$ emission peaks in Favre et al. (2011a), which coincide with mm3b (MF1), HC (MF2), mm3a (MF3) and mm2 (MF4-5) in our continuum.

4. Consistent with the estimations in Sutton et al. (1995) and Wright et al. (1996), CO and SO have stronger emission and higher abundances in the plateau of both the high and low velocity outflows, which has been suggested to be due to shock enhancement in these regions.

5. The estimated column densities of COMs (CH_3CH_2CN, CH_3COCH_3, $HCOOCH_3$) in HC are found to be lower than the values in Friedel & Snyder (2008) by a factor of 10 because the latter observations have a smaller synthetic beam; however, $HCOOCH_3$ has comparable column densities to Favre et al. (2011a) in HC (MF2), as does CH_3OCH_3 compared to Brouillet et al. (2013) at mm3a (MF4-5) and mm3b (MF1), and the abundance of CH_3COCH_3 compared to Peng et al. (2013) at HC (MF2) and mm2 (Ace-3).

2.5.2 Chemistry in the Hot Core

With a spatial resolution of 3″, our data resolve Orion-KL into several condensations. The peak specific intensity (Jy beam^{-1}) of the dust continuum exhibits a gradient from the central condensations to the periphery, and the dust temperature exhibits the same gradient: The hot core is the strongest continuum substructure, having both the highest dust temperature and the largest column density; mm2, mm3a and mm3b are slightly fainter and less dense; while NE and S have weaker continuum and line emission than the former sources, but stronger emission than OF1N(S).

Differentiation in the spatial distribution of S-, N- and O- bearing species clearly shows that chemistry in the central condensations of Orion-KL is not homogeneous. Simple N- and O-bearing molecules show the strongest emission toward the central condensations. However, unlike the N-bearing species (including N-bearing COMs), most of which are not detected in S, NE or the outflow, simple organic molecules ($H_2^{13}CO$, CH_2CO) and CO (^{13}CO, $C^{18}O$) have bright extended emission even toward the cooler and less dense regions (S, OF1N, OF1S). Compared to the above extreme cases, the S-bearing molecules are widely distributed over the central condensations, NE and (or) S. A possible reason for this is that the S-bearing molecules are mainly formed via warm gas-phase chemistry or shock chemistry (e.g., Pineau des Forets et al. 1993; Charnley et al. 1997), and then coincide with both N- and O-bearing molecules in the plateau (NE) of BN/KL (e.g., Chandler & Wood 1997; Schreyer & Henning 1999, see discussion in Section 2.5.3) .

For the COMs, it is widely suggested that "N-/O- chemical differentiation" can be caused by lower/higher temperatures during the cold pre-hot core phase and a different pace of the warm-up phase in these regions (Caselli et al. 1993; Garrod et al. 2008; Laas et al. 2011; Neill et al. 2011). In our study, besides confirming the HC peak of N-bearing COMs (CH_2CHCN, CH_3CH_2CN,

CH_3CN and $CH_3^{13}CN$) and the mm3a (or/and mm3b) peak of several O-bearing COMs (e.g., $HCOOCH_3$ and CH_3OCH_3), we found several other COMs which can not be classified within these dichotomous peaks groups (also see Guélin et al. 2008; Friedel & Widicus Weaver 2012; Peng et al. 2013). For example, the peak of CH_3OH is velocity dependent, shifting from the HC (3.6 km s^{-1}) through mm3a (6 km s^{-1}) to mm3b (7.2 km s^{-1}), and the peak of CH_3CH_2OH is in-between the hot core and mm3a. In contrast, CH_3COCH_3 shares a morphology with N-bearing molecules–peaking towards the hot core with a "V"-shape distribution. This similarity in morphologies may indicate a link between HC peaking N-bearing species and mm3a (or/and mm3b)-peaking species, therefore their formation pathways likely involve NH_3 (ammonia) or another major N-bearing molecule (e.g., Chen & Woon 2011), or need similar physical conditions appropriate for their production and/or sublimation, e.g., shocks (Peng et al. 2013).

The favoured model of hot core chemistry so far is the gas-grain model, where frozen radicals, partly produced by photolysis, become mobile during the warm-up phase and their reactions produce COMs (Markwick et al. 2000; Garrod et al. 2008). Three phases are usually modelled, the cold, warm-up and hot-core stage. During these stages, different species are defined as zeroth-generation (e.g., CH_3OH), first-generation (e.g., $HCOOCH_3$), and second-generation organic molecules (see Herbst & van Dishoeck 2009). In such a scenario, since the critical densities are fairly similar for N- and O-bearing species, the distribution diversity of species in Orion-KL may also be explained by different initial compositions or different "ages" (evolutionary stage, the time that the molecular gas has had to evolve from an initial composition after being released from ice mantles, Friedel & Snyder 2008). If that is the case, COMs like CH_3OCH_3/CH_3OH can act as chemical clocks implying that the different substructures in BN/KL could have different ages (Charnley et al. 1997; Wakelam et al. 2004a).

In addition to dust surface and gas-phase chemical processing, it is also possible that varying physical conditions, including temperature, density, and kinematics cause the differentiation in the spatial distributions of molecular line emission seen in the Orion-KL region. Taking the modelling result from Garrod et al. (2008) (especially their Figure 8) as an example, as the source being warmed-up (e.g., from 100 K to 200 K), the abundance of some molecules increase (e.g., HNCO, CH_3CN, CH_3OH) because of their evaporation from the grain surface to the gas phase, while the abundance of some large molecules cannot be synthesised on grains any longer as their precursor species have desorbed to the gas phase. They decrease (e.g., $HCOOCH_3$, CH_3OCH_3) or start to decrease (CH_3OH), because of being destroyed by ion-molecule chemistry (e.g., by protonation via XH^+ molecules), and followed by dissociative recombination into multiple small fragments. In this scenario, the different emission peaks of different species can be explained by

the higher temperature in HC (120–160 K) than in mm3a and mm3b (80–100 K), meaning that N-bearing species are still evaporating in HC but molecules such as $HCOOCH_3$ are dissociating there.

2.5.3 Chemistry in the outflow

Outflows from young stars can destroy grain material and/or liberate ices when they impact the surrounding the cold matter, meaning that chemical reactions can be driven by the associated shocks even in cold gas (Herbst & van Dishoeck 2009). For years, the outflows in the Orion-KL region have been the main subject of chemical studies of this region (Wright et al. 1996 and references therein). Although COMs are less abundant or not detected in these outflows, chemistry of simple molecules especially shock tracers can provide an alternative way to investigate the gas structure of the outflows.

Two outflows have been reported in Orion-KL, almost perpendicular to each other. In addition, along the NE–SW direction, a large-scale "integral-shaped" filament has been detected aligned with the low-velocity one (Wright et al. 1992; Lis et al. 1998; Di Francesco et al. 2008). To confirm whether the NE condensation is associated with the filament or the outflow, we selected several wide-spread species, and use a gaussian function to fit their line profile extracted from NE (Figure 2.7). Broad line wings ($C^{18}O$) and a second component (HNCO, SO_2 and ^{34}SO) with $V_{lsr} \sim$ 20–23 km s^{-1} indicate that line emission in NE contains significant contribution from the outflow, and is part of the plateau.

To study the chemistry in the outflows, we image the blue- and red-shifted gas of several shock-tracing molecules along the outflow direction (Figure A4). To avoid contamination from blending, we image as broad a velocity range as possible (labeled in each panel), though, $-20 \sim +30$ km s^{-1} is the limit for most lines other than SO, CO and ^{13}CO. Due to the range limit, and because of the limits of 52″ primary beam, the high-velocity outflow (30–100 km s^{-1}) cannot be imaged in its entirety. However, the low-velocity outflow ($\sim$ 18 km s^{-1}) with NE–SW elongated structure is clearly detected, showing bipolar structure in the intensity-integrated map of $H_2^{13}CO$. In addition, intensity-integrated maps of such molecules as OCS, $^{34}SO_2$, SO, HNCO, CH_2CO, CO and ^{13}CO all have a "butterfly" morphology, with blueshifted radial velocities of the moving gas toward the northwest, and the redshifted velocities in the southeast. Such morphology is exactly the same as that found in SiO (Wright et al. 1995; Niederhofer et al. 2012; Zapata et al. 2012) and H_2O maser observations (Plambeck et al. 2009) on scales of tens of AU. Whether this morphology is due to the bipolar lobes of the high-velocity outflow or the expanding low-velocity outflow is still not clear. Possibilities are discussed in Zapata et al. (2012) (e.g., two bipolar outflows from a precessing binary, ballistic ejecta from a rotating disk, a single

expanding wide-angle NE–SW outflow). The asymmetry shape of the lobes (e.g., "U" shape blue-shifted and half "U" red shifted lobes in the map of SO) is suggested to come from some density inhomogeneities in the surroundings.

Therefore, a picture of explosive NW–SE outflow can be suggested to explain the excitation temperature gradient from the center to periphery in Orion-KL (Zapata et al. 2012): the decelerated bullets can be absorbed by the BN/KL cloud, and their kinetic energy can be transferred to thermal energy (Peng et al. 2012b); the closer a gas parcel is to the explosion center (e.g., the closer encounter of BN, source I and maybe also source N, suggested by proper motion studies from Gómez et al. 2005; Rodríguez et al. 2005; Gómez et al. 2008 and 3D modelling from Nissen et al. 2012), the larger the thermal energy available to affect the chemical properties of the gas in the HC and mm2.

Of all the shock-related molecules, S-bearing species are of special interest, not only because their abundance may be enhanced by shocks (Martin-Pintado et al. 1992; Pineau des Forets et al. 1993; Chernin et al. 1994; Bachiller & Pérez Gutiérrez 1997; Charnley et al. 1997; Schilke et al. 1997; Bachiller et al. 2001; Viti et al. 2004; Garrod 2013), but also because they have been proposed to be potential chemical clocks to date outflows (and hence their protostellar driving source; e.g., Charnley et al. 1997; Wakelam et al. 2004a). The angular resolution of our study does not allow us to investigate the post/pre-shocked chemistry. In spite of that, we do find that some S-bearing molecules (e.g., SO_2, $^{34}SO_2$ and SO) have almost the same abundances in NE as in the central sources, which are higher than those in OF1N(S), even though we assume the temperatures in NE and OF1N(S) are similarly low[12]. the enhancement of their abundance may indicate stronger shocks in this direction than the rest of Orion-KL. On the other hand, although we can not tell the precise ages of different substructures, we can compare the variations of abundance ratios SO_2/SO in our observations to the modelling result from Wakelam et al. (2004a). To simplify the case, we assume that the temperatures in all substructures are 100 K, and all substructures have the same density $\sim 10^7$ cm^{-3}; and we estimate the value of SO_2 (lines are possibly optically thick) by using $^{34}SO_2$ and a ratio of $^{34}S/^{32}S = 22$ (Wilson & Rood 1994). Comparing the SO_2/SO ratio to modelling of Wakelam et al. (2004a) in all substructures (Figure 2.11), we find that, the HC has the largest SO_2/SO ratio, which suggests it is the most evolved substructure; then mm2, mm3a and mm3b are younger; and the lowest ratios are in the outflows, which indicate the age of the outflows should be $\ll 1 \times 10^3$ years (if derived from 45 K, the ratio should be lower than the upper limit we plot).

[12]CO and SO are more abundant in the plateau, which is suggested by Sutton et al. (1995) and Wright et al. (1996) to be a result of shock enhancement.

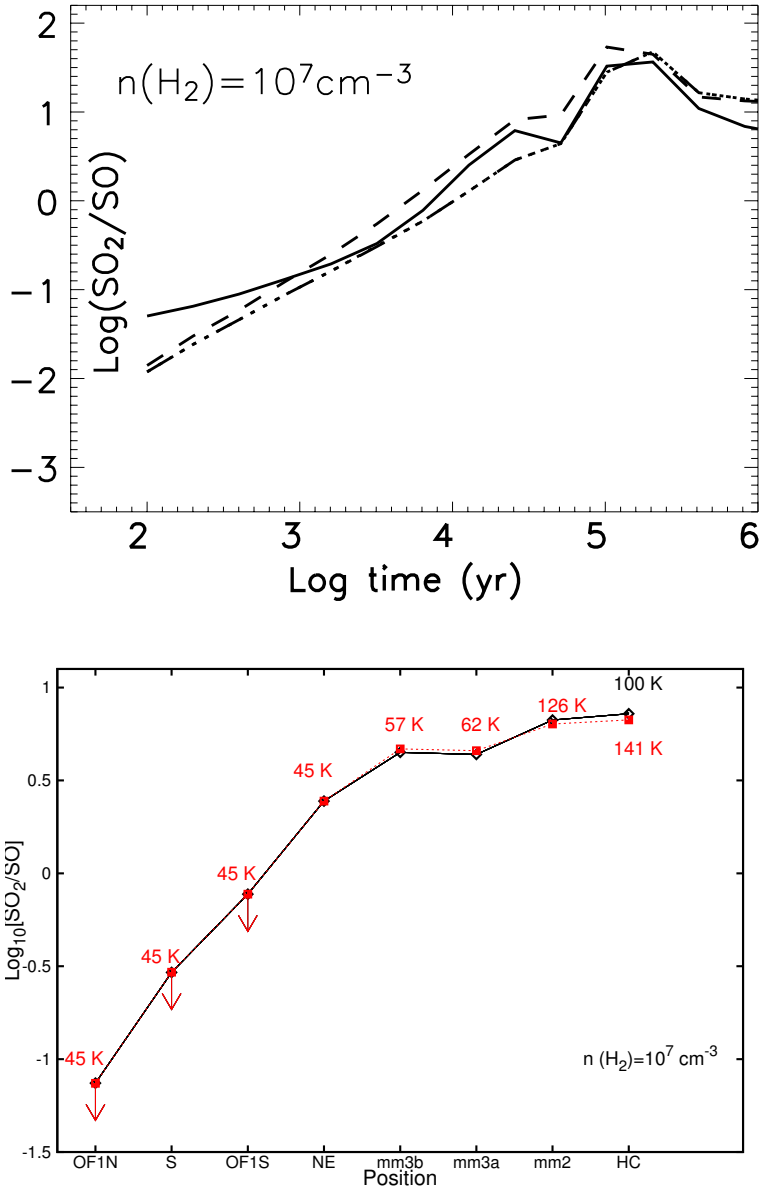

Figure 2.11: The upper panel is from Figure 5 of Wakelam et al. (2004a) (100 K, 10^7 cm^{-3}). The lower panel is from the calculation of SO_2/SO ratio by assuming (1) all substructures have similar density 10^7 cm^{-3}; (2) $N_{SO_2}/N_{^{34}SO_2}$ = 22 (Wilson & Rood 1994). The black solid line comes from the assumption that all substructures have similar temperature 100 K, and the red dashed line comes from different temperatures derived in Section 2.4.1 (labelled in red).

The shocks could also be responsible for the observed chemical differentiation in COMs (e.g., by stripping ices from grains). The CR (together with mm3a and mm3b) is thought to be the place where icy grains are released into the gas phase by an outflow from the hot core (Blake et al. 1987; Liu et al. 2002). Therefore, based on the reported association between the emissions of $HCOOCH_3$ and the 2.12 μm vibrationally excited H_2 (Lacombe et al. 2004), shocks between the ISM and high-velocity gas "bullets" from the outflow (Zapata et al. 2009; Bally et al. 2011) was suggested to explain the production of COMs, which has the same morphology as $HCOOCH_3$ (Favre et al. 2011b). In a similar scenario, N-bearing COMs may be released to the gas phase north-east of the hot core (e.g., HC_3N, CH_2CHCN), where the low-velocity outflow is impacting the ambient dusty material, and the weak emission/non-detection of these molecules along the high-velocity outflow may be due to lack of dusty material in the NW–SE direction (Friedel & Widicus Weaver 2012).

2.5.4 Search for COMs

The chemistry of Orion-KL is rich, not only in high-density tracers and shock-tracers, but also with numerous transitions of COMs, which are less abundant than the other tracers, and have a less well understood formation mechanism. Three possibilities have been discussed for the formation of the COMs: (1) ion-molecule chemistry involving large radicals (Ehrenfreund & Charnley 2000); (2) formation on dust grains, and then released to the gas at higher temperatures in the later stages of star formation (Garrod et al. 2008; Herbst & van Dishoeck 2009); (3) a hybrid approach that COMs are ejected into the gas via efcient reactive desorption, after a sequence of gas-phase reactions between precursor species formed on grain surfaces Vasyunin & Herbst (2013).

In our dataset, we search for several COMs (Table 2.2), and find that saturated molecules are likely to be more abundant than unsaturated molecules (e.g., HC_3N, C_6H, HC_7N, with the last two being the first tentative detections of these species in Orion-KL). This supports the scenario in which these species are being formed on dust grain surfaces, by subsequent hydrogenation of their precursor species (like CO, O, N or their more complex combinations).

Unfortunately, we lack the sensitivity to detect HCOOH (formic acid), which has been previously reported in Orion-KL by Liu et al. (2002). Line blending also prevents us from robustly detecting CH_3CHO (acetaldehyde), CH_2OHCHO (glycolaldehyde), and $(CH_2OH)_2$ (ethylene glycol) in our data. We also fail to detect other prebiotic molecules, e.g., NH_2CH_2COOH (glycine, Garrod 2013), CH_3COOH (acetic acid), NH_2CH_2CN (amino acetonitrile, Belloche et al. 2008),

CH_3CONH_2 (acetamide, van Dishoeck 2009), and the ring molecules [c-$C_3N_2H_4$ (imidazole), c-C_2H_5N (aziridine) and c-$C_4H_4N_2$ (pyrimidine)]. More sensitive observations (e.g., with ALMA) are required to determine whether these molecules exist in the Orion-KL environment.

2.6 Conclusions

Based on the analysis of combined SMA and 30 m observations of Orion-KL, we have drawn the following conclusions:

1. From interferometric observations with the SMA, Orion-KL has been resolved into several continuum substructures with different peak flux densities, at the spatial resolution of 3″ (1 200 AU at a distance of 414 pc). In addition to the previous well-known compact continuum sub-structures like the Hot Core (HC) and mm2, our data resolves the clump southwest of HC into two condensations: mm3a and mm3b. In addition, we confirmed the detection of strong continuum emissions ($> 5\sigma$) from two resolved condensations (S and NE), which lie along the axis of both the low-velocity outflow and the large-scale dusty filament.

2. We present the first interferometric map of Orion KL for which the missing short spacings have been complemented with single-dish observations. Covering a field of view of 52″, we map the distribution of all the identified molecules and their isotopologues. In particular, we obtain the first maps of molecules such $^{34}SO_2$, O^{13}CS, HNCO, $H_2^{13}CO$, ^{13}CO and CH_2CO with both high resolution and sensitivity to spatial information on all scales. We also identify several transitions of low abundance ($< 10^{-8}$ cm^{-2}) COMs, such as CH_3COCH_3 and CH_3CH_2OH, as well as make the first tentative detection of long carbon chains like C_6H and HC_7N.

3. The Orion KL region exhibits clear chemical differentiation on the scales probed by the SMA-30 m observations. The emission from S-bearing molecules, CO isotopologues and simple organic molecules are extended, covering not only the central regions (HC, mm2, mm3a and mm3b), but also the NE condensation, the southern ridge, and even the outflow regions. In comparison, the distributions of COMs are more concentrated and varied. The segregation of species which peak at either the HC (e.g., N-bearing) or CR (together with mm3a and mm3b, e.g., $HCOOCH_3$, CH_3OCH_3), indicates different formation pathways for O-bearing and N-bearing molecules. However, some COMs peak in-between the HC

and mm3a (e.g., CH_3CH_2OH), or have dual velocity dependent peaks (CH_3OH), or share the same morphology as N-bearing species (CH_3COCH3), which may indicate the linking of some formation pathways between O-bearing and N-bearing molecules.

4. By studying the chemistry within outflows of Orion-KL, we find that the high-velocity outflow has the bipolar lobes similar to the low-mass chemically active outflows. This is consistent with previous observations and supports the scenario that similar dynamic processes occur in high-mass and low-mass star formation. Higher abundances of such shock tracers as $^{34}SO_2$, SO_2 and SO in the plateau of the low-velocity outflow (NE) indicate stronger shocks in this direction than the rest of Orion-KL.

2.7 Appendix

Table A1: Identified emission lines from the SMA-30 m combined dataset.

Freq. (GHz)	Mol.	E_u/k_B (K)		Freq. (GHz)	Mol. (candidates)	E_u/k_B (K)	
218.903	$OCS_{(v=0)}(18 \rightarrow 17)$	100					
218.966	$HCOOCH_{3(v=1)}(18_{12,6} \rightarrow 17_{12,5})$E	384					
218.981	$HNCO_{(v=0)}(10_{1,10} \rightarrow 9_{1,9})$	101					
219.068	$HCOOCH_{3(v=1)}(18_{17,2} \rightarrow 17_{17,1})$E	481					
219.079	$HCOOCH_{3(v=1)}(28_{3,25} \rightarrow 28_{2,26})$E	434					
219.090	$HCOOCH_{3(v=0)}(34_{7,28} \rightarrow 34_{5,29})$E	387	*	219.090	$HCOOCH_{3(v=0)}(34_{7,28} \rightarrow 34_{5,29})$A	387	
219.154	$HCOOCH_{3(v=1)}(18_{11,7} \rightarrow 17_{11,6})$E	369	*	219.153	$HCOOCH_{3(v=1)}(10_{4,6} \rightarrow 9_{3,6})$E	230	*
219.174	$HC_3N_{(v_7=1)}(24 \rightarrow 23)$	452	†				
219.195	$HCOOCH_{3(v=1)}(18_{16,3} \rightarrow 17_{16,2})$E	459	*	219.196	$HCOOCH_{3(v=0)}(36_{6,30} \rightarrow 36_{6,31})$E	429	
219.220	$CH_3COCH_{3(v=0)}(21_{1,20} \rightarrow 20_{2,19}$AE)	122	*	219.220	$CH_3COCH_{3(v=0)}(21_{2,20} \rightarrow 20_{1,19}$AE)	122	
				219.220	$CH_3COCH_{3(v=0)}(21_{2,20} \rightarrow 20_{2,19}$EA)	122	
				219.220	$CH_3COCH_{3(v=0)}(21_{1,20} \rightarrow 20_{1,19}$EA)	122	
219.242	$CH_3COCH_{3(v=0)}(21_{1,20} \rightarrow 20_{2,19}$EE)	122	*	219.242	$CH_3COCH_{3(v=0)}(21_{2,20} \rightarrow 20_{1,19}$EE)	122	
				219.242	$CH_3COCH_{3(v=0)}(21_{2,20} \rightarrow 20_{2,19}$EE)	122	
				219.220	$CH_3COCH_{3(v=0)}(21_{1,20} \rightarrow 20_{1,19}$EE)	122	
219.264	$CH_3COCH_{3(v=0)}(21_{1,20} \rightarrow 20_{2,19}$AA)	122	*	219.264	$CH_3COCH_{3(v=0)}(21_{2,20} \rightarrow 20_{1,19}$AA)	122	
219.276	$SO_{2(v=0)}(22_{7,15} \rightarrow 23_{6,18})$	352					
219.311	$CH_3COCH_{3(v=0)}(12_{9,4} \rightarrow 11_{8,3}$AA)	66					
219.325	UL		?				
219.331	$HCOOCH_{3(v=1)}(18_{15,4} \rightarrow 17_{15,3})$E	438	*	219.328	$HCOOCH_{3(v=1)}(36_{9,28} \rightarrow 36_{8,29})$E	635	
219.355	$^{34}SO_{2(v=0)}(11_{1,11} \rightarrow 10_{0,10})$	60	†				
219.401	$CH_2CHCN_{(v=0)}(23_{3,20} \rightarrow 22_{3,19})$	145					
219.412	$HCOOCH_{3(v=1)}(18_{10,8} \rightarrow 17_{10,7})$E	355					
219.417	$HCOOCH_{3(v=0)}(30_{5,26} \rightarrow 30_{4,27})$E	291					
219.466	$CH_3OCH_3(28_{5,24} \rightarrow 27_{6,21})$	406	A(E)A(E)				
219.479	$HCOOCH_{3(v=1)}(18_{14,5} \rightarrow 17_{14,4})$E	419					
219.484	$HCOOCH_{3(v=0)}(30_{5,26} \rightarrow 30_{4,27})$A	291					
219.506	$CH_3CH_2CN_{(v=0)}(24_{2,22} \rightarrow 23_{2,21})$	136					
219.547	$HNCO_{(v=0)}(10_{4,6} \rightarrow 9_{4,5})$	750					
219.560	$C^{18}O(2 \rightarrow 1)$	16	†				
219.566	$HCOOCH_{3(v=1)}(18_{15,4} \rightarrow 17_{15,3})$A	438	*	219.566	$HCOOCH_{3(v=1)}(18_{15,3} \rightarrow 17_{15,2})$A	438	
219.568	$HCOOCH_{3(v=1)}(18_{14,5} \rightarrow 17_{14,4})$A	419	*	219.568	$HCOOCH_{3(v=1)}(18_{14,4} \rightarrow 17_{14,3})$A	419	
219.571	$HCOOCH_{3(v=1)}(18_{16,3} \rightarrow 17_{16,2})$A	458	*	219.571	$HCOOCH_{3(v=1)}(18_{16,2} \rightarrow 17_{16,1})$A	458	
219.579	$HCOOCH_{3(v=0)}(28_{9,19} \rightarrow 28_{8,20})$A	294	*	219.579	$HCOOCH_{3(v=1)}(18_{17,2} \rightarrow 17_{17,1})$A	481	
				219.579	$HCOOCH_{3(v=1)}(18_{17,1} \rightarrow 17_{17,0})$A	481	
				219.578	$HCOOCH_{3(v=1)}(29_{9,21} \rightarrow 29_{8,21})$E	498	
219.584	$HCOOCH_{3(v=1)}(18_{13,6} \rightarrow 17_{13,5})$A	401	*	219.584	$HCOOCH_{3(v=1)}(18_{13,5} \rightarrow 17_{13,4})$A	401	
				219.586	$HCOOCH_{3(v=0}(30_{9,22} \rightarrow 30_{8,23})$A	330	
219.592	$HCOOCH_{3(v=0}(28_{9,19} \rightarrow 28_{8,20})$E	294					
219.600	$HCOOCH_{3(v=0}(30_{9,22} \rightarrow 30_{8,23})$E	330					
219.607	$HCOOCH_{3(v=0}(30_{5,26} \rightarrow 30_{3,27})$E	291	*	219.610	$CH_3COCH_{3(v=0)}(33_{8,25} \rightarrow 33_{8,26}$EE)	368	
				219.610	$CH_3COCH_{3(v=0)}(33_{9,25} \rightarrow 33_{7,26}$EE)	368	
219.622	$HCOOCH_{3(v=1)}(18_{12,7} \rightarrow 17_{12,6})$A	384	*	219.622	$HCOOCH_{3(v=1)}(18_{12,6} \rightarrow 17_{12,5})$A	384	*
219.642	$HCOOCH_{3(v=1)}(18_{13,6} \rightarrow 17_{13,5})$E	401					
219.657	$HNCO(10_{3,8} \rightarrow 9_{3,7})$	447					
219.696	$HCOOCH_{3(v=1)}(18_{11,8} \rightarrow 17_{11,7})$A	369	*	219.696	$HCOOCH_{3(v=1)}(18_{11,7} \rightarrow 17_{11,6})$A	369	
219.705	$HCOOCH_{3(v=1)}(18_{4,15} \rightarrow 17_{4,14})$A	299					
219.734	$HNCO_{(v=0)}(10_{2,9} \rightarrow 9_{2,8})$	231					
219.737	$HNCO_{(v=0)}(10_{2,8} \rightarrow 9_{2,7})$	231					
219.764	$HCOOCH_{3(v=1)}(18_{9,9} \rightarrow 17_{9,8})$E	342					
219.798	$HNCO_{(v=0)}(10_{0,10} \rightarrow 9_{0,9})$	58	†				

219.822	$HCOOCH_{3(\nu=1)}(18_{10,9} \rightarrow 17_{10,8})A$	355	*	219.822	$HCOOCH_{3(\nu=1)}(18_{10,8} \rightarrow 17_{10,7})A$	355	
219.827	$HCOOCH_{3(\nu=1)}(18_{12,7} \rightarrow 17_{12,6})E$	384					
219.908	$H_2^{13}CO(3_{1,2} \rightarrow 2_{1,1})$	33	†				
219.949	$SO_{(\nu=0)}(6_5 \rightarrow 5_4)$	35	†				
219.984	$CH_3OH_{(\nu_t=0)}(25_{3,22} \rightarrow 24_{4,20})E$	802					
219.994	$CH_3OH_{(\nu_t=0)}(23_{5,19} \rightarrow 22_{6,17})E$	776					
220.030	$HCOOCH_{3(\nu=1)}(18_{9,10} \rightarrow 17_{9,9})A$	342	*	220.030	$HCOOCH_{3(\nu=1)}(18_{9,9} \rightarrow 17_{9,8})A$	342	
220.043	$HCOOCH_{3(\nu=1)}(18_{11,8} \rightarrow 17_{11,7})E$	368					
220.078	$CH_3OH_{(\nu_t=0)}(8_{0,8} \rightarrow 7_{1,6})E$	97					
220.154	t-$CH_3CH_2OH(24_{3,22} \rightarrow 24_{2,23})$	263					
220.167	$HCOOCH_{3(\nu=0)}(17_{4,13} \rightarrow 16_{4,12})E$	103	‡				
220.178	$CH_2CO(11_{1,11} \rightarrow 10_{1,10})$	76	†				
220.190	$HCOOCH_{3(\nu=0)}(17_{4,13} \rightarrow 16_{4,12})A$	103					
220.258	$HCOOCH_{3(\nu=1)}(18_{8,10} \rightarrow 17_{8,9})E$	330	‡				
220.296	$CH_3^{13}CN(12_9 \rightarrow 11_9)$	646					
220.307	$HCOOCH_{3(\nu=1)}(18_{10,9} \rightarrow 17_{10,8})E$	354					
220.324	$CH_3CN_{(\nu=0)}(12_{10} \rightarrow 11_{10})$	782					
220.355	$CH_3COCH_{3(\nu=0)}(22_{0,22} \rightarrow 21_{0,21})$	124	AE,EA*	220.355	$CH_3COCH_{3(\nu=0)}(22_{1,22} \rightarrow 21_{1,21})$	124	AE,EA
				220.355	C_6H(J = 159/2-157/2,Ω=3/2, l=e-1.95050)	425	?
220.362	$CH_3COCH_{3(\nu=0)}(22_{0,22} \rightarrow 21_{1,21})$	124	EE*	220.362	$CH_3COCH_{3(\nu=0)}(22_{1,22} \rightarrow 21_{1,21})$	124	EE
				220.362	$CH_3COCH_{3(\nu=0)}(22_{1,22} \rightarrow 21_{0,21})$	124	EE
				220.362	$CH_3COCH_{3(\nu=0)}(22_{0,22} \rightarrow 21_{0,21})$	124	EE
220.368	$HCOOCH_{3(\nu=1)}(18_{8,11} \rightarrow 17_{8,10})A$	331	*	220.370	$HCOOCH_{3(\nu=1)}(18_{8,10} \rightarrow 17_{8,9})A$	331	*
				220.368	$CH_3COCH_{3(\nu=0)}(22_{1,22} \rightarrow 21_{1,21})$	124	AA
				220.368	$CH_3COCH_{3(\nu=0)}(22_{0,22} \rightarrow 21_{0,21})$	124	AA
				220.368	$CH_3^{13}CN(12_8 \rightarrow 11_8)$	526	*
220.399	$^{13}CO(2 \rightarrow 1)$	16	†				
220.404	$CH_3CN_{(\nu=0)}(12_9 \rightarrow 11_9)$	646					
220.416	$HCOOCH_{3(\nu=1)}(18_{3,16} \rightarrow 17_{2,15})A$	293					
220.431	$CH_3^{13}CN(12_7 \rightarrow 11_7)$	417	*				
220.433	$HCOOCH_{3(\nu=0)}(35_{5,28} \rightarrow 33_{5,29})A$	357	*				
220.444	g-$CH_3CH_2OH(28_{7,22} \rightarrow 28_{6,22}\nu_t = 0-1)$	455	*	220.443	g-$CH_3CH_2OH(30_{7,23} \rightarrow 30_{6,25}\nu_t = 0-1)$	503	
220.465	$CH_3COCH_{3(\nu=0)}(11_{11,1} \rightarrow 10_{10,0}AE)$	63	*	220.466	$CH_3COCH_{3(\nu=0)}(11_{11,0} \rightarrow 10_{10,1}AE)$	63	
220.476	$CH_3CN_{(\nu=0)}(12_8 \rightarrow 11_8)$	526					
220.486	$CH_3^{13}CN(12_6 \rightarrow 11_6)$	326	*	220.487	C_6H(J = 159/2-157/2, Ω=3/2,, l=f-1.95030)	426	?
220.525	$HCOOCH_{3(\nu=1)}(10_{4,6} \rightarrow 9_{3,7})A$	231					
220.533	$CH_3^{13}CN(12_5 \rightarrow 11_5)$	247	*				
220.539	$CH_3CN_{(\nu=0)}(12_7 \rightarrow 11_7)$	419					
220.561	$CH_2CHCN(24_{1,24} \rightarrow 23_{1,23})$	134					
220.570	$CH_3^{13}CN(12_4 \rightarrow 11_4)$	183	*				
220.585	$HNCO_{(\nu=0)}(10_{1,9} \rightarrow 9_{1,8})$	101					
220.594	$CH_3CN_{(\nu=0)}(12_6 \rightarrow 11_6)$	326					
220.621	$CH_3^{13}CN(12_2 \rightarrow 11_2)$	97	‡				
220.641	$CH_3CN_{(\nu=0)}(12_5 \rightarrow 11_5)$	248					
220.661	$CH_3CH_2CN_{(\nu=0)}(25_{2,24} \rightarrow 24_{2,23})$	143					
220.679	$CH_3CN_{(\nu=0)}(12_4 \rightarrow 11_4)$	183					
220.709	$CH_3CN_{(\nu=0)}(12_3 \rightarrow 11_3)$	133					
220.730	$CH_3CN_{(\nu=0)}(12_2 \rightarrow 11_2)$	98	‡				
220.743	$CH_3CN_{(\nu=0)}(12_1 \rightarrow 11_1)$	76					
220.747	$CH_3CN_{(\nu=0)}(12_0 \rightarrow 11_0)$	69					
220.764	$CH_3COCH_{3(\nu=0)}(11_{11,0} \rightarrow 10_{10,0}EE)$	63					
220.786	$HCOOCH_{3(\nu=0)}(28_{3,25} \rightarrow 28_{3,26})E$	248	*				
220.812	$HCOOCH_{3(\nu=0)}(18_{3,16} \rightarrow 17_{2,15})E$	105					
220.815	$HCOOCH_{3(\nu=0)}(18_{3,16} \rightarrow 17_{2,15})A$	105					
220.820	$HCOOCH_{3(\nu=0)}(24_{2,23} \rightarrow 24_{1,24})A$	169					
220.848	$CH_3OCH_3(24_{4,20} \rightarrow 23_{5,19})$	297	A(E)A(E)				
220.866	$HCOOCH_{3(\nu=0)}(28_{3,25} \rightarrow 28_{3,26})A$	248	*	220.866	$HCOOCH_{3(\nu=1)}(19_{2,17} \rightarrow 18_{3,16})A$	303	
220.889	$HCOOCH_{3(\nu=0)}(18_{17,1} \rightarrow 17_{17,0})A$	293	*	220.889	$HCOOCH_{3(\nu=0)}(18_{17,2} \rightarrow 17_{17,1})A$	293	
220.893	$CH_3OCH_3(23_{4,20} \rightarrow 23_{3,21})$	274	A(E)A(E)				

220.901	$HCOOCH_{3(v=0)}(18_{17,1} \rightarrow 17_{17,0})$E	293					
220.913	$HCOOCH_{3(v=1)}(18_{7,12} \rightarrow 17_{7,11})$A	320		220.910	$HCOOCH_{3(v=0)}(18_{17,2} \rightarrow 17_{17,1})$E	293	*
220.926	$HCOOCH_{3(v=0)}(18_{16,2} \rightarrow 17_{16,1})$A	271	*	220.926	$HCOOCH_{3(v=0)}(18_{16,3} \rightarrow 17_{16,2})$A	271	
220.935	$HCOOCH_{3(v=0)}(18_{16,2} \rightarrow 17_{16,1})$E	271					
220.946	$HCOOCH_{3(v=1)}(18_{7,11} \rightarrow 17_{7,10})$A	321		220.947	$HCOOCH_{3(v=0)}(18_{16,3} \rightarrow 17_{16,2})$E	271	*
220.967	$HC_7N_{(v=0)}$(J = 196 – 195)	1045	?				
220.978	$HCOOCH_{3(v=0)}(18_{15,4} \rightarrow 17_{15,3})$A	250		220.978	$HCOOCH_{3(v=0)}(18_{15,3} \rightarrow 17_{15,2})$A	250	
220.985	$HCOOCH_{3(v=1)}(18_{7,11} \rightarrow 17_{7,10})$E	320	*	220.984	$HCOOCH_{3(v=0)}(18_{15,3} \rightarrow 17_{15,2})$E	250	
220.998	$HCOOCH_{3(v=0)}(18_{15,4} \rightarrow 17_{15,3})$E	250	*	220.999	g-$CH_3CH_2OH(13_{0,13} \rightarrow 12_{0,12}\nu_t = 0 - 1)$	136	
221.048	$HCOOCH_{3(v=0)}(18_{14,5} \rightarrow 17_{14,4})$A	231	*	221.048	$HCOOCH_{3(v=0)}(18_{14,4} \rightarrow 17_{14,3})$A	231	
				221.048	$HCOOCH_{3(v=0)}(18_{14,4} \rightarrow 17_{14,3})$E	231	
221.067	$HCOOCH_{3(v=0)}(18_{14,5} \rightarrow 17_{14,4})$A	231					
221.076	$HCOOCH_{3(v=0)}(29_{9,21} \rightarrow 29_{8,22})$A	312					
221.086	$HCOOCH_{3(v=0)}(29_{9,21} \rightarrow 29_{8,22})$E	312					
221.111	$HCOOCH_{3(v=1)}(18_{8,11} \rightarrow 17_{8,10})$E	330					
221.115	$^{34}SO_{2(v=0)}(22_{2,20} \rightarrow 22_{1,21})$	248					
221.124	$CH_2CHCN_{(v=0)}(23_{1,22} \rightarrow 22_{1,21})$	130					
221.140	$HCOOCH_{3(v=0)}(18_{13,5} \rightarrow 17_{13,4})$E	213	*	221.141	$HCOOCH_{3(v=0)}(18_{13,5} \rightarrow 17_{13,4})$A	213	
				221.141	$HCOOCH_{3(v=0)}(18_{13,6} \rightarrow 17_{13,5})$A	213	
229.056	$CH_3COCH_{3(v=0)}(22_{1,21} \rightarrow 21_{2,20}$EE)	133	*	229.056	$CH_3COCH_{3(v=0)}(22_{1,21} \rightarrow 21_{1,20}$EE)	133	
				229.056	$CH_3COCH_{3(v=0)}(22_{2,21} \rightarrow 21_{2,20}$EE)	133	
				229.056	$CH_3COCH_{3(v=0)}(22_{2,21} \rightarrow 21_{1,20}$EE)	133	
				229.058	$CH_3COCH_{3(v=0)}(14_{9,6} \rightarrow 13_{8,5}$EE)	85	
229.078	$CH_3COCH_{3(v=0)}(22_{1,21} \rightarrow 21_{2,20}$AA)	133	*	229.078	$CH_3COCH_{3(v=0)}(22_{2,21} \rightarrow 21_{1,20}$AA)	133	
229.087	$CH_2CHCN_{(v=0)}(24_{3,21} \rightarrow 23_{3,20})$	156					
229.117	$HCOOCH_{3(v=1)}(19_{3,17} \rightarrow 18_{2,16})$E	303					
229.127	$CH_3COCH_{3(v=0)}(12_{10,2} \rightarrow 11_{9,2}$EE)	68					
229.203	UL		?				
229.224	$HCOOCH_{3(v=0)}(23_{9,14} \rightarrow 23_{8,15})$A	217					
229.259	$HCOOCH_{3(v=0)}(23_{9,14} \rightarrow 23_{8,15})$E	217					
229.265	$CH_3CH_2CN_{(v=0)}(26_{2,25} \rightarrow 25_{5,24})$	154	‡				
229.320	$HCOOCH_{3(v=0)}(23_{9,15} \rightarrow 23_{8,16})$E	217					
229.348	$SO_{2(v=0)}(11_{5,7} \rightarrow 12_{4,8})$	122	†				
229.389	$HCOOCH_{3(v=0)}(23_{9,15} \rightarrow 23_{8,16})$A	217					
229.405	$HCOOCH_{3(v=0)}(18_{3,15} \rightarrow 17_{3,14})$E	111					
229.420	$HCOOCH_{3(v=0)}(18_{3,15} \rightarrow 17_{3,14})$A	111					
229.474	$HCOOCH_{3(v=0)}(20_{3,17} \rightarrow 19_{4,16})$E	134					
229.491	t-$CH_3CH_2OH(17_{5,12} \rightarrow 17_{4,13})$	160	*	229.498	g-$CH_3CH_2OH(41_{11,31} \rightarrow 40_{12,29}\nu_t = 1 - 0)$	925	
				229.498	g-$CH_3CH_2OH(41_{11,30} \rightarrow 40_{12,28}\nu_t = 1 - 0)$	925	
229.505	$HCOOCH_{3(v=0)}(20_{3,17} \rightarrow 19_{4,16})$A	134					
229.539	$HCOOCH_{3(v=0)}(31_{5,27} \rightarrow 31_{3,28})$E	309					
229.589	$CH_3OH_{(\nu_t=0)}(15_{4,11} \rightarrow 16_{3,13})$E	374					
229.607	$HCOOCH_{3(v=0)}(31_{5,27} \rightarrow 31_{3,28})$A	309					
229.648	$CH_2CHCN_{(v=0)}(25_{1,25} \rightarrow 24_{1,24})$	146					
229.661	$HCOOCH_{3(v=1)}(25_{9,16} \rightarrow 25_{8,17})$A	432	*				
229.759	$CH_3OH_{(\nu_t=0)}(8_{-1,8} \rightarrow 7_{0,7})$E	89	‡				
229.858	$^{34}SO_{2(v=0)}(4_{2,2} \rightarrow 3_{1,3})$	19					
229.864	$CH_3OH_{(\nu_t=0)}(19_{5,15} \rightarrow 20_{4,16})$A + +	578					
229.888	$^{34}SO_{2(v=0)}(17_{3,15} \rightarrow 18_{0,18})$	162					
229.939	$CH_3OH_{(\nu_t=0)}(19_{5,14} \rightarrow 20_{4,17})$A – –	578					
229.987	$^{34}SO_{2(v=0)}(42_{6,36} \rightarrow 41_{7,35})$	921					
230.027	$CH_3OH_{(\nu_t=0)}(3_{-2,2} \rightarrow 4_{-1,4})$E	40					
230.108	C_6H(J = 165/2-163/2, Ω=1/2, l=f-1.98020)	482	? ‡				
230.140	$CH_3OCH_3(25_{4,22} \rightarrow 25_{3,22}$EA)	319	A(E)A(E)‡				
230.170	$CH_3COCH_{3(v=0)}(23_{0,23} \rightarrow 22_{1,22}$AE)	135	*	230.170	$CH_3COCH_{3(v=0)}(23_{1,23} \rightarrow 22_{0,22}$AE)	135	
				230.170	$CH_3COCH_{3(v=0)}(23_{0,23} \rightarrow 22_{0,22}$EA)	135	
				230.170	$CH_3COCH_{3(v=0)}(23_{1,23} \rightarrow 22_{1,22}$EA)	135	
230.177	$CH_3COCH_{3(v=0)}(23_{0,23} \rightarrow 22_{1,22}$EE)	135	*	230.177	$CH_3COCH_{3(v=0)}(23_{1,23} \rightarrow 22_{0,22}$EE)	135	
				230.177	$CH_3COCH_{3(v=0)}(23_{0,23} \rightarrow 22_{0,22}$EE)	135	

				230.177	$CH_3COCH_{3(\nu=0)}(23_{1,23} \rightarrow 22_{1,22}EE)$	135	
230.183	$CH_3COCH_{3(\nu=0)}(23_{0,23} \rightarrow 22_{1,22}AA)$	135	‡*	230.183	$CH_3COCH_{3(\nu=0)}(23_{1,23} \rightarrow 22_{0,22}AA)$	135	
230.238	$CH_3OCH_3(17_{2,15} \rightarrow 16_{3,14})$	148	A(E)A(E)	230.234	C_6H(J = 165/2-163/2, Ω=1/2, l=e-1.98010)	483	?
230.283	$CH_3COCH_{3(\nu=0)}(16_{8,8} \rightarrow 15_{9,7}EE)$	107					
230.293	$CH_3OH_{(\nu_t=0)}(22_{2,20} \rightarrow 21_{-3,19})E$	609					
230.318	$O^{13}CS(19 \rightarrow 18)$	111	†				
230.369	$CH_3OH_{(\nu_t=0)}(22_{4,18} \rightarrow 21_{5,17})E$	683					
230.377	$HCOOCH_{3(\nu=0)}(22_{9,14} \rightarrow 22_{8,15})A$	203	*				
230.436	$HCOOCH_{3(\nu=0)}(25_{1,24} \rightarrow 25_{1,25})E$	182	*	230.436	$HCOOCH_{3(\nu=0)}(25_{1,24} \rightarrow 25_{0,25})E$	182	
230.441	$HCOOCH_{3(\nu=0)}(25_{2,24} \rightarrow 25_{1,25})E$	182	*	230.441	$HCOOCH_{3(\nu=0)}(25_{2,24} \rightarrow 25_{0,25})E$	182	
230.476	$CH_3OCH_3(10_{8,3} \rightarrow 11_{7,5})$	140	EE*	230.478	$CH_3OCH_3(10_{8,2} \rightarrow 11_{7,5})$	140	AA,AE
				230.478	$CH_3OCH_3(10_{8,3} \rightarrow 11_{7,4})$	140	AA,AE
				230.482	$CH_3OCH_3(10_{8,2} \rightarrow 11_{7,4})$	140	EE,EA
230.488	$CH_2CHCN_{(\nu=0)}(24_{1,23} \rightarrow 23_{1,22})$	141					
230.505	$CH_3OCH_3(26_{4,23} \rightarrow 25_{5,20})$	343	A(E)A(E)				
230.538	$CO_{(\nu=0)}(2 \rightarrow 1)$	17	†				
230.673	g-$CH_3CH_2OH(13_{2,11} \rightarrow 12_{2,10}\nu_t = 0-0)$	139					
230.697	g-$CH_3CH_2OH(8_{3,5} \rightarrow 8_{2,7}\nu_t = 1-0)$	103					
230.739	$CH_2CHCN_{(\nu=0)}(25_{0,25} \rightarrow 24_{0,24})$	146	‡				
230.794	g-$CH_3CH_2OH(6_{5,1} \rightarrow 5_{4,1}\nu_t = 0-1)$	105	*	230.794	g-$CH_3CH_2OH(6_{5,2} \rightarrow 5_{4,2}\nu_t = 0-1)$	105	
230.844	$HCOOCH_{3(\nu=1)}(19_{17,2} \rightarrow 18_{17,1})E$	493	*				
230.852	$HCOOCH_{3(\nu=1)}(19_{16,3} \rightarrow 18_{16,2})E$	470	*				
230.879	$HCOOCH_{3(\nu=1)}(18_{4,14} \rightarrow 17_{4,13})A$	301					
230.889	$HCOOCH_{3(\nu=1)}(19_{15,4} \rightarrow 18_{15,3})E$	450					
230.933	$^{34}SO_{2(\nu=0)}(5_{4,2} \rightarrow 6_{3,3})$	52		230.936	$HCOOCH_{3(\nu=0)}(29_{3,26} \rightarrow 29_{2,27})E$	265	*
230.954	t-$CH_3CH_2OH(16_{5,11} \rightarrow 16_{4,12})$	145					
230.960	$HCOOCH_{3(\nu=1)}(19_{14,5} \rightarrow 18_{14,4})E$	430					
230.991	t-$CH_3CH_2OH(14_{0,14} \rightarrow 13_{1,13})$	86	*‡	230.992	g-$CH_3CH_2OH(6_{5,1} \rightarrow 6_{4,2}\nu_t = 1-1)$	110	
				230.993	g-$CH_3CH_2OH(6_{5,2} \rightarrow 6_{4,3}\nu_t = 1-1)$	110	
231.019	$HCOOCH_{3(\nu=0)}(12_{4,9} \rightarrow 11_{3,8})E$	57	*	231.020	$HCOOCH_{3(\nu=0)}(29_{3,26} \rightarrow 29_{2,27})A$	264	
231.046	$HCOOCH_{3(\nu=0)}(12_{4,9} \rightarrow 11_{3,8})A$	57					
231.061	$OCS_{(\nu=0)}(19 \rightarrow 18)$	111	†				
231.102	HC_7N(J = 205 – 204)	1142	?‡				
231.188	$HCOOCH_{3(\nu=0)}(21_{9,13} \rightarrow 21_{8,14})E$	190					
231.199	$HCOOCH_{3(\nu=0)}(21_{9,12} \rightarrow 21_{8,13})A$	190	*	231.199	$HCOOCH_{3(\nu=0)}(21_{9,12} \rightarrow 21_{8,13})E$	190	
231.221	$^{13}CS_{(\nu=0)}(5 \rightarrow 4)$	33	†				
231.231	$HCOOCH_{3(\nu=1)}(19_{12,7} \rightarrow 18_{12,6})E$	396		231.231	g-$CH_3CHO(12_{8,5} \rightarrow 11_{8,4}E)$	216	

* Due to the frequency resolution (0.8125 MHz, ~ 1.2km s^{-1}), lines with broad FWHM width can be attributed to different species, so lines with stronger CDMS/JPL intensity are listed in the left column with "*", and the potential blended weaker transitions are listed in the right column. Tentative detections and unidentified lines are marked with "?". Lines with "†" are imaged in Figure 2.4, with ''‡" are imaged in Figure 2.5.

**"A(E)A(E)" represents 4 types of transitions are possible: AA, EE, AE, EA

I(a). Laboratory parameters and integrated intensities $\int T_B(\upsilon)d\upsilon$ of CH_3CN (J = 12 − 11)*]

Freq (GHz)	K	$S\mu^2$ (D^2)	E_L (cm^{-1})	g_u	o-/p-	HC (K km s^{-1})	mm2 (K km s^{-1})	mm3a (K km s^{-1})	mm3b (K km s^{-1})	NE (K km s^{-1})
220.476	8	141.307	357.938	50	p-	372.96 ± 2.81	211.34 ± 1.14	255.62 ± 0.85	348.84 ± 1.06	≤ 11.19
220.539	7	167.802	283.608	50	p-	144.31 ± 3.70	49.48 ± 1.90	27.68 ± 1.16	33.72 ± 1.52	≤ 0.61
220.594	6	381.536	219.154	100	o-	356.10 ± 7.70	150.47±10.38	90.69 ± 11.98	190.53 ± 2.74	0.71 ± 0.53
220.641	5	210.189	164.592	50	p-	327.23±32.55	146.62 ± 4.76	106.37±10.00	178.31 ± 5.00	1.34 ± 0.63
220.679	4	226.122	119.933	50	p-	307.21±25.39	150.29 ± 5.73	142.61 ± 2.77	170.24±10.00	5.11 ± 0.36
220.709	3	476.933	85.187	100	o-	484.10±10.61	209.82±15.40	278.38 ± 7.16	319.87±13.08	11.92 ± 0.56
220.730	2	247.327	60.363	50	p-	397.54 ± 9.19	281.55±10.27	256.41±27.26	331.98±21.20	15.17 ± 1.00
220.743	1	252.577	45.467	50	p-	371.68±28.18	229.32 ± 8.17	247.64±10.46	284.65±25.77	13.52 ± 0.66
220.747	0	254.410	40.501	50	p-	372.96±28.18	211.34 ± 4.55	255.62 ± 1.40	348.84±25.77	11.19 ± 0.37

* None detection is given by an upper limit of 3σ rms
Laboratory parameters are given from CDMS.

I(b). Laboratory parameters and integrated intensities $\int T_B(\upsilon)d\upsilon$ of $CH_3^{13}CN$ (J = 12 − 11)*]

Freq (GHz)	K	$S\mu^2$ (D^2)	E_L (cm^{-1})	g_u	o-/p-	HC (K km s^{-1})
220.430	7	241.835	283.587	50	p-	2.92 ± 0.61
220.485	6	549.868	219.133	100	o-	14.29 ± 1.21
220.532	5	302.923	164.571	50	p-	16.78 ± 1.47
220.570	4	325.812	119.912	50	p-	29.83 ± 4.25
220.621	2	356.367	60.343	50	p-	55.55 ± 4.41

Laboratory parameters are given from CDMS.

II. Laboratory parameters and integrated intensities $\int T_B(\upsilon)d\upsilon$ of CH_3OH]

Freq (GHz)	$S\mu^2$ (D^2)	E_L (cm^{-1})	g_u	HC (K km s^{-1})	mm2 (K km s^{-1})	mm3a (K km s^{-1})	mm3b (K km s^{-1})
219.984	8.397	550.204	51	23.44 ± 0.53	5.96 ± 0.96	9.44 ± 6.00	6.13 ± 1.28
219.994	6.643	531.938	47	18.37 ± 1.44	8.99 ± 3.00	6.88 ± 0.57	10.65 ± 2.33
220.078	3.447	59.809	17	175.00±9.00	163.50 ± 16.00	285.56 ± 23.00	300.80±6.77
229.589	4.592	252.591	31	106.85±2.03	56.47 ± 0.95	94.80±16.00	114.36±3.63
229.759	5.048	54.266	17	193.14±2.06	209.17±2.45	326.94±1.27	359.76±1.47
229.939	5.711	394.477	39	38.47 ± 1.03	14.97 ± 0.68	27.50 ± 1.10	28.46 ± 0.71
230.027	0.734	20.009	7	106.32±1.44	100.37±1.57	162.28±1.84	179.02±2.06
230.293	1.004	415.980	45	7.48 ± 1.02	6.23 ± 1.70	8.19 ± 1.58	14.36 ± 1.60
230.369	6.594	466.848	45	29.52 ± 1.24	12.79 ± 1.32	12.78 ± 1.02	16.73 ± 1.69

Laboratory parameters are given from CDMS.

Table A2: The intensity integrated over the width of each line $\int T_B(\upsilon)d\upsilon$, which is used for rotation diagrams Figure 2.8 and Figure 2.9. Uncertainties on the measured intensities are typically ≤ 10%, as determined from Gaussian fitting. For lines of CH_3CN, CH_3OH and $^{34}SO_2$ which are not detected, an upper limit equal to the 3σ rms is given.

III. Laboratory parameters and integrated intensities $\int T_B(\upsilon)d\upsilon$ of $^{34}SO_2$]

Freq (GHz)	$S\mu^2$ (D^2)	E_L (cm^{-1})	g_u	HC (K km s^{-1})	mm2 (K km s^{-1})	mm3a (K km s^{-1})	mm3b (K km s^{-1})
219.355	20.753	34.438	23	192.87±6.47	177.38±3.74	78.92 ± 1.48	103.15±2.72
221.115	33.774	164.876	45	77.29 ± 6.98	28.80 ± 4.13	27.83 ± 1.59	23.11 ± 2.11
229.858	4.540	5.311	9	145.14±3.13	79.54 ± 2.07	32.57 ± 2.65	30.12 ± 3.15
229.888	0.322	104.865	35	10.12 ± 0.75	≤ 0.91	≤ 0.51	≤ 0.30
229.987	17.700	631.573	85	4.01 ± 0.85	1.78 ± 0.44	≤ 0.75	≤ 1.20
230.933	0.675	28.220	11	7.63 ± 1.72	19.26 ± 1.63	6.97 ± 1.02	8.70 ± 1.75

* None detection is given by an upper limit of 3σ rms
Laboratory parameters are given from CDMS.

IV(a). Laboratory parameters and integrated intensities $\int T_B(\upsilon)d\upsilon$ of $HCOOCH_3$ ($\nu = 1$)*]

Freq (GHz)	$S\mu^2$ (D^2)	E_L (cm^{-1})	g_u	HC (K km s^{-1})	mm2 (K km s^{-1})	mm3a (K km s^{-1})	mm3b (K km s^{-1})
218.966	26.629	259.918	74	2.17 ± 0.00	2.25 ± 0.75	2.87 ± 1.03	6.32 ± 1.03
219.155	30.028	249.175	74	6.26 ± 0.43	4.81 ± 0.58	6.26 ± 0.55	9.44 ± 0.55
219.479	19.004	283.781	74	−−	−−	0.82 ± 0.39	2.06 ± 0.39
219.584	22.979	271.154	74	3.18 ± 0.63	3.05 ± 0.63	7.04 ± 0.77	10.08 ± 0.77
219.623	26.667	259.539	74	4.81 ± 0.30	5.55 ± 0.56	8.12 ± 0.94	12.94 ± 0.94
219.642	23.008	271.148	74	−−	−−	1.90 ± 0.42	3.39 ± 0.42
219.696	30.057	248.860	74	6.14 ± 1.07	6.47 ± 0.43	9.24 ± 0.62	14.74 ± 0.62
219.705	45.230	200.469	74	28.88 ± 0.89	12.16 ± 0.34	9.88 ± 0.46	18.45 ± 0.46
219.764	35.954	230.499	74	6.03 ± 0.49	6.18 ± 0.40	6.27 ± 0.34	11.04 ± 0.34
219.822	33.141	239.119	74	3.61 ± 0.64	5.22 ± 0.86	9.10 ± 1.09	14.66 ± 1.09
219.827	26.712	259.457	74	1.80 ± 0.45	1.50 ± 0.71	2.70 ± 0.92	5.69 ± 0.92
220.030	35.936	230.319	74	5.86 ± 0.70	8.35 ± 1.32	12.28 ± 1.32	20.35 ± 1.32
220.043	30.121	248.708	74	1.41 ± 0.93	2.99 ± 0.00	2.73 ± 0.81	5.84 ± 0.81
220.258	38.487	222.578	74	7.52 ± 0.70	6.85 ± 0.67	10.65 ± 1.02	16.40 ± 1.02
220.307	33.230	238.906	74	3.04 ± 0.47	4.45 ± 0.35	4.91 ± 0.40	9.25 ± 0.40
220.368	38.428	222.466	74	12.33 ± 2.53	15.04 ± 1.36	19.00 ± 1.55	32.09 ± 1.55
220.914	40.621	215.570	74	7.70 ± 0.80	11.26 ± 1.22	13.42 ± 1.34	21.02 ± 1.34
220.946	40.619	215.571	74	9.18 ± 1.40	11.30 ± 0.53	18.88 ± 0.91	31.07 ± 0.91
220.985	40.717	215.616	74	11.98 ± 5.21	15.49 ± 2.53	14.17 ± 4.45	27.29 ± 4.45
221.111	38.549	222.159	74	−−	−−	12.95 ± 1.96	19.97 ± 1.96
230.879	45.618	201.531	74	4.79 ± 1.53	8.03 ± 0.68	11.76 ± 0.71	22.34 ± 0.71

* None detection is marked with "–"
Laboratory parameters are given from JPL.

Table A2: (continued)

IV(b). Laboratory parameters and integrated intensities $\int T_B(\upsilon)d\upsilon$ of $HCOOCH_3$ ($\nu = 0$)*]

Freq (GHz)	$S\mu^2$ (D^2)	E_L (cm^{-1})	g_u	HC (K km s^{-1})	mm2 (K km s^{-1})	mm3a (K km s^{-1})	mm3b (K km s^{-1})
219.417	5.494	195.355	122	−−	−−	1.57 ± 0.38	3.66 ± 0.38
219.484	5.490	195.354	122	−−	1.32 ± 0.44	2.00 ± 0.43	3.32 ± 0.43
219.592	7.189	197.439	114	0.90 ± 0.32	1.32 ± 0.85	2.77 ± 1.00	5.16 ± 1.00
220.167	42.925	64.350	70	38.44 ± 2.02	36.01 ± 1.44	57.74 ± 1.40	78.96 ± 1.40
220.190	42.934	64.344	70	24.45 ± 1.39	35.99 ± 2.36	60.42 ± 2.59	78.54 ± 2.59
220.812	4.435	66.218	74	5.91 ± 0.98	6.77 ± 0.36	10.22 ± 0.85	15.57 ± 0.85
220.815	4.434	66.210	74	5.24 ± 0.93	4.09 ± 0.33	8.71 ± 0.93	18.34 ± 0.93
220.926	10.092	180.745	74	4.25 ± 0.54	7.14 ± 1.30	9.34 ± 1.19	14.46 ± 1.19
220.935	10.091	180.739	74	5.12 ± 0.98	2.69 ± 0.44	4.89 ± 0.51	9.68 ± 0.51
220.978	14.686	166.459	74	−−	8.52 ± 1.66	11.64 ± 2.81	20.14 ± 2.81
220.998	14.686	166.446	74	4.31 ± 1.04	6.80 ± 0.98	11.86 ± 0.82	17.70 ± 0.82
221.048	18.980	153.092	74	15.11 ± 0.98	30.75 ± 0.93	45.62 ± 1.07	73.34 ± 1.07
221.067	18.980	153.081	74	2.59 ± 1.28	9.24 ± 0.48	11.91 ± 0.47	21.32 ± 0.47
221.086	7.569	209.447	118	1.75 ± 0.35	1.43 ± 1.09	3.45 ± 0.81	5.03 ± 0.81
221.140	22.973	140.647	74	11.28 ± 2.28	37.37 ± 0.70	50.30 ± 0.99	88.58 ± 0.99
229.224	5.427	143.199	94	−−	2.25 ± 0.60	2.71 ± 0.53	5.09 ± 0.53
229.259	4.669	143.201	94	−−	−−	−−	3.27 ± 0.90
229.389	5.425	143.193	94	−−	4.31 ± 0.27	2.99 ± 0.46	6.82 ± 0.46
229.405	46.117	69.316	74	20.44 ± 0.80	37.31 ± 1.09	47.60 ± 2.26	72.27 ± 2.26
229.420	46.121	69.310	74	25.89 ± 1.04	37.54 ± 1.72	47.68 ± 1.86	73.39 ± 1.86
230.377	5.083	133.656	90	−−	1.52 ± 0.47	4.07 ± 0.41	7.19 ± 0.41
230.436	1.380	118.982	102	1.40 ± 0.01	−−	1.79 ± 0.01	3.20 ± 0.01
230.441	1.380	118.983	102	2.90 ± 0.16	2.37 ± 0.43	1.99 ± 0.19	4.53 ± 0.19
231.019	1.799	31.810	50	1.69 ± 0.83	5.69 ± 0.51	8.45 ± 0.91	14.60 ± 0.91
231.046	1.799	31.801	50	−−	−−	4.90 ± 1.24	13.58 ± 1.24
231.188	4.707	124.543	86	2.81 ± 0.83	−−	4.06 ± 0.76	5.91 ± 0.76
231.199	4.746	124.546	86	6.55 ± 0.96	5.42 ± 0.48	11.01 ± 0.96	21.05 ± 0.96

* None detection is marked with "–"

Laboratory parameters are given from JPL.

Table A2: (continued)

		Integrated intensity $\int T_B(\upsilon)d\upsilon$ (K km s^{-1})							
Species	Freq (GHz)	HC	mm2	mm3a	mm3b	NE	S	OF1N	OF1S
$C^{18}O$	219.560	126.00 ± 4.23	108.00 ± 4.61	79.10 ± 2.41	83.60 ± 4.07	79.00 ± 1.55	24.40 ± 0.34	26.20 ± 0.52	13.90 ± 0.47
CO	230.538	3204.00±40.97	3411.50 ± 8.27	1777.80±17.41	2346.00±15.90	3553.00 ± 1.13	853.91 ± 5.08	2062.80±10.77	1028.70±12.43
^{13}CO	220.399	828.40 ± 7.77	702.33 ± 9.91	502.14 ± 6.32	568.77 ± 9.99	437.89 ± 9.19	134.30 ± 1.22	197.20 ± 2.72	129.92 ± 0.56
CH_2CO	220.178	27.32 ± 2.56	19.68 ± 1.48	29.82 ± 1.65	32.98 ± 1.55	≤1.06	5.51 ± 0.53	1.24 ± 0.05	2.90 ± 0.28
$HCOOCH_3$	220.258	6.09 ± 0.84	6.12 ± 0.66	11.38 ± 0.73	16.82 ± 0.83	≤0.39	≤0.46	≤0.35	≤0.39
CH_3OCH_3	230.140	6.66 ± 0.89	7.79 ± 0.80	12.77 ± 0.85	16.29 ± 0.96	≤0.31	≤0.27	≤0.28	≤0.26
CH_3COCH_3	230.183	8.62 ± 0.43	6.26 ± 0.49	3.59 ± 0.63	2.45 ± 1.07	≤0.37	≤0.18	≤0.18	≤0.24
CH_3CH_2OH	230.991	2.70 ± 0.61	2.30 ± 0.39	6.19 ± 0.40	4.38 ± 0.52	≤0.41	0.65 ± 0.25	≤0.27	0.86 ± 0.22
$H_2^{13}CO$	219.909	72.12 ± 2.85	37.92 ± 2.97	50.04 ± 0.70	43.40 ± 1.54	3.20 ± 0.10	11.70 ± 0.35	4.20 ± 0.46	16.40 ± 0.31
$CH_3OH^{(1)}$	229.759	192.80 ± 2.10	208.03 ± 2.27	326.26 ± 1.33	357.30 ± 1.69	6.90 ± 0.67	30.07 ± 0.52	15.62 ± 0.67	58.02 ± 0.63
$CH_3OH^{(2)}$	229.939	38.47 ± 1.03	14.97 ± 0.68	27.50 ± 1.10	28.46 ± 0.71	≤ 0.48	≤ 0.45	≤ 0.45	≤ 0.48
HNCO	219.798	264.52 ± 3.03	150.10 ± 3.68	98.25 ± 3.84	138.14 ± 2.66	34.99 ± 1.78	2.41 ± 0.20	9.10 ± 0.46	11.75 ± 0.75
$HC_3N(v_7 = 1)$	219.174	196.48 ± 2.51	67.91 ± 2.26	19.75 ± 1.36	19.87 ± 2.36	≤0.51	≤0.06	≤0.32	≤0.43
CH_3CN	220.730	397.54 ± 9.19	281.55 ± 10.27	256.41 ± 27.26	331.98 ± 21.20	15.17 ± 1.00	11.86 ± 1.03	≤1.76	≤2.22
$CH_3^{13}CN$	220.621	32.15 ± 1.34	13.57 ± 1.04	9.46 ± 0.73	12.58 ± 0.82	1.04 ± 0.17	≤0.12	≤0.18	≤0.16
CH_2CHCN	230.739	56.86 ± 1.32	12.25 ± 1.51	≤0.56	≤0.77	≤0.59	≤0.48	≤0.44	≤0.53
CH_2CH_3CN	229.265	175.00 ± 1.85	67.36 ± 1.43	21.99 ± 1.74	33.60 ± 2.38	≤0.39	≤0.39	≤0.42	≤0.38
OCS	218.903	367.07 ± 5.32	211.61 ± 5.00	200.76 ± 2.93	209.54 ± 4.38	9.09 ± 0.58	14.74 ± 0.54	≤0.46	≤0.42
$O^{13}CS$	230.318	24.06 ± 2.03	26.25 ± 1.37	19.12 ± 1.26	28.06 ± 1.26	≤0.51	≤0.57	≤0.21	≤0.47
SO_2	229.348	295.36 ± 3.65	225.41 ± 3.96	120.92 ± 3.94	166.97 ± 3.86	54.45 ± 1.15	≤0.47	≤0.38	≤0.83
$^{34}SO_2$	219.355	186.10 ± 4.83	174.25 ± 3.54	83.60 ± 1.57	112.97 ± 2.60	52.70 ± 1.24	≤0.37	≤0.44	≤0.55
SO	219.949	2281.00±16.36	2244.90±24.92	1500.70±17.58	1981.60±19.50	1748.00 ± 4.61	102.16 ± 3.93	487.06 ± 2.87	58.30 ± 5.33
^{13}CS	231.221	136.26 ± 2.15	87.38 ± 2.96	90.85 ± 2.70	109.09 ± 6.25	5.77 ± 0.48	19.53 ± 0.65	3.71 ± 0.80	≤0.99

$CH_3OH^{(1)}$: the line which shows extended SE tail;
$CH_3OH^{(2)}$: the line which has no extended SE tail

Table A3: The intensity integrated over the width of each line. Uncertainties on the measured intensities are typically ≤ 10%, as determined from Gaussian fitting. For species which are not detected, an upper limit equal to the 3σ rms is given. .

I. Molecular Column density [x ± y(z) = (x ± y) × $10^z cm^{-2}$]

A1.

Species	HC (123 ± 11 K)	mm2 (110 ± 7 K)	mm3a (103 ± 5 K)	mm3b (105 ± 5 K)	NE (45 ± 2 K)	S (45 ± 2 K)	OF1N (45 ± 2 K)	OF1S (45 ± 2 K)
$C^{18}O$	2.10 ± 0.10(17)	1.64 ± 0.02(17)	1.13 ± 0.01(17)	1.22 ± 0.01(17)	6.10 ± 0.05(16)	1.88 ± 0.03(16)	2.02 ± 0.02(16)	1.07 ± 0.01(16)
CO *	2.65 ± 0.17(20)	2.52 ± 0.13(20)	2.74 ± 0.08(20)	3.43±0.11((20)	1.90±0.05((20)	5.51 ± 0.12(19)	5.49 ± 0.11(19)	1.66 ± 0.03(19)
^{13}CO *	2.27 ± 0.16(18)	1.19 ± 0.05(18)	1.59 ± 0.04(18)	1.66 ± 0.05(18)	7.77 ± 0.05(17)	1.99 ± 0.04(17)	1.53 ± 0.02(17)	1.04 ± 0.02(17)
CH_2CO	1.55 ± 0.03(15)	1.03 ± 0.03(15)	1.48 ± 0.03(15)	1.66 ± 0.02(15)	≤ 4.05(13)	2.10 ± 0.23(14)	4.73 ± 0.24(13)	1.11 ± 0.12(14)
$HCOOCH_3$	3.64 ± 0.93(16)	4.13 ± 0.87(16)	8.39 ± 1.26(16)	1.21 ± 0.15(17)	≤ 4.59(16)	≤ 5.37(16)	≤ 4.13(16)	≤ 4.55(16)
CH_3OCH_3	5.81 ± 1.29(16)	7.46 ± 1.42(16)	1.32 ± 0.19(17)	1.64 ± 0.21(17)	≤ 4.57(16)	≤ 3.90(16)	≤ 4.07(16)	≤ 3.75(16)
CH_3COCH_3	6.56 ± 1.16(15)	3.57 ± 0.27(15)	1.75 ± 0.10(15)	1.25 ± 0.36(15)	≤ 2.15(14)	≤ 1.07(14)	≤ 1.08(14)	≤ 1.42(14)
CH_3CH_2OH	2.86 ± 0.32(15)	2.17 ± 0.21(15)	5.47 ± 0.08(15)	3.94 ± 0.26(15)	≤ 2.19(14)	3.44 ± 1.33(14)	≤ 1.43(14)	4.54 ± 1.14(14)
$H_2^{13}CO$	1.28 ± 0.09(15)	5.89 ± 0.02(14)	7.19 ± 0.31(14)	6.38 ± 0.14(14)	2.02 ± 0.01(13)	7.37 ± 0.03(13)	2.65 ± 0.19(13)	1.03 ± 0.02(14)
$CH_3OH^{(1)}$	6.63 ± 0.52(16)	6.41 ± 0.30(16)	9.47 ± 0.35(16)	1.06 ± 0.04(17)	1.53 ± 0.17(15)	6.65 ± 0.22(15)	3.46 ± 0.20(15)	1.28 ± 0.03(16)
$CH_3OH^{(2)}$	6.25 ± 2.39(17)	3.49 ± 1.16(17)	8.16 ± 2.21(17)	7.85 ± 1.89(17)	≤ 4.96(18)	≤ 4.65(18)	≤ 4.65(18)	≤ 4.96(18)

A2.

Species	HC (155 ± 15 K)	mm2 (129 ± 11 K)	mm3a (120 ± 9 K)	mm3b (121 ± 11 K)	NE (45 ± 2 K)	S (45 ± 2 K)	OF1N (45 ± 2 K)	OF1S (45 ± 2 K)
$H_2^{13}CO$	1.71 ± 0.15(15)	7.15 ± 0.24(14)	8.64 ± 0.67(14)	7.56 ± 0.59(14)	2.02 ± 0.01(13)	7.37 ± 0.03(13)	2.65 ± 0.19(13)	1.03 ± 0.02(14)
$CH_3OH^{(1)}$	8.61 ± 0.90(16)	7.52 ± 0.59(16)	1.09 ± 0.08(17)	1.21 ± 0.10(17)	1.53 ± 0.17(15)	6.65 ± 0.22(15)	3.46 ± 0.20(15)	1.28 ± 0.03(16)
$CH_3OH^{(2)}$	3.57 ± 0.98(17)	2.12 ± 0.76(17)	4.81 ± 1.64(17)	4.85 ± 1.94(17)	≤ 4.96(18)	≤ 4.65(18)	≤ 4.65(18)	≤ 4.96(18)

B.

Species	HC (156 ± 10 K)	HC (124 ± 7 K)	mm2 (110 ± 10 K)	mm3a (103 ± 5 K)	mm3b (88 ± 5 K)	NE (45 ± 2 K)	S (45 ± 2 K)	OF1N (45 ± 2 K)	OF1S (45 ± 2 K)
HNCO	1.17 ± 0.07(16)	9.15 ± 0.43(15)	4.60 ± 0.30(15)	2.83 ± 0.02(15)	3.44 ± 0.10(15)	5.98 ± 0.25(14)	4.12 ± 0.30(13)	1.56 ± 0.06(14)	2.01 ± 0.11(14)
$HC_3N(v_7 = 1)$	5.85 ± 0.91(15)	9.83 ± 1.86(15)	4.80 ± 2.00(15)	1.73 ± 0.47(15)	3.14 ± 1.37(15)	≤ 5.56(15)	≤ 6.58(14)	≤ 3.55(15)	≤ 4.74(15)
CH_3CN *	1.23 ± 0.05(17)	9.91 ± 0.23(16)	3.64 ± 0.09(16)	2.70 ± 0.20(16)	3.32 ± 0.12(16)	2.64 ± 0.27(15)	≤ 3.19(14)	–	–
$CH_3^{13}CN$	1.58 ± 0.02(15)	1.32 ± 0.00(15)	5.15 ± 0.10(14)	3.45 ± 0.17(14)	4.25 ± 0.18(14)	3.72 ± 0.74(13)	≤ 4.31(12)	≤ 6.55(12)	≤ 5.52(12)
CH_2CHCN	3.38 ± 0.13(15)	2.83 ± 0.02(15)	5.74 ± 0.52(14)	≤ 2.56(13)	≤ 3.47(13)	≤ 4.57(13)	≤ 3.74(13)	≤ 3.37(13)	≤ 4.11(13)
CH_3CH_2CN	1.25 ± 0.02(16)	1.15 ± 0.00(16)	4.33 ± 0.07(15)	1.41 ± 0.11(15)	2.19 ± 0.19(15)	≤ 4.99(13)	≤ 4.95(13)	≤ 5.29(13)	≤ 4.80(13)

C.

Species	HC (141 ± 28 K)	mm2 (126 ± 32 K)	mm3a (62 ± 16 K)	mm3a (129 ± 24 K)	mm3b (57 ± 14 K)	mm3b (138 ± 34 K)	NE (45 ± 2 K)	S (45 ± 2 K)	OF1N (45 ± 2 K)	OF1S (45 ± 2 K)
OCS *	1.80 ± 0.05(17)	1.59 ± 0.00(17)	1.42 ± 0.45(17)	1.19 ± 0.00(17)	2.15 ± 0.78(17)	–	1.18 ± 0.15(16)	1.30 ± 0.13(16)	–	–
$O^{13}CS$	1.91 ± 0.11(15)	2.04 ± 0.12(15)	1.81 ± 0.85(15)	1.49 ± 0.08(15)	2.86 ± 1.38(15)	2.21 ± 0.05(15)	≤ 6.91(13)	≤ 7.72(13)	≤ 2.83(13)	≤ 6.27(13)
SO_2	3.14 ± 0.32(17)	2.24 ± 0.21(17)	1.12 ± 0.34(17)	1.22 ± 0.07(17)	1.63 ± 0.56(17)	1.75 ± 0.19(17)	6.58 ± 0.54(16)	≤ 5.69(14)	≤ 4.59(14)	≤ 9.99(14)
$^{34}SO_2$	2.03 ± 0.36(16)	1.69 ± 0.38(16)	4.58 ± 0.41(15)	8.31 ± 1.39(15)	5.94 ± 0.34(15)	1.20 ± 0.27(16)	2.57 ± 0.04(15)	≤ 1.80(13)	≤ 2.17(13)	≤ 2.71(13)
SO	6.16 ± 0.93(16)	5.55 ± 1.04(16)	2.31 ± 0.28(16)	3.78 ± 0.51(16)	2.92 ± 0.32(16)	5.26 ± 0.98(16)	2.31 ± 0.03(16)	1.35 ± 0.03(15)	6.43 ± 0.07(15)	7.70 ± 0.56(14)
^{13}CS	4.67 ± 1.29(14)	2.51 ± 0.81(14)	1.02 ± 0.24(14)	2.71 ± 0.65(14)	1.12 ± 0.21(14)	3.61 ± 1.11(14)	4.76 ± 0.21(12)	1.61 ± 0.01(13)	3.06 ± 0.52(12)	≤ 8.19(11)

$CH_3OH^{(1)}$: the line which shows extended SE tail;
$CH_3OH^{(2)}$: the line which has no extended SE tail

Table A4: Column densities and abundances for molecules with respect to H_2 (derived from $C^{18}O$ by assuming $N_{C^{18}O}/N_{H_2} \sim 1.79 \times 10^{-7}$) from different substructures in Orion-KL marked in Figure 2.4, listed in the form of x ± y(z) = (x ± y) × 10^z, obtained with the excitation temperatures from the rotation map fittings of Figure 2.8 and Figure 2.9: for central 4 regions (HC, mm2,mm3a,mm3b), temperatures in A1 are from $HCOOCH_3$, in A2 from CH_3OH, in B from CH_3CN and in C from $^{34}SO_2$, while for outflow regions (NE, S, OF1N,OF1S), temperatures are from CH_3CN at NE. For species which are not detected, an upper limit derived from 3σ rms is given. Column densities of molecules marked with "*" are likely obtained from optically thick lines and for those we did the optical depth correction. The values in red are from optical depth estimation, the values of S-bearing species in blue are derived from upper limit of T_{rot}. Uncertainties on the measured values are typically ≤ 10%, as determined from T_{rot}, partition function $Q(T_{rot})$, and Gaussian fitting to $\int T_B(\upsilon)d\upsilon$.

II. Molecular Abundance to H_2 (derived from $C^{18}O$ by assuming $N_{C^{18}O}/N_{H_2} \sim 1.79 \times 10^{-7}$) [x ± y(z) = (x ± y) × 10^z]

A1.

Species	HC (123 ± 11 K)	mm2 (110 ± 7 K)	mm3a (103 ± 5 K)	mm3b (105 ± 5 K)	NE (45 ± 2 K)	S (45 ± 2 K)	OF1N (45 ± 2 K)	OF1S (45 ± 2 K)
$C^{18}O$	1.79 ± 0.17(−7)	1.79 ± 0.05(−7)	1.79 ± 0.04(−7)	1.79 ± 0.02(−7)	1.79 ± 0.03(−7)	1.79 ± 0.05(−7)	1.79 ± 0.03(−7)	1.79 ± 0.02(−7)
CO *	2.26 ± 0.26(−4)	2.76 ± 0.18(−4)	4.33 ± 0.18(−4)	5.04 ± 0.20(−4)	5.58 ± 0.20(−4)	5.24 ± 0.18(−4)	4.85 ± 0.15(−4)	2.77 ± 0.06(−4)
^{13}CO *	1.93 ± 0.23(−6)	1.31 ± 0.07(−6)	2.61 ± 0.10(−6)	2.34 ± 0.07(−6)	2.28 ± 0.04(−6)	1.89 ± 0.06(−6)	1.35 ± 0.03(−6)	1.73 ± 0.05(−6)
CH_2CO	1.32 ± 0.09(−9)	1.12 ± 0.05(−9)	2.34 ± 0.07(−9)	2.45 ± 0.05(−9)	≤ 1.19(−10)	2.00 ± 0.25(−9)	4.19 ± 0.25(−10)	1.85 ± 0.21(−9)
$HCOOCH_3$	3.11 ± 0.98(−8)	4.51 ± 1.03(−8)	1.33 ± 0.22(−7)	1.77 ± 0.24(−7)	≤ 1.35(−7)	≤ 5.10(−7)	≤ 3.66(−7)	≤ 7.60(−7)
CH_3OCH_3	4.95 ± 1.40(−8)	8.16 ± 1.68(−8)	2.08 ± 0.32(−7)	2.42 ± 0.33(−7)	≤ 1.34(−7)	≤ 3.70(−7)	≤ 3.60(−7)	≤ 6.26(−7)
CH_3COCH_3	5.59 ± 1.30(−9)	3.91 ± 0.36(−9)	2.77 ± 0.19(−9)	1.84 ± 0.55(−9)	≤ 6.31(−10)	≤ 1.02(−9)	≤ 9.55(−10)	≤ 2.37(−9)
CH_3CH_2OH	2.44 ± 0.40(−9)	2.38 ± 0.26(−9)	8.64 ± 0.23(−9)	5.79 ± 0.42(−9)	≤ 6.43(−10)	3.27 ± 1.33(−9)	≤ 1.26(−9)	7.58 ± 1.96(−9)
$H_2^{13}CO$	1.09 ± 0.14(−9)	6.44 ± 0.11(−10)	1.13 ± 0.06(−9)	9.37 ± 0.28(−10)	5.92 ± 0.07(−11)	7.01 ± 0.13(−10)	2.34 ± 0.19(−10)	1.72 ± 0.04(−9)
$CH_3OH^{(1)}$	5.65 ± 0.74(−8)	7.01 ± 0.43(−8)	1.50 ± 0.07(−7)	1.55 ± 0.07(−7)	4.48 ± 0.55(−9)	6.33 ± 0.30(−8)	3.06 ± 0.21(−8)	2.14 ± 0.07(−7)
$CH_3OH^{(2)}$	5.32 ± 2.40(−7)	3.81 ± 1.34(−7)	1.29 ± 0.37(−6)	1.15 ± 0.29(−6)	≤ 1.46(−5)	≤ 4.42(−5)	≤ 4.12(−5)	≤ 8.28(−5)

A2.

Species	HC (155 ± 15 K)	mm2 (129 ± 11 K)	mm3a (120 ± 9 K)	mm3b (121 ± 11 K)	NE (45 ± 2 K)	S (45 ± 2 K)	OF1N (45 ± 2 K)	OF1S (45 ± 2 K)
$H_2^{13}CO$	1.46 ± 0.20(−9)	7.82 ± 0.37(−10)	1.36 ± 0.12(−9)	1.11 ± 0.09(−9)	5.92 ± 0.07(−11)	7.01 ± 0.13(−10)	2.34 ± 0.19(−10)	1.72 ± 0.04(−9)
$CH_3OH^{(1)}$	7.34 ± 1.16(−8)	8.23 ± 0.76(−8)	1.73 ± 0.14(−7)	1.78 ± 0.16(−7)	4.48 ± 0.55(−9)	6.33 ± 0.30(−8)	3.06 ± 0.21(−8)	2.14 ± 0.07(−7)
$CH_3OH^{(2)}$	3.04 ± 1.03(−7)	2.32 ± 0.87(−7)	7.59 ± 2.71(−7)	7.13 ± 2.92(−7)	≤ 1.46(−5)	≤ 4.42(−5)	≤ 4.12(−5)	≤ 8.28(−5)

B.

Species	HC (156 ± 10 K)	HC (124 ± 7 K)	mm2 (110 ± 10 K)	mm3a (103 ± 5 K)	mm3b (88 ± 5 K)	NE (45 ± 2 K)	S (45 ± 2 K)	OF1N (45 ± 2 K)	OF1S (45 ± 2 K)
HNCO	9.96 ± 1.11(−9)	7.80 ± 0.76(−9)	5.03 ± 0.40(−9)	4.46 ± 0.09(−9)	5.06 ± 0.19(−9)	1.76 ± 0.09(−9)	3.91 ± 0.35(−10)	1.38 ± 0.07(−9)	3.35 ± 0.20(−9)
$HC_3N(v_7 = 1)$	4.99 ± 1.06(−9)	8.38 ± 2.06(−9)	5.25 ± 2.29(−9)	2.73 ± 0.78(−9)	4.61 ± 2.07(−9)	≤ 1.63(−8)	≤ 6.26(−9)	≤ 3.15(−8)	≤ 7.91(−8)
CH_3CN *	1.05 ± 0.10(−7)	8.46 ± 0.60(−8)	3.98 ± 0.16(−8)	4.26 ± 0.37(−8)	4.88 ± 0.22(−8)	7.76 ± 0.87(−9)	≤ 3.03(−9)	–	–
$CH_3^{13}CN$	1.34 ± 0.09(−9)	1.13 ± 0.06(−9)	5.64 ± 0.18(−10)	5.45 ± 0.33(−10)	6.25 ± 0.31(−10)	1.09 ± 0.23(−10)	≤ 4.10(−11)	≤ 5.80(−11)	≤ 9.21(−11)
CH_2CHCN	2.88 ± 0.26(−9)	2.41 ± 0.14(−9)	6.28 ± 0.66(−10)	≤ 4.04(−11)	≤ 5.10(−11)	≤ 1.34(−10)	≤ 3.56(−10)	≤ 2.98(−10)	≤ 6.86(−10)
CH_3CH_2CN	1.07 ± 0.07(−8)	9.80 ± 0.50(−9)	4.74 ± 0.15(−9)	2.22 ± 0.21(−9)	3.22 ± 0.31(−9)	≤ 1.46(−10)	≤ 4.71(−10)	≤ 4.69(−10)	≤ 8.01(−10)

C.

Species	HC (141 ± 28 K)	mm2 (126 ± 32 K)	mm3a (62 ± 16 K)	mm3a (129 ± 24 K)	mm3b (57 ± 14 K)	mm3b (138 ± 34 K)	NE (45 ± 2 K)	S (45 ± 2 K)	OF1N (45 ± 2 K)	OF1S (45 ± 2 K)
OCS *	1.53 ± 0.12(−7)	1.74 ± 0.02(−7)	2.23 ± 0.75(−7)	1.87 ± 0.02(−7)	3.16 ± 1.17(−7)	–	3.45 ± 0.48(−8)	1.24 ± 0.14(−7)	–	–
$O^{13}CS$	1.62 ± 0.17(−9)	2.23 ± 0.16(−9)	2.86 ± 1.39(−9)	2.35 ± 0.16(−9)	4.20 ± 2.07(−9)	3.25 ± 0.10(−9)	≤ 2.03(−10)	≤ 7.34(−10)	≤ 2.51(−10)	≤ 1.05(−9)
SO_2	2.67 ± 0.41(−7)	2.45 ± 0.26(−7)	1.78 ± 0.57(−7)	1.92 ± 0.14(−7)	2.39 ± 0.84(−7)	2.57 ± 0.30(−7)	1.93 ± 0.18(−7)	≤ 5.41(−9)	≤ 4.06(−9)	≤ 1.67(−8)
$^{34}SO_2$	1.73 ± 0.41(−8)	1.85 ± 0.45(−8)	7.23 ± 0.73(−9)	1.31 ± 0.24(−8)	8.74 ± 0.57(−9)	1.77 ± 0.42(−8)	7.55 ± 0.19(−9)	≤ 1.71(−10)	≤ 1.92(−10)	≤ 4.52(−10)
SO	5.25 ± 1.09(−8)	6.08 ± 1.24(−8)	3.64 ± 0.50(−8)	5.97 ± 0.88(−8)	4.29 ± 0.50(−8)	7.74 ± 1.51(−8)	6.78 ± 0.16(−8)	1.28 ± 0.05(−8)	5.70 ± 0.11(−8)	1.29 ± 0.10(−8)
^{13}CS	3.98 ± 1.34(−10)	2.75 ± 0.94(−10)	1.61 ± 0.40(−10)	4.28 ± 1.09(−10)	1.65 ± 0.32(−10)	5.31 ± 1.68(−10)	1.40 ± 0.07(−11)	1.53 ± 0.03(−10)	2.71 ± 0.49(−11)	≤ 1.37(−11)

$CH_3OH^{(1)}$: the line which shows extended SE tail;
$CH_3OH^{(2)}$: the line which has no extended SE tail

Table A4: (continued)

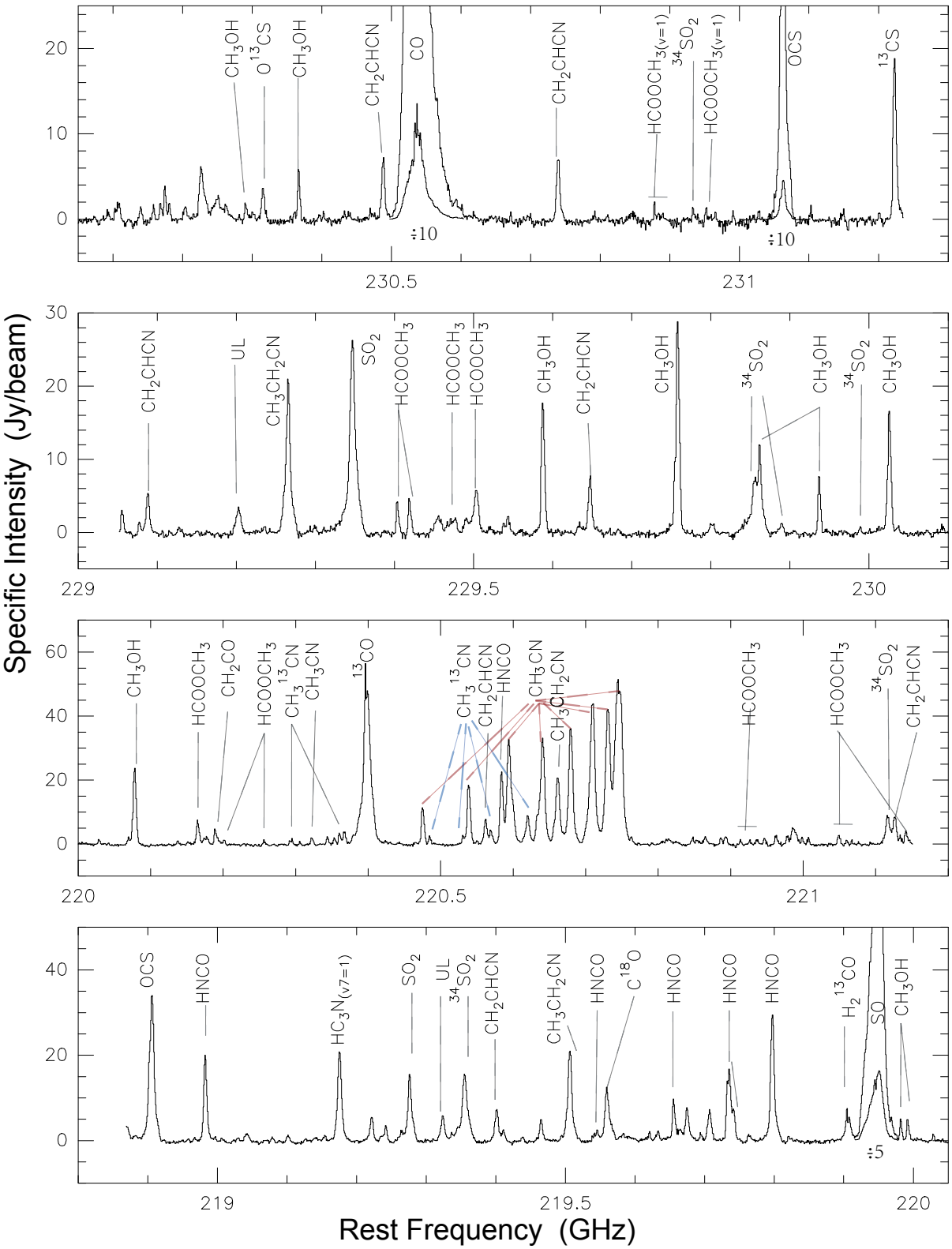

Figure A1: The spectrum from HC of Orion-KL, with identified strong lines marked. From 220.5 GHz to 220.8 GHz, CH_3CN and $CH_3^{13}CN$ are labeled in red and blue, respectively. COM with only C, H, O and tentatively carbon chain detection are labeled in Figure A2.

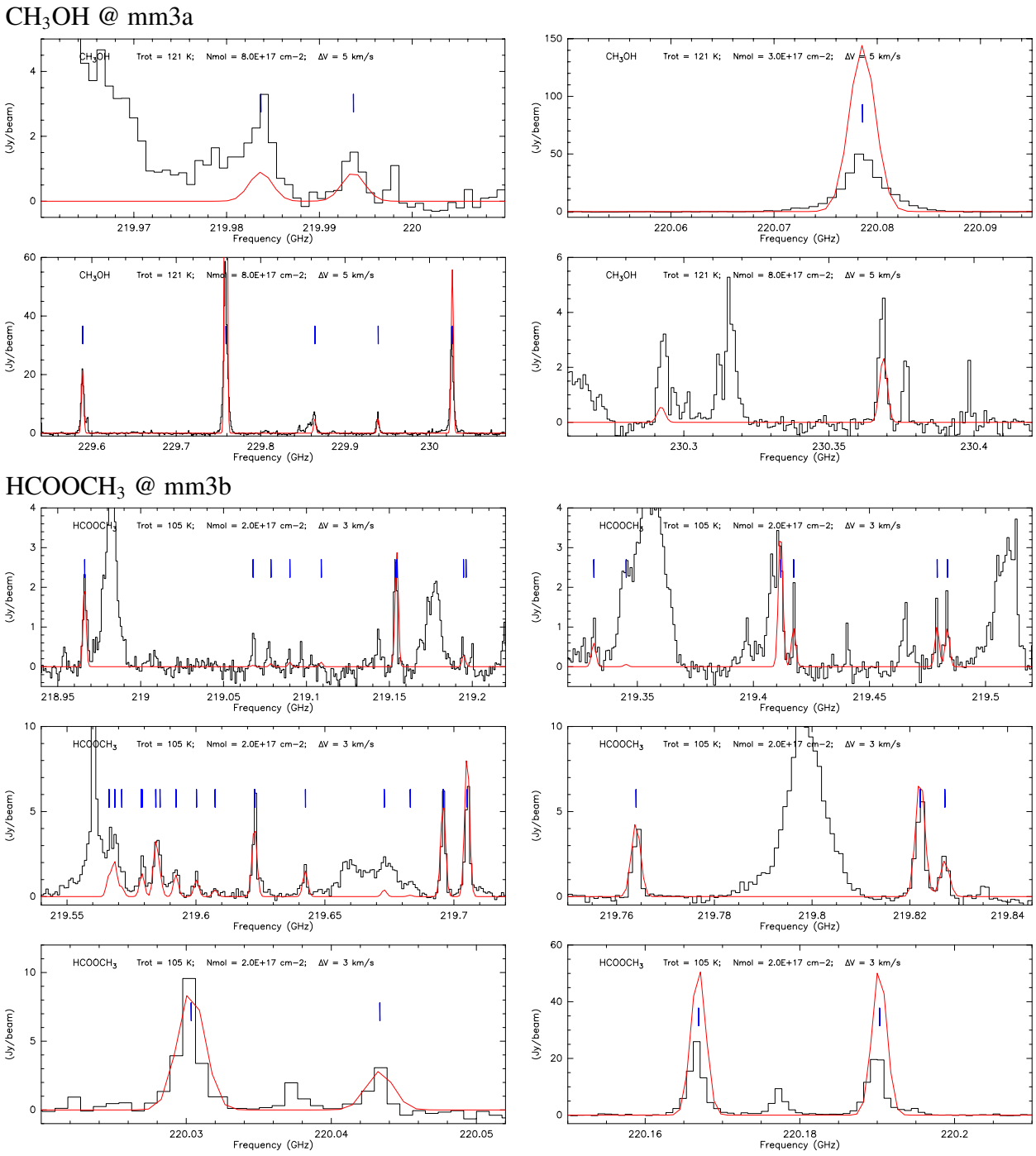

Figure A2: Synthetic spectrum fitting of Complex Organic Molecules (COMs) toward their emission peaks of Orion-KL. The black histograms are the observed spectra, overlaid with a best fit model spectrum for given uniform FWHM linewidth ($\triangle$V), T_{rot} (assumed from an adjacent substructure) and N_{mol} listed on top of each panel. Blue lines mark the central frequency of each transition. Uncertainty of the fitting to observation come from the assumption that under Local Thermodynamic equilibrium (LTE), the candidate molecule lines are optically thin, and it has the same line width at different transitions. Referenced molecular data are from CDMS/JPL (Palau et al. 2011; Sanchez-Monge 2011).

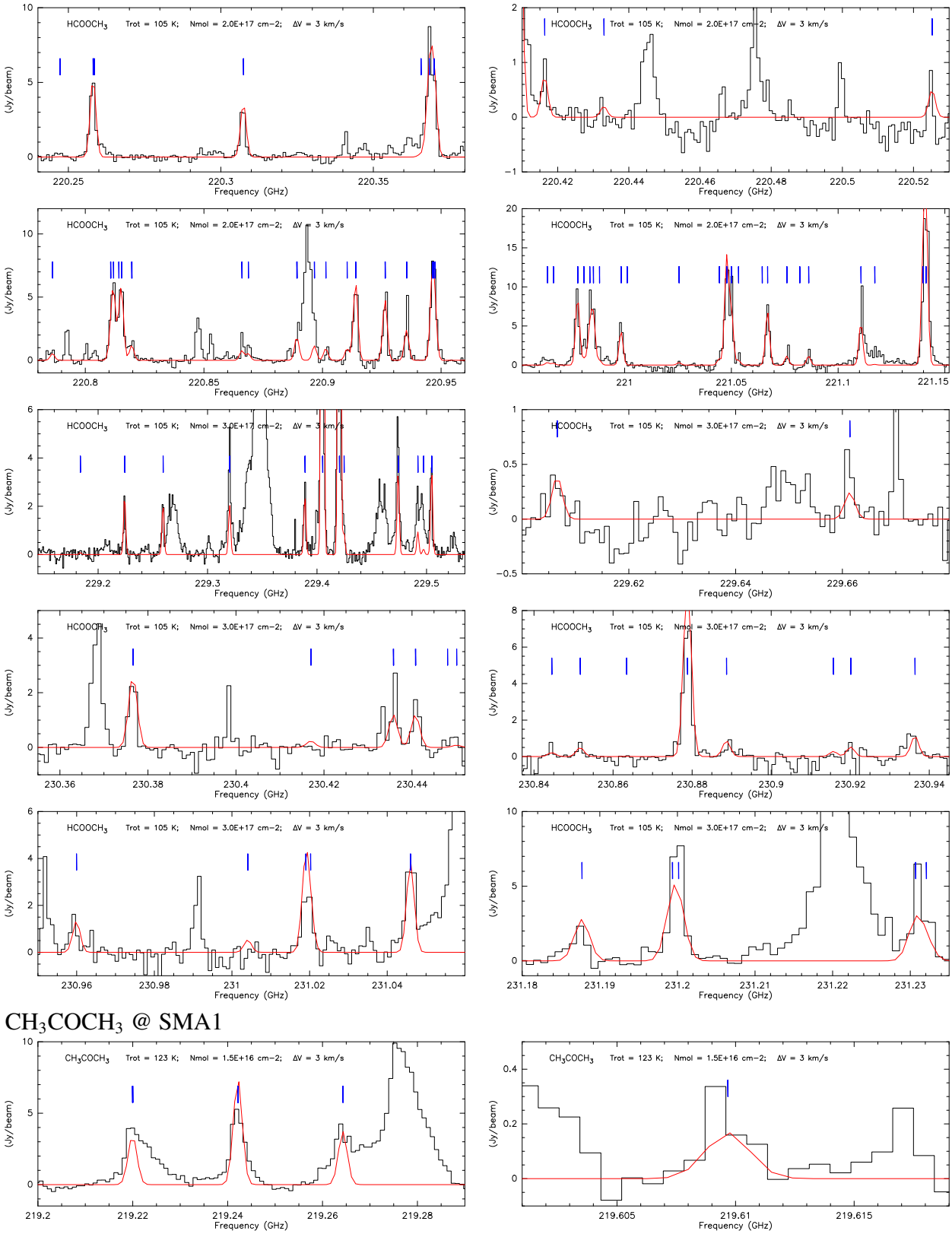

Figure A2: (continued)

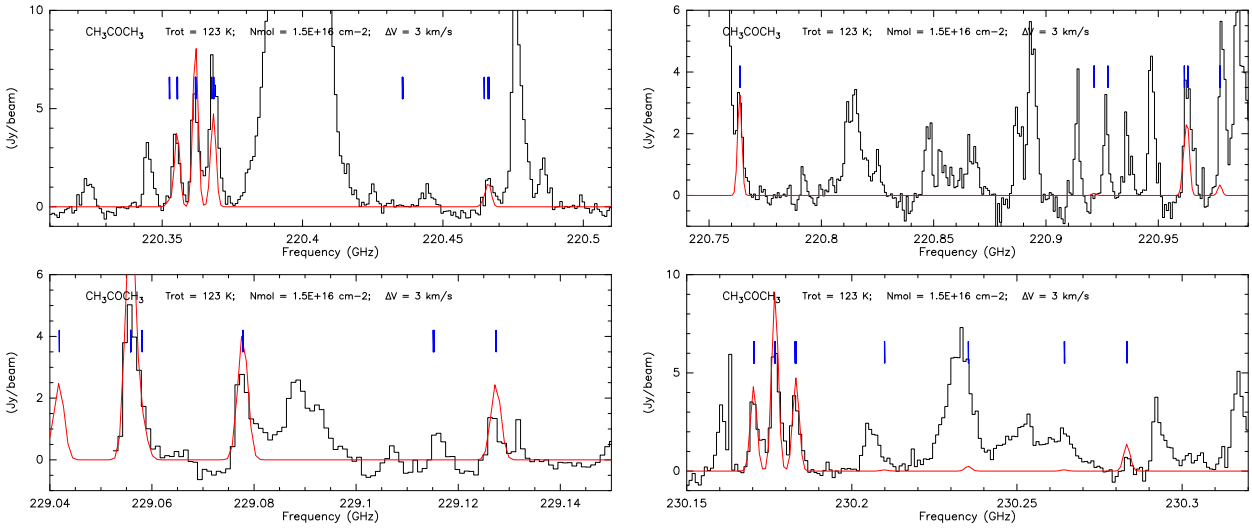

CH_3OCH_3 @ mm3b

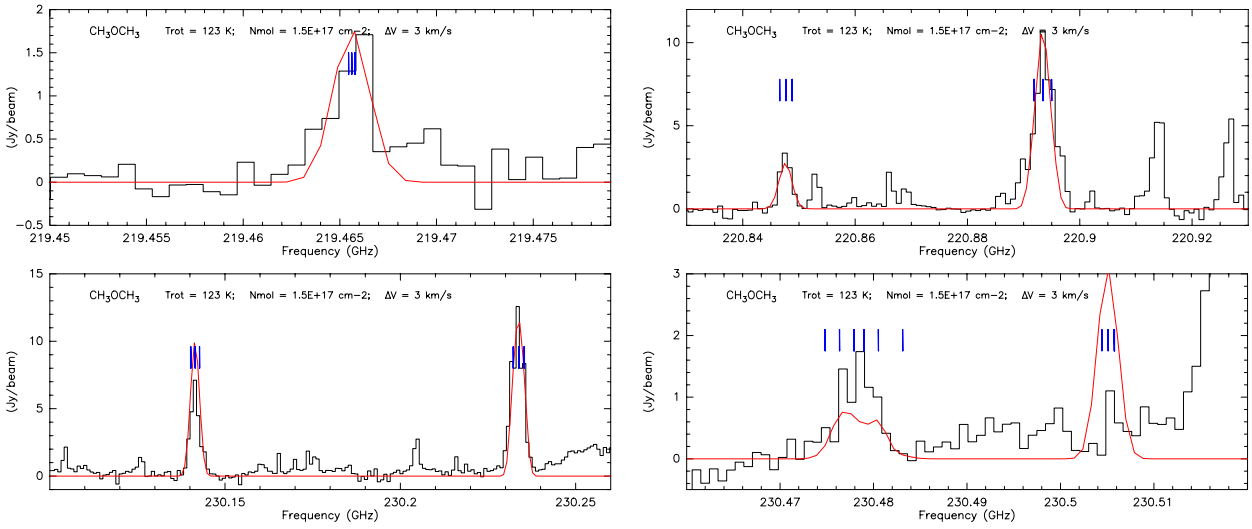

CH_3CH_2OH @ near SMA1 & source N

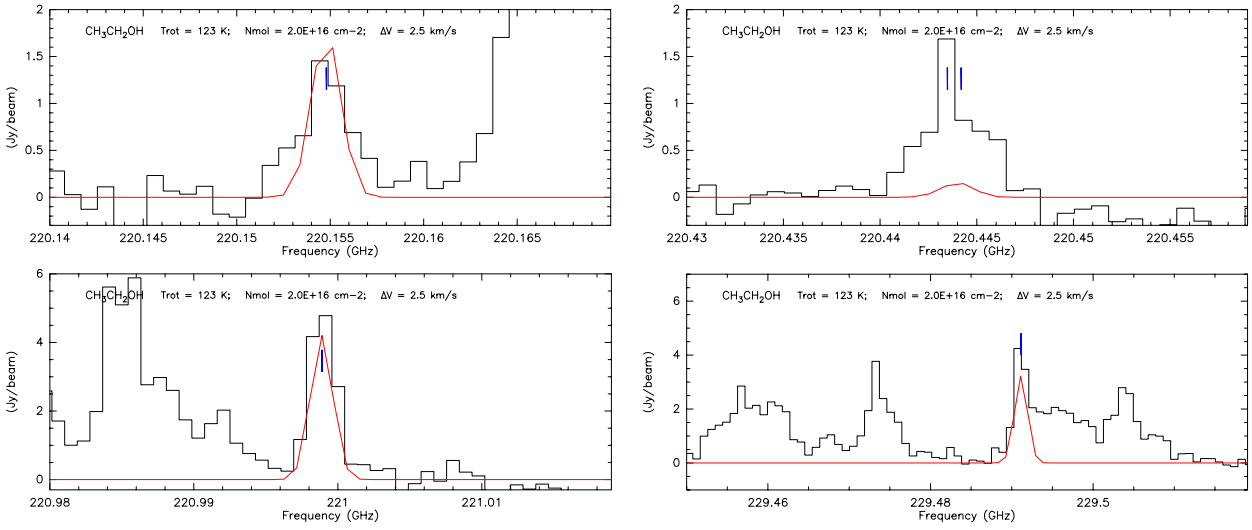

Figure A2: (continued)

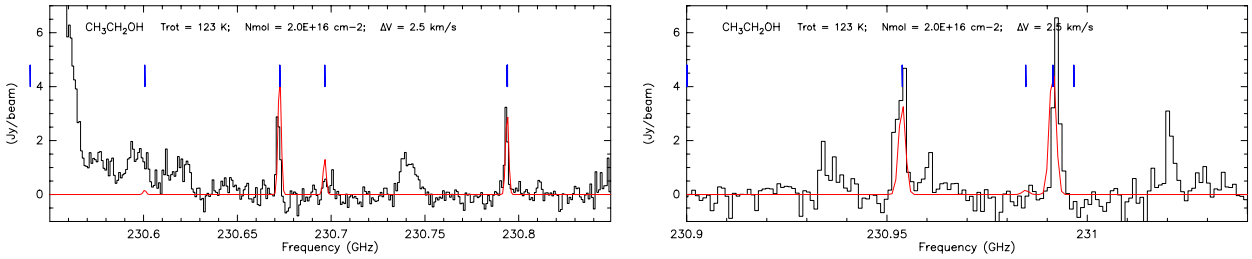

CH_3CH_2CN @ hotcore

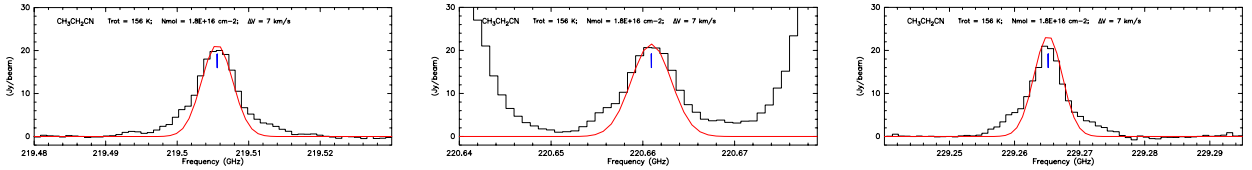

CH_2CHCN @ North to hotcore

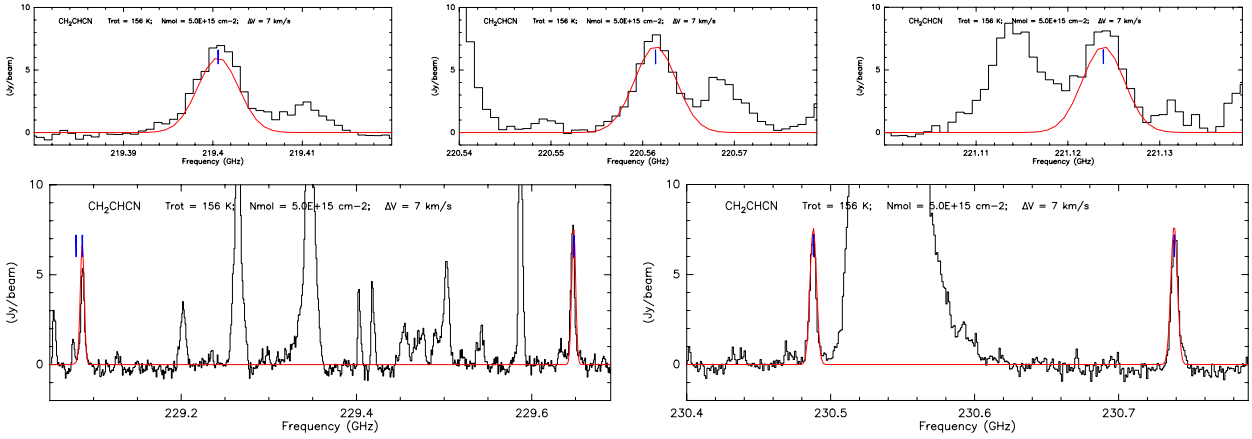

C_6H @ SMA1

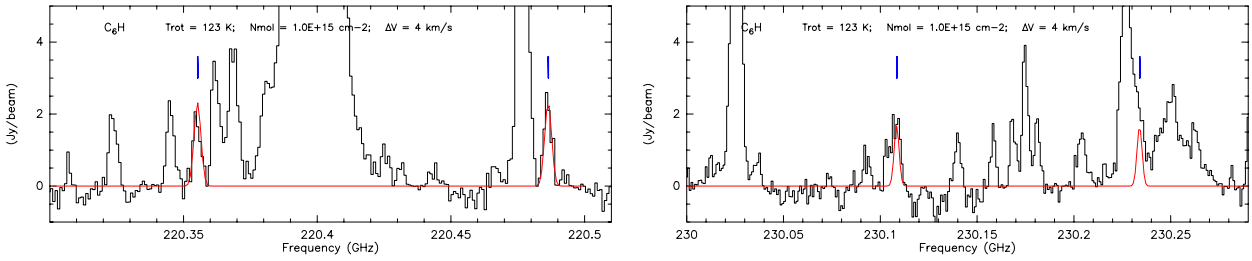

HC_7N @ North to hotcore

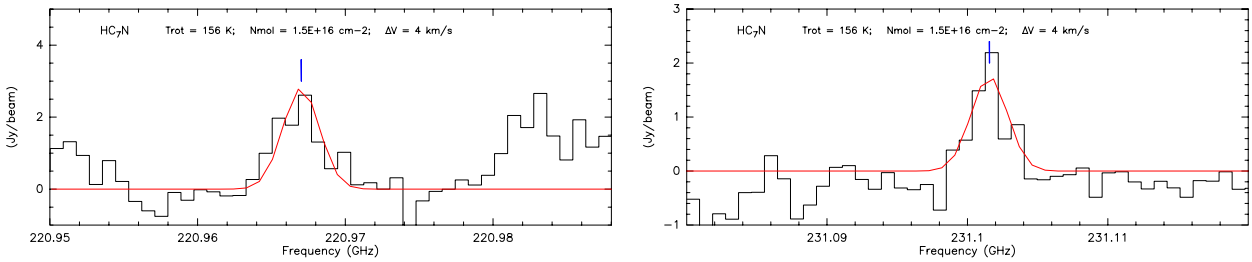

Figure A2: (continued)

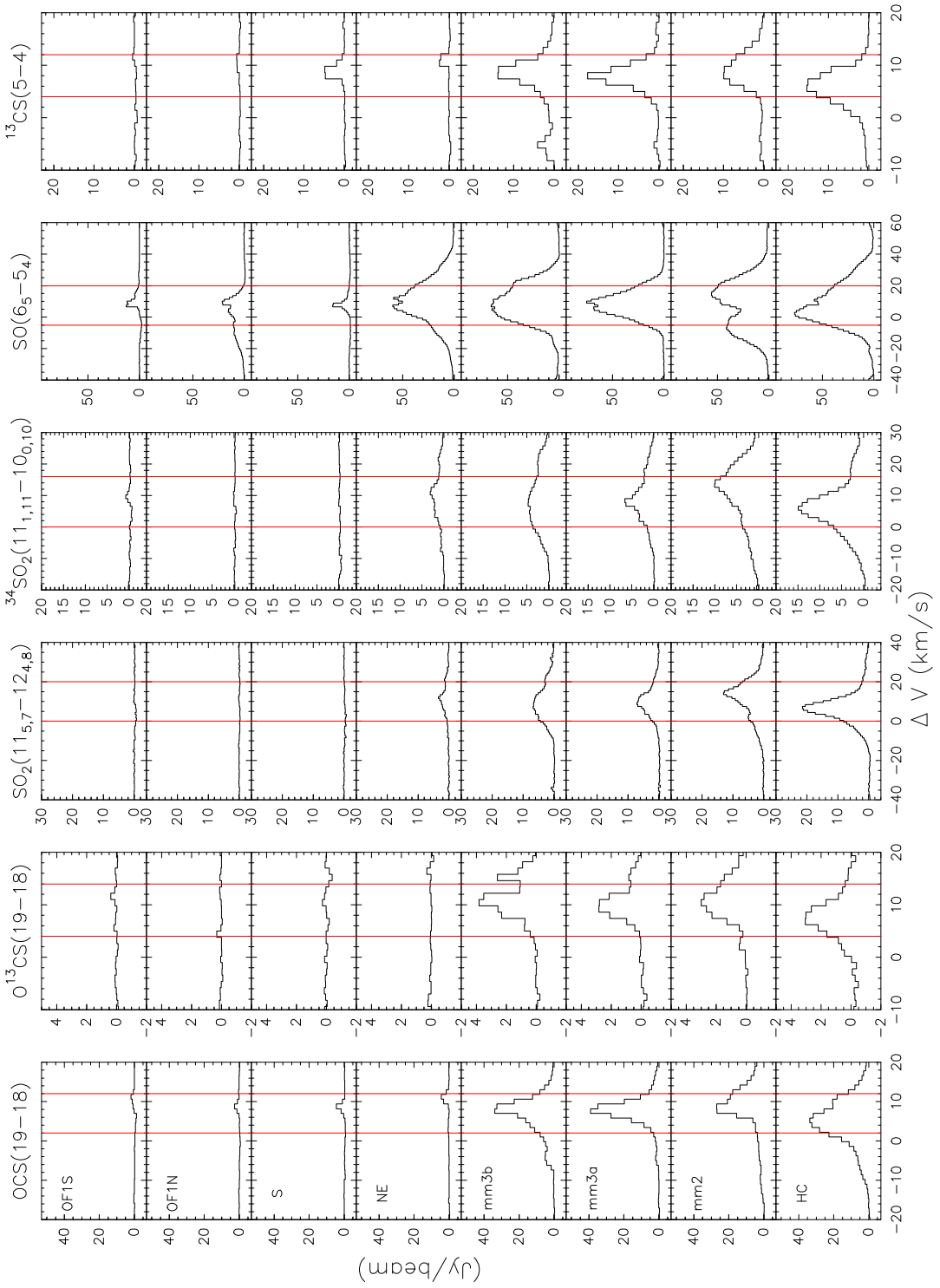

Figure A3: The line profile of identified species from each continuum peak of Orion-KL. Two red vertical lines in each panel mark the velocity range over which the emission from each species is integrated to make the distribution maps shown in Figure 2.4 and Figure 2.5.

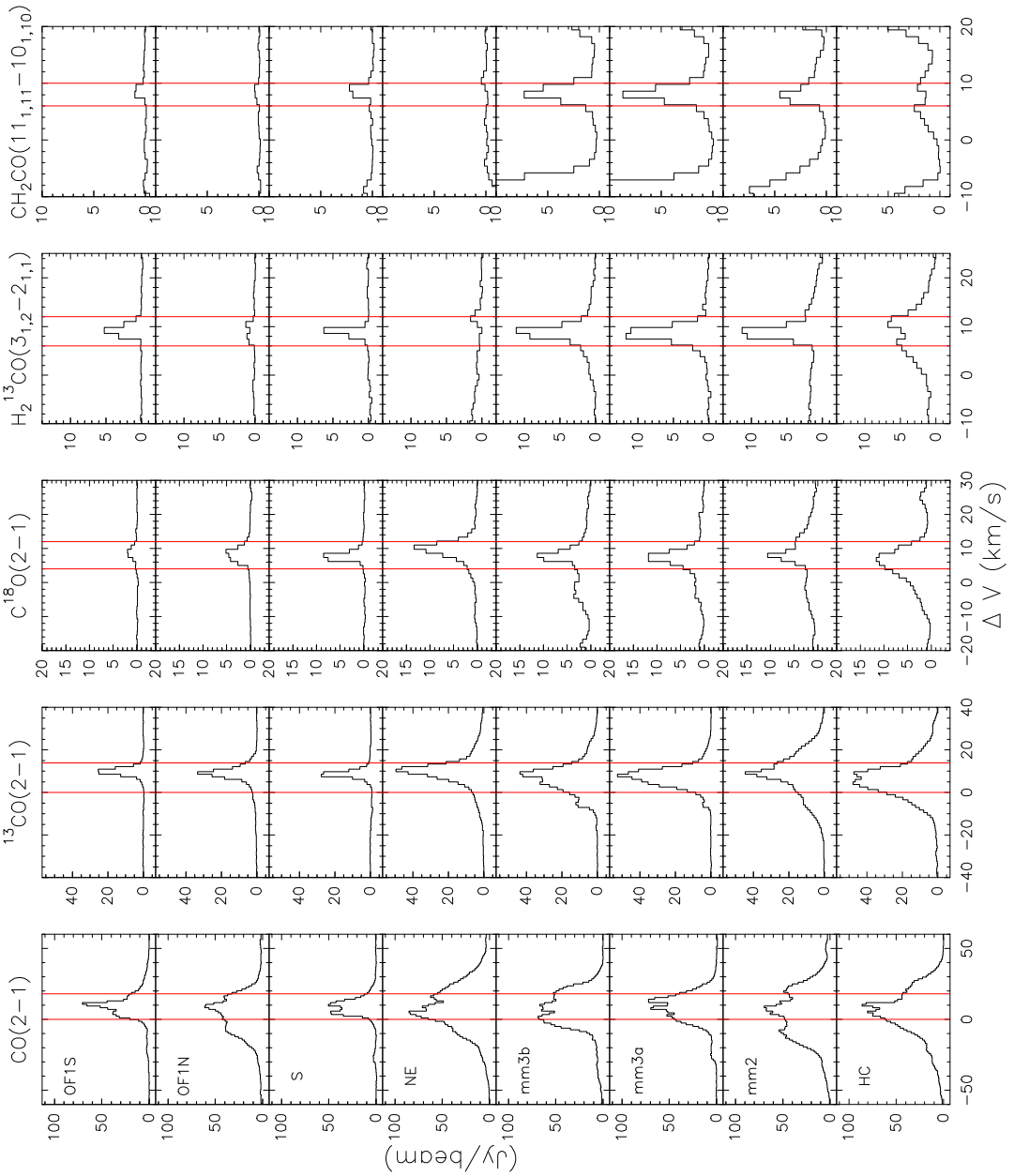

Figure A3: (continued)

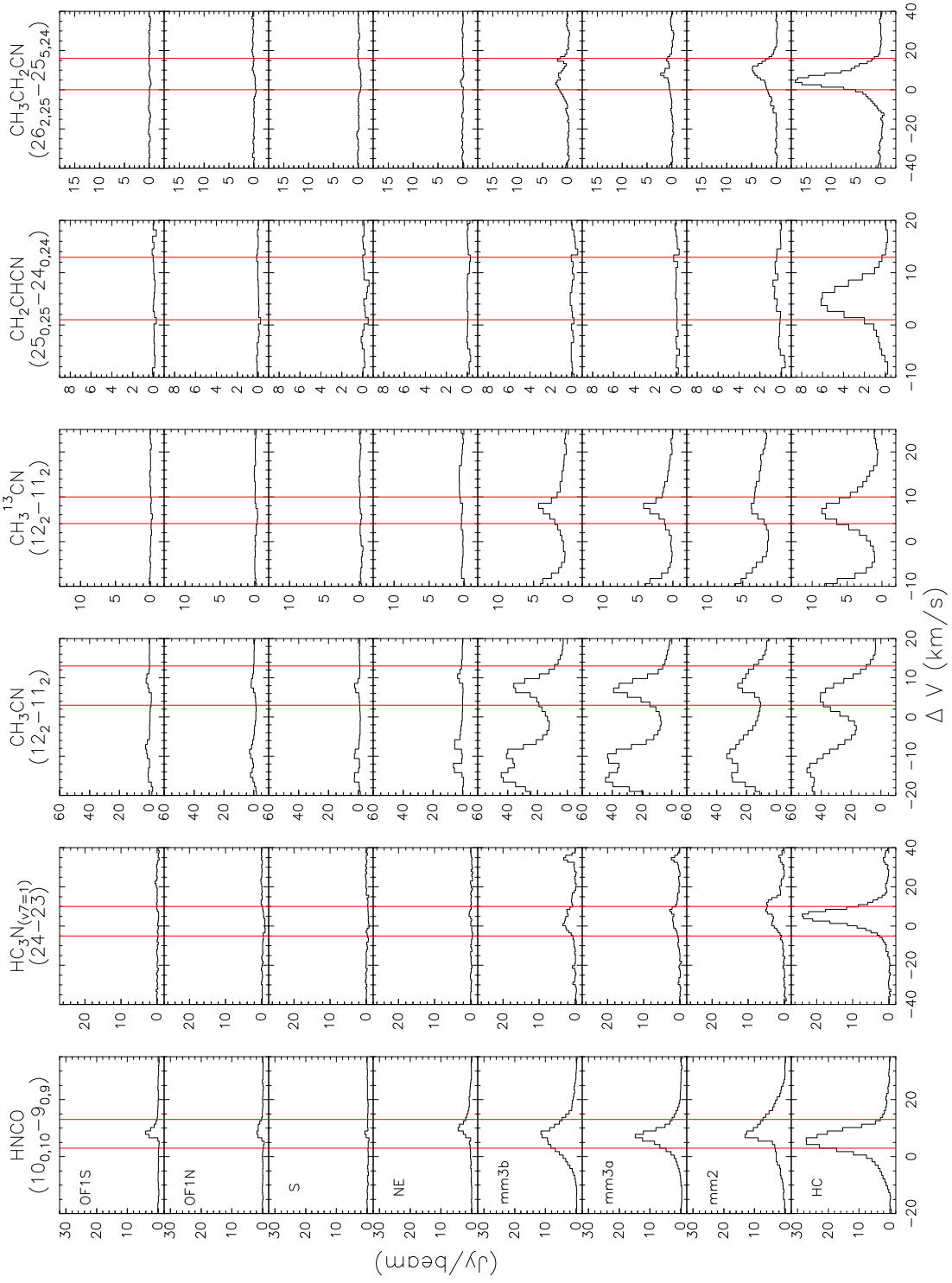

Figure A3: (continued)

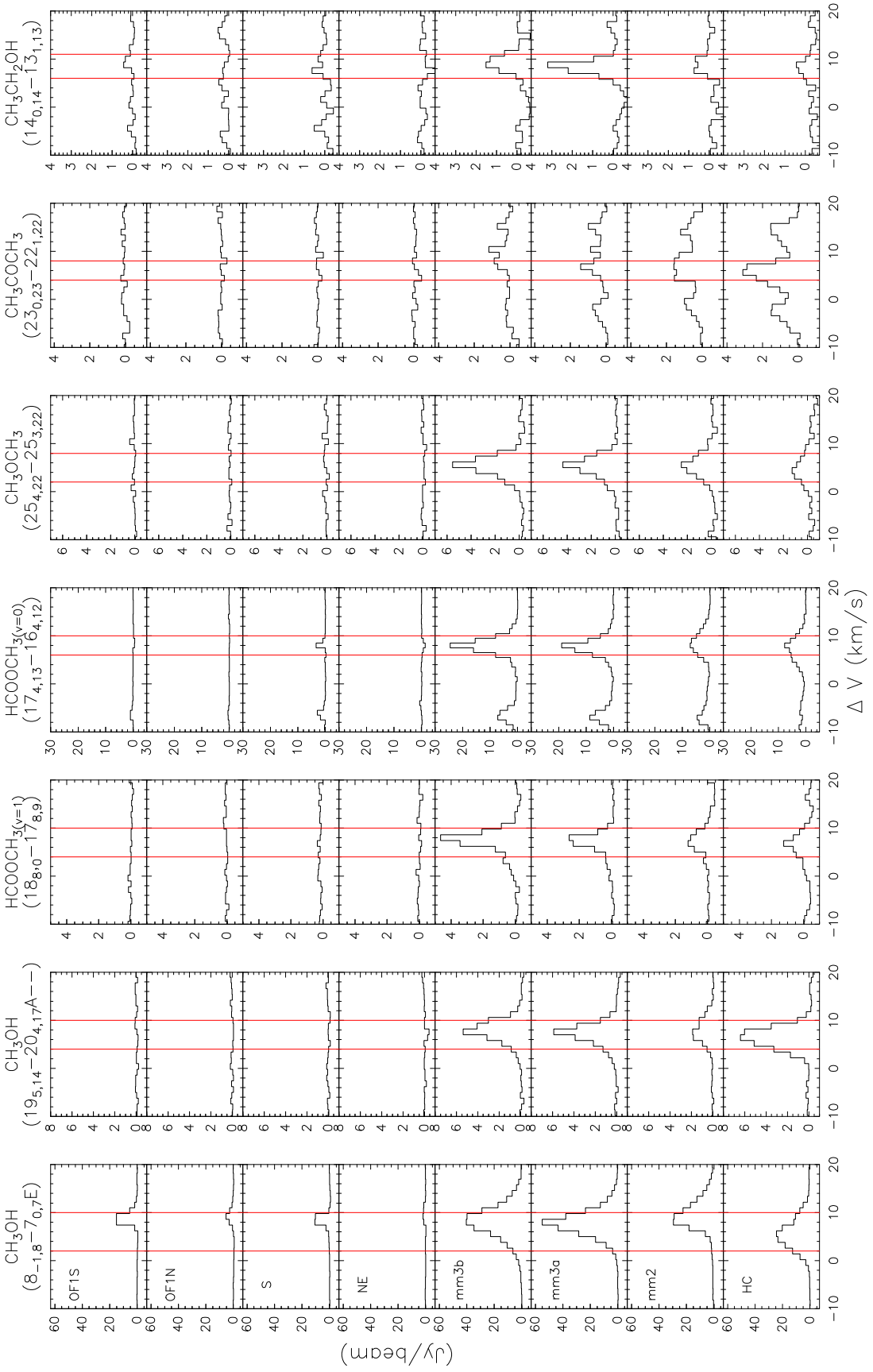

Figure A3: (continued)

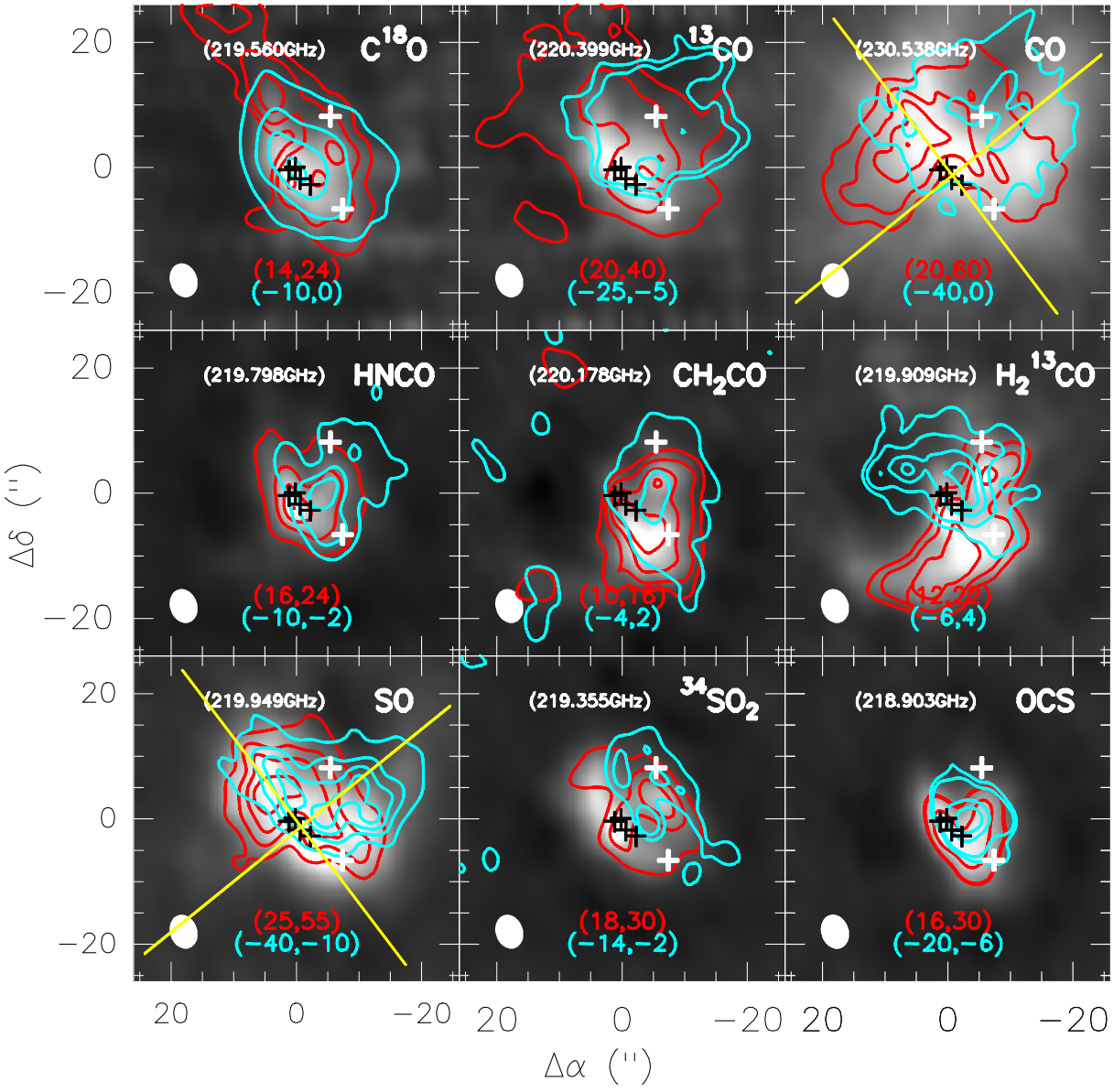

Figure A4: The line wing flux integration maps from the combined SMA-30 m data at 1.3 mm. The grey maps show the intensity integrated ranging through the main emission of their linewidth in Figure A3. Red and blue contours show the red-shifted and blue-shifted gas, with the intensity integrated as labelled. Green lines sketch the outflow directions. Black crosses mark the hotcore, SMA1, Source I and Source N, white crosses mark the BN object and CR.

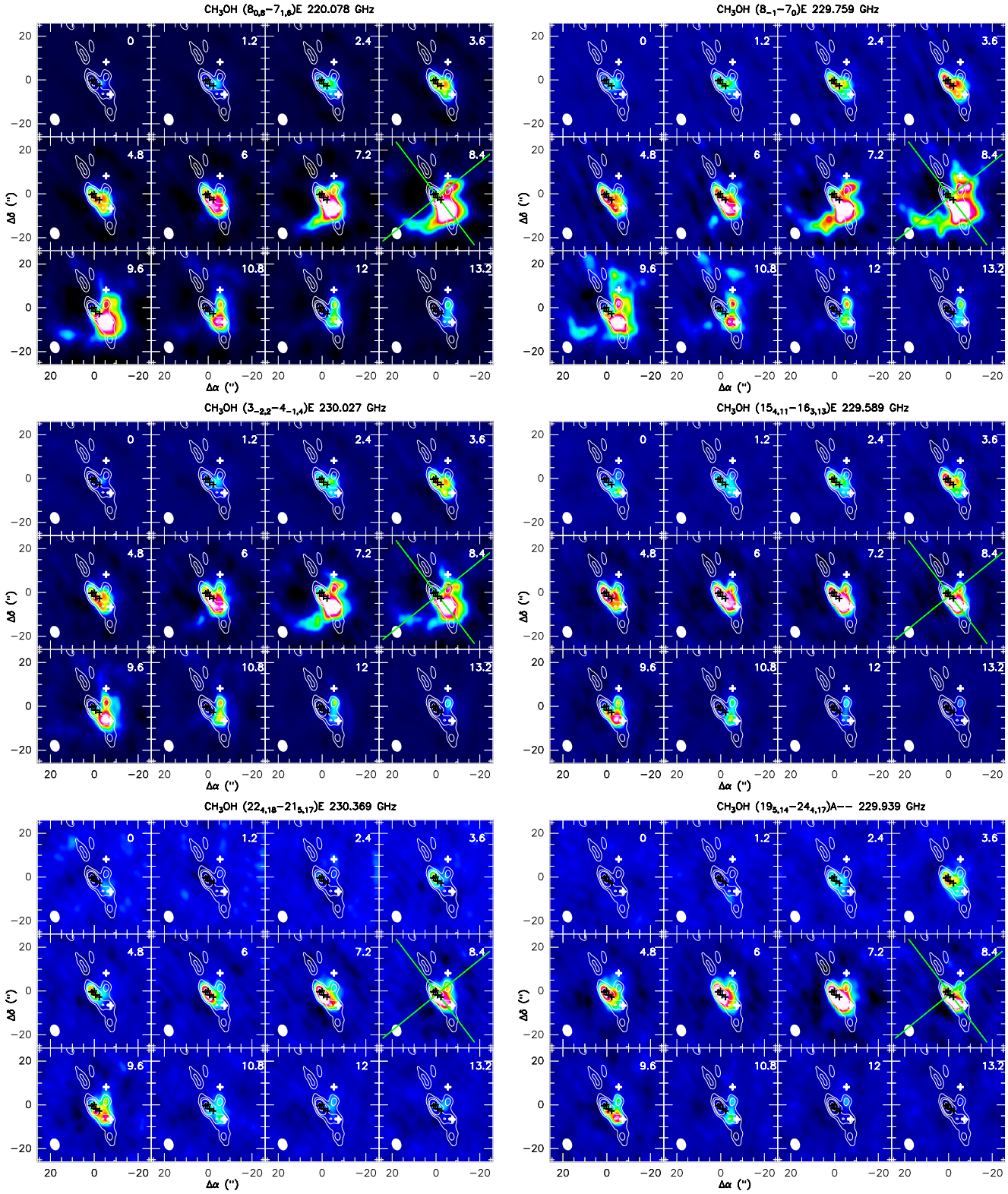

Figure A5: Channel maps of unblended CH_3OH lines show multiple velocity dependent emission peaks: 2.4–3.6 km s^{-1} towards SMA1, $\sim$ 4.8–6 km s^{-1} towards HC, 7.2–9.6 km s^{-1} towards HC/mm3a/(mm3b), 10.8 km s^{-1} towards mm3a/mm3b/mm2 and $>$ 12 km s^{-1} towards mm2. Green lines sketch the outflow directions. Black crosses mark the hotcore, SMA1, Source I and Source N, white crosses mark the BN object and the CR.

3

Inferring the evolutionary stages of NGC 7538 S and NGC 7538 IRS1 from chemistry

3.1 Motivation

As described in Chapter 1, MYSOs may form via "hierarchical fragmentation": GMCs collapse into clumps ($\sim$ 1 pc in size), then clumps collapse into cores ($\sim$ 0.1 pc in size), and subsequently collapse into condensations ($\sim$ 0.01 pc in size), which form the protostellar objects. Can we find direct observational confirmation to this theoretical picture? As presented in Chapter 2, chemical variations in Orion-KL, a HMC source, may be caused by forming paths diversity of molecular species. Is this a rare case? With the aim of providing direct observational constraints on detailed aspects of formation theories such as hierarchical fragmentation, and investigating the homogeneity at small scales of HMSFRs, we turn our attention to more distant HMSFRs.

In this chapter, we focus on studying the chemistry of two HMSFRs: NGC 7538 S and IRS1, whose kinematic properties we previously studied in Beuther et al. (2012a). following a description of the targets in Section 3.2, a brief summary of the observations is given in Section 3.3. Results from the full bandwidth spectra are shown in Section 3.4. A chemical analysis of the data is presented in Section 3.5, and results from a 1-D radiation transfer model are presented in Section 3.6. Finally, a discussion of the results is presented in Section 3.7, along with our conclusions in Section 3.8.

3.2 Targets

Located in the Perseus arm of our Galaxy at a distance of 2.65 kpc (Moscadelli et al. 2009), NGC 7538 is one of the most studied complex HMSFRs. Embedded in an optically visible HII zone, this region harbours several clusters composed of infrared (Martin 1973; Wynn-Williams et al. 1974) and radio continuum sources (Campbell & Thompson 1984), of which at least three sources (IRS1, IRS9 and NGC 7538 S) drive powerful molecular outflows and appear to be surrounded by accretion disks (e.g., De Buizer & Minier 2005; Kraus et al. 2006; Sandell & Wright 2010; Barentine & Lacy 2012; Beuther et al. 2012a, 2013a). An evolutionary sequence has been suggested, which propagates from older IRS1 in the NW to younger NGC 7538 S in the SE (Elmegreen & Lada 1977; Werner et al. 1979; McCaughrean et al. 1991; Ojha et al. 2004; Balog et al. 2004; Qiu et al. 2011). The whole region of NGC 7538 is suggested to represent a case of triggered or induced star formation (Martin-Pintado & Cernicharo 1987).

IRS1 is the brightest source in millimeter (mm) continuum maps of NGC 7538 (Scoville et al. 1986). This source is a hyper-compact HII region with systemic local standard of rest velocity $V_{lsr} = -57.4$ km s^{-1} (van der Tak et al. 2000; Sandell et al. 2009), whose central star has been suggested to be an O6/O7.5 type (8×10^4 L$_\odot$, 30 M$_\odot$, Werner et al. 1979; Campbell 1984; Akabane & Kuno 2005). In maps of mm HCO^+ and HCN emission within 1′ of IRS1 (Pratap et al. 1989) appears a shell-like structure with $V_{lsr} \sim -56.5$ km s^{-1} and a size of 10–20″. On scales of 72 000 AU (van der Tak et al. 2000), IR absorption by dust grains and their icy mantles probes an outer cool envelope (Willner 1976; Willner et al. 1982; Zheng et al. 2001; Gibb et al. 2004). Absorption is also detected from a high column density of NH_3, centered on $V_{lsr} \sim -60$ km s^{-1}, which is believed to trace warm gas from the inner region (Wilson et al. 1983; Henkel et al. 1984; van der Tak et al. 2000). Within 1 000 AU of the source center, numerous masers outline two small scale knotty outflows (e.g., from OH, H_2O, NH_3, CH_3OH and H_2CO, Gaume et al. 1991, 1995; Hutawarakorn & Cohen 2003; Hoffman et al. 2003; Kurtz et al. 2004), with some masers having kinematics indicative of accretion (Pestalozzi et al. 2004, 2009).

80″ to the south of IRS1 lies **NGC 7538 S**, the youngest core in NGC 7538, an extended ($\sim$ 0.5 pc in size) and unstructured source with lower luminosity than IRS1 (1.3×10^4 L$_\odot$). This source has associated H_2O, OH and CH_3OH maser emission, as well as weak free-free emission (Sandell & Sievers 2004; Pestalozzi et al. 2006; Zapata et al. 2009) and optically thick line emission due to the surrounding high column density cloud (Sandell & Wright 2010). Mapping of the SiO and HCO^+ lines suggests that this source is composed of a enclosed protostar with a mass on the order of 14–24 M$_\odot$, which is surrounded by a 85–115 M$_\odot$ disk, and that in turn drives a compact (0.2 pc), powerful molecular outflow (Sandell & Wright 2010). However, recent observations at mm wavelengths indicate that, instead of a single O star surrounded by an extremely large disk, NGC 7538 S is more likely to be a group of young stellar objects with

10–110 $M_\odot$ (YSOs, Corder 2009; Wright et al. 2012; Naranjo-Romero et al. 2012; Beuther et al. 2012a). Higher spatial resolution observations revealed at least two collimated ($< 10''$) bipolar outflows traced by SiO, which are suggested to be emanated from these YSOs (Corder 2009; Naranjo-Romero et al. 2012).

Previous studies of NGC 7538 S and IRS1 modelled both sources as massive protostellar disks. However, details of these models, e.g., the geometry of IRS1 and the multiplicity of NGC 7538 S are still uncertain. Refinement of these models requires high spatial resolution molecular line observations to constrain their structure, chemistry and evolutionary status.

3.3 Observations

Our observations with the PdBI at 1.3 mm as well as the reduction of the NGC 7538 S and IRS1 data have already been described in Beuther et al. (2012a). Here we therefore only summarise the observations, and the essential parameters, relevant to the following chemical study.

Observations of the two fields were carried out in both A and B configurations on January 26th, 2011, and February 10th, 2011, respectively. The phase center for IRS1 was $\alpha_{2000} = 23^h13^m45.36^s$, $\delta_{2000.0} = 61^o28'10.55''$ and for NGC 7538 S was $\alpha_{2000} = 23^h13^m44.86^s$, $\delta_{2000.0} = 61^o28'48.10''$. Phase calibration was done via regularly interleaved observations of the quasars 2146+608, 0059+581 and 0016+731. The bandpass and flux were calibrated with observations of 3C345, 3C273 and MWC349, resulting in an estimated 20% accuracy in the absolute flux level.

The continuum emission was extracted from broad-band data obtained from the WIDEX correlator, with four units and two polarizations covering the frequency range from 217.167 to 220.836 GHz. We produced the continuum image for NGC 7538 S from the line-free parts of the spectrum, but produced the IRS1 continuum map using the whole bandpass, because it is an extremely line-rich source with few line-free regions to extract. A quantitative comparison of the IRS1 continuum images with and without line contamination are almost identical, suggesting that the relative contribution from the IRS1 lines to the dust continuum is not strongly affecting its continuum imaging (see Beuther et al. 2012a for a more thorough discussion of this procedure). The 1σ continuum rms values for NGC 7538 S and IRS1 are 0.94 mJy beam^{-1} and 22 mJy beam^{-1}, respectively. The higher rms for IRS1 is a result of the strength of this source[1].

[1]The rms here is not the thermal rms, but is dominated by the side-lobes of the strongest source in the field.

For spectral line observations, the intrinsic resolution of WIDEX covering the total bandpass is 1.9 MHz (2.66 km s^{-1}). Because of this spectral resolution, we mainly concentrate in this chapter on the chemistry, with less emphasis on the kinematics. The resulting 1σ spectral line rms per channel in emission-free regions on the visibility plane is 2.8 mJy beam^{-1} for continuum subtracted NGC 7538 S and 26 mJy beam^{-1} for continuum included IRS1.

Calibration and imaging of the data were performed with CLIC[2] and MAPPING[3] software. The data were inverted with a "robust" weighting scheme and cleaned with the Clark algorithm. The resulting synthesised beams are $\sim 0.40'' \times 0.36''$ for IRS1 and $\sim 0.57'' \times 0.37''$ for NGC 7538 S, which is a spatial resolution of $\sim$ 1 000 AU at the assumed source distance of 2.65 kpc.

3.4 Observational Results

3.4.1 Continuum emission

In Figure 3.1, we present the 1.3 mm continuum image of NGC 7538 S and IRS1 as contours overlaid on flux-density colormaps. Several compact, distinct bright substructures clearly appear in the continuum maps, consistent with previous observations (e.g., Beuther et al. 2012a; Naranjo-Romero et al. 2012; Wright et al. 2012; Zhu et al. 2013). We list the nominal absolute positions and peak specific intensity per beam for all resolved substructures in Table 3.1, and describe them in more detail below:

- **NGC 7538 S**: The source is resolved into 3 compact condensations, with nearly identical continuum specific intensities. From northeast to southwest (Figure 3.1 lower panel), we name them as MM1, MM2 and MM3. Compared to condensations MM2 and MM3, MM1 is more extended, and contains multiple substructures, marked in Figure 3.1 as 1a, 1b, 1c. Except for 1c, these substructures have also been detected at 1.3 mm with the SMA and a beam size of 1.23″(Sandell & Wright 2010; Naranjo-Romero et al. 2012), as well as at 1.4 mm and 3 mm with CARMA/BIMA (Wright et al. 2012; see Table 3.1 for corresponding observations). Substructures 1a and 1b (separated by 0.5″) are associated with a heavily obscured mid-IR counterpart (Spitzer IRAC and IRS data, Wright et al. 2012), and so are suggested to be more evolved than the other compact mm condensations. However, it is not clear whether 1a and 1b are truly distinct sources, or whether 1c is an artifact of the sidelobes (CARMA observations by Wright et al. (2012) found no continuum counterpart for 1c at 1.3 mm, however it was detected by Naranjo-Romero et al. (2012) using the SMA at the same wavelength), so we will not discuss them in detail. In addition, MM1

[2]http://www.iram.fr/IRAMFR/GILDAS/doc/html/clic-html/clic.html
[3]http://www.iram.fr/IRAMFR/GILDAS/doc/html/map-html/map.html

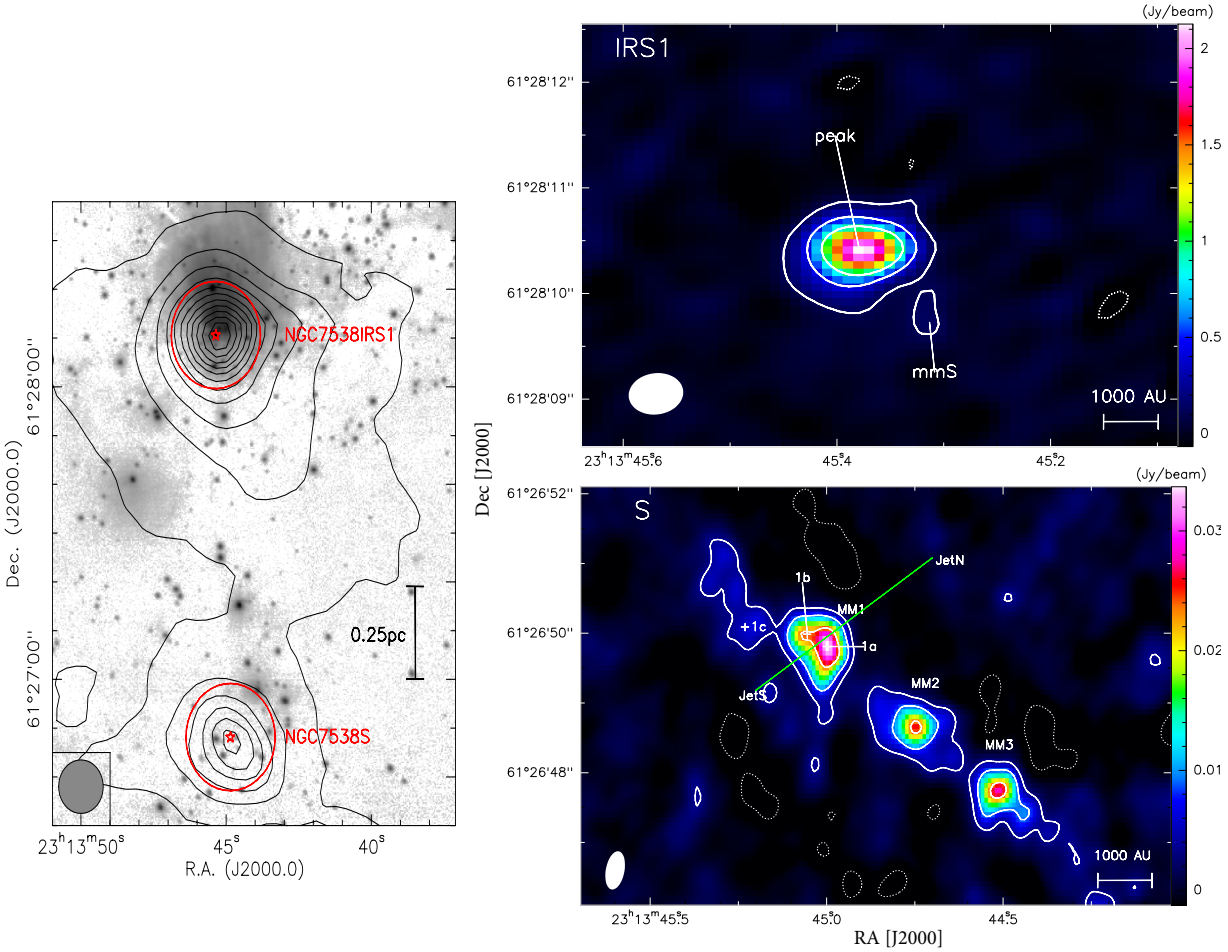

Figure 3.1: Left: Overview of the NGC 7538 complex (adopted from Beuther et al. 2012a). The grey-scale presents the K-band image from Puga et al. (2010), and the contours show the single-dish 1.2 mm continuum data from Sandell & Sievers (2004). The colored stars and circles show the central positions and FWHM of the primary beam of the PdBI at 1.3 mm wavelength for NGC 7538 IRS1 and NGC 7538 S in the north and south, respectively. The contour levels are from 250 mJy beam^{-1} to 5.25 Jy beam^{-1} in steps of 500 Jy beam^{-1}. The beam of the 30 m observations and a scale bar are shown at the bottom-left and right, respectively.
Right: Colormaps of the continuum flux obtained with the PdBI at 1.3 mm. For IRS1 (upper panel), the white solid contours start at 5σ and continue in 20σ steps (σ = 22 mJy beam^{-1}). In NGC 7538 S (lower panel), the contour levels start at 4σ and continue in 10σ steps (σ = 0.94 m Jy beam^{-1}). The dashed contours represent negative emission at the same level as the solid (positive) contours. The synthesised beams are shown at the bottom left of each panel. The direction of the studied outflow is shown with a green line. Labels mark individual substructures identified in this work.

Table 3.1: Properties of continuum substructures in NGC 7538 S and IRS1, identified in Figure 3.1.

Source	R.A. [J2000] 23^h13^m	Dec. [J2000] 61°	Peak Flux I_ν (mJy/beam)	T_{rot} (K)	$N^d_{H_{2,1}}$ (10^{23}cm^{-2})	$N^e_{H_{2,2}}$ (10^{23}cm^{-2})	Alternative Designations
peak	$45^s.4$	$28'10''.4$	1945.1 ± 182.3	136 ± 24[f]	–	18.15 ± 8.01	
mmS	$45^s.3$	$28'09''.8$	126.4 ± 3.1	136 ± 24[g]	–	–	SW extension[a]
MM1	$45^s.0$	$26'49''.8$	32.2 ± 1.1	157 ± 14[g]	19.5 ± 2.72	15.10 ± 1.37	1a:SMA3[b],CARMA S_{A1}[c] 1b:SMA4[b],CARMA S_{A2}[c] 1c:SMA5[b]
MM2	$44^s.7$	$26'48''.7$	25.7 ± 0.8	130 ± 12[g]	18.96 ± 2.67	2.54 ± 0.39	2:SMA2[b], S_B[c]
MM3	$44^s.5$	$26'47''.8$	27.0 ± 1.1	50[h]	55.34 ± 2.25	0.32 ± 0.06	3:SMA1[b], S_C[c]
JetN	$44^s.7$	$26'51''.9$	σ = 0.12	150[h]	≤ 0.28	2.56 ± 0.19	
JetS	$45^s.2$	$26'48''.7$	σ = 0.27	150[h]	≤ 0.63	3.30 ± 0.18	

a. Zhu et al. (2013).

b. Naranjo-Romero et al. (2012).

c. Wright et al. (2012).

d. H_2 column densities are calculated from the continuum using Eq. 2.10.

The uncertainties come from the measurement of the continuum fluxes and the calculation of the excitation temperatures.

e. H_2 column densities are calculated from $C^{18}O$ conversion.

The uncertainties come from the gaussian fitting to $C^{18}O$ and the calculation of the excitation temperatures.

f. Temperature taken by assuming the same as in mmS.

g. Temperature is derived from rotation map in Section. 3.5.

h. Temperature assumed based on estimation from Sandell & Wright (2010).

has been reported to drive a compact (0.1–0.4 pc) free-free ionized bipolar outflow from VLA observations by Sandell & Wright (2010). This outflow is perpendicular to the major axis of the proposed edge-on disk (Sandell et al. 2003), and coincides with an OH maser (Argon et al. 2000), a Class II CH_3OH maser (Pestalozzi et al. 2006), and a cluster of H_2O maser spots (Kameya et al. 1990). There is no clear continuum detection of this outflow in our observations (likely emission from the jet is primarily on larger angular scales than those our observations are sensitive to), though, we mark its location as JetN and JetS in Figure 3.1.

- **IRS1**: The peak continuum flux specific intensity of IRS1 at 1.3 mm is 60 times higher than NGC 7538 S, but it is unresolved at the spatial resolution of 1 000 AU. We do however also detect a additional component in the SW (namely, mmS) having specific intensity $> 5\sigma$ rms. Similar extended structure has also been detected in continuum maps of this source from SMA and CARMA observations at 0.7″ (Zhu et al. 2013). However, there is no centimeter counterpart has been detected, and it was not detected in higher spatial resolution continuum observations (0.2″, $\sim$ 500 AU, Beuther et al. 2013a) at 843 μm, which shows at least 3 substructures embedded in this source. At this point, it is therefore still unclear whether mmS is an artifact of the sidelobe or a real dust condensation in IRS1.

3.4.2 Spectral line

Line identification

After imaging the whole data cube, we extract the beam-averaged spectrum from the continuum peak of each substructure listed in Table 3.1, and show them in Figure 3.2. The spectra from MM1 in NGC 7538 S and from the peak of IRS1 exhibit the strongest line emissions (absorptions), so we use these to identify species. However, as a result of multiple velocity components, large linewidths compared to the $\sim$ 2.7 km s^{-1} velocity resolution of our data, these line identifications are not always unambiguous. We therefore also compared the spectra to those from a single-dish + interferometry line survey in Orion-KL at the same frequency (velocity resolution of $\sim$ 1.2 km s^{-1}, Table A1), in order to verify the identification of strongest lines. In addition, we cross-checked these identifications and identified additional weaker transitions by using the synthetic spectrum fitting program mentioned in Chapter 2.

Employing the above two approaches, we identify more than 90 lines over the entire 4 GHz band and list them in Table B1. Tentative identifications of weak lines ($\sim 3\sigma$ rms) are marked with "*", while the strongest line in each species is marked with "†".

Comparing the identified lines in all substructures, we find large spectral variations within both NGC 7538 S and IRS1.

- **NGC 7538 S** has a large number of emission lines in the observed band, as is typical of HMSFRs. condensations MM1–3 which are separated by less than 1.5″ and have nearly identical continuum specific intensities but distinctly different line spectra. MM1 exhibits the strongest line emissions, while the majority of the lines in MM2 are weaker than in MM1. Toward MM3, we only detect weak emission from OCS, ^{13}CO and CH_3OH. In the outflow regions, although the continuum is weak because of the sensitivity, species known to be outflow tracers such as H_2CO, CH_3OH, SO, C^{18}O and ^{13}CO (Bachiller et al. 2001) are detected, and are even stronger in the outflows than in MM3.

- Unlike the above source, the spectrum of **IRS1** exhibits numerous absorption lines or likely inverse P-cygni profiles (e.g., in lines of HC_3N, HNCO and DCN) in the mm wavelengths at the peak position, indicating the infalling of the gas (Beuther et al. 2012a). However, there are also 4 strong lines (marked as "?CH_3OCH_3" and "?CH_3OH") showing in purely emission. We discuss a probable identification for these lines and their unique properties in Section 3.7. Away from the peak (∼ 0.4″, Beuther et al. 2013a), there are more lines detected in mmS than in NGC 7538 S (the primary difference being the detection of multiple lines of $HCOOCH_3$ in mmS which are absent in NGC 7538 S, Figure B1), and all species are observed in emission (Figure 3.2).

Line Imaging

In total, all the lines listed in Table B1 can be attributed to 15 different species (and 21 isotopologues thereof). As IRS1 is unresolved in our 1.3 mm continuum map, and mmS has not yet been demonstrated to be a real source, we will leave the molecular spatial distribution study of this source for a future study which employs the high spatial resolution data presented in Beuther et al. (2013a). NGC 7538 S is however resolved into multiple condensations, so we choose one of the strongest unblended transitions of each molecule (marked as "†" in Table B1) to produce intensity maps of these condensations, integrated through the range coving their FWHM linewidths (as shown in Figure B2, the chosen velocity ranges are actually slightly larger than the FWHM of the lines, in order to account for the small variation in the peak velocity between different substructures), which are presented in Figure 3.3.

The line images of different species have distinct intensity peaks, primarily toward MM1 and (or) MM2. However, as our data are not sensitive to emission on scales larger than ∼ 10 ″, we do not recover all of the emission from the extended outflows. The main results from these images are:

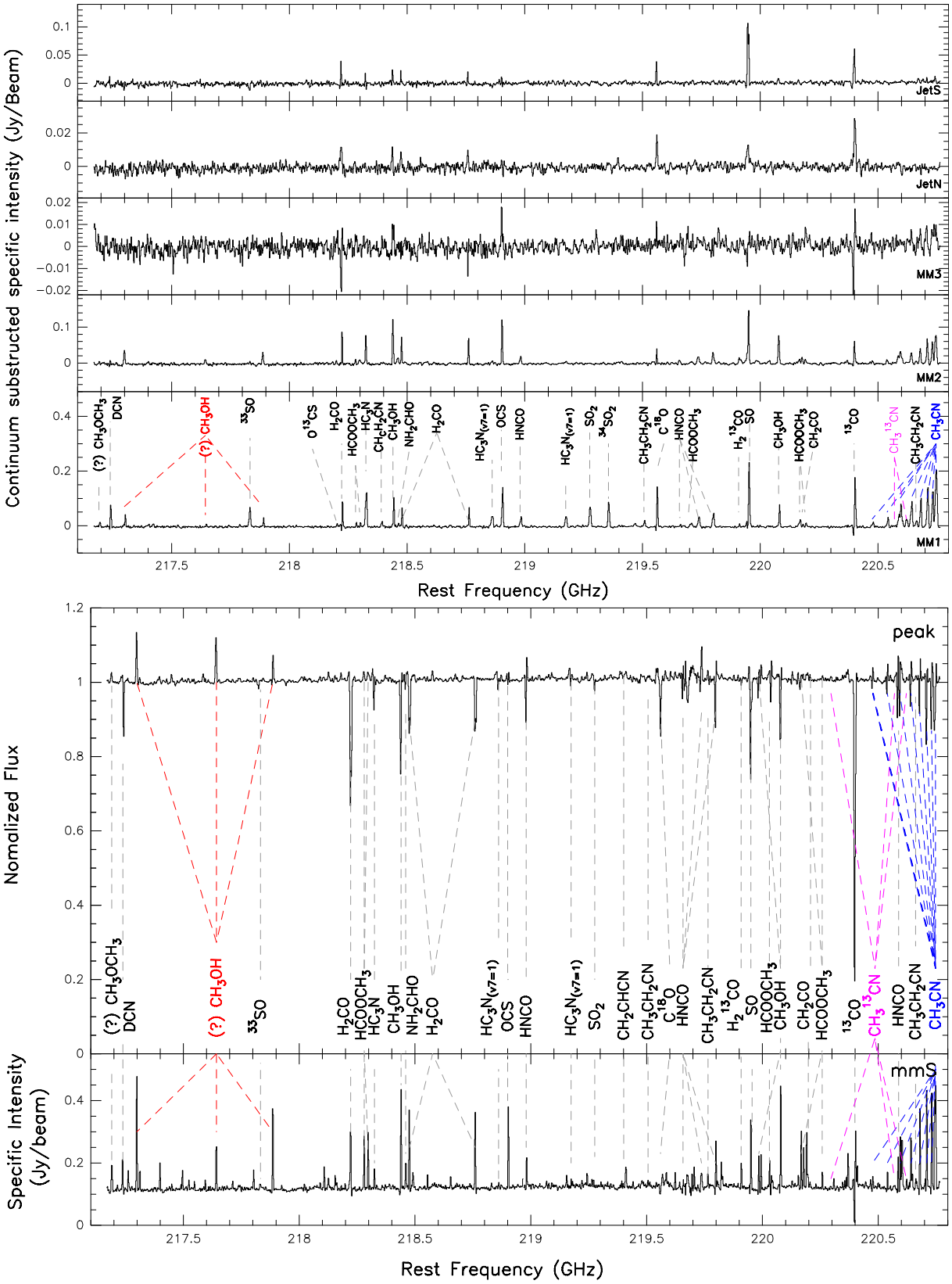

Figure 3.2: Spectra extracted from selected positions (marked in Figure 3.1) after imaging the whole data cube. The spectral resolution is 2.66 km s^{-1}. All strong lines are labeled, including identified and unidentified lines. Continuum-subtracted spectra from different substructures in NGC 7538 S are shown in the upper panel, while the lower panel presents unsubtracted spectra from two positions in IRS1 (spectrum of mmS shows the continuum level). All of the detected $HCOOCH_3$ transitions are shown in Figure B1.

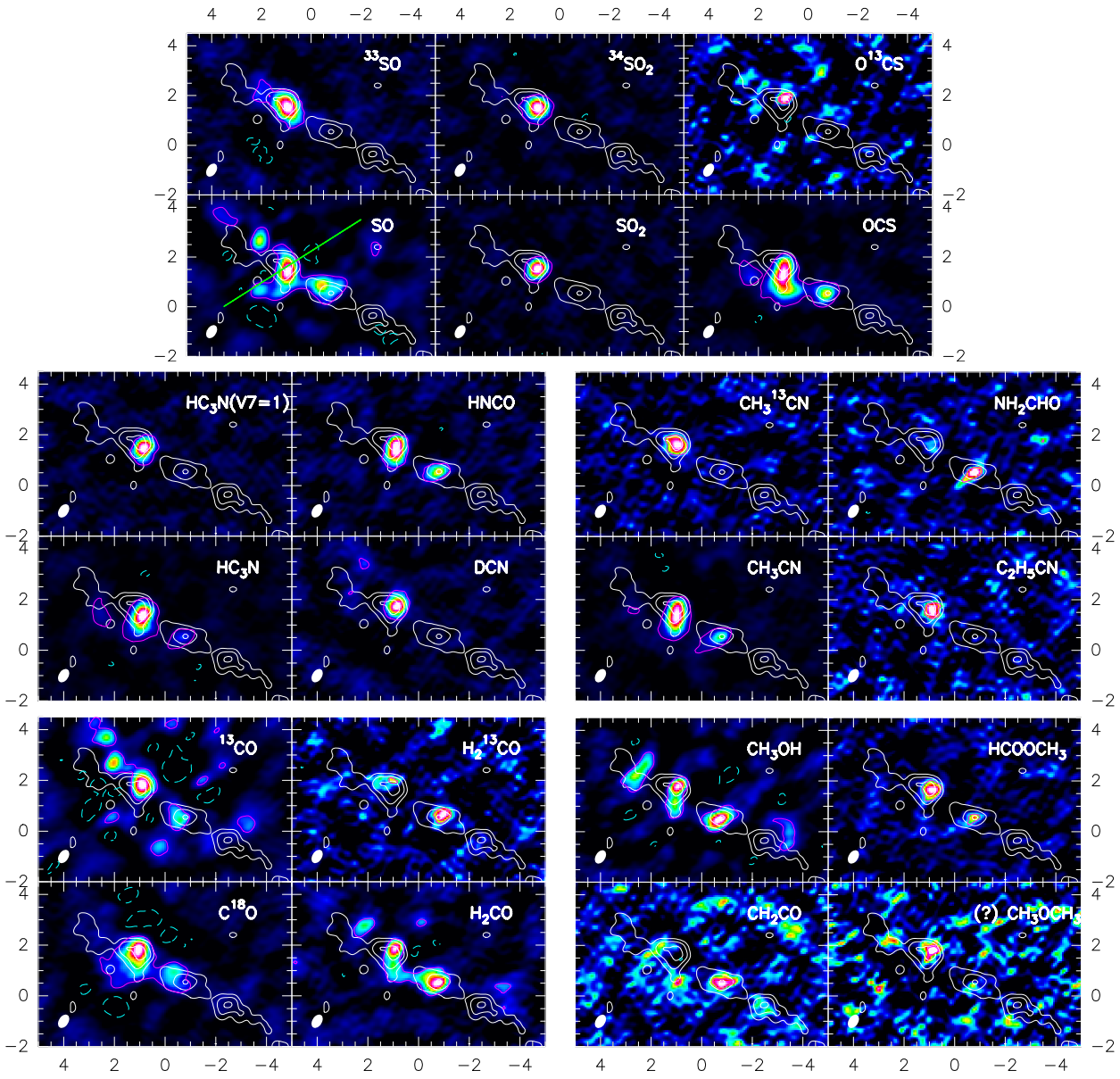

Figure 3.3: Maps of the intensity distribution of molecules detected in PdBI data at 1.3 mm. The intensities have been derived by integrating the line emission over the velocity range shown in Figure B2 (excluding the line wings). The synthetic beam is shown at the bottom left of each panel. White contours show the continuum (at 4σ, 14σ and 24σ levels), purple contour revels the region where molecular specific intensity $> 1\sigma$, and the dashed green contour revels negative specific intensity beyond -1σ because of the interferometric side lobe effect. Green lines in the SO map sketch the outflow directions. All images have different color scales (in mJy beam^{-1} km s^{-1}), increasing from black to white, which are optimised to emphasise the features in the distribution of each molecules.

1. Most of the main species and isotopologues (18 out of 21) in our dataset peak at MM1 (of these, notably SO, H_2CO and ^{13}CO exhibit strong emission even in MM1c), with velocity at line center $V_{lsr} = -60\,km\,s^{-1}$. Of all these MM1-peak species, several COMs (e.g., CH_3CN, $CH_3^{13}CN$ and C_2H_5CN) are high temperature indicators. Furthermore, the presence of vibrationally-excited line HC_3N ($v_7 = 1$) indicates mid-IR pumping, and hence suggests the existence of a hot embedded IR-emitting source. These molecular distribution peaks indicates that MM1 is a HMC. Most of the species can also be clearly detected in MM2 with velocity at line center $V_{lsr} =\sim -58\,km\,s^{-1}$ and lower specific intensities than in MM1, including both molecules which evaporate from the grain surface early in the warm-up phase, e.g., CH_3OH, $HCOOCH_3$, HNCO, $C^{18}O$, ^{13}CO, H_2CO and species with optically thick lines, such as OCS, SO, CH_3CN, whose isotopologues with optically thin transitions are comparably much weaker in MM2.

2. Unlike the majority of species described above, $H_2^{13}CO$, CH_2CO (ketene) and NH_2CHO (formamide) are stronger in MM2 than in MM1.

3.5 Calculation

A more precise approach for studying the chemical variations in the above mentioned substructures is to measure quantitative differentiation in their chemical parameters (e.g., temperature, column density).

3.5.1 Temperature estimates

In NGC 7538 S and IRS1, the majority of species have similar spatial distributions, and CH_3CN, the typical temperature tracer in high-density gas, has multiple transitions in our data, so we use it to measure the gas temperatures in condensations of these cores. Due to its optical depth transitions, the temperatures calculated from CH_3CN ladder with the LTE and optically thin assumption is not valid, as demonstration of the dashed line fittings in panel 1 & 2 of Figure 3.4. On the other hand, compared to CH_3CN, lines of its rare isotopologue $CH_3^{13}CN$ should be optically thin. However, except for $CH_3^{13}CN$ ($12_2 \rightarrow 11_2$), all the other transitions of this molecule are blended with the broad line wings of CH_3CN transitions. Therefore, we use the iterative approach described in Section 2.4.1, and calculate the optical depth corrected temperatures in condensations where CH_3CN ladder is available (panel 3–5 in Figure 3.4).

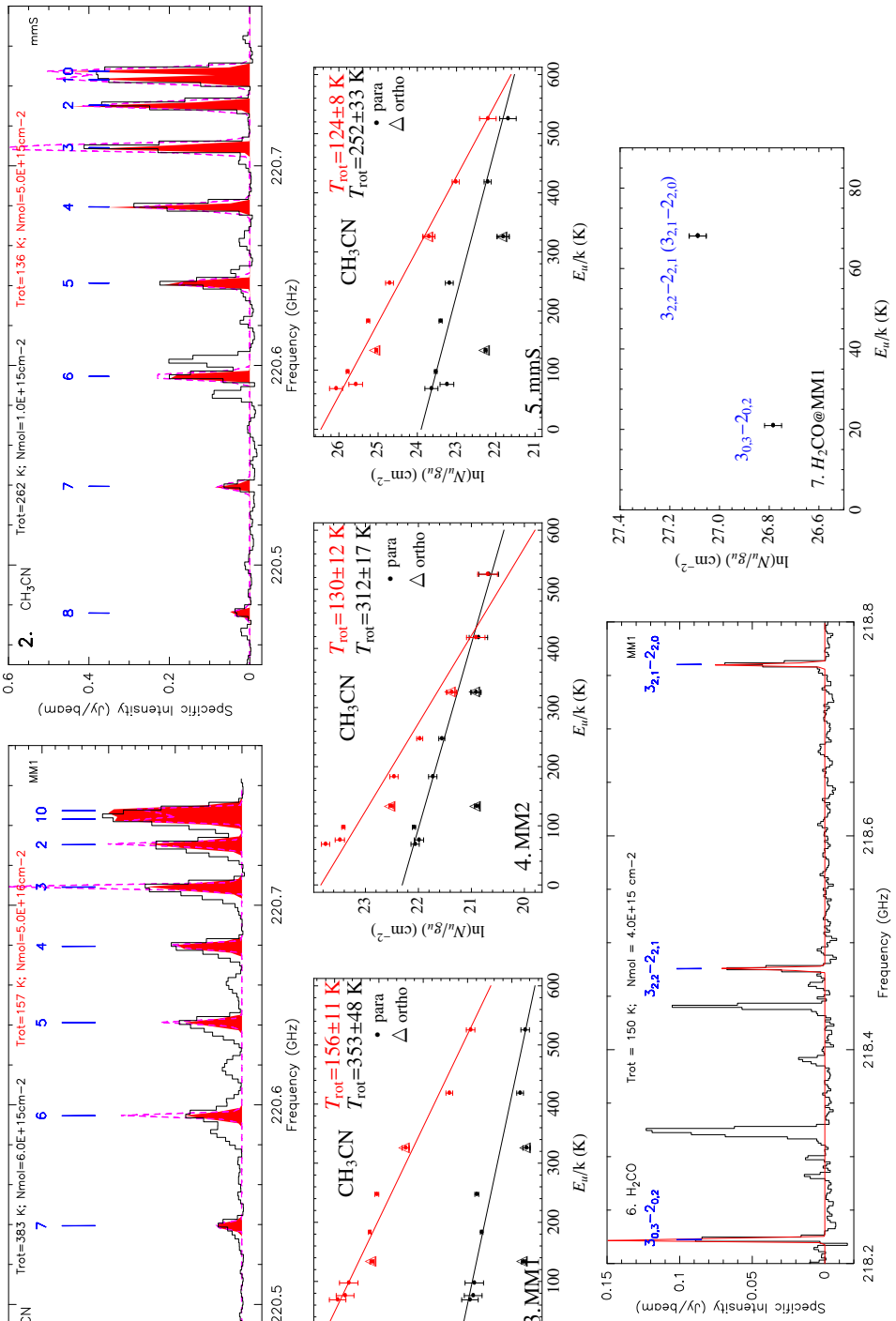

Figure 3.4: Panel 1 & 2 presents the CH_3CN spectrum towards MM1 and mmS in black, LTE model fit in dashed purple, and fitting with optical depth correction in filled red. Panel 6 presents the H_2CO spectrum in the whole observation band towards MM1 in black, and the LTE model fit in red shows lines of this molecule are optically thick. Panels 3–5 show the rotation diagram of CH_3CN derived for each substructure, with black dots and fitting in optically thin assumption, and red dots and fitting by optical depth correction. The estimated rotation temperature from each rotation diagram is indicated in each panel. Panels 7 shows the data points of H_2CO transitions in MM1, which can not be fitted in the rotation diagram. Error bars reflect only the uncertainties in the Gaussian fit of the lines.

Another possible temperature tracer H_2CO (Mangum & Wootten 1993; Ao et al. 2013) is not applicable to derive the rotation temperature from our data, because only 3 transitions of H_2CO and 1 transition of $H_2^{13}CO$ are available in the whole band. However, from Figure 3.4, the optically thin assumption is not applicable at least to H_2CO ($3_{0,3} \rightarrow 2_{0,2}$), whose $E_u/k_B \sim 21$ K. In addition, the only ortho- transition of the rare isotopologue ($3_{1,2} - 2_{1,1}$) is not the same as the transitions of the main para- isotopologues ($3_{2,2} \rightarrow 2_{2,1}$, $3_{2,1} \rightarrow 2_{2,0}$ and $3_{0,3} \rightarrow 2_{0,2}$), so T_{rot} can not be derived from H_2CO transitions without optical depth correction (panel 7 of Figure 3.4).

The above approach is applicable to sources MM1, MM2 and mmS, where the CH_3CN ladders can be clearly detected. In contrast, detection of CH_3CN in the outflow regions and MM3 are $< 3\sigma$, so we do not determine their temperatures. We assume that JetN and JetS have the same temperature as MM1, and that MM3 is similar to the envelope ~ 50 K, according to Sandell & Wright (2010) (where rotation maps of $H^{13}CN$, DCN and CH_3CN suggest the whole of MM1–3 is 52 ± 10 K while the outflow is 147 ± 40 K). For IRS1, multiple components along the line of sight to this core (e.g., outflow, envelope, core) makes it difficult to derive the rotation temperature from the absorption lines at the continuum peak. Instead, we adopt a (lower limit) temperature derived from the off-peak position mmS.

3.5.2 Column densities

Molecular column densities

For all the isotopologues we detect, we calculate their column densities from the integrated spectral line intensities. Using the same assumptions and equations (from Eq. 2.1 to Eq. 2.5) described in Section 2.4.2 .

The spectra from NGC 7538 S consist of pure emission lines, while spectra from the peak of IRS1 are a mixture of emission and absorption lines, so we calculate the molecular column densities $N_{T,\alpha}$ separately for these two cases.

1. For absorption lines in IRS1, the optical depth can be calculated from the flux intensity ratio between a particular line F_υ and the continuum $F_{\upsilon,c}$, $\tau_\upsilon = -\ln(F_\upsilon/F_{\upsilon,c})$. Then, Eq. 2.3 yields:

$$N_{T,\alpha} = \frac{8\pi\nu}{\ell(T_{rot})\eta c^3} \int \tau_\upsilon d\upsilon \qquad (cm^{-2}) \qquad \text{(absorption)} \qquad (3.1)$$

2. For the emission lines, we assume that the Rayleigh-Jeans approximation ($\frac{h\nu}{kT_{rot}} \ll 1$) is valid (Eq. 2.6 and Eq. 2.7), and that the observed emission in each substructure is homogeneous and fills the combined beam (Eq. 2.8). Therefore, with the integration of measured main beam brightness temperature within the velocity range $\int T_B(\upsilon)d\upsilon$, we can estimate the molecular column density at one transition N_u as:

$$\begin{aligned} N_u &\cong \frac{8\pi k\nu^2}{hc^3 A_{ul}} \frac{\tau_{\alpha,0}}{1-e^{-\tau_{\alpha,0}}} \int T_B(\upsilon)d\upsilon \quad (cm^{-2}) \\ N_{T,\alpha} &= \frac{8\pi k}{hc^3} \frac{(e^{\frac{h\nu}{kT_{rot}}}-1)}{\ell(T_{rot})\eta} \frac{\tau_{\alpha,0}}{1-e^{-\tau_{\alpha,0}}} \int T_B(\upsilon)d\upsilon \quad (cm^{-2}) \end{aligned} \quad \text{(emission)} \tag{3.2}$$

Here $\tau_{\alpha,0}$ is the optical depth at line center.

In general, we assume that the observed transitions are optically thin ($\tau_{\alpha,0} \leq 1$, $\frac{\tau_{\alpha,0}}{1-e^{-\tau_{\alpha,0}}} \approx 1$). However, for several molecules with large abundances, we also observe the corresponding transition of their rare isotopologues, e.g., SO ($6_5 \rightarrow 5_4$)- ^{33}SO ($6_5 \rightarrow 5_4$), OCS ($18 \rightarrow 17$)- O^{13}CS ($18 \rightarrow 17$), ^{13}CO ($2 \rightarrow 1$)- C^{18}O ($2 \rightarrow 1$) and $CH_3^{13}CN$ ($12_2 \rightarrow 11_2$)- CH_3CN ($12_2 \rightarrow 11_2$). By measuring the ratio between main beam brightness temperature of the main line $T_{B,\,\alpha,0}$ and its isotopologue $T_{B,\,\beta,0}$, we can estimate the optical depth at line center of a given transition $\tau_{\alpha,0}$ from Eq. 2.9, given in Table 3.2.

$$\frac{1-\exp(-\tau_{\alpha,0}/\mathfrak{R}^{\alpha})}{1-\exp(-\tau_{\alpha,0})} \approx \frac{T_{B,\,\beta,0}}{T_{B,\,\alpha,0}}$$

The remaining molecules, for which we cannot calculate the optical depth of their lines, are assumed to be optically thin.

Using the above method, we calculate the column densities of 21 isotopologues (in both optically thin and thick cases) in each substructure, and present them in Table B3I and Figure 3.5. We show in Table 3.2 that all the transitions which we correct their optical depth are significantly optically thick (τ = 4–44) in all sources where they are detected. Whether the assumption that lines from all the rest of the molecules are optically thin is valid or not will be discussed in Section 3.5.4.

Large variations in column density exist among the studied substructures, and they are presented in Figure 3.5. The majority of the molecules studied here have larger column densities in MM1 than MM2, except for NH_2CHO, $H_2^{13}CO$ and CH_2CO (as shown in Figure 3.3). With more or less the similar condensation size (Figure 3.1) and dust emission (see Section 3.5.2), masses of MM1–3 are close, so the sharp decrease of molecular column densities in MM3 compared to MM2 (apart from OCS, DCN, SO_2) indicates that many, particularly heavy molecules in MM3 are likely frozen out and not in the gas-phase.

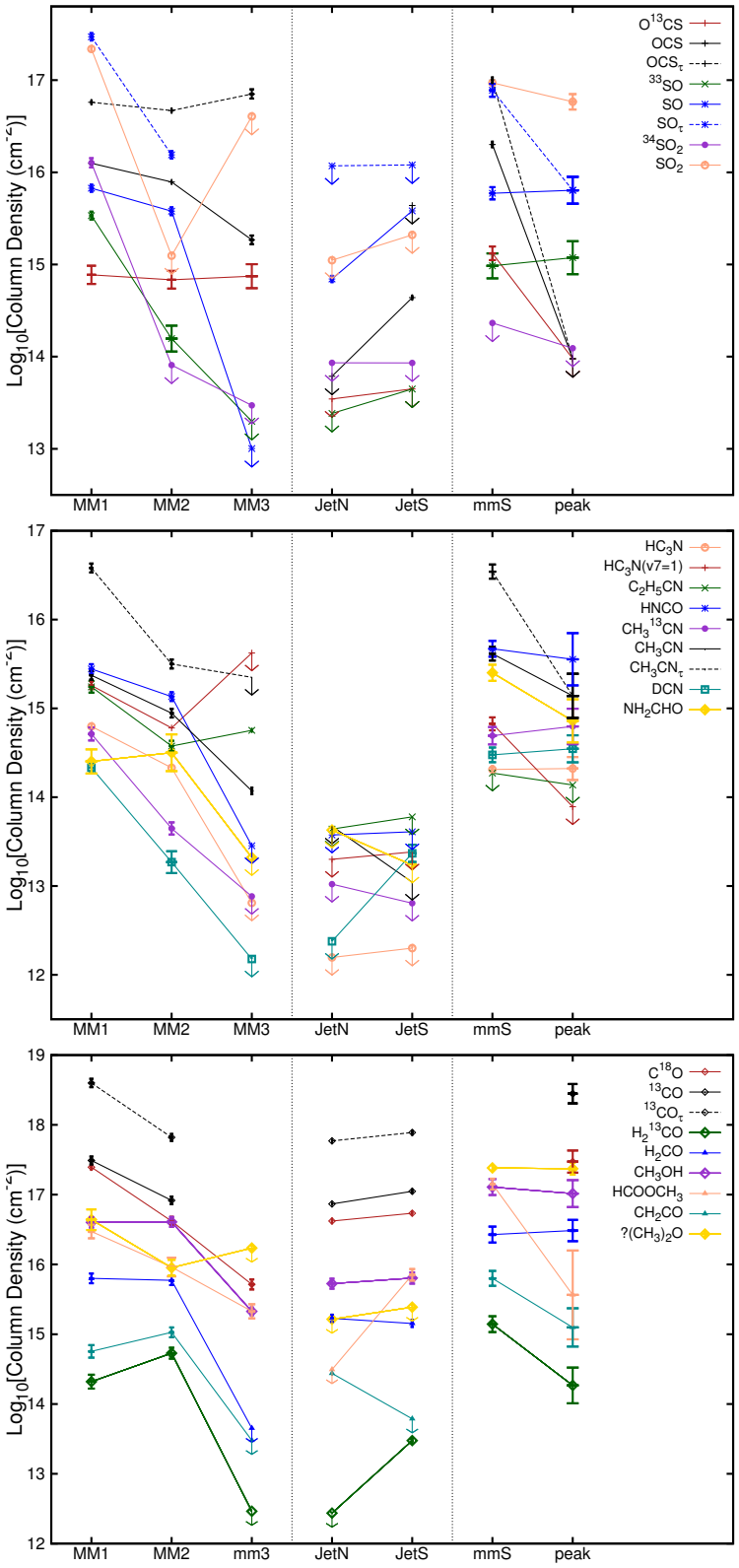

Figure 3.5: Molecular column densities toward 5 positions in NGC 7538 S and 2 positions in IRS1. Colored solid lines show the differentiation for each isotopologue calculated from optically thin assumption (arrows highlight the upper limits), while dashed lines show the differentiation calculated with optical depth correction from Eq. 2.9. Uncertainty of each line at each position is determined from T_{rot}, partition function $Q(T_{rot})$, and Gaussian fitting to $\int T_B(\upsilon)d\upsilon$. For abundant molecules (e.g., HNCO, SO_2) which we have not measured their optical depths, their column densities could be underestimated by a factor of 5–10.

H_2 Column densities

In NGC 7538 S, the continuum is dominated by dust and gas emission. Based on the assumption same as in Orion-KL (i.e., the dust emission at mm wavelength is optically thin and has the same excitation temperature as the rotation temperature derived from CH_3CN, $T_{ex} \equiv T_{rot} = T_{dust}$), we calculate the H_2 column densities for different substructures according to Eq. 2.10:

$$N_{H_2} = \frac{I_\nu R}{B_\nu(T_{dust})\Omega_a \kappa_\nu \mu m_H}$$

where parameters I_ν, R, $B_\nu(T_{dust})$, μ and m_H are defined in Section 2.4.2, Ω_a is the solid angle of the PdBI beam (in rad^2), the dust absorption coefficient at 1.3 mm is $\kappa_\nu = 1.1$ cm^{2}g^{-1} in MM1–3, and $\kappa_\nu = 0.899$ cm^{2}g^{-1} in JetN (S) (assuming a model of agglomerated grains with thin ice mantles for densities 10^8 cm^3 in MM1–3, and 10^6 cm^3 in JetN(S)[4], from Ossenkopf & Henning 1994).

We find peak column densities for substructures of NGC 7538 S that range from a few times 10^{22} to 10^{24} cm^{-2} (Table 3.1). Although the intensities at peaks are more or less the same in MM1–3, the significant differences in adopted dust temperatures between MM3 and MM1–2 means that the colder MM3 is much denser than MM1–2. The outflow regions are measured to have the lowest column densities, but this may be partly because the large scale extended emission has been filtered out.

The contribution of free-free emission in MM1–3 of NGC 7538 S to the millimeter continuum flux is reported to be negligible by Wright et al. (2012). However, the 1.3 mm continuum in IRS1 is dominated by free-free emission (e.g., Pratap et al. 1992; Keto et al. 2008; Sandell et al. 2009), so Eq. 2.10 is not applicable in IRS1. In addition, since the PdBI data resolves out large-scale features, the upper limits on the H_2 column density in JetS and JetN measured from the continuum (3σ rms in Eq. 2.10) are likely underestimates. In contrast, we notice that $C^{18}O$ is detected toward IRS1 and all of the identified substructures of NGC7358 S, even though its large scale emission also has been filtered out. As a rare isotopologue, it can be reasonably assumed to be optically thin, so we use it to make a second, independent estimate of the H_2 column density for these substructures. By assuming a constant abundance $\frac{N_{C^{18}O}}{N_{H_2}} = \frac{N_{C^{18}O}}{N_{CO}}\frac{N_{CO}}{N_{H_2}} \sim \frac{10^{-4}}{607} \sim 1.64 \times 10^{-7}$ (Wilson & Rood 1994; Giannetti et al. 2014), we can convert the column density from the assumed optically thin $C^{18}O$ to a column density of H_2 (reported in the column $N_{H_{2,2}}$ of Table 3.1).

[4]Grains are probably not only stripped of ices due to jet/outflow-induced shocks, but also partly destroyed.

3.5.3 Molecular abundances

Subsequently, to study the chemical properties within the general framework of evolutionary phases of HMSFRs, we derive the molecular abundances with respect to H_2 in each substructure (Table B3II). In MM1–3, dust-derived H_2 column density $N_{H_{2,1}}$ are used as standards (reasons are discussed in Section 3.5.4 part 3). Although we have no clear detection of dust emission in JetN (S), and we do not know whether the associated shock changes the chemistry, we give an estimation of the molecular abundances with respect to $C^{18}O$-derived H_2 column density $N_{H_{2,2}}$, because we note that $C^{18}O$ abundance in MM1 (HMC) where the outflow forms is reliably close to the canonical value in the ISM (Wilson & Rood 1994). In addition, since IRS1 is also a HMC, we assume its $C^{18}O$ abundances is similar to that in MM1, and use $N_{H_{2,2}}$ for the derivation of abundances in this source as well.

3.5.4 Error budget

In this section, we consider the effect that the various assumptions we made in our quantitative analysis have on the results presented in this chapter.

1. T_{rot} (rotation temperature): The traditional rotation diagram method is subject to a number of uncertainties due to various assumptions (the emission is assumed to be optically thin and LTE is assumed to apply; see discussion in Snyder et al. 2005; Herbst & van Dishoeck 2009). If these assumptions are valid, the points on the population diagram will be well-fit by a straight line, with the slope proportional to the negative reciprocal of the temperature. However, this is not the case (see Figure 3.4). According to Table 3.1, the volume densities of MM1–MM3 are $> 10^8$ cm^{-3} if the condensation sizes are roughly similar to (or 3–5 times larger than) the beam size, so the assumption of LTE is valid for all molecules at T_{rot}, and the main reason for uncertainties is the optical depth of CH_3CN. In Section 3.5.1, we obtain the optical depth of CH_3CN ($12_2 \rightarrow 11_2$) by comparing its main beam brightness temperature to that of $CH_3^{13}CN$ ($12_2 \rightarrow 11_2$). Then, we use this optical depth as a standard in non-LTE radiative transfer fitting and derive a lower T_{rot} in each substructure. To verify our CH_3CN rotational temperatures in Figure 3.4, we compare them with the temperatures derived for NGC 7538 S as a whole from NH_3 by Zheng et al. (2001) ($\sim$ 25 K), as well as from $H^{13}CN$, DCN and CH_3CN by Sandell & Wright (2010) (52 $\pm$ 10 K from the whole of MM1–3 and 147 $\pm$ 40 K in the outflow, and found our temperatures are significantly higher. This is not unexpected, as the smaller beam of our observations can better resolve any inner concentration of warm gas in these sources. However, the off-peak temperature we derived after optical thick correction in IRS1 is much lower than that derived from LVG fitting of Qiu et al. (2011) (245 $\pm$ 25 K) and optical depth corrected rotation diagram

of Zhu et al. (2013) (∼ 260 K). Possible reasons are: (1) our higher angular resolution (∼ 0.4″×0.4″ for our data, while 0.8″× 0.6″ in Zhu et al. 2013 and 3″× 2″in Qiu et al. 2011) allows us to probe a denser and cooler region, and (2) the optical depths we adopt to correct the rotation diagram (ranging from τ = 1 at K=8 to τ = 16 at K=3) is higher than those adopted by the aforementioned literatures (ranging from τ = 0.16 at K=8 to τ = 2.99 at K=3).

2. N_T (molecular column density): In Section 3.5.2, we first assume that all the identified molecule lines are optically thin, then we use Eq. 2.9 to obtain the optical depth of those species that have both main and rare isotopologues with the same transition, and use Eq. 2.8 to correct the column densities of the main isotopologues. In this approach, we assume the rare isotopologue lines are optically thin, and list the optical depths and abundance ratios for SO, ^{13}CO, OCS and CH_3CN with respect to their rare isotopologues with and without optical depth correction in Table 3.2.

However, there are some other uncertainties which might impact our estimation and we do not measure:
(1) The isotopic S-elements ratio in NGC 7538 Source is assumed to be close to the ratio in solar system (e.g., $^{32}S/^{33}S$ = 127, Lodders 2003). However, solar system values might have a bias since the Galactic disk outside the solar system is affected by ongoing isotope changes, which we don't see when looking at chondrules locally where are several billion years old. Therefore, a more precise optical correction for SO requires credible $^{32}S/^{33}S$ ratio in NGC 7538.
(2) Fractional reaction can also be an effect which may change minor/major isotopologue ratios, in particular, for CO, ^{13}CO and C^{18}O, as well as ^{32}S, ^{33}S and ^{34}S bearing molecules.
(3) Equation 2.8 is based on the assumption that the molecule and its isotopologue have the same excitation temperature, which is often not the case. Therefore, a more accurate calculation requires LVG + proper chemical modelling.

In short, our analytic calculations suggest that, the optical depth is the main issue which dominates the error in the estimated molecular column density. For abundant molecules such as HNCO, SO_2, which we do not observe a corresponding transition of a rare isotopologue, our assumption that they are optically thin may result in the underestimation of their column densities by a factor of 5–10 (as estimated from the average differences for OCS, SO, and CH_3CN column density values before and after optical depth correction, Figure 3.5).

Species		$\mathfrak{R}^a$	MM1 (157 ± 14 K)	MM2 (130 ± 12 K)	MM3 (50 K)	JetN (150 K)	JetS (150 K)	mmS (136 ± 24 K)
$\tau_{SO\ (6_5\rightarrow5_4)}$			44	4	–	≤ 17	≤ 3	13
$N_{SO_\tau}/N_{^{33}SO}$	†	127	87.39 ± 1.01	98.19±19.84	–	≤ 489.20	≤ 270.60	79.79±11.72
$N_{SO}/N_{^{33}SO}$	⋆		1.99 ± 0.02	24.10 ± 4.87	–	≥ 28.77	≥ 85.70	6.14 ± 0.90
$\tau_{^{13}CO\ (2\rightarrow1)}$			13	8	–	8	7	−−
$N_{^{13}CO_\tau}/N_{C^{18}O}$	†	8.3	16.22 ± 0.69	15.86 ± 0.25	–	14.07±0.45	14.44±0.17	−−
$N_{^{13}CO}/N_{C^{18}O}$	⋆		1.25 ± 0.05	1.98 ± 0.03	–	1.76 ± 0.06	2.06 ± 0.02	−−
$\tau_{OCS\ (18\rightarrow17)}$			4.5	6	38	−−	≤10	5
$N_{OCS_\tau}/N_{O^{13}CS}$	†	73.5	73.97 ± 12.44	69.22±11.78	94.14±16.38	–	≤ 94.14	76.37 ± 7.36
$N_{OCS}/N_{O^{13}CS}$	⋆		16.26 ± 2.73	11.51 ± 1.96	2.48 ± 0.43	–	≥ 9.79	15.17 ± 1.46
$\tau_{CH_3CN\ (12_2\rightarrow11_2)}$			16	3.5	≤19	–	–	8.5
$N_{CH_3CN_\tau}/N_{CH_3^{13}CN}$	†	73.5	73.30 ± 3.94	71.68 ± 3.38	≤ 292.20	–	–	71.20 ± 3.52
$N_{CH_3CN}/N_{CH_3^{13}CN}$	⋆		4.58 ± 0.25	19.86 ± 0.94	≥ 15.38	–	–	8.38 ± 0.41

Table 3.2: Optical depth and abundance ratios for SO, ^{13}CO, OCS and CH_3CN with respect to their isotopologues in each substructure of NGC 7538 S and IRS1 mmS. † or ⋆ mark the estimations with or without optical depth correction. ≥ (≤) come from the 3σ limit of the non-detection. The ratios $\mathfrak{R}_\alpha$ between isotopologues of $^{12}C/^{13}C$ and $^{16}O/^{18}O$ are provided from the galactic ISM ratio measured in Giannetti et al. (2014) (with R_{GC}(NGC 7538) ∼ 9.7 kpc), while $^{32}S/^{33}S$ is provided from the local ISM ratio measured in Lodders (2003). Uncertainties on the measured values are typically ≤ 10%, as determined from T_{rot}, partition function $Q(T_{rot})$, and Gaussian fitting to $T_B(\upsilon)d\upsilon$.

Apart from the optical depth, errors in the molecular column density based on T_{rot} and $\int T_B(V)dV$ are negligible compared to the chemical differentiation among the substructures (Table B3, on average < 10%).

3. N_{H_2} & molecular abundance: Because $C^{18}O$ is detected in all substructures of NGC 7538 S (including JetN and JetS where we detect no dust continuum), we use two methods to calculate the column density of H_2 (Table 3.1): from dust continuum ($N_{H_{2,1}}$) and from $C^{18}O$ ($N_{H_{2,2}}$). Comparing the column density of $H_{2,1}$ and $H_{2,2}$, we found $N_{H_{2,2}}/N_{H_{2,1}}$ is $\sim$ 0.7 in MM1, $\sim$ 0.2 in MM2, but only 0.005 in MM3. Several reasons may lead to such inconsistence: (1) we simply assume that the volume densities in all substructures are the same (10^8 cm^{-3}), therefore so are the gas-to-dust ratio and the dust opacity. Since we do not know the size and thickness of the ice mantle in each substructure, it is possible that gas is less denser in the warmer sources MM1 and MM2 than it in the cooler condensation MM3, making our assumption that "these small substructures being homogeneous" may be far from reality. (2) assuming that $N_{C^{18}O}/N_{H_2}$ = const in all the studied substructures, the derived $N_{H_{2,2}}$ in MM1 is a factor of 7 higher than that in MM2 and of 100 higher than that in MM3. However, this assumption may not be true, because the fractional variation of $N_{C^{18}O}/N_{H_2}$ ratio in different condensations (e.g., see Figure 3.6, also Figure 4-9 in Garrod et al. 2008), or the varying optical depth of $C^{18}O$ in MM1–3 (e.g., dust is much denser in MM3 than in MM1–2, so $C^{18}O$ may not be optically thin) can be other factors that introduce uncertainties in our analysis. Therefore, molecular abundances in MM1–3 are more reliable with respect to H_2 column densities derived from dust continuum.

4. The missing short spacings in our interferometric data can lead to underestimated column densities, especially in the extended regions JetS and JetN. Compared to the specific intensity extrapolated from single-dish measurement with 1.2 mm MAMBO data (Sandell & Sievers 2004), we estimate that 48% of the flux has been filtered out from IRS1, compared to 90% of flux from NGC 7538 S (Beuther et al. 2012a). This suggests that emission from NGC 7538 S is more extended than that from IRS1, where emission is extremely concentrated toward the central mm continuum peak. In addition, since the fraction of filtered-out flux should be lower in the center than the edge of field of view, uncertainties in column densities are larger in the outflow of NGC 7538 S than in the dense condensations MM1–3.

5. Another simplification in our calculation is an assumed constant beam filling factor. Determination of molecular abundances in the substructures of NGC 7538 S and IRS1 relies upon an accurate source structure model for each molecule. When the source is smaller than the beam size, the main beam brightness temperature is diluted, leading to an under-

estimated brightness temperature. To correct this, an appropriate correction factor Ω_a/Ω_s (the ratio of the solid angle of the antenna beam to that of the source) needs to be applied. Since we do not know the true source sizes, we simply assume that they are 3–5 times larger than the beam consistent with our measurements of the $> 4\sigma$ continuum, so the filling factor is taken as one in all the calculations.

6. However, our assumption that "all molecules being thermalized" and "beam filling being one" may not be co-valid. For example, because of thermalized assumption ($T_{ex} = T_{rot}$), the optically thick molecules (e.g., SO) should have the brightness temperature $T_B \sim T_{ex} \sim T_{rot}$. However, instead of $T_{rot} \sim 150$ K in MM1, the observed brightness temperature of SO in MM1 is measured as $T_B \sim 30$ K, indicating strongly beam dilution. Nevertheless, without higher resolution observations on sub-structures within each condensation of MM1–3 nor precise measurement of each source size, we do not know whether it is the clumpiness or the non-LTE environment of our condensations or the beam dilution that causes this controversy.

3.6 Model

Adjacent condensations MM1–3 resolved in NGC 7538 S have similar H_2 column densities, suggesting their similar timescale of collapse. However, their temperatures and spectral line properties exhibit differentiation along the northeast-southwest direction within $\sim 4\,000$ AU, which we suggest to be an evolutionary sequence from MM1 to MM3. We hypothesise that, MM1 evolves fast, with its large abundance of COMs consistent with being in a HMC phase. In contrast, none detection of most species in MM3 indicates it is in a very early evolutionary stage (e.g., HMSC phase). Clear detection of COMs but generally lower temperatures and molecular abundances in MM2 than in MM1 indicates it to be in an intermediate stage between MM1 and MM3. To verify our hypothesis, we iteratively fit the observed molecular column densities with our 'MUSCLE' ('MUlti Stage CLoud codE') 1-D model, which was earlier successfully applied to fit the rich molecular data from several tens of HMSFRs at various evolutionary stages (Gerner et al. 2014).

3.6.1 Physical model

In a 1-D approximation, we modelled the physical structure of each MM condensation by assuming them to be spherically symmetric, to have a fixed outer radius of $r_{out} = 1\,100$ AU (equal to the size of the PdBI synthesised beam), and to be embedded in large-scale, low-density envelope which shields it from the interstellar Far Ultra Violet (FUV) radiation with a visual extinction of

10 mag. In addition, we define a parameter $r_{\rm in}$ as the inner radius, below which temperature and density are assumed to be constants. The radial densities and temperature profiles are therefore described by broken power laws,

$$\begin{aligned} \rho(r) &= \rho_{\rm in}(r/r_{\rm in})^{-p}, \quad r_{\rm out} \geq r \geq r_{\rm in}; \\ \rho(r) &= \rho_{\rm in}, \qquad\qquad 0 \leq r < r_{\rm in} \end{aligned} \tag{3.3}$$

and

$$\begin{aligned} T(r) &= T_{\rm in}(r/r_{\rm in})^{-q}, \quad r_{\rm out} \geq r \geq r_{\rm in}; \\ T(r) &= T_{\rm in}, \qquad\qquad 0 \leq r < r_{\rm in}, \end{aligned} \tag{3.4}$$

respectively. Here, p and q are the corresponding radial profiles of density and temperature, respectively. The gas and dust are assumed to be in LTE (for an analysis of this assumption, see Section 3.5.4 part 1), so their temperatures are assumed to be the same. In obtaining the best fitting to the observed values, we adjust the parameters p, $\rho_{\rm in}$, $T_{\rm in}$ and $r_{\rm in}$ (Section 3.6.4). To derive the total modelled H_2 column density of a large-scale cloud, we adopt a grid of 40 radial cells and integrate Eq. 3.3 numerically.

3.6.2 Chemical model

The time dependent gas-grain chemical model we adopt in this chapter is based on the 'ALCHEMIC' code[5], which is described in Semenov et al. (2010) and updated in Albertsson et al. (2013). The model is briefly summarised below.

(1) The chemical network is based on the OSU'2007 network[6], and updated by implementing the most recent reaction rates (e.g., from the KIDA database[7], Albertsson et al. 2013).
(2) Both gas-phase and gas-grain interactions are included in this network, which consists of 656 species made of 13 elements, and 7907 reactions in total. In particular, the synthesis of COMs was included using a set of surface reactions (together with desorption energies) and photodissociation reactions of ices (Garrod & Herbst 2006; Semenov & Wiebe 2011).
(3) Cosmic-ray particles (CRP, $\zeta_{\rm CR} = 5 \times 10^{-17}$ s^{-1}) and CRP-induced FUV radiation[8] are considered to be the only external ionising sources.

[5] ALCHEMIC chemical code is based on the double-precision variable-coefficient ordinary differential equation solver with the preconditioned Krylov (DVODPK) method GMRES for the solution of linear systems, http://www.netlib.org/ode/vodpk.f

[6] OSU'2007 network is supplied with a set of ~ 1 000 high-temperature reactions from Harada et al. (2010) and Harada et al. (2012), http://www.physics.ohio-state.edu/ eric/research.html

[7] http://kida.obs.u-bordeaux1.fr

[8] We adopt the UV dissociation and ionization photorates from van Dishoeck et al. (2006) (http://www.strw.leidenuniv.nl/ ewine/photo/), assuming the case corresponding to the spectral shape of the interstellar FUV radiation field.

(4) No chemical parameter (e.g., grains sizes, dust/gas mass ratio, ionization rate, sticking efficiencies, desorption energies, etc.) was varied during the iterative fitting of the observational data.

It is assumed that at sufficiently low temperatures, molecules stick to grain surfaces with 100% probability, except for H_2 because of its binding energy as low as $\sim$ 100 K (Lee 1972). On the surface sites, H and H_2 tunnelling through the potential walls is not considered (Katz et al. 1999). Dissociative recombination is modelled resulting in the ion-ion neutralization and electron attachment on the grains, while chemisorption of surface molecules is not considered. Assuming that each 0.1 μm spherical olivine grain provides $\approx 1.88 \times 10^6$ surface sites for accreting gaseous species, the surface recombination proceeds solely through the Langmuir-Hinshelwood formation mechanism. As temperature increases, the ices are released back to the gas phase by thermal, CRP, and CRP-induced UV-photodesorption (3×10^{-3}, Öberg et al. e.g., 2009). In addition, we assumed that all freshly formed surface molecules have 1% chance to leave the grain surface upon recombination.

3.6.3 Initial abundances

In our modelling, we have assumed that initially MM1, MM2 and MM3 are fragmented from a larger precursor IRDC-like object. Since the MM3 condensation is roughly twice as cold as the other 2 condensations, it seems reasonable to assume that it is less chemically evolved. Thus, to model and fit the chemistry of the condensations, we used a staged scheme: To calculate the chemistry in MM3, the coldest condensation with a peak temperature of $\sim$ 50 K, we first ran a 0-D IRDC model by taking the best-fit IRDC result from Gerner et al. (2014) as the pre-MM3 IRDC-like environment— a T = 15 K isothermal condensation with a hydrogen particle density of 2×10^5 cm^{-3}, age of 10^4 years, and a low initial metallicity (Table 3.3, also see Lee et al. (1998), and Table 7 of Gerner et al. (2014)). For modelling the chemistry in the MM1 and MM2 condensations which are likely at a more advanced evolutionary stage, we used initial abundances which were the same as the final chemical abundances from the best-fit MM3 condensation model (Table 3.5).

3.6.4 Iterative fitting of the data

Using the physical and chemical models described above, we iteratively fitted the mean observed molecular column densities for each 1-D condensation model by varying the inner radius $r_{\rm in}$, the density at the inner radius $\rho_{\rm in}$, the temperature at the inner radius $T_{\rm in}$ and the density slope p subject to the following constraints.
(1) p is restricted to be in a valid range of 1.0–2.5 (Guertler et al. 1991; Beuther et al. 2002;

Table 3.3: Top 35 initial abundances with respect to H for the MM3 condensation.

Species	Abundance	Species	Abundance	Species	Abundance	Species	Abundance
H_2	5.00(−01)	H	9.75(−02)	H	3.77(−04)	C	1.79(−05)
CO	2.35(−05)	N	1.24(−05)	O	8.16(−05)	CH_4 ice	2.63(−05)
H_2O ice	6.79(−05)	NH_3 ice	1.02(−05)	C_3	1.17(−06)	CH_3OH ice	5.39(−06)
CH_4	4.07(−07)	H_2O	9.43(−07)	N_2	7.75(−07)	C_3H_4 ice	3.27(−07)
CO_2 ice	1.43(−07)	N_2 ice	1.62(−07)	CH_2CO	1.43(−08)	CH_2OH	2.11(−08)
CH_3OH	1.35(−08)	CN	1.04(−08)	CO_2	1.85(−08)	e^-	1.96(−08)
HCN	2.41(−08)	HNC	2.36(−08)	NH_3	2.54(−08)	O_2	1.63(−08)
OH	1.16(−08)	S	8.29(−08)	CO ice	1.71(−08)	H_2CO ice	1.77(−08)
HCN ice	1.22(−08)	C^+	1.77(−09)	C_2H	2.05(−09)	[*. x(y) = x × 10^y]	

Mueller et al. 2002; Hatchell & van der Tak 2003).
(2) The appropriate ranges of r_{in} (1–300 AU) and ρ_{in} are derived within the uncertainties of the observed beam-averaged H_2 column densities by a factor of 3.
(3) T_{in} is limited to $30-80$ K for MM3 and to 100–300 K for the MM2 and MM1 condensations, respectively.
By varying the above parameters and fixing the rest (including the temperature profile $q = 0.4$ for a highly optically thick medium, van der Tak et al. 2000), each condensation model realisation consists of 1 000–3 000 1D-models.

We modelled the chemical structures of MM1–3 over 10^5 years (with 99 logarithmic time steps), and calculated the beam-averaged column densities for each observed molecule. The goodness-of-fit (χ^2) in each condensation model at each time step is estimated by using a confidence criterion from Equation 3 in Garrod et al. (2007), where the standard deviation σ for all observed molecules is an order of magnitude between the modelled and the observed column densities. For molecules with only upper limits of the observed column densities, we set the goodness-of-fit to be 0 when the modelled column density was lower than 10 times of the upper limit. Subsequently, a total goodness-of-fit was obtained from the mean value of the confidence criteria for all molecules at a given time step and for a given cloud model. Finally, searching for the lowest total χ^2-value yields the best-fit physical model and the best-fit chemical age. Our best fit parameters for the 3 condensations are shown in Table 3.4. Molecular abundances with respect to H_2 are shown in Figure 3.6, with the black lines representing observed values and the red filled area representing the modelling value, which shows the chemical variations from MM1 to MM3.

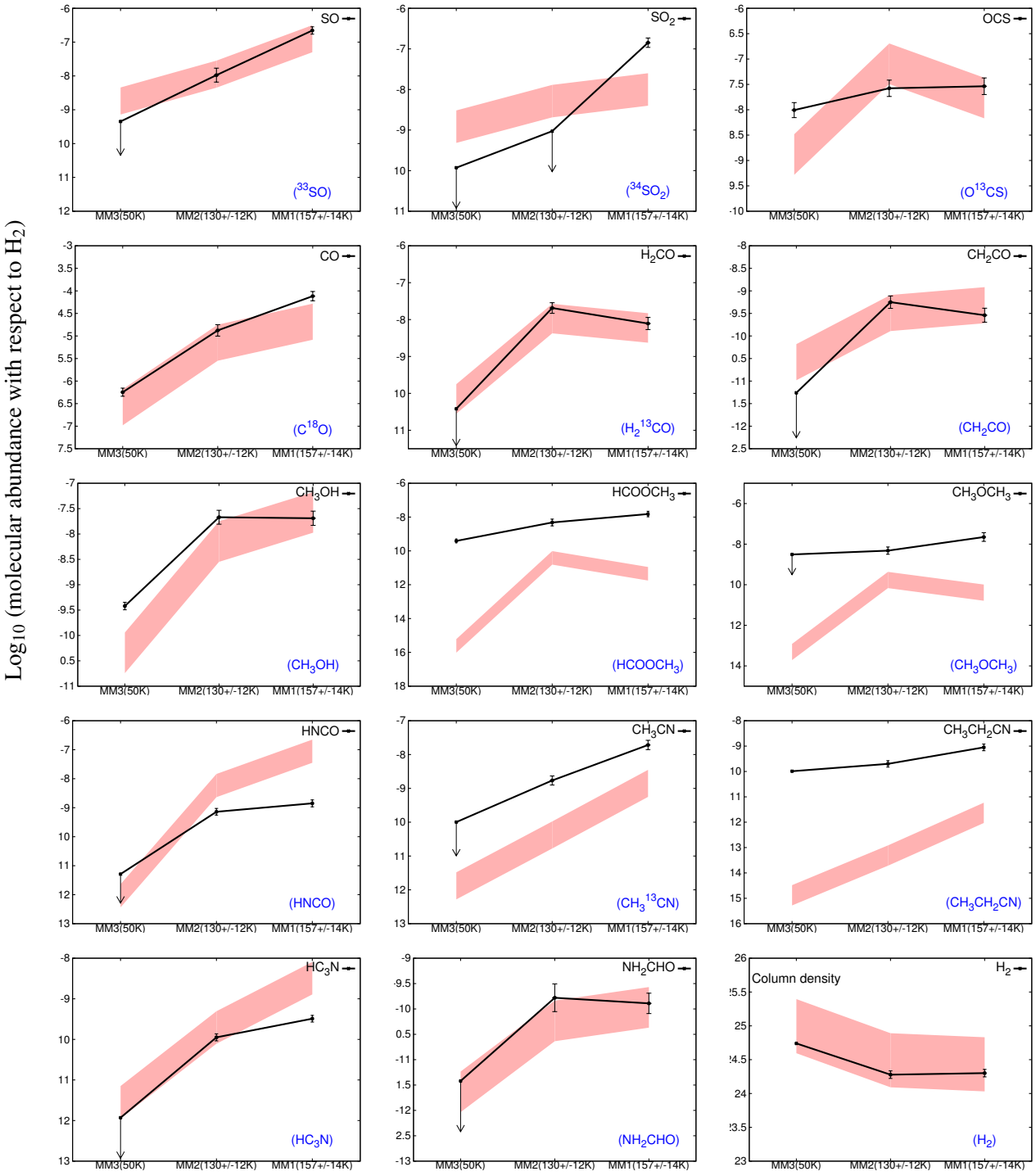

Figure 3.6: Best fit of molecular abundances in MM1-MM3. The last panel shows the best fit of H_2 column density from dust emission. The modelled values and tolerance (0.1-10) are shown as a red filled region, while the observed values are plotted as solid black lines, with the uncertainties determined from T_{rot}, partition function $Q(T_{rot})$, and Gaussian fitting to $\int T_B(\upsilon)d\upsilon$. Abundances of molecules (name in black at the upper-right corner of each panel) are derived either from their detected rare isotopologues or from optically thin assumption (name in blue in parentheses at the lower-right corner of each panel).

Table 3.4: Best fit physical parameters of NGC 7538 S-MM1–MM3 from 1-D gas-grain model.

Parameter	Symbol	MM3	MM2	MM1
Inner radius	$r_{\rm in}$	3.7 AU	1.1 AU	1.1 AU
Outer radius	$r_{\rm out}$	1100 AU[a]	1100 AU[a]	1100 AU[a]
Density within the inner radius	$\rho_{\rm in}$	1.01×10^{13} cm^{-3}	1.1×10^{11} cm^{-3}	6.1×10^{12} cm^{-3}
Density beyond the outer radius	$\rho_{\rm out}$	1.2×10^{8} cm^{-3}	1.1×10^{8} cm^{-3}	4.8×10^{7} cm^{-3}
Density profile	p	2.0	1.0	1.7
Beam-averaged density	$\bar{\rho}$	4.7×10^{9} cm^{-3}	4.1×10^{8} cm^{-3}	8.7×10^{8} cm^{-3}
Temperature within the inner radius	$T_{\rm in}$	59.4 K	229.2 K	278.6 K
Temperature beyond the outer radius	$T_{\rm out}$	10.0 K	14.5 K	17.6 K
Temperature profile	q	0.4	0.4	0.4
Beam-averaged temperature	$\bar{T}$	14.1 K	20.6 K	28.5 K

a. This value is limited by the 0.4″ PdBI synthesised beam size used in our observations.

3.6.5 Uncertainties of the fitting

Table 3.5 and Figure 3.6 show that 60%-70% of the modelled molecular column densities agree with the observed values (with the tolerance $N_{Modeled}/N_{Observed}$=0.1-10). Uncertainties may come from the following reasons:

1. To estimate the observational column densities of the detected molecules, we assume the molecules that have no detection of rare isotopologues (marked with red † in Table 3.5) in our data to be optically thin. As discussed in Section 3.5.4, this assumption may lead to the observational column densities underestimated by a factor of 1 magnitude, which may explain the disagreement of model fitting to such molecules as HC_3N and HNCO.

2. In Table 3.5, we derived the observed column densities of the main S-bearing isotopologues (e.g., SO and SO_2) from their detected rare isotopologues by assuming constant intrinsic ratios in the local ISM similar to those in solar system (e.g., $^{32}S/^{33}S$ = 127, $^{32}S/^{34}S$ = 22, Lodders 2003). As mentioned in Section 3.5.4, the differences of the element ratios between solar system and NGC 7538 local region may lead to the uncertainties of molecular column densities especially the upper limit of none detections, which is unable to be given in this chapter and causes the disagreement of the fitting.

Molecule	MM3		MM2		MM1		Notes on the Observed Values
	$N_{Observed}$ (cm^{-2})	$N_{Modeled}$ (cm^{-2})	$N_{Observed}$ (cm^{-2})	$N_{Modeled}$ (cm^{-2})	$N_{Observed}$ (cm^{-2})	$N_{Modeled}$ (cm^{-2})	
H_2	5.53 ± 0.23(24)	9.9(24)	1.90 ± 0.27(24)	3.1(24)	1.95 ± 0.27(24)	2.7(24)	derived from dust continuum
CO	3.13 ± 0.57(18)	2.6(18)	2.53 ± 0.39(19)	2.2(19)	1.51 ± 0.13(20)	5.6(19)	derived from $C^{18}O$ with $^{16}O/^{18}O$ = 607[a]
H_2CO	≤ 2.11(14)	7.0(14)	3.89 ± 0.76(16)	3.3(16)	1.52 ± 0.39(16)	1.6(16)	derived from $H_2^{13}CO$ with $^{12}C/^{13}C$ = 73[a]
CH_3OH †	2.13 ± 0.29(15)	4.5(14)	4.06 ± 0.73(16)	2.2(16)	4.01 ± 0.76(16)	7.2(16)	
$HCOOCH_3$ †	2.13 ± 0.56(15)	2.4(09)	9.17 ± 3.30(15)	1.2(14)	2.97 ± 0.75(16)	1.2(13)	
CH_2CO †	≤ 3.01(13)	2.6(14)	1.06 ± 0.19(15)	1.0(15)	5.68 ± 1.31(14)	1.3(15)	
OCS	5.45 ± 1.91(16)	1.3(16)	4.99 ± 1.22(16)	2.5(17)	5.63 ± 1.44(16)	4.6(16)	derived from $O^{13}CS$ with $^{12}C/^{13}C$ = 73[a]
SO	≤ 2.52(15)	1.8(16)	2.00 ± 0.76(16)	3.5(16)	4.30 ± 0.45(17)	3.4(17)	derived from ^{33}SO with $^{32}S/^{33}S$ = 127[b]
SO_2	≤ 6.51(14)	1.2(16)	≤ 1.78(15)	1.6(16)	2.79 ± 0.34(17)	2.7(16)	derived from $^{34}SO_2$ with $^{32}S/^{34}S$ = 22[b]
HC_3N †	≤ 6.46(12)	2.8(13)	2.14 ± 0.10(14)	6.1(14)	6.27 ± 0.24(14)	8.7(15)	
CH_3CH_2CN †	5.66 ± 0.21(14)	1.3(10)	3.77 ± 0.69(14)	1.5(11)	1.75 ± 0.29(15)	6.3(12)	
HNCO †	≤ 2.84(13)	9.1(12)	1.36 ± 0.16(15)	1.8(16)	2.78 ± 0.37(15)	2.4(17)	
CH_3CN	≤ 5.59(14)	1.3(13)	3.25 ± 0.56(15)	1.3(14)	3.75 ± 0.84(16)	3.8(15)	derived from $CH_3^{13}CN$ with $^{12}C/^{13}C$ = 73[a]
NH_2CHO †	≤ 2.09(13)	2.3(13)	3.17 ± 1.94(14)	1.8(14)	2.53 ± 0.93(14)	2.9(14)	
$?CH_3OCH_3$ †	≤ 1.72(16)	4.8(11)	8.97 ± 2.66(15)	5.3(14)	4.37 ± 1.77(16)	1.1(14)	
Agreement		10/15 = 67%		9/15 = 60%		9/15 = 60%	Tolerence: $N_{Modeled}/N_{Observed}$=0.1-10
Chemical Age		10200 yrs		10210 yrs		10660 yrs	

a. derived from galactic local isotope ratio (Giannetti et al. 2014);
b. derived from isotope ratio in solar system (Lodders 2003).

Table 3.5: Best fit results of NGC 7538 S-MM1–MM3 from 1-D gas-grain model, with column densities inconsistent with the model predictions in red ($N_{Modeled}/N_{Observed} < 0.1$ or > 10). Uncertainties of the observed value are determined from T_{rot}, partition function $Q(T_{rot})$, and Gaussian fitting to $\int T_B(\upsilon)d\upsilon$. For the molecules which do not have rare isotopologues (marked with "†"), we derive their values by assuming they are optically thin.

3. Comparing $N_{observed}$ to $N_{modelled}$, SO_2 is at least 1–2 magnitude lower in MM3 and MM2 from observation than from modelling, while 1 magnitude higher from observation in MM1. The enhancement of gas phase SO_2 in MM1 may come from stronger shocks in the source, which is produced by outflows only detected in MM1. This may also explain the slightly enhanced of SO in MM1 compared to MM3 (indicated by the rising slopes in Figure 3.6).

4. Our simplistic 1-D model is limited in fitting the observations by the following circumstances. (1) Although the modelled r_{out} is simply taken as the size of PdBI synthesised beam, we do not know the size of each condensation, so the uncertainties from Eq. 3.3 and Eq. 3.4 can not be obtained. (2) Of all the three condensations, we model MM3 first, and take the best fitting result of this condensation as the earliest star forming phase, from which MM2 and MM1 have evolved. However, 9/15 of the molecules are not detected, so we must estimate the upper limit of their column densities from the measured 3σ rms. Without the precise molecular quantities in the earliest phase (e.g., CH_2CO, SO_2, HC_3N, HNCO, CH_3CN, CH_3OCH_3), it is difficult to constrain their abundances in more evolved phases. (3) The formation of COMs are modelled by a set of surface reactions and photodissociation reactions of ices in the framework of two-phase chemical model, so the disagreement of the modelled abundances to the observations (e.g., $HCOOCH_3$, C_2H_5CN, CH_3CN, CH_3OCH_3) may indicate that more complex chemical processes or better description of surface processes are needed to improve the gas-grain model. (4) The 1-D model fits are based on the assumption of spherically-symmetric sources, however, velocity gradients across MM1 and MM2 indicate rotation in both condensations (Beuther et al. 2012a). Therefore, 2-D disk-like structure may be more appropriate for these sources.

3.7 Discussion

The presented observations comprise a large set of molecular lines (over 90 lines from 15 species, including 21 isotopologues) from PdBI with high resolution (0.4″) at 1.3 mm toward the HMSFRs NGC 7538 S and IRS1. Resolving NGC 7538 S into at least 3 condensations and by grouping the S-, N- and O-bearing molecules, we find strong chemical variation over the observed condensations.

3.7.1 Comparison with the other results

Combined with the model fitting, this is the first comprehensive chemical study of NGC 7538 S and IRS1 on small scales. Compared to the previous studies with low spatial resolution that do not resolve the individual substructures studied here, our observations obtained at the high spatial resolution of ~ 1 000 AU reveal quantitatively chemical differences among these adjacent substructures.

All of the three resolved condensations of NGC 7538 S (MM1–3) have H_2 column density as high as 1–5 $\times$ 10^{24} cm^{-2}, which are consistent with the observation and simulation results from Naranjo-Romero et al. (2012). In addition, we note that lines of 7 molecules ($C^{18}O$, H_2CO, CH_3OH, OCS, SO, HNCO and CH_3CN) are also covered by observations in Gerner et al. (2014), where a large sample chemical study on different evolutionary stages of HMSFRs was conducted. Abundances of these molecules in MM1 and MM2 all quantitatively agree with the statistic abundance range in HMC and HMPO cases respectively, given by the aforementioned literature. Although the (upper limit) abundances of $C^{18}O$, H_2CO and HNCO in MM3 from our observations are lower than those for IRDCs in Gerner et al. (2014) by orders of of 2-3 magnitude, $C^{18}O$ and H_2CO fit well with our 1-D model (Section 3.6.4), and the abundance of the remaining 4/7 molecules are consistent within the given statistic IRDC range, which supports our hypothesis that MM3 is still a HMSC.

In IRS1, we obtain the rotation temperature from the CH_3CN ladder only at the off-peak position (mmS), and find it to be lower than the value derived from Knez et al. (2009); Qiu et al. (2011); Zhu et al. (2013) by a factor of 2 (discussed in Section 3.5.4 part 1). Nevertheless, the (lower limit) column densities of HNCO, ^{13}CO and CH_3CN at the continuum peak estimated by these different T_{rot} agree. In particularly, CH_3CN abundance with respect to thermal-dust H_2 emission in IRS1 calculated from our observations (~ 10^{-10}) agree with the typical abundance in HMC (Hatchell et al. 1998; Chen et al. 2006; Zhang et al. 2007). Furthermore, IRS1 appears to be more evolved than MM1, due to the following reasons: (1) Since free-free emission dominates the continuum of IRS1, we derive the molecular abundances with respect to H_2 in this source on the reliable assumption that $N_{C^{18}O}/N_{H_2} = 1.64 \times 10^{-7}$ (this agrees with $N_{C^{18}O}/N_{H_{2,1}} = 1.27 \times 10^{-7}$ in MM1 as typical HMC, Table B3II). On this assumption, the lower limits of COMs (CH_3OH, and CH_3OCH_3) have their abundances in the peak of IRS1 higher than in MM1 by a factor of more than 3. (2) There are more COM line detections in mmS than in MM1 (Table B1). (3) From the fact that IRS1 has the highest luminosity in NGC 7538 region (Scoville et al. 1986), and that a evolution tendency appears from NE to SW of this region (McCaughrean et al. 1991), IRS1 is also suggested to be the most evolved source in NGC 7538.

3.7.2 Hierarchical fragmentation in NGC 7538 S: synthesis of observations and models

The three resolved condensations are separated on the order of 3 800–5 000 AU in the large-scale gas clump NGC 7538 S, so chemistry is particularly useful for distinguishing between their evolutionary stages at small scale. By analysing the continuum and molecular spectrum of each condensation, we find that condensations close to each other have continuum emission very similar in sizes and in column densities. Since they are embedded in the same clump, if their fragmentation is due to global collapse, they should have a similar physical age. However, the significant variation of molecular line intensities and abundances among them may imply an evolutionary gradient from MM1 through MM2 to MM3. High temperature (> 150 K), high optical depth and high abundance of COMs all characterise MM1 as a typical HMC. Consistent with our observations, the presence of bright IR emission suggests that this condensation is at a relatively more evolved stage compared to many other HMCs (e.g., Chen et al. 2006; Zhang et al. 2007; Girart et al. 2009; Qiu & Zhang 2009). Southwest of MM1 are MM2 and MM3, which have no radio emission detected from VLA (Wright et al. 2012), suggesting that they are in early protostellar phases. In particular, as MM2 exhibits strong emission from less excited molecules close to (e.g., H_2CO, CH_3OH, $HCOOCH_3$, OCS) or even higher than (e.g., $H_2^{13}CO$, CH_2CO, NH_2CHO) those in MM1, it should be more evolved than MM3, where these lines are barely detected. As a result, we suggest MM2 could be in the HMPO stage while MM3 is still a cold HMSC.

Admittedly, our 1-D gas-grain model is limited in its ability to reproduce our observations (60%-70% agreement, as discussed in Section 3.6.5) and in explaining all the MM2-peaking molecules (it provides a good fit to $H_2^{13}CO$ but not to CH_2CO or NH_2CHO). Analytically, in the frame of gas-grain model of Garrod et al. (2008), gas-phase abundances of 18 MM1-peaking isotopologues in our dataset increase as the hot core gradually warms-up. In contrast, after reaching their maximum at certain temperature, gas-phase abundances of H_2CO and CH_2CO start to decrease as the temperature increases, and NH_2CHO appears, see Figure 8(d) of Garrod et al. (2008). CH_2CO is commonly expected to be formed on grains by repetitive hydrogenation in significant quantities during the cold phase; but once the evaporation starts at low temperature ($\sim$ 40 K), the survival of gas-phase CH_2CO is dependent on the abundance of CH_2O in the gas phase. $H_2^{13}CO$ is an isotopologue of H_2CO, and it can more precisely indicate the abundance differentiation among substructures because H_2CO is optically thick. Both H_2CO and $H_2^{13}CO$ are thought to originate from grain-surface chemistry through successive hydrogenation of carbon monoxide (CO and ^{13}CO) at low temperature, (Hiraoka et al. 2002; Watanabe et al. 2004), and then to interact with other radicals to produce more complex molecules (e.g., CH_3OH, $HCOOCH_3$ and CH_3OCH_3). These molecules are suggested to be good tracers of the low temperature gas in the cold envelope surrounding NGC 7538 S (Bisschop et al. 2007). In the same way, gas-phase NH_2CHO is formed by the reaction of evaporated H_2CO and NH_2 when the con-

densation is > 40 K, then it becomes an important contributor of HCO radicals when it is later destroyed (Kahane et al. 2013). As the condensation warms up, it can be destroyed via hydrogen abstraction on the grain-surface prior evaporation, or via its CR-induced photodissociation later in the gas-phase, appearing two peaks in Garrod et al. (2008).

In light of the above quantitative (1-D) and analytical Garrod et al. (2008) gas-grain models, we adopt the terminology of "chemical warm-up timescale" (the period over which the temperature of a source increases from the initial 10–20 K to > 100 K[9], Garrod et al. 2008) and derive a general picture of hierarchical fragmentation in NGC 7538 S. Although whether MM1–3 formed from a massive and unstable rotating torus, or from a dusty core that fragmented into multi protostars is still debated (Corder 2009; Wright et al. 2012; Naranjo-Romero et al. 2012), both scenarios will lead to the condensations having a similar "physical age" (collapsing simultaneously). However, the different condensations are not completely synchronised (differences in the chemical age are not large but $\sim$ 10–10^2 years in our 1-D fitting) Slight variations caused by mechanisms like turbulence, gravitational potential, magnetic fields, etc (Ballesteros-Paredes et al. 2007). make difference in the ignition and by that the different warm-up timescales. In this picture, MM1 warms up faster than MM2 and MM3. At a certain physical age ($\sim$ 10^4 years in our 1-D fitting), when the abundances of H_2CO, CH_2CO, and NH_2CHO reach their maximum in MM2 with medium speed, their abundances start to decrease in MM1 because they are reacting to form more complex daughter molecules, while MM3 is still in the least evolved phase and most of the molecules are still on the grain surfaces due to its slowest warm-up speed. In addition, because of its low temperature, the large molecular optical depths due to denser dust results in MM3 having the weakest line emissions.

3.7.3 The absorption and emission feature in IRS1

In contrast to the resolved fragmentation of NGC 7538 S, IRS1 remains an unresolved compact core at 1.3 mm, with much higher intensities of both continuum and lines in it than in NGC 7538 S. From H_2 column density estimated by $C^{18}O$, we can estimate the thermal dust emission at the continuum peak corresponds to $\sim$ 0.024 Jy beam^{-1}, which is 1.2% of the interferometric observed emission, and the rest can be attributed to the free-free emission. Since the size of the 5σ contours of the continuum is similar to the beam size, free-free emission can be assumed around 98.8% of the total flux, which is $\sim$ 2.59 Jy of 2.76 Jy. This corresponds to 2.72 Jy free-free emission at 843 μm band (assuming the spectral index of -0.1 from the total flux

[9]In fact, the whole process is more complicated than just the increase of the temperature. When an IRDC is forming, it may initially be warmer, ~20 K, and then it cools off as it becomes denser to T ~10 K (in the center). When collapse begins, T rises from 10 to > 100 K. (Garrod et al. 2008) has found T(t) $\sim$ t^2 in their 0-D models, while we found T rises exponentially with time in the center of the source in our 1-D model.

in the same area of 2.82 Jy). Considering that the total flux being filtered out is the same at both 843 μm and 1.3 mm, we find the thermal dust flux increases with frequency as $\sim \nu^{4.2}$. However, without knowing the the turnover frequency of free-free optically thin/thick region, this is a only a rough estimation.

One interesting feature of IRS1 at 1.3 mm is the existence of generally strong absorption lines within 0.4″ of the continuum peak. This has been noted by previous kinematics studies (Wilson et al. 1983; Henkel et al. 1984; Sandell et al. 2009; Qiu et al. 2011; Beuther et al. 2012a, 2013a; Zhu et al. 2013), with the most popular explanation for the absorption being an inverse P-cygni feature indicating rotation and infalling gas on a disk around the source. However, whether the protostellar disk is face-on (Kawabe et al. 1992; Beuther et al. 2013a) or edge-on (e.g., Pestalozzi et al. 2004; Lugo et al. 2004; De Buizer & Minier 2005; Knez et al. 2009), and whether the direction of the associated outflow is perpendicular (e.g., De Buizer & Minier 2005; Knez et al. 2009; Zhu et al. 2013) or along (e.g., Beuther et al. 2013a) our line of sight or precessing (e.g., Kraus et al. 2006) is debated.

Although the spectrum from the strong continuum peak of IRS1 is dominated by absorption lines, there are at least four strong lines exhibiting purely emission (marked with "?"). Because these lines are also detected in NGC 7538 S MM1 and mmS, we fit them by the synthetic spectrum programme and map their spatial distribution in NGC 7538 S (Figure 3.7) and IRS1 (Figure 3.8). We suggest three of them (at 217.299 GHz, 217.643 GHz and 217.886 GHz) are CH_3OH transitions (FWHM $\sim$ 5 km s^{-1}). In addition, a transition of CH_3OH from separate higher frequency observations (at 356.007 GHz, Beuther et al. 2013a) also exhibits emission at the continuum peak of IRS1. We note that these four CH_3OH transitions have excitation temperature $E_u/k_B > 250$ K (2 are torsionally excited ($\nu_t = 1$) and 2 are in the vibration ground state ($\nu_t = 0$)), while the other two absorption E-CH_3OH lines are in the vibration ground state and have $E_u/k_B < 100$ K (Table 3.6).

In addition, we note that some $HCOOCH_3$ transitions also show tentatively ($\sim 3\sigma$ rms) pure emission in IRS1 continuum peak, marked in Table B1 and shown in Figure B1. Compare to CH_3OH, their emissions are weaker, so we do not discuss them in detail, but 8/10 of reliable pure emission $HCOOCH_3$ are torsionally excited ($\nu_t = 1$) with $E_u/k_B > 250$ K, so it is likely that they have the similar origin as CH_3OH pure emission in IRS1 peak. However, as all the other detected lines exhibit absorption at the peak (including 15/42 transitions which also have $E_u/k_B > 250$ K), it is not immediately clear why only these CH_3OH (and $HCOOCH_3$) lines appear in pure emission.

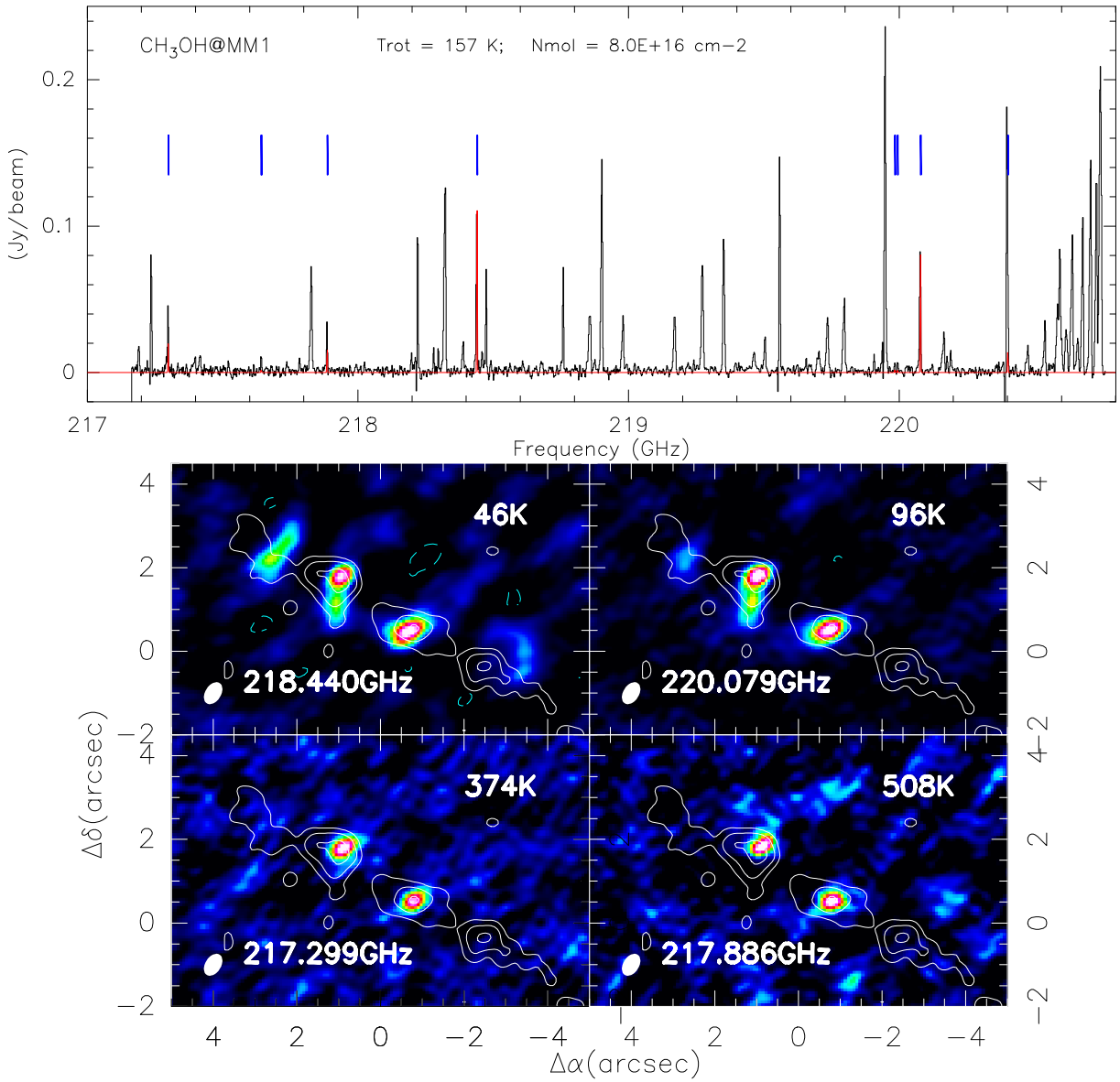

Figure 3.7: The upper panel shows synthetic spectrum fitting of CH_3OH in MM1. The black histogram is the observed spectrum, overlaid with the fit from the input parameters listed on top of the panel. Blue lines mark transition frequencies, and confirm that the UL at 217.299 GHz, 217.643 GHz, 217.886 GHz are CH_3OH. The lower panel presents maps of the line wing excluded intensity integrated over the velocity range from -65 to -50 km s^{-1} ($V_{lsr} \sim -60$ km s^{-1} in MM1), with dashed green contours showing $-\sigma$ rms. White contours show the continuum (at 4σ, 14σ, and 24σ levels).

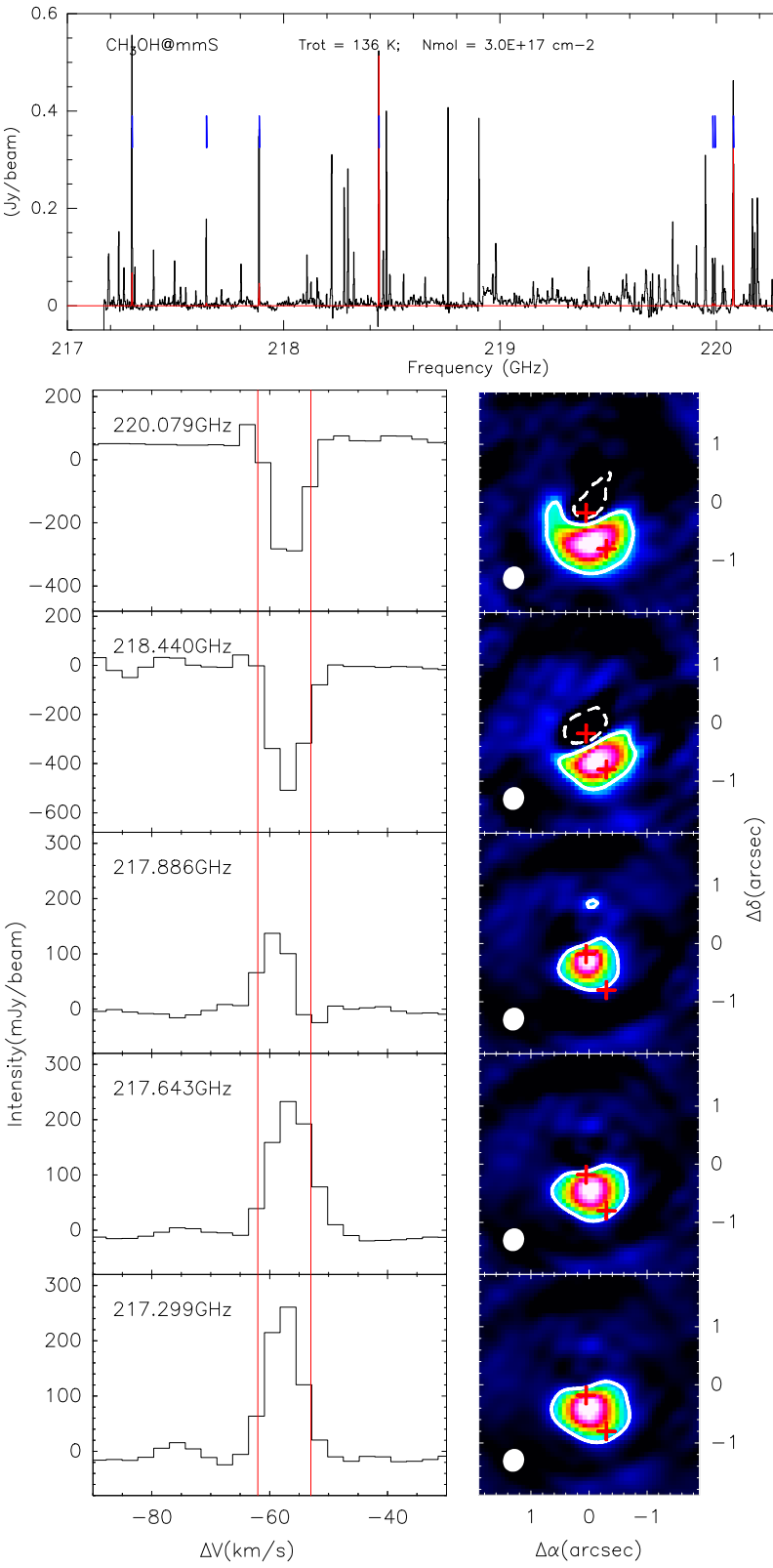

Figure 3.8: The upper panel shows synthetic spectrum fitting of CH_3OH in mmS. The black histogram is the observed spectrum, overlaid with the fit from the input parameters listed on top of the panel. Blue lines mark transition frequencies, and confirm that the UL at 217.299 GHz, 217.643 GHz, 217.886 GHz are CH_3OH. The lower panel presents maps of the line wing excluded intensity integrated over the velocity range from -63 to -53 km s^{-1} ($V_{lsr} \sim -58$ km s^{-1} at the continuum peak). Red cross mark the continuum peak position and mmS, and the white solid (dashed) contour show $\pm 4\sigma$ rms level of molecule.

Table 3.6: The detected CH_3OH lines ("*" from Beuther et al. (2013a)), with parameters from CDMS

ν (MHz)	Transition	E_u/k_B (K)	
217299	$\nu_t = 1(6_{1,5} \rightarrow 7_{2,6}A--)$	374	emission
217643	$\nu_t = 1(15_{6,9} \rightarrow 16_{5,12}A++)$	746	emission
	$\nu_t = 1(15_{6,10} \rightarrow 16_{5,11}A--)$		
217886	$\nu_t = 0(20_{1,19} \rightarrow 20_{0,20}E)$	508	emission
218440	$\nu_t = 0(4_{2,2} \rightarrow 3_{1,2}E)$	46	absorption
220079	$\nu_t = 0(8_{0,8} \rightarrow 7_{1,6}E)$	96	absorption
356007*	$\nu_t = 0(15_{1,14} \rightarrow 15_{0,15}A-+)$	295	emission

As IRS1 is unresolved in our observations, multiple components may contribute to the spectrum along the single line of sight. Therefore, in light of the blue/red-shifted profile studied in Beuther et al. (2013a), one hypothesis for the simultaneous pure absorption and emission seen in the spectrum is, the outflow penetrates the envelope, producing a collimated, jet-like cavity along the line of sight, where transitions with higher E_u/k_B from the inner hot core are detected in emission; while the other lines of CH_3OH with lower E_u/k_B are produced outside of the cavity, and are absorbed by the colder envelope. However, the velocity resolution of our data (2.66 km s^{-1}) did not reveal a velocity offset, which might be expected in this hypothesis (Figure 3.8).

Apart from an unlikely effect of the source geometry, another explanation is non-LTE or maser emission in these transitions. The strong compact continuum radiation of IRS1 (having a certain brightness temperature) can excite most gas lines with lower E_u/k_B, and pump them up to the upper level of their rotational transitions. Since the energy here has been used to push the molecules to upper states, this part of the continuum at certain line frequency is then weaker than in the surrounding continuum, and hence one sees an absorption line. Such effects have been found especially towards UCHII region peaks (e,g., NH_3, Hofner et al. 1999), where blue- and red-shifted absorption can be interpreted as absorption of outflowing and infalling gas, respectively, with respect to the (ionised) continuum gas. In contrast, for CH_3OH lines, as their E_u/k_B increases, population inversion can occur leading to maser emission. CH_3OH masers are traditionally classified into two groups (Menten 1991): collisionally pumped (Cragg et al. 1992) Class I and radiatively pumped Class II (Sobolev et al. 2007 and references therein, Cragg et al. 2005). Class I masers appear to trace shocks from molecular outflows and jets during the earliest stages of star formation (Plambeck & Menten 1990; Sutton et al. 2004; Voronkov et al. 2006). Class II masers are typically associated with hot molecular cores, and hypercompact HII regions (e.g.,Minier et al. 2001; Ellingsen 2006), where strong free-free emission in some cases dominates the dust emission up to frequencies as high as 300 GHz (Kurtz 2005; Sobolev et al. 2007).

Although there are no other observations confirming which class of masers our observed CH_3OH emission lines (2 in the ground state and 2 that are torsionally excited) are likely to be, centimeter large scale (FWHP $\sim 43''$) observations of IRS1 suggests a different torsionally excited CH_3OH emission line ($9_2 \rightarrow 10_1$A+) to be a probable Class II maser (Wilson et al. 1984), and another torsionally excited CH_3OH absorption line ($10_1 \rightarrow 11_2$A+) not to be in LTE (Menten et al. 1986). Therefore possibilities that "quasi masering"[10] induces the emissions from torsionally excited CH_3OH can not be ruled out.

Overall, the simultaneous presence of both pure emission and absorption (and inverse P-Cygni) features in the spectrum of IRS1 continuum peak remains a mystery. It may result from geometrical reason (a collimated outflow cavity in the line of sight) of this HMSFR, and/or may come from the special physical state of CH_3OH regarding the radiative transfer (energy states at the verge of masering due to high E_u/k_B). Therefore, high resolution observations are required in the future to resolve such mystery.

3.8 Conclusions

This is the first comprehensive (model-observation) study on the chemistry of two high mass disk candidates NGC 7538 S and IRS1, which illustrates the strength of chemical analysis for interpreting HMSFRs. Below, we summarise the results from our observations and model fitting:

1. IRS1 is the most evolved hot core in all the regions of NGC 7538 S studied here. From its unique spectra at the continuum peak, non-LTE is suggested to interpret the primarily absorption lines, and population inversion may indicate a small number of pure emission lines (e.g., CH_3OH, $HCOOCH_3$) in this region.

2. At a spatial resolution of $< 1\,000$ AU, NGC 7538 S is resolved into at least three condensations, with similar continuum specific intensities but significant differences in the chemical composition of each condensation. Combining the observation and 1-D gas-grain model fitting results, we suggest an evolutionary sequence along the northeast-southwest filament within $\sim 5\,000$ AU. Such hierarchical fragmentation is not caused by the unsynchronised collapse of the core but by different paces of heating from their internal protostars. With a similar collapse timescale for each other, Our chemical model suggests that MM1 ignites fast and shortens its warm-up timescale, making it the most evolved source as a HMC; while MM2 has the medium warm-up timescale and is in the HMPO stage; and the source

[10] A non-LTE status of the line with high E_u/k_B, which can be detected in much lower temperature environment (than E_u/k_B) because of certain pumping mechanism.

slowest to evolve is MM3, which probably has not warmed-up yet, and is still a cold HMSC. Although the chemical histories of MM1–3 are not the same, the differences in their chemical ages are small, which suggest that the warm-up ($\sim 10^4$–10^5 years) through the different stages characterised by these chemistries is rapid.

3. Although our 1-D gas-grain model does not agree well with the observations of COMs in MM1–3 because of the intrinsically weak nature of these lines (especially in MM3) and the limitations of this network in dealing with more complex chemistries, its performance is improved for less complex species. Our model successfully fits 6/9 of the molecules with < 6 atoms. More precise fitting will require constraints on the observational uncertainties and a more complex (2-D, 3-D) model.

3.9 Appendix

Table B1: Identified lines from PdBI dataset.

Freq. (GHz)	Mol.	E_u/k_B (K)		Freq. (GHz)	Mol. (candidates)	E_u/k_B (K)	
217.19 ± 0.01	UL		2.2?	217.191	$CH_3OCH_3(22_{4,19} - 22_{3,20})$A(E)A(E)	253	
				217.194	g − $(CH_2OH)_2(17_{4,14}\nu = 1 \rightarrow 16_{3,13}\nu = 1)$	83	
				217.194	$HCOOCH_{3(\nu=0)}(30_{4,26} \rightarrow 30_{3,27})$E	291	
217.216	$HCOOCH_{3(\nu=0)}(32_{9,24} \rightarrow 32_{8,25})$A	368	1.3				
217.236	$HCOOCH_{3(\nu=0)}(32_{9,24} \rightarrow 32_{8,25})$E	368	1.3∗				
217.239	DCN(J = 3 → 2)	21	†				
217.3 ± 0.01	UL		2.2?	217.300	$CH_2^{13}CHCN(23_{5,19} \rightarrow 22_{5,18})$	178	
				217.301	$CH_2^{13}CHCN(23_{5,18} \rightarrow 22_{5,17})$	178	
				217.290-217.307	^{13}CN(N = 2 − 1)	16	
				217.299	$CH_3OH_{(v_t=1)}(6_{1,5} \rightarrow 7_{2,6} - -)$	374	
217.313	$HCOOCH_{3(\nu=1)}(17_{4,13} \rightarrow 16_{4,12})$A	290	1.2				
217.64 ± 0.01	UL		2.2?	217.639	$^{13}CH_3CH_2CN(25_{1,24} \rightarrow 24_{1,23})$	139	
				217.642	$CH_2CH^{13}CN(23_{4,19} \rightarrow 22_{4,18})$	160	
				217.646	$CH_2^{13}CHCN(23_{14,9} \rightarrow 22_{14,8})$	533	
				217.646	$CH_2^{13}CHCN(23_{14,10} \rightarrow 22_{14,9})$	533	
				217.633-217.640	^{13}CN(N = 2 − 1)	15	
				217.643	$CH_3OH_{(v_t=1)}(15_{6,10} \rightarrow 16_{5,11} - -)$	746	
				217.643	$CH_3OH_{(v_t=1)}(15_{6,9} \rightarrow 16_{5,12} + +)$	746	
217.833	$^{33}SO(6_5 \rightarrow 5_4)$	35	†				
217.89 ± 0.005	UL		2.2?	217.886	$CH_3OH_{(v_t=0)}(20_{1,19} \rightarrow 20_{0,20})$	508	
				217.889	$CH_2CH^{13}CN(23_{14,9} \rightarrow 22_{14,8})$	544	
				217.889	$CH_2CH^{13}CN(23_{14,10} \rightarrow 22_{14,9})$	544	
				217.895	$^{13}CH_2CHCN(23_{1,23} \rightarrow 22_{0,22})$	121	
218.108	$HCOOCH_{3(\nu=1)}(17_{4,13} \rightarrow 16_{4,12})$E	290	1.2				
218.198	$O^{13}CS(18 \rightarrow 17)$	99	3∗ †				
218.222	$H_2CO(3_{0,3} \rightarrow 2_{0,2})$	21					
218.260	$HCOOCH_{3(\nu=0)}(31_{9,23} \rightarrow 31_{8,24})$A	349	1.3				
218.281	$HCOOCH_{3(\nu=0)}(17_{3,14} \rightarrow 16_{3,13})$E	100	2.2				
218.298	$HCOOCH_{3(\nu=0)}(17_{3,14} \rightarrow 16_{3,13})$A	100	2.2				
218.325	$HC_3N_{(\nu=0)}$(J = 24 → 23)	131	†				
218.390	$C_2H_5CN_{(\nu=0)}(24_{3,21} \rightarrow 23_{3,20})$	140	3 †				
218.440	$CH_3OH_{(\nu=0)}(4_{2,2} \rightarrow 3_{1,2})$	46	†				
218.460	$NH_2CHO(10_{1,9} \rightarrow 9_{1,8})$	61	†				
218.476	$H_2CO(3_{2,2} \rightarrow 2_{2,1})$	68	†				
218.585	$HCOOCH_{3(\nu=0)}(36_{9,28} \rightarrow 36_{8,29})$A	450	2.2∗				
218.593	$HCOOCH_{3(\nu=0)}(27_{7,21} \rightarrow 27_{5,22})$A	258	2.2∗				
218.607	$HCOOCH_{3(\nu=0)}(36_{9,28} \rightarrow 36_{8,29})$E	450	2.2∗				
218.633	$HCOOCH_{3(\nu=0)}(27_{7,21} \rightarrow 27_{5,22})$E	258	2.2∗				
218.655	$HCOOCH_{3(\nu=1)}(18_{16,2} \rightarrow 17_{16,1})$E	460	1.3				
218.738	$HCOOCH_{3(\nu=1)}(18_{14,4} \rightarrow 17_{14,3})$E	419	2.3				
218.760	$H_2CO(3_{2,1} \rightarrow 2_{2,0})$	68					
218.831	$HCOOCH_{3(\nu=1)}(18_{13,5} \rightarrow 17_{13,4})$E	401	1.3				
218.861	$HC_3N_{(v_7=1)}$(J = 24 → 23,l = 1e)	452	†				
218.903	$OCS_{(\nu=0)}(18 \rightarrow 17)$	100	†				
218.966	$HCOOCH_{3(\nu=1)}(18_{12,6} \rightarrow 17_{12,5})$E	384	1.3				
218.981	$HNCO_{(\nu=0)}(10_{1,10} \rightarrow 9_{1,9})$	101	†				
219.068	$HCOOCH_{3(\nu=1)}(18_{17,2} \rightarrow 17_{17,1})$E	481	2.2∗				
219.079	$HCOOCH_{3(\nu=1)}(28_{3,25} \rightarrow 28_{2,26})$E	434	2.2∗				
219.090	$HCOOCH_{3(\nu=0)}(34_{7,28} \rightarrow 34_{5,29})$E	388	2.2∗				
219.109	$HCOOCH_{3(\nu=0)}(34_{7,28} \rightarrow 34_{5,29})$A	388	2.3∗				
219.153	$HCOOCH_{3(\nu=1)}(10_{4,6} \rightarrow 9_{3,6})$E	230	2.3∗	219.155	$HCOOCH_{3(\nu=1)}(18_{11,7} \rightarrow 17_{11,6})$E	369	2.3∗
219.174	$HC_3N_{(v_7=1)}(24 \rightarrow 23)$	452					
219.195	$HCOOCH_{3(\nu=1)}(18_{16,3} \rightarrow 17_{16,2})$E	459	2.3∗				

219.264	$HCOOCH_{3(v=0)}(36_{6,30} \rightarrow 36_{6,31})A$	429	2.2*				
219.276	$SO_{2(v=0)}(22_{7,15} \rightarrow 23_{6,18})$	352	†				
219.331	$HCOOCH_{3(v=1)}(18_{15,4} \rightarrow 17_{15,3})E$	438	2.3*				
219.355	$^{34}SO_{2(v=0)}(11_{1,11} \rightarrow 10_{0,10})$	60	3 †				
219.412	$HCOOCH_{3(v=1)}(18_{10,8} \rightarrow 17_{10,7})E$	355					
219.417	$HCOOCH_{3(v=0)}(30_{5,26} \rightarrow 30_{4,27})E$	292	2.3*				
219.479	$HCOOCH_{3(v=1)}(18_{14,5} \rightarrow 17_{14,4})E$	419	2.3				
219.484	$HCOOCH_{3(v=0)}(30_{5,26} \rightarrow 30_{4,27})A$	292	2.3*				
219.506	$CH_3CH_2CN_{(v=0)}(24_{2,22} \rightarrow 23_{2,21})$	136	2.3				
219.560	$C^{18}O(2 \rightarrow 1)$	16	†				
219.566	$HCOOCH_{3(v=1)}(18_{14,4} \rightarrow 17_{14,3})A$	419		219.566	$HCOOCH_{3(v=1)}(18_{14,5} \rightarrow 17_{14,5})A$	419	
				219.566	$HCOOCH_{3(v=1)}(18_{15,4} \rightarrow 17_{15,3})A$	438	
				219.566	$HCOOCH_{3(v=1)}(18_{15,3} \rightarrow 17_{15,3})A$	438	
				219.571	$HCOOCH_{3(v=1)}(18_{16,2} \rightarrow 17_{16,1})A$	459	
				219.571	$HCOOCH_{3(v=1)}(18_{16,3} \rightarrow 17_{16,2})A$	459	
219.579	$HCOOCH_{3(v=0)}(28_{9,19} \rightarrow 28_{8,20})A$	295	2.3				
219.584	$HCOOCH_{3(v=1)}(18_{13,5} \rightarrow 17_{13,4})A$	401	2.3	219.584	$HCOOCH_{3(v=1)}(18_{13,6} \rightarrow 17_{13,5})A$	401	2.3
219.592	$HCOOCH_{3(v=0)}(28_{9,19} \rightarrow 28_{8,20})E$	295	1.3				
219.600	$HCOOCH_{3(v=0)}(30_{9,22} \rightarrow 30_{8,23})E$	330	1.1				
219.607	$HCOOCH_{3(v=0)}(30_{5,26} \rightarrow 30_{3,27})E$	292					
219.623	$HCOOCH_{3(v=1)}(18_{12,6} \rightarrow 17_{12,5})A$	384	1.1	219.623	$HCOOCH_{3(v=1)}(18_{12,7} \rightarrow 17_{12,6})A$	384	1.1
219.642	$HCOOCH_{3(v=1)}(18_{13,6} \rightarrow 17_{13,5})E$	400	1.1				
219.657	$HNCO(10_{3,8} \rightarrow 9_{3,7})$	447					
219.696	$HCOOCH_{3(v=1)}(18_{11,8} \rightarrow 17_{11,7})A$	369	1.3	219.696	$HCOOCH_{3(v=1)}(18_{11,7} \rightarrow 17_{11,6})A$	369	1.3
219.705	$HCOOCH_{3(v=1)}(18_{4,15} \rightarrow 17_{4,14})A$	299	2.2				
219.737	$HNCO_{(v=0)}(10_{2,8} \rightarrow 9_{2,7})$	231					
219.764	$HCOOCH_{3(v=1)}(18_{9,9} \rightarrow 17_{9,8})E$	342	1.2				
219.798	$HNCO_{(v=0)}(10_{0,10} \rightarrow 9_{0,9})$	58					
219.822	$HCOOCH_{3(v=1)}(18_{10,9} \rightarrow 17_{10,8})A$	355	1.2	219.822	$HCOOCH_{3(v=1)}(18_{10,8} \rightarrow 17_{10,7})A$	355	1.2
219.827	$HCOOCH_{3(v=1)}(18_{12,7} \rightarrow 17_{12,6})E$	384	2.3*				
219.908	$H_2^{13}CO(3_{1,2} \rightarrow 2_{1,1})$	33	†				
219.949	$SO_{(v=0)}(6_5 \rightarrow 5_4)$	35	†				
220.030	$HCOOCH_{3(v=1)}(18_{9,10} \rightarrow 17_{9,9})A$	342		220.030	$HCOOCH_{3(v=1)}(18_{9,9} \rightarrow 17_{9,8})A$	342	
220.043	$HCOOCH_{3(v=1)}(18_{11,8} \rightarrow 17_{11,7})E$	368	2.3				
220.078	$CH_3OH_{(v_t=0)}(8_{0,8} \rightarrow 7_{1,6})$	97					
220.167	$HCOOCH_{3(v=0)}(17_{4,13} \rightarrow 16_{4,12})E$	103	†				
220.178	$CH_2CO(11_{1,11} \rightarrow 10_{1,10})$	76	†				
220.190	$HCOOCH_{3(v=0)}(17_{4,13} \rightarrow 16_{4,12})A$	103					
220.258	$HCOOCH_{3(v=1)}(24_{2,23} \rightarrow 24_{1,24})E$	355	1.3				
220.296	$CH_3^{13}CN(12_9 \rightarrow 11_9)$	646	1.3				
220.307	$HCOOCH_{3(v=1)}(18_{10,9} \rightarrow 17_{10,8})E$	354	1.2				
220.368	$HCOOCH_{3(v=1)}(18_{8,11} \rightarrow 17_{8,10})A$	331	2.2	220.370	$HCOOCH_{3(v=1)}(18_{8,10} \rightarrow 17_{8,9})A$	331	2.2
				220.366	$HCOOCH_{3(v=0)}(33_{5,28} \rightarrow 33_{5,29})E$	357	2.2
220.399	$^{13}CO(2 \rightarrow 1)$	16	†				
220.409	$HCOOCH_{3(v=1)}(18_{4,15} \rightarrow 17_{4,14})E$	299	1.3				
220.476	$CH_3CN_{(v=0)}(12_8 \rightarrow 11_8)$	526					
220.539	$CH_3CN_{(v=0)}(12_7 \rightarrow 11_7)$	419					
220.570	$CH_3^{13}CN(12_4 \rightarrow 11_4)$	183					
220.594	$CH_3CN_{(v=0)}(12_6 \rightarrow 11_6)$	326					
220.621	$CH_3^{13}CN(12_2 \rightarrow 11_2)$	97	†				
220.641	$CH_3CN_{(v=0)}(12_5 \rightarrow 11_5)$	248					
220.647	$HCOOCH_{3(v=1)}(18_{9,10} \rightarrow 17_{9,9})E$	342	2.2				
220.661	$CH_3CH_2CN_{(v=0)}(25_{2,24} \rightarrow 24_{2,23})$	143	2.3				
220.679	$CH_3CN_{(v=0)}(12_4 \rightarrow 11_4)$	183					
220.709	$CH_3CN_{(v=0)}(12_3 \rightarrow 11_3)$	133					
220.730	$CH_3CN_{(v=0)}(12_2 \rightarrow 11_2)$	98	†				
220.743	$CH_3CN_{(v=0)}(12_1 \rightarrow 11_1)$	76					
220.747	$CH_3CN_{(v=0)}(12_0 \rightarrow 11_0)$	69					

* Due to the frequency resolution (0.8125 MHz, $\sim 1.2\,\mathrm{km\,s^{-1}}$), lines with broad FWHM width can be attributed to different species, so lines with stronger CDMS/JPL
intensity are listed in the left column with "*", and the potential blended weaker transitions are listed in the right column.
Tentative detections and unidentified lines are marked with "?".
Lines with "†" are imaged in Figure 3.3.
"A(E)A(E)" indicates 4 types of transitions are possible for a certain line: AA, EE, AE, EA
[1.1] indicates that the molecule is detected only in IRS1, and toward the IRS1 peak shows absorption or an inverse P-cygni profile.
[1.2] indicates that the molecule is detected only in IRS1, and toward the IRS1 peak shows pure emission.
[1.3] indicates that the molecule is detected only in IRS1, without a clear detection at the IRS1 peak.
Without any digital annotation indicates that the molecule is detected both in IRS1 and MM1, and toward the IRS1 peak shows absorption or an inverse P-cygni profile.
[2.2] indicates that the molecule is detected both in IRS1 and MM1, and toward the IRS1 peak shows pure emission.
[2.3] indicates that the molecule is detected both in IRS1 and MM1, and is not detected toward the IRS1 peak.
[3] indicates that the molecule is detected only in MM1

Integrated intensity $\int T_B(\upsilon)d\upsilon$ (K km s^{-1}) for NGC 7538 S and IRS1 mmS, $\int \tau_(\upsilon)d\upsilon$ (km s^{-1}) for IRS1 peak

Species	Freq (GHz) (GHz)	MM1 (157 ± 14 K)	MM2 (130 ± 12 K)	MM3 (50 K)	JetN (150 K)	JetS (150 K)	mmS (136 ± 24 K)	peak (136 ± 24 K)
$C^{18}O$	219.56	119.80 ± 1.27	23.87 ± 1.58	6.27 ± 1.13	21.10 ± 1.55	27.31 ± 1.47	–	1.25 ± 0.07
^{13}CO	220.399	150.42 ± 8.06	47.65 ± 2.29	–	37.36 ± 1.50	56.64 ± 3.77	–	11.81 ± 0.06
$H_2^{13}CO$	219.909	8.68 ± 1.10	28.05 ± 2.04	≤ 0.42	≤ 0.12	1.31 ± 0.13	69.14 ± 3.90	0.07 ± 0.02
H_2CO	218.476	44.41 ± 3.14	50.28 ± 3.64	≤ 0.69	12.49 ± 1.57	10.52 ± 1.28	217.90 ± 21.88	1.91 ± 0.03
CH_3OH	218.44	76.40 ± 2.95	102.13 ± 3.91	15.35 ± 2.11	10.82 ± 1.94	13.03 ± 2.68	302.98 ± 6.21	1.87 ± 0.06
$HCOOCH_3$	220.167	27.25 ± 3.72	10.30 ± 2.47	3.38 ± 0.89	≤ 0.30	6.83 ± 1.43	151.71 ± 0.03	0.03 ± 0.06
CH_2CO	220.178	8.15 ± 0.93	17.97 ± 1.76	≤ 0.80	4.14 ± 0.20	≤ 0.92	102.94 ± 10.49	0.16 ± 0.06
$?CH_3OCH_3$	217.191	21.44 ± 8.15	4.29 ± 1.40	≤ 1.59	≤ 0.81	≤ 1.20	116.98 ± 4.76	0.87 ± 0.03
$O^{13}CS$	218.199	9.13 ± 1.95	8.54 ± 1.85	7.14 ± 2.50	≤ 0.42	≤ 0.54	16.36 ± 2.03	≤ 0.01
OCS	218.903	149.00 ± 1.39	98.75 ± 1.09	17.67 ± 2.04	≤ 0.74	5.28 ± 0.26	249.02 ± 4.37	≤ 0.01
^{33}SO	217.833	34.83 ± 0.99	1.88 ± 0.54	≤ 0.44	≤ 0.26	≤ 0.48	11.13 ± 2.20	0.10 ± 0.01
SO	219.949	228.57 ± 3.76	149.29 ± 4.13	≤ 0.73	24.57 ± 2.00	134.79 ± 1.56	225.60 ± 5.33	1.86 ± 0.07
$^{34}SO_2$	219.355	103.80 ± 1.97	≤ 0.81	≤ 0.59	≤ 0.74	≤ 0.74	≤ 2.21	≤ 0.01
SO_2	219.276	97.57 ± 0.94	≤ 0.46	≤ 0.82	≤ 0.48	≤ 0.90	36.58 ± 5.81	0.17 ± 0.03
HC_3N	218.325	165.41 ± 3.53	57.36 ± 2.54	≤ 0.90	≤ 0.42	≤ 0.53	54.85 ± 3.71	0.43 ± 0.05
$HC_3N(v_7 = 1)$	218.861	61.51 ± 3.36	13.58 ± 2.99	≤ 0.95	≤ 0.62	≤ 0.75	16.84 ± 3.07	≤ 0.02
C_2H_5CN	218.39	23.28 ± 2.38	5.51 ± 0.55	6.20 ± 0.24	≤ 0.60	≤ 0.82	≤ 2.68	≤ 0.02
HNCO	218.981	45.08 ± 2.25	25.43 ± 1.28	≤ 0.64	≤ 0.63	≤ 0.69	84.99 ± 6.88	0.50 ± 0.23
$CH_3^{13}CN$	220.621	10.43 ± 1.00	1.05 ± 0.10	≤ 0.23	≤ 0.22	≤ 0.14	11.20 ± 1.11	0.11 ± 0.02
CH_3CN	220.73	136.57 ± 1.93	61.22 ± 1.92	10.75 ± 0.93	≤ 2.87	≤ 0.67	274.52 ± 3.41	0.71 ± 0.19
DCN	217.239	64.01 ± 3.34	6.50 ± 1.51	≤ 1.05	≤ 0.74	7.25 ± 1.81	101.15 ± 5.53	0.90 ± 0.04
NH_2CHO	218.46	7.92 ± 2.00	12.09 ± 5.68	≤ 1.58	≤ 1.40	≤ 0.56	91.47 ± 3.82	0.20 ± 0.05

Table B2: The intensity integrated over the width of each line. Uncertainties on the measured intensities are typically ≤ 10%, as determined from Gaussian fitting. For species which are not detected, an upper limit equal to the 3σ rms is given. .

I. Molecular Column density [x ± y(z) = (x ± y) × 10^zcm^{-2}]

Species	MM1 (157 ± 14 K)	MM2 (130 ± 12 K)	MM3 (50 K)	JetN (150 K)	JetS (150 K)	mmS (136 ± 24 K)	peak (136 ± 24 K)
$C^{18}O$	2.48 ± 0.23(17)	4.18 ± 0.63(16)	5.18 ± 0.94(15)	4.19 ± 0.31(16)	5.42 ± 0.29(16)	−−	2.98 ± 1.31(17)
^{13}CO *	4.02 ± 0.55(18)	6.63 ± 0.88(17)	–	5.89 ± 0.24(17)	7.83 ± 0.52(17)	–	2.79 ± 1.04(18)
$H_2^{13}CO$	2.09 ± 0.54(14)	5.34 ± 1.05(14)	≤ 2.90(12)	≤ 2.73(12)	2.99 ± 0.30(13)	1.39 ± 0.41(15)	1.84 ± 1.48(14)
H_2CO	6.31 ± 1.10(15)	5.91 ± 1.00(15)	≤ 4.49(13)	1.69 ± 0.21(15)	1.42 ± 0.17(15)	2.68 ± 0.80(16)	3.06 ± 1.29(16)
CH_3OH	4.01 ± 0.76(16)	4.06 ± 0.73(16)	2.13 ± 0.29(15)	5.30 ± 0.95(15)	6.38 ± 1.31(15)	1.29 ± 0.39(17)	1.04 ± 0.58(17)
$HCOOCH_3$	2.97 ± 0.75(16)	9.17 ± 3.30(15)	2.13 ± 0.56(15)	≤ 3.11(14)	7.09 ± 1.49(15)	1.41 ± 0.28(17)	3.66 ± 12.20(15)
CH_2CO	5.68 ± 1.31(14)	1.06 ± 0.19(15)	≤ 3.01(13)	2.74 ± 0.13(14)	≤ 6.12(13)	6.31 ± 1.77(15)	1.25 ± 1.10(15)
$?CH_3OCH_3$	4.37 ± 1.77(16)	8.97 ± 2.66(15)	≤ 1.72(16)	≤ 1.64(15)	≤ 2.44(15)	2.41 ± 0.07(17)	2.36 ± 0.51(17)
$O^{13}CS$	7.72 ± 1.97(14)	6.83 ± 1.68(14)	7.47 ± 2.61(14)	≤ 3.47(13)	≤ 4.47(13)	1.32 ± 0.24(15)	≤ 9.52(13)
OCS *	5.72 ± 0.26(16)	4.72 ± 0.17(16)	7.03 ± 0.80(16)	–	≤ 4.38(15)	1.01 ± 0.07(17)	≤ 9.48(13)
^{33}SO	3.39 ± 0.35(15)	1.57 ± 0.60(14)	≤ 1.99(13)	≤ 2.42(13)	≤ 4.46(13)	9.66 ± 3.51(14)	1.19 ± 0.60(15)
SO *	2.96 ± 0.27(17)	1.54 ± 0.16(16)	–	≤ 1.18(16)	≤ 1.21(16)	7.71 ± 1.27(16)	6.38 ± 2.56(15)
$^{34}SO_2$	1.27 ± 0.16(16)	≤ 8.08(13)	≤ 2.96(13)	≤ 8.58(13)	≤ 8.54(13)	≤ 2.32(14)	≤ 1.24(14)
SO_2	2.18 ± 0.10(17)	≤ 1.24(15)	≤ 4.04(16)	≤ 1.11(15)	≤ 2.09(15)	9.35 ± 0.01(16)	5.82 ± 1.24(16)
HC_3N	6.27 ± 0.24(14)	2.14 ± 0.10(14)	≤ 6.46(12)	≤ 1.57(12)	≤ 2.00(12)	2.05 ± 0.18(14)	2.10 ± 0.73(14)
$HC_3N(v_7 = 1)$	1.81 ± 0.17(15)	6.02 ± 0.04(14)	≤ 4.21(15)	≤ 2.00(13)	≤ 2.41(13)	6.70 ± 1.04(14)	≤ 7.81(13)
C_2H_5CN	1.75 ± 0.29(15)	3.77 ± 0.55(14)	5.66 ± 0.21(14)	≤ 4.37(13)	≤ 6.00(13)	≤ 1.87(14)	≤ 1.37(14)
HNCO	2.78 ± 0.37(15)	1.36 ± 0.16(15)	≤ 2.84(13)	≤ 3.76(13)	≤ 4.08(13)	4.69 ± 1.07(15)	3.57 ± 3.45(15)
$CH_3^{13}CN$	5.15 ± 0.95(14)	4.45 ± 0.76(13)	≤ 7.66(12)	≤ 1.05(13)	≤ 6.41(12)	4.92 ± 1.25(14)	6.27 ± 3.68(14)
CH_3CN *	3.78 ± 0.45(16)	3.19 ± 0.37(15)	≤ 2.24(15)	–	–	3.50 ± 0.67(16)	1.38 ± 1.06(15)
DCN	2.15 ± 0.29(14)	1.86 ± 0.61(13)	≤ 1.51(12)	≤ 2.39(12)	2.34 ± 0.58(13)	3.00 ± 0.64(14)	3.50 ± 1.47(14)
NH_2CHO	2.53 ± 0.93(14)	3.17 ± 1.94(14)	≤ 2.09(13)	≤ 4.27(13)	≤ 1.72(13)	2.52 ± 0.59(15)	7.23 ± 5.43(14)

Table B3: Column densities and abundances for molecules with respect to H_2 (derived from dust continuum in MM1–3 and converted from $C^{18}O$ in the rest substructures by assuming $N_{C^{18}O}/N_{H_2} \sim 1.64 \times 10^{-7}$) from different substructures in NGC 7538 S and IRS1 marked in Figure 3.3, listed in the form of x ± y(z) = (x ± y) × 10^z, obtained with the excitation temperatures from the rotation map fittings of Figure 3.4. For species which are not detected, an upper limit derived from 3σ rms is given. Molecules marked with "*" are likely optically thick and for those we did the optical depth correction. The values in red are from optical depth estimation. Uncertainties on the measured values are typically ≤ 10%, as determined from T_{rot}, partition function $Q(T_{rot})$, and Gaussian fitting to $\int T_B(\upsilon)d\upsilon$.

II. Molecular Abundance to H_2 [x ± y(z) = (x ± y) × 10^z] derived from dust continuum in MM1–3 and from C18O in the rest substructures

Species	MM1 (157 ± 14 K)	MM2 (130 ± 12 K)	MM3 (50 K)	JetN (150 K)	JetS (150 K)	mmS (136 ± 24 K)	peak (136 ± 24 K)
$C^{18}O$	1.27 ± 0.34(−7)	2.20 ± 0.75(−8)	9.36 ± 2.16(−10)	1.64(−7)	1.64(−7)	−−	1.64(−7)
^{13}CO *	2.1(-6)	3.5(-7)	–	2.3(-6)	2.4(-6)	−−	1.54 ± 0.57(−6)
$H_2^{13}CO$	1.07 ± 0.49(−10)	2.82 ± 1.11(−10)	≤ 5.24(−13)	≤ 1.07(−11)	9.05 ± 0.89(−11)	−−	1.02 ± 0.82(−10)
H_2CO	3.23 ± 1.18(−9)	3.12 ± 1.12(−9)	≤ 8.10(−12)	6.63 ± 0.83(−9)	4.31 ± 0.52(−9)	−−	1.69 ± 0.71(−8)
CH_3OH	2.05 ± 0.78(−8)	2.14 ± 0.80(−8)	3.84 ± 0.71(−10)	2.07 ± 0.37(−8)	1.93 ± 0.40(−8)	−−	5.71 ± 3.19(−8)
$HCOOCH_3$	1.52 ± 0.69(−8)	4.83 ± 2.82(−9)	3.85 ± 1.22(−10)	≤ 1.22(−9)	2.15 ± 0.45(−8)	−−	2.01 ± 6.73(−9)
CH_2CO	2.91 ± 1.25(−10)	5.61 ± 2.07(−10)	≤ 5.44(−12)	1.08 ± 0.05(−9)	≤ 1.85(−10)	−−	6.89 ± 6.05(−10)
$?CH_3OCH_3$	2.24 ± 1.41(−8)	4.73 ± 2.41(−9)	≤ 3.10(−9)	≤ 6.42(−9)	≤ 7.39(−9)	−−	1.30 ± 0.28(−7)
$O^{13}CS$	3.95 ± 1.81(−10)	3.60 ± 1.62(−10)	1.35 ± 0.55(−10)	≤ 1.36(−10)	≤ 1.35(−10)	−−	≤ 5.24(−11)
OCS *	2.9(-8)	2.5(-8)	1.3(-8)	–	≤1.3(-8)		≤ 5.22(−11)
^{33}SO	1.73 ± 0.49(−9)	8.29 ± 5.03(−11)	≤ 3.59(−12)	≤ 9.47(−11)	≤ 1.35(−10)	−−	6.54 ± 3.33(−10)
SO *	1.5(-7)	8.1(-9)	–	≤4.6(-8)	≤3.7(-8)		3.83 ± 9.61(−9)
$^{34}SO_2$	6.50 ± 1.97(−9)	≤ 4.26(−11)	≤ 5.35(−12)	≤ 3.67(−10)	≤ 2.59(−10)	−−	≤ 6.80(−11)
SO_2	1.12 ± 0.12(−7)	≤ 6.56(−10)	≤ 7.30(−9)	≤ 4.36(−9)	≤ 6.33(−9)	−−	3.20 ± 0.68(−8)
HC_3N	3.21 ± 0.66(−10)	1.13 ± 0.25(−10)	≤ 1.17(−12)	≤ 6.15(−12)	≤ 6.05(−12)	−−	1.16 ± 0.40(−10)
$HC_3N(v_7 = 1)$	9.27 ± 0.50(−10)	3.18 ± 0.50(−10)	≤ 7.60(−10)	≤ 7.83(−11)	≤ 7.31(−11)	−−	≤ 4.30(−11)
C_2H_5CN	8.96 ± 3.16(−10)	1.99 ± 0.66(−10)	1.02 ± 0.08(−10)	≤ 1.71(−10)	≤ 1.81(−10)	−−	≤ 7.54(−11)
HNCO	1.42 ± 0.45(−9)	7.16 ± 2.17(−10)	≤ 5.13(−12)	≤ 1.47(−10)	≤ 1.23(−10)	−−	1.97 ± 1.90(−9)
$CH_3^{13}CN$	2.64 ± 0.99(−10)	2.35 ± 0.85(−11)	≤ 1.38(−12)	≤ 4.11(−11)	≤ 1.94(−11)	−−	3.45 ± 2.02(−10)
CH_3CN *	1.9(-8)	1.7(-9)	≤4.1(-10)	–	–		7.62 ± 5.86(−10)
DCN	1.10 ± 0.35(−10)	9.79 ± 5.33(−12)	≤ 2.72(−13)	≤ 9.36(−12)	7.07 ± 1.77(−11)	−−	1.93 ± 0.81(−10)
NH_2CHO	1.30 ± 0.76(−10)	1.67 ± 1.47(−10)	≤ 3.78(−12)	≤ 1.67(−10)	≤ 5.21(−11)	−−	3.98 ± 2.99(−10)

Table B3: (continued)

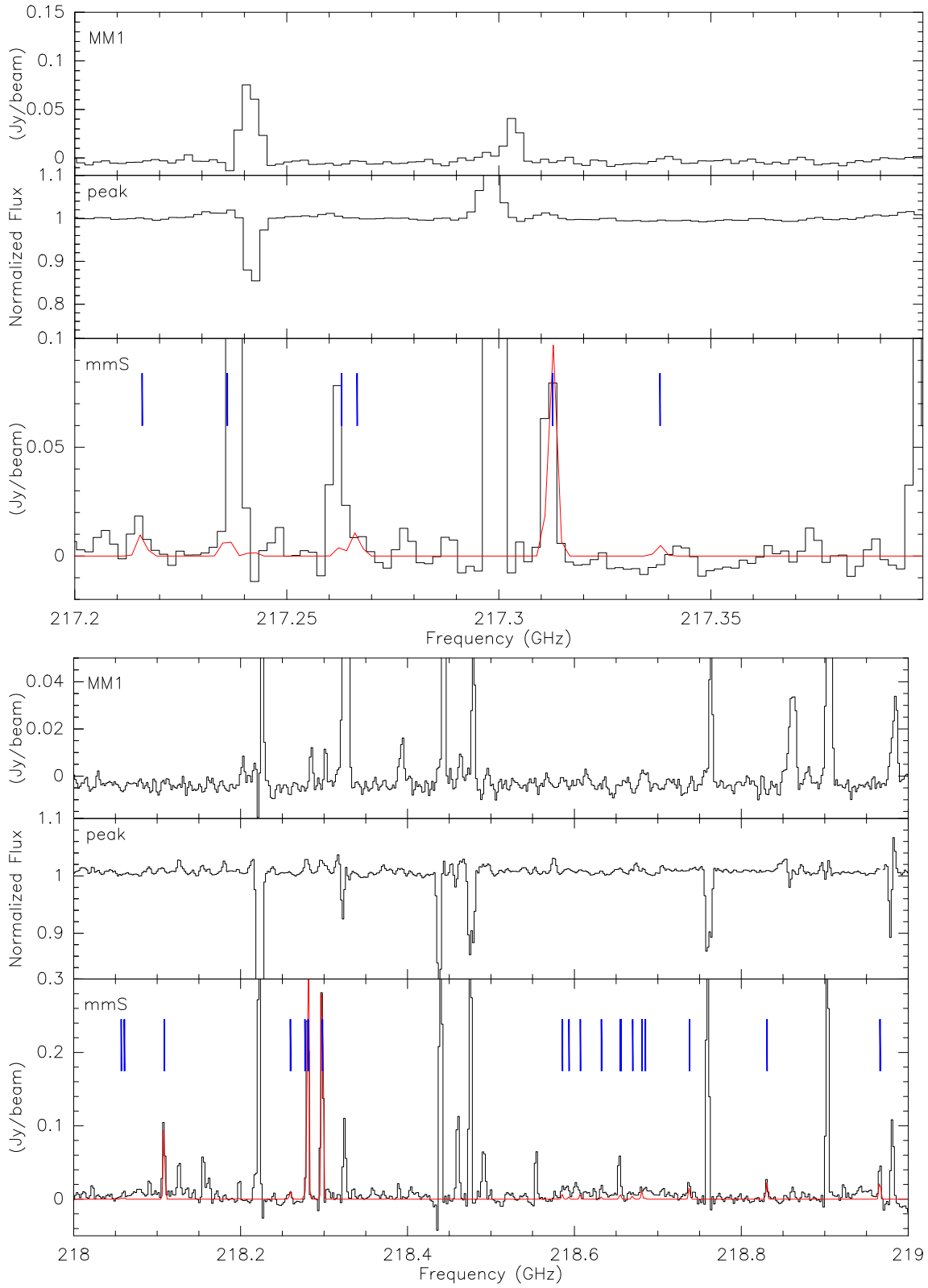

Figure B1: Synthetic fitting of $HCOOCH_3$ in NGC 7538 IRS1 (mmS and continuum peak) and MM1. Black lines represent the observed spectra while red lines show the best fitting model based on optically thin assumption.

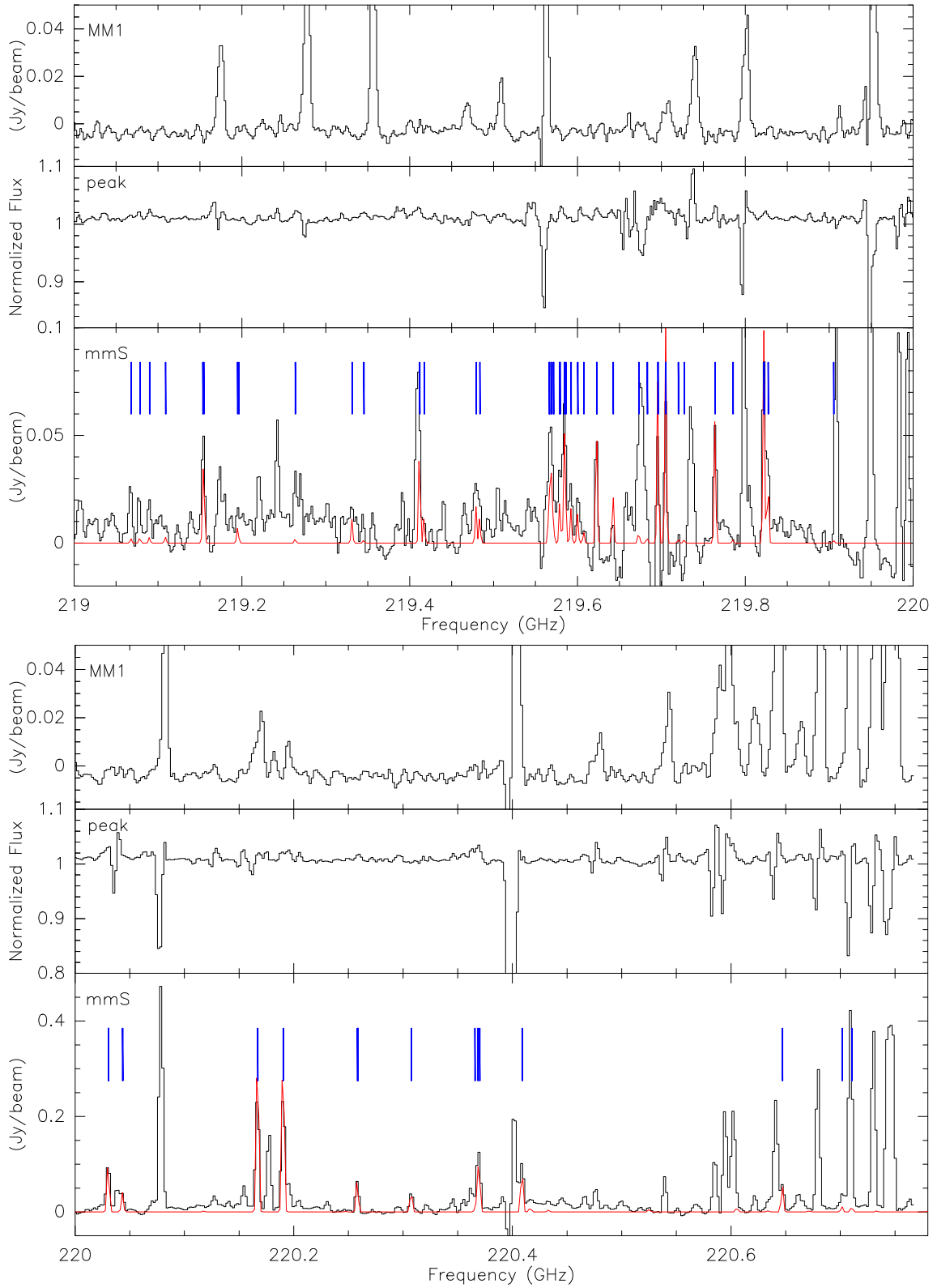

Figure B1: (continued)

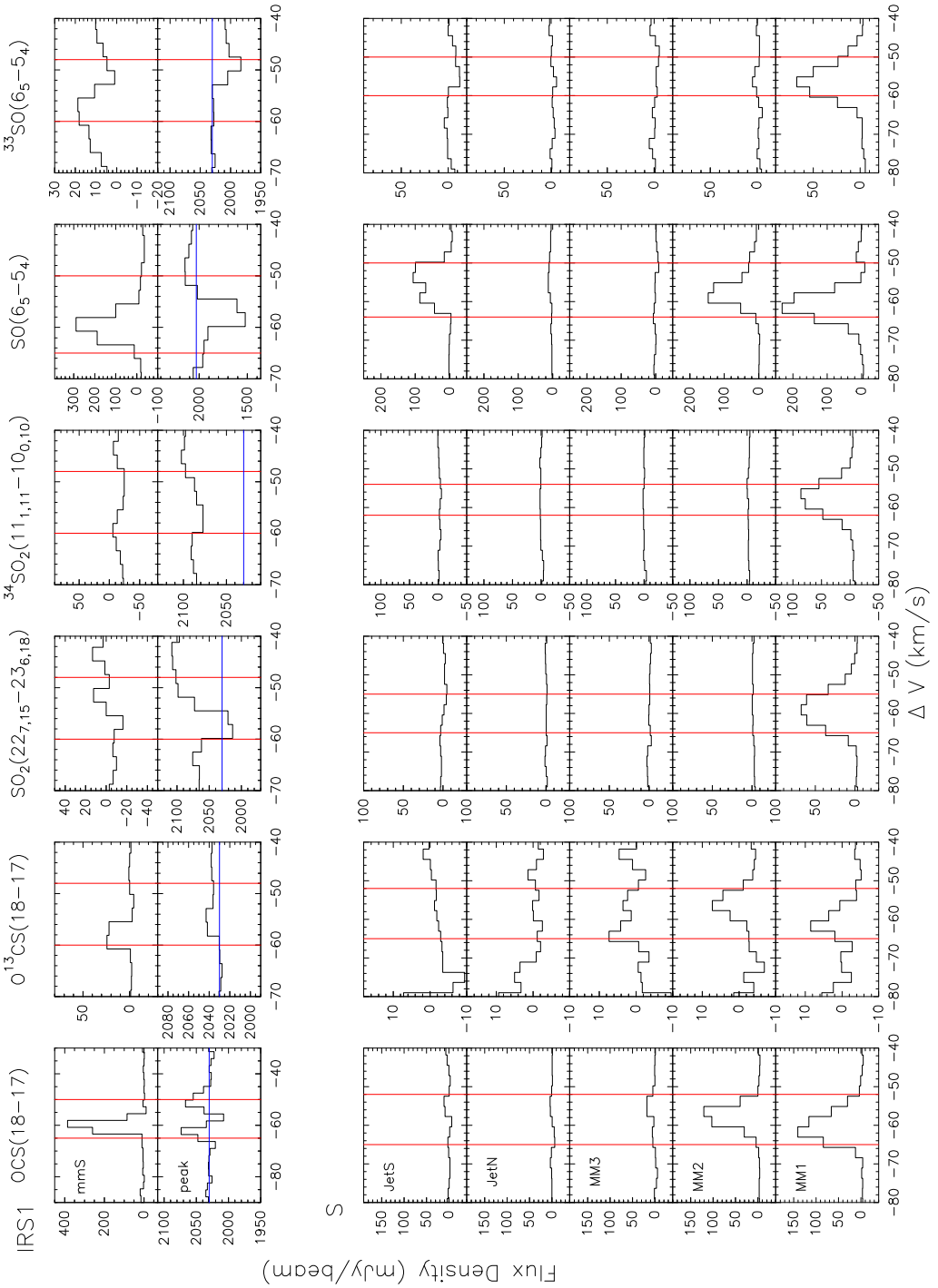

Figure B2: Line profiles of identified species toward the continuum substructures identified in NGC 7538 S and IRS1 (given in Table 3.1). Two red vertical lines in each panel mark the velocity range we use to integrate the intensity and obtain the distribution maps of Figure 3.3.

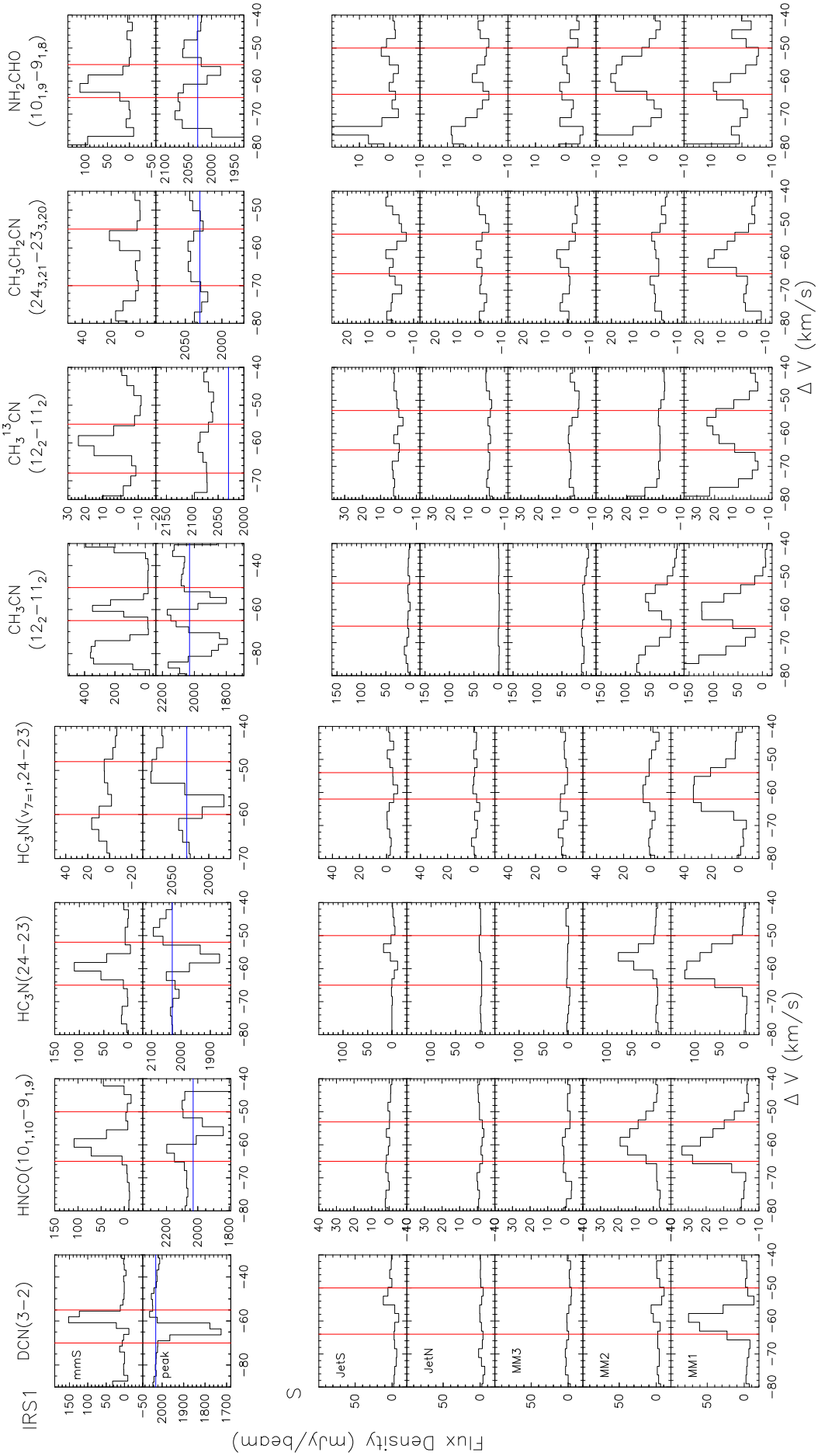

Figure B2: (continued)

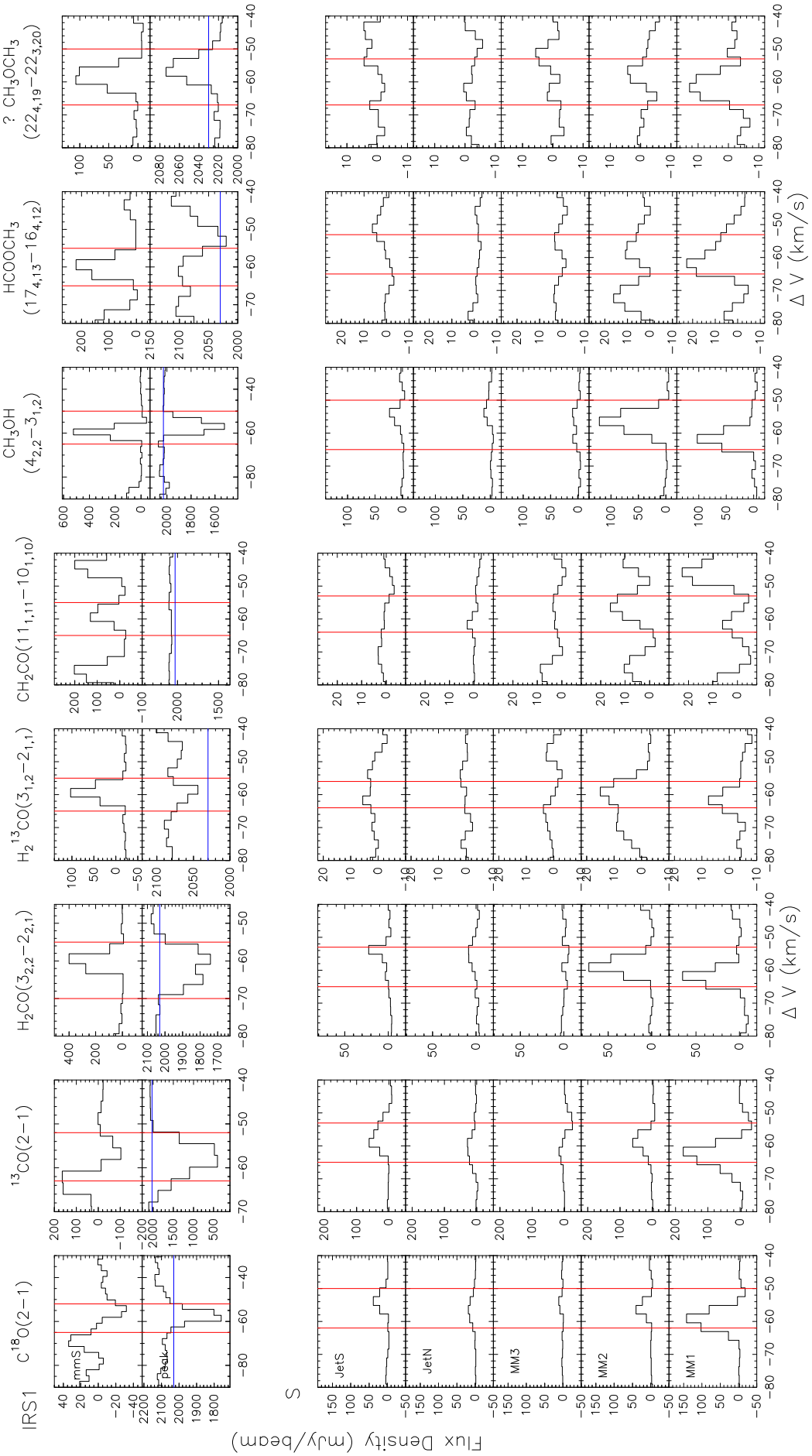

Figure B2: (continued)

4 Are the Infrared Dark Clouds Really Quiescent?

4.1 Motivation

In Chapter 2 and Chapter 3, HMC and HMPO sources are characterised by high temperatures and high gas density, producing rich spectra of molecular lines, particularly higher J level transitions from COMs. In contrast, dense regions where protostellar objects have not yet formed are poorly characterised, mainly due to their low temperature ($T < 20\,K$) and fewer gas phase molecules present. However, within most of these regions, no heating or outflow activity is present which would quickly destroy signatures of the early kinematic and chemical properties. Therefore, observations of these regions is crucial to characterise the initial conditions for high mass star formation theories.

For a long period, identification of the earliest evolutionary stages have been limited to observations with low spatial resolution at far-infrared wavelength, which called into question the existence of HMSCs (e.g., Motte et al. 2007). More recent studies indicate the existence of HMSCs, which have a relatively short collapse timescale (on the order of 5×10^4 yrs) when no protostellar objects are embedded (e.g., Russeil et al. 2010; Tackenberg et al. 2012). Moreover, thanks to the high spatial resolution of the *Herschel* satellite (Pilbratt et al. 2010), a recent far-infrared observational project "The Earliest Phases of Star Formation"(EPoS[1]) revealed several young HMSCs, which show absorption feature or appear none detection at $70\,\mu m$ but exhibit strong emission lines at (sub)mm wavelength (e.g., "The APEX Telescope Large Area Survey of

[1] "The Earliest Phases of Star Formation" (EPoS) is a *Herschel* guarantee time project (PI O. Krause, Beuther et al. 2010a; Henning et al. 2010; Stutz et al. 2010), which maps a sample of 45 very young HMSFRs with the PACS and SPIRE instruments in all available wavelengths bands between 70 and $500\,\mu m$. The sample contains the evolutionary stages from HMSC candidates to IRDCs with already embedded very young protostars.

the Galaxy" (ATLASGAL) at 870 μm, Schuller et al. 2009), indicating the initial evolutionary phase (e.g., Beuther et al. 2010a; Henning et al. 2010; Linz et al. 2010; Beuther et al. 2012b; Ragan et al. 2012b).

In spite of our improving understanding of HMSCs, many questions still remain: What is the dynamic process from HMSCs to the forming of MYSOs? Does the initial cloud collapse into a single core or fragment into multiple cores (e.g., Zhang et al. 2009; Bontemps et al. 2010; Zhang & Wang 2011; Beuther et al. 2013b)? What is the mass of each initial fragment? Is the thermal pressure sufficient to support the mass of the core(s) (e.g., Wang et al. 2011a, 2014)? What are the dynamic and chemical properties of these cores? Are the HMSCs so cold and quiescent that the whole clump is kinematically and chemically homogeneous? Characterised by the chemical-dynamic properties, are the HMSCs different from, or similar to, low mass dark clouds (e.g., Miettinen et al. 2011; Vasyunina et al. 2011)?

To investigate these questions, we select a small sample of four HMSCs from the EPoS catalogue: G 28.34 S, IRDC 18530, IRDC 18306 and IRDC 18308. These sources exhibit strong (sub)mm continuum emission towards the 70 μm extinction features (the left column of Figure 4.1). At the kinematic distances (D) of 3.6–4.6 kpc, these regions do not show any sign of active star formation.

In this chapter, we study the selected IRDCs via SMA and IRAM 30 m observations. Following a description of the observations in Section 4.2, we present the source continuum maps obtained from SMA at 1.1 mm and their 16 GHz spectra obtained from the 30 m at 1 mm & 3 mm in Section 4.3. A kinetic and chemical analysis of the data, along with the discussion is presented in Section 4.4. Finally, our conclusions are given in Section 4.5.

4.2 Observations

4.2.1 Submillimeter Array (SMA)

We carried out 4 tracks of observations on our sample with the SMA at 260/270 GHz (1.1 mm) in the extended (EXT) and compact (COMP) configurations (summarised in Table 4.1I). From May to July 2013, we observed 2 sources per track, sharing the same bandpass and flux calibrators. For all the observations, phase and amplitude calibrations were performed via frequent observations (every 20 min) of the quasars 1743-038 and 1751+096. The primary beam is 47″, and the phase center for each source is pinned down to the 870 μm ATLASGAL continuum peak (Schuller et al. 2009), list in Table 4.1II. The baselines (BL) range from 16–226 m with 6 or 7 antennas (N_{ant}), resulting in the $\geq 20''$ structures of the source being filtered out. Bandpass calibrations were done with BL Lac (EXT), 3C 279 (EXT, COM) and 3C 84 (COMP). Flux calibrations

were estimated from Neptune (EXT) and Uranus (COMP). The zenith opacities, measured with water vapour monitors mounted on Caltech Submillimeter Observatory (CSO) or James Clerk Maxwell Telescope (JCMT), were satisfactory during all tracks with τ(225 GHz) $\sim$ 0.01–0.3. Further technical descriptions of the SMA and its calibration schemes can be found in Ho et al. (2004).

The receiver in a double sideband mode was tuned to a local oscillate frequency of 260.255 GHz at S22 of the lower sideband. Separated by 10 GHz, each correlator has a bandwidth of 4 GHz, covering the range of 258.100–216.981 GHz and 269.998–273.876 GHz. The target line is $H^{13}CO^+$ ($3 \rightarrow 2$) at 260.255 GHz, so the channel separation is 0.406 MHz (corresponding to a velocity resolution of 0.468 km s^{-1}) in the range of 260.221–260.299 GHz and 271.679–271.757 GHz; 1.625 MHz (velocity resolution of 1.872 km s^{-1}) in the range of 260.041–260.221 GHz and 271.757–271.937 GHz; and 0.812 MHz (velocity resolution of 0.936 km s^{-1}) for the rest.

The initial flagging and calibration was done with the IDL superset MIR, which was originally developed for the Owens Valley Radio Observatory and adapted for the SMA[2]. The imaging and data analysis was conducted in MIRIAD (Sault et al. 1995). The synthesised beams and 1σ rms of the continuum image from dual-sidebands at each configuration are listed in Table 4.1II, along with the results by combining configurations with natural weighting. No line is detected in either source within 8 GHz band.

4.2.2 Single-dish observations with the IRAM 30 m telescope

In addition to the high spatial resolution observations performed with the SMA, we conducted line survey of our sample with the IRAM 30 m telescope at 1 mm & 3 mm. Observations were performed in the on-the-fly mode from May 28th –May 30th 2014, mapping an $1.5' \times 1.5'$ area of each source. A broad bandpass (8 GHz bandwidth for each sideband) of EMIR covers the range of 85.8–93.6 GHz with a velocity resolution of 0.641 km s^{-1}, and 215.1–222.8 GHz with a velocity resolution of 0.265 km s^{-1}. After achieving the expected sensitivity, we tuned the band center on May 31st and observed an "extra band" of 85.2–89.2 GHz and 217.0–224.8 GHz to search for more lines. The phase center, the weather conditions, focus and pointing information are list in in Table 4.2[3]. Using a forward efficiency (Feff, 94% at 1mm and 95% at 3 mm) and a

[2]http://cfa-www.harvard.edu/~cqi/mircook.html.

[3]The SMA continuum peak of each source has some shift from its observational phase center. Therefore, we set the 30 m phase center to the SMA continuum peak, and use Gildas software to "reproject" the SMA offset accordingly.

Table 4.1: SMA observations toward four IRDCs

I. Configurations

Configuration	Date (yyyymmdd)	Source	N_{ant}	BL (m)	Calibrator Bandpass	Calibrator Flux	T_{sys} (K)	$\tau_{225\,GHz}$
EXT	20130530	IRDC 18306 IRDC 18308	7	44-226	BL Lac 3C 279	Neptune	200-400	0.05-0.2
EXT	20130611	G 28.34 S IRDC 18530	6	68-226	BL Lac 3C 279	Neptune Titan	200-600	0.2-0.3
COMP	20130717	IRDC 18306 IRDC 18308	6	16-69	3C 279 3C 84	Uranus	200-500	0.1-0.25
COMP	20130719	G 28.34 S IRDC 18530	6	16-69	3C 279 3C 84	Uranus	100-300	0.01-0.2

II. Phase center of each source and the synthetic imagine quality at different configurations

Source		G 28.34 S	IRDC 18530	IRDC 18306	IRDC 18308
R.A.	[J2000]	$18^h42^m47^s$	$18^h55^m30^s$	$18^h33^m32^s$	$18^h33^m35^s$
Dec.	J2000]	$-04°04'07''$	$02°17'06''$	$-08°32'27''$	$-08°35'53''$
D	(kpc)	4.8	4.6	3.6	4.4
V_{lsr}	(km s^{-1})	78.4	75.9	54.8	73.7
COM	(Maj × Min, P.A)	$3.47'' \times 1.79''$, 32.8°	$3.29'' \times 1.77''$, 34.8°	$3.28'' \times 2.17''$, − 7.7°	$3.26'' \times 2.14''$, 9.6°
	σ rms (mJy/beam)	1.00	0.86	1.28	1.40
EXT	(Maj × Min, P.A)	$0.88'' \times 0.69''$, − 82.2°	$0.88'' \times 0.67''$, − 78.9°	$0.93'' \times 0.79''$, − 85.4°	$0.93'' \times 0.79''$, − 88.6°
	σ rms (mJy/beam)	1.26	1.29	1.31	1.29
COMP+EXT	(Maj × Min, P.A)	$2.55'' \times 1.51''$, 33.5°	$2.44'' \times 1.49''$, 35.1°	$1.79'' \times 1.56''$, 5.9°	$1.67'' \times 1.50''$, 9.6°
	σ rms (mJy/beam)	0.97	0.77	0.99	0.98

a. Synthetic beam of compact configuration.
b. Synthetic beam of extended configuration.
c. Synthetic beam of compact+extended configuration.

Table 4.2: IRAM 30 m observations on the four IRDCs

Source	R.A. [J2000]	Dec. [J2000]	abbrev.	Source	R.A. [J2000]	Dec. [J2000]	abbrev.
G 28.34 S	$18^h42^m46^s.597$	$-04°04'11''.940$	G28.34	IRDC 18530	$18^h55^m30^s.128$	$02°17'09''.300$	18530
IRDC 18306	$18^h33^m32^s.044$	$-08°32'28''.620$	18306	IRDC 18308	$18^h33^m35^s.090$	$-08°36'00''.120$	18308

Date (yyyymmdd)	Source	Pointing	Focus	T_{sys} 1mm (K)	T_{sys} 3mm (K)	$\tau_{225\,GHz}$
20140528	G28.34, 18530	Saturn, K3-50A, Venus, 1749+096	Saturn, Venus	450-550	115-130	0.5-0.6
20140529	18306, 18530	Saturn, K3-50A,1749+096	Saturn	270-310	90-110	0.2-0.4
20140530	18306, 18308	Saturn, 1749+096	Saturn	275-285	90-100	0.2-0.4
20140531*	G28.34, 18306, 18308	W3OH, 1749+096	W3OH	210-280	90-110	0.1-0.3

T_{sys} and τ are averaged system temperature and precipitable water vapour in each observation
*. Observational band were tuned from 85.8–93.6 GHz to 85.2–92.9 GHz,
and from 215.1–222.8 GHz to 217.0–224.8 GHz.

main beam efficiency (Beff, 63% at 1mm and 81% at 3 mm), we converted the data from antenna temperature (T_A) to main beam brightness temperature (T_{mb} = Feff/Beff × T_A[4]). The beam of the 30 m telescope is ∼ 12″ at 1 mm and ∼ 30″ at 3 mm. We used the Gildas[5] software for data reduction and the first step line identification (Table 4.3)[6].

4.3 Observational Results

4.3.1 Fragmentation at small scale from SMA observations

Comprised from previous observations, our sources are all dark clouds when observed via *Herschel* at 70 μm (Ragan et al. 2012a), which are away from the bright sources at a projected distance of 1′–2′ (∼ 1–2 pc). However, they exhibit filamentary structures (sizes of several pc, shown as red contours in the left column of Figure 4.1) when observed by ATLASGAL at 870 μm (Schuller et al. 2009). At a spatial resolution of ∼2″ (corresponding to the linear resolution of 10^4 AU), the 1.1 mm SMA observations resolve each 870 μm continuum peak into several fragments (shown as white contours in the middle and right columns of Figure 4.1). Because of the spatial filtering effect, the COMP+EXT configuration picks up the compact structures tracing the inner region of the condensations, while the COMP configuration recovers the extended envelopes, which are essential in studying the kinetic properties of the fragments. Using the letters to mark the fragments showing > 3σ rms continuum emission in both COMP and COMP+EXT maps, we found the fragments in each source are separated at a projected distance of 0.1–0.2 pc (Table 4.4). In particular, G 28.34 S and IRDC 18308 are well aligned along the large scale filamentary direction.

4.3.2 Line survey from IRAM 30 m at 1 mm & 3 mm

The SMA band covers several dense gas tracers, such as $H^{13}CO^+$ (3 → 2, E_u/k_B = 25 K), $H^{13}CN$ (3 → 2, E_u/k_B = 25 K), $HN^{13}C$ (3 → 2, E_u/k_B = 25 K) and HNC (3 → 2, E_u/k_B = 26 K). However, none of them is detected at 1.1 mm, raising several questions. Are these lines tracing the extended structures, so they are filtered out by interferometric observations? Or is it because the environment of these young HMSCs are so cold that lines with higher-J transitions are not excited? Both are possibilities without further kinematic studies. Nevertheless, the IRAM 30 m line survey recovers the extended structure information, and shows line emission from lower-J transitions at 1 mm & 3 mm.

[4]http://www.iram.es/IRAMES/mainWiki/Iram30mEfficiencies
[5]http://www.iram.fr/IRAMFR/GILDAS
[6]The "Weeds" is an extension of Gildas for line identification (Maret et al. 2011).

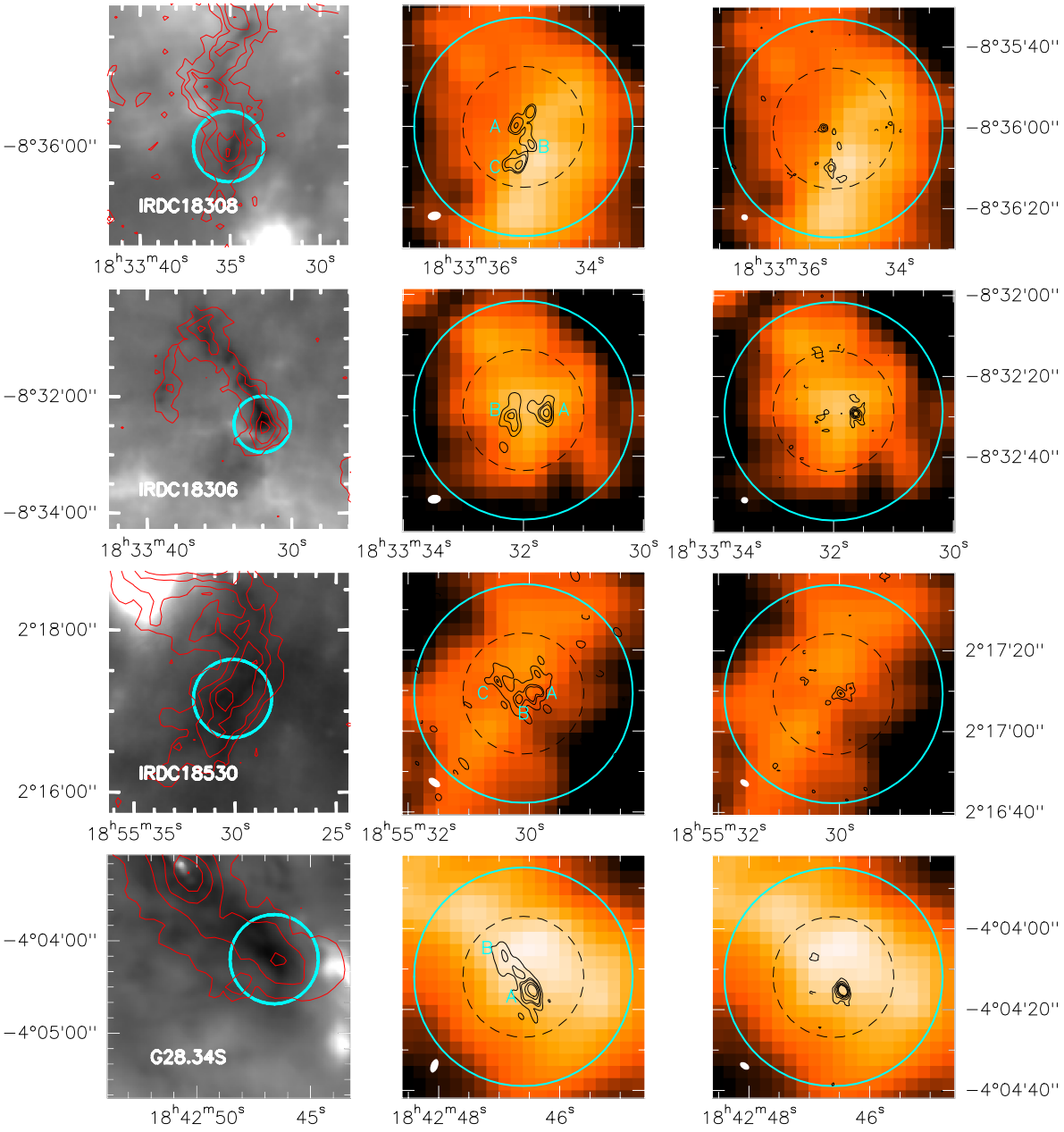

Figure 4.1: Compilation of the continuum data from 70 μm to 1.2 mm wavelength for G 28.34 S, IRDC 18530, IRDC 18306 and IRDC 18308. Left column: colormaps of the continuum are obtained with *Herschel* at 70 μm Ragan et al. (2012a). The red contours show continuum obtained with ATLASGAL at 870 μm Schuller et al. (2009), starting at 10σ rms and continue in 10σ rms steps. Middle and Right column: black contours show continuum obtained with SMA COMP configuration (middle) and COMP+EXT combination (right), overlaying on the moment 0 colormaps of $H^{13}CO^+$ from IRAM 30 m observations. COMP contours start at 5σ rms and continue in 5σ rms steps, while COMP+EXT contours start at 3σ and continue in 3σ steps). Cyan letters mark the fragments with > 3σ rms continuum emission in both COMP and COMP+EXT maps. In each panel, SMA synthetic beam is in the bottom left, black dashed circle shows beam of 30 m at 3 mm, and cyan circle in each panel shows the primary beam of PdBI in the upcoming observations at 3.4 mm.

Line identification

To reduce the noise level and enhance the contrast of the weak emission in cold environment, we present the average 30 m spectra of each source extracted from a square region ([20″, 20″] to [-20″, -20″] offset) around the SMA continuum peak (Figure 4.2). Using the "Splatalogue" database, we identified 32 lines from 14 species (including 20 isotopologues) in the 1 mm & 3 mm band (Table 4.3, with the lines detected in the "extra band" in blue). Most of them are "late depleters" which have low critical densities, low E_u/k_B and low binding energies, and thus are hard to deplete onto grain surfaces (Bergin 2003).

Molecular spatial distribution

We plot the profile of each line in Figure C1, list the linewidths ($\Delta\upsilon$) of all the detected transitions in Table C1, and integrate their intensities along 5 channels around the V_{lsr} (corresponding to the velocity range from $V_{lsr} - 1\,km\,s^{-1}$ to $V_{lsr} + 1\,km\,s^{-1}$ for 3 mm lines, and from $V_{lsr} - 2\,km\,s^{-1}$ to $V_{lsr} + 2\,km\,s^{-1}$ for 1 mm lines). For the lines with hyperfine structures, we map the one with strongest relative intensity $\ell(300\,K)$. These integrations cover the FWHM of each line, and reveal to us the molecular spatial distribution with adequate contrast from emission peak to deficient regions, shown in Figure 4.3I–IV. In comparing to the 870 μm continuum, most species are found to have the strongest emission at the continuum peak, while a few of them show special features:

- **NH_2D** is detected in all sources, with the emission peak shift from the continuum peak 5″–10″ (G 28.34S, IRDC 18530, 18306) or appearing ring shaped structure surrounding the continuum peak (IRDC 18308). This species traces the cold (T < 20 K) dense gas, and can have enhanced abundance by deuteration from NH_3 ($H_3^+ + HD \rightarrow H_2D^+ + H_2 + \Delta E$) when CO has frozen out onto the grain (Crapsi et al. 2005; Chen et al. 2011; Pillai et al. 2011).

- **HCN** and **$H^{13}CN$** have 3 hyperfine lines, and they are detected co-spatially at the continuum peak in G 28.34 S and IRDC 18308. In IRDC 18306, their strongest emission is detected 20″ north from the continuum peak. Furthermore, the line with the strongest relative intensity (F = 2 → 1) is anomalously weak compared to the other two (Figure 4.4C). This species has been suggested as a high density gas tracer and is a well-known infall motion tracer in low mass star forming regions (e.g., Sohn et al. 2007); the boost or suppress of the individual hyperfine line indicates they are in non-LTE (Loughnane et al. 2012).

- **HNCO** shows strong emission in G 28.34 S and IRDC 18530, but is undetected in the other two sources. It is the simplest organic species containing C, H, O and N, and it has been suggested as a shock tracer in protostellar objects from its correlated spatial distribution with SiO (e.g., Zinchenko et al. 2000) and CH_3OH (e.g., Meier & Turner 2005).

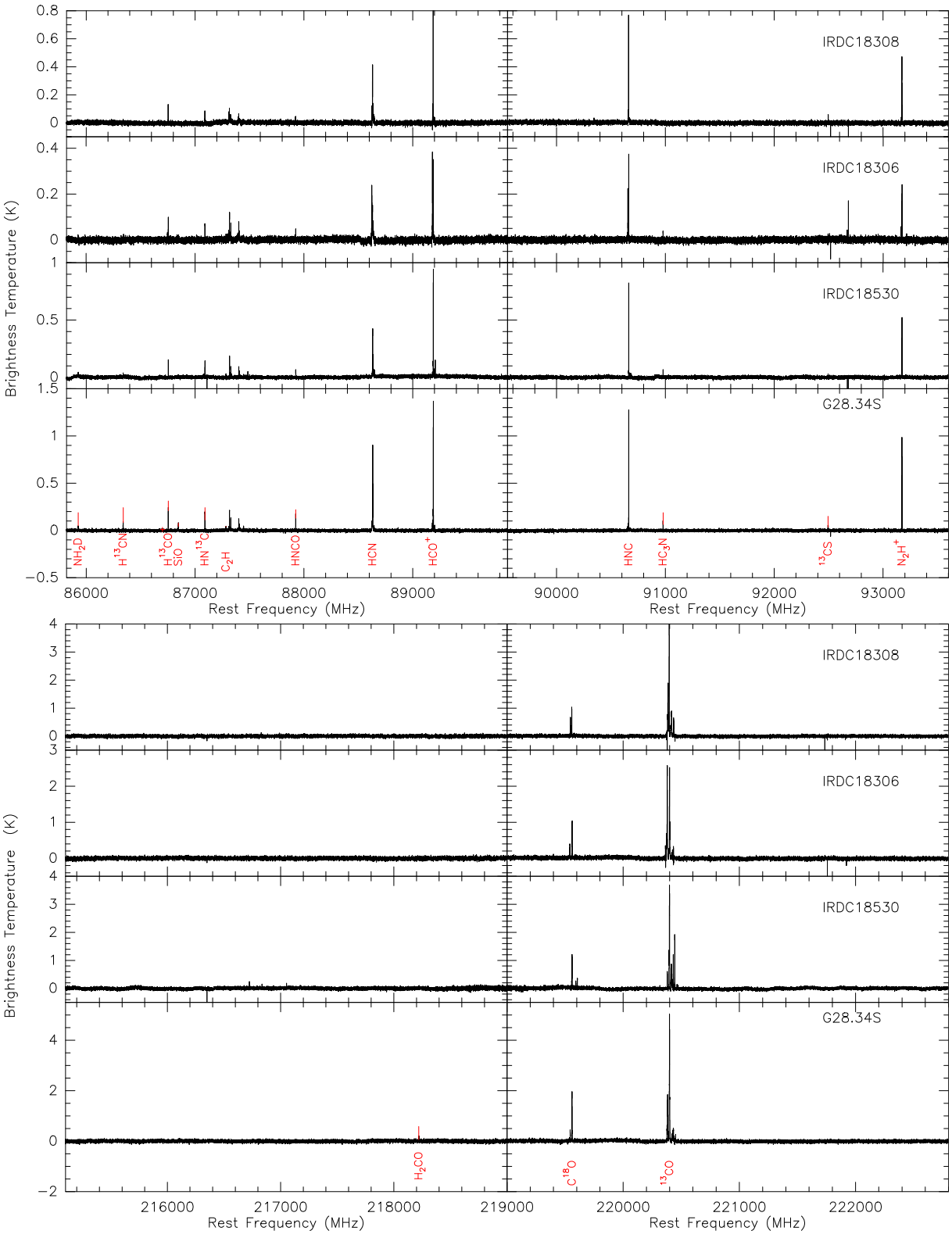

Figure 4.2: Averaged spectra from IRAM 30 m line survey at 1 mm & 3 mm, which is extracted from a square region ([20″, 20″] to [-20″, -20″] offset) around the SMA continuum peak. The spectral resolution is 0.194 MHz (0.265 km s^{-1} at 1 mm and 0.641 km s^{-1} at 3 mm). All detected lines are labeled.

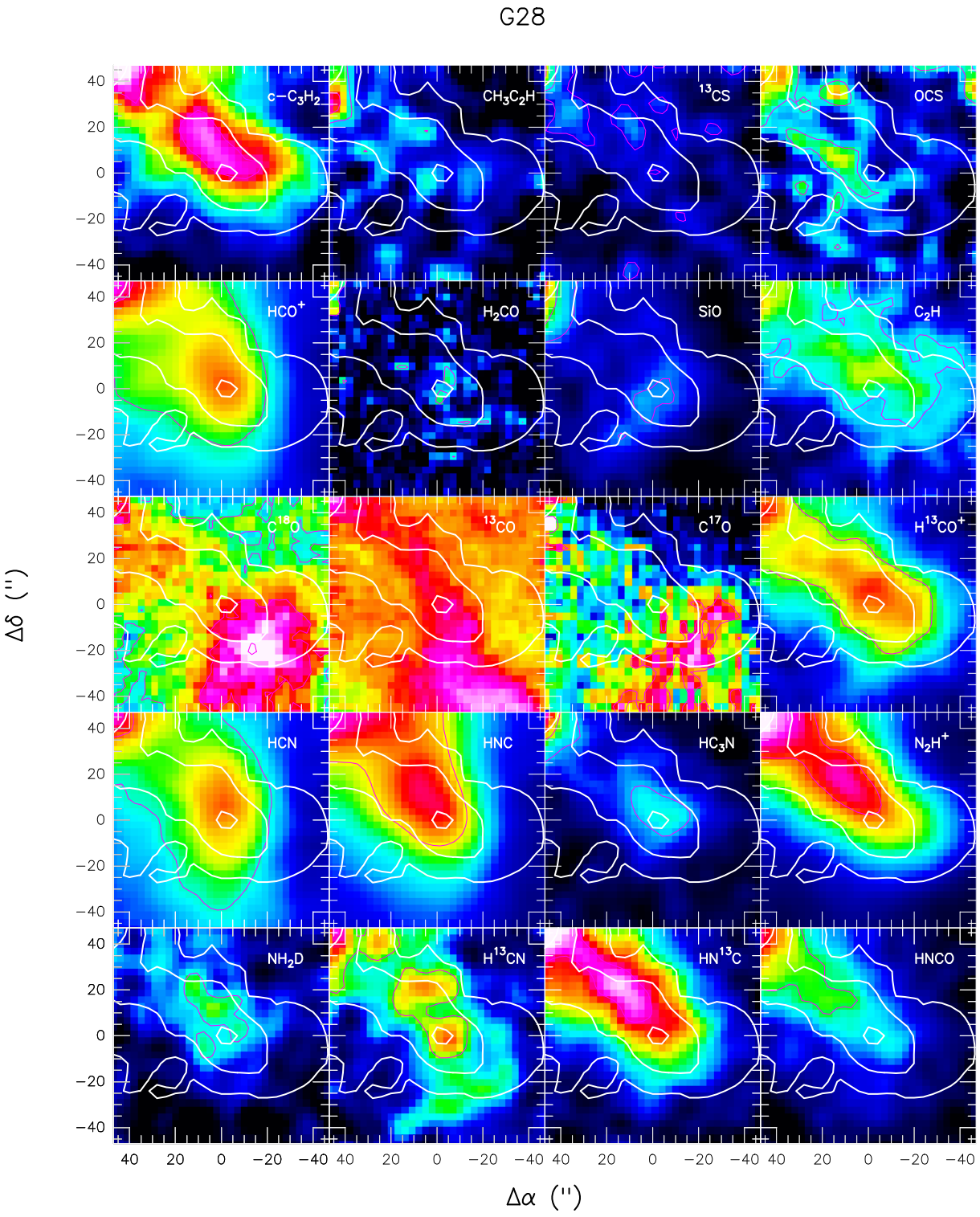

Figure 4.3: Molecular spatial distribution in G 28.34 S, IRDC 18530, IRDC 18306 and IRDC 18308. Colormaps show the intensity integrations in the velocity range from $V_{lsr} - 1\,km\,s^{-1}$ to $V_{lsr} + 1\,km\,s^{-1}$ for 3 mm lines and from $V_{lsr} - 2\,km\,s^{-1}$ to $V_{lsr} + 2\,km\,s^{-1}$ for 1 mm lines. The red contour in each panel show 3σ rms of the integrated intensity. The white contours show the continuum emission from 870 μm ATLASGAL data, starting from 10σ and increase with 10σ.

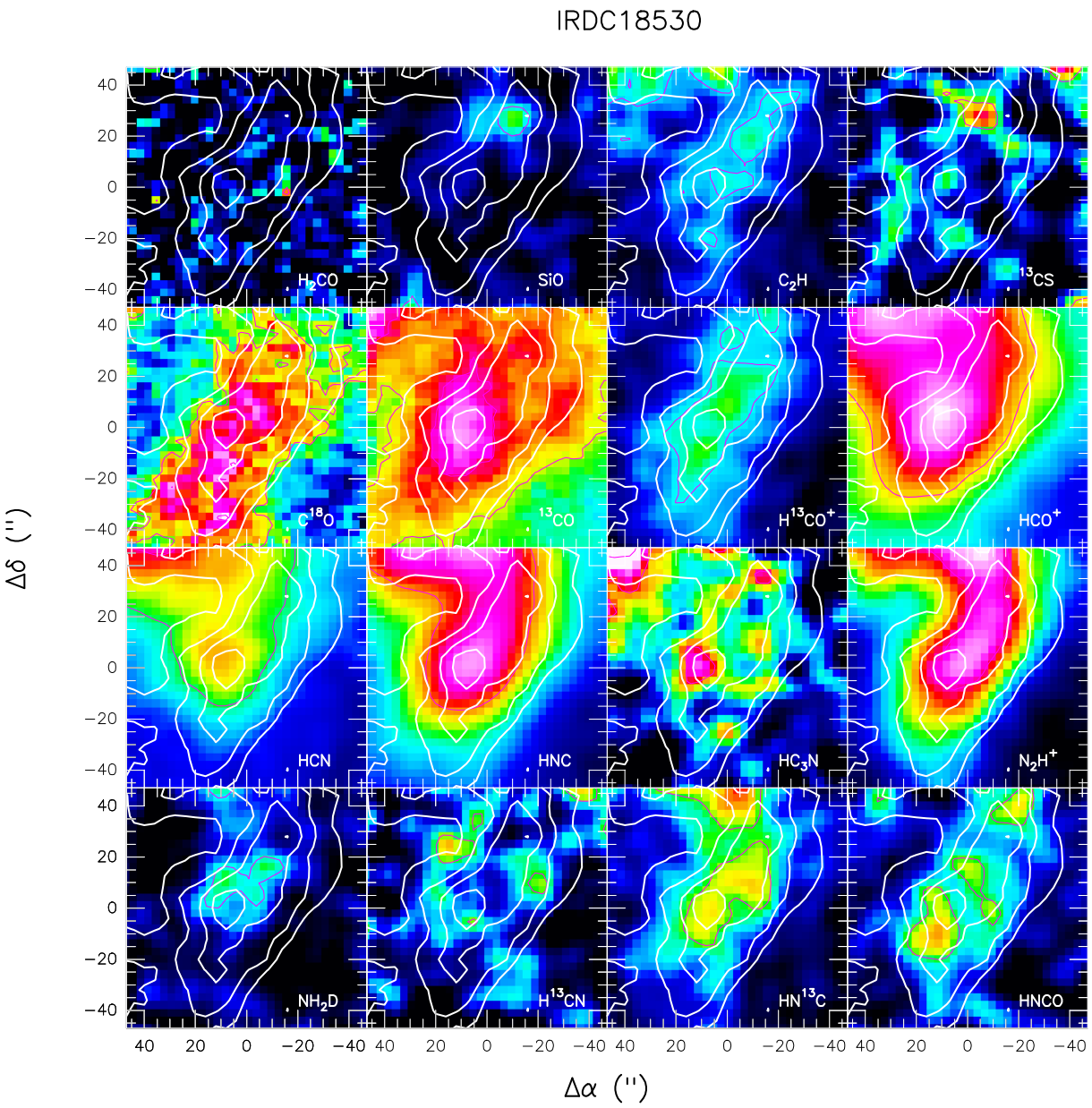

Figure 4.3: (continued)

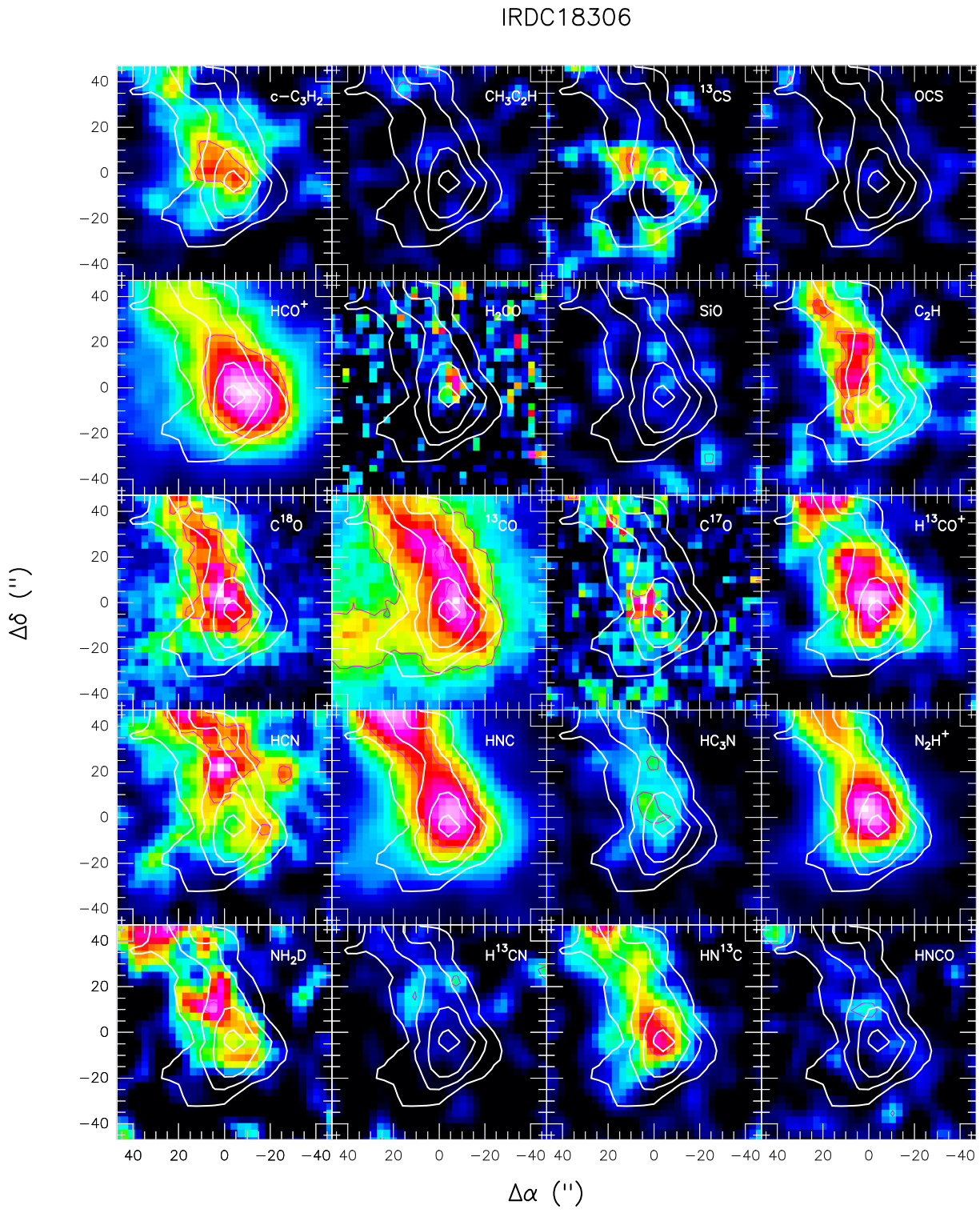

Figure 4.3: (continued)

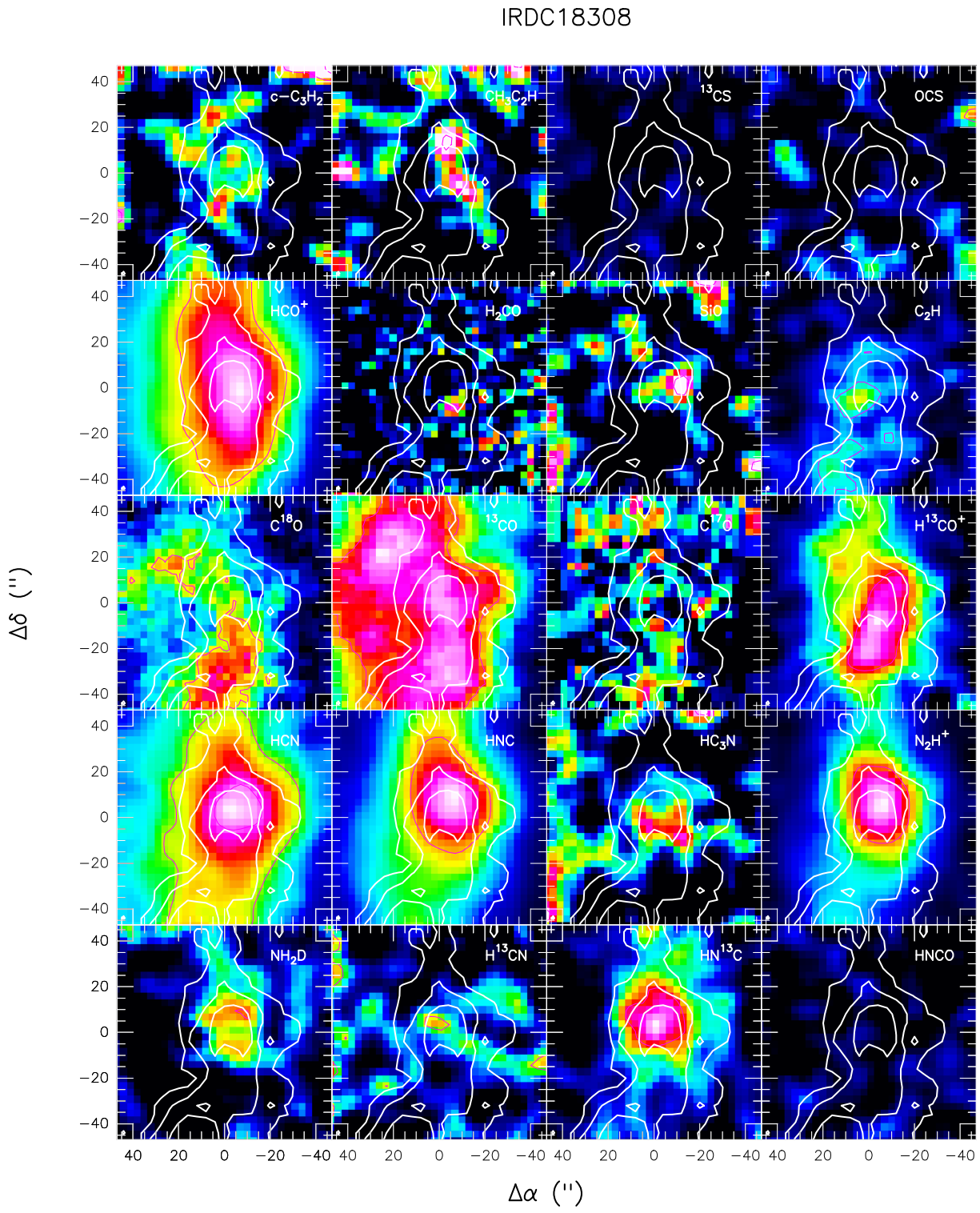

Figure 4.3: (continued)

Table 4.3: Identified lines from 30 m dataset, with the lines detected in the "extra band" in blue. Lines are imaged in Figure 4.3.

Freq. (MHz)	Mol.	Transition	ℓ(300K)	Sμ^2 (D^2)	E_l (cm)	E_u/k (K)
85139.103	OCS	J = 7 → 6	-3.79540	3.58037	8.51990	16.34417
85338.894	c-C_3H_2	$2_{1,2} \rightarrow 1_{0,1}$	-3.74410	48.14839	1.63320	6.44539
85455.667	CH_3C_2H	$5_1 \rightarrow 4_1$	-4.81870	1.79654	10.72420	19.53084
85457.300	CH_3C_2H	$5_0 \rightarrow 4_0$	-4.79050	1.87136	5.70120	12.30399
85926.270	NH_2D	$1_{1,1,0s} \rightarrow 1_{0,1,0a}$, F = 2 → 2	-3.83790	11.91549	11.50630	20.67869
86338.733	$H^{13}CN$	J = 1 → 0, F = 1 → 1	-3.02460	8.91106	0.00000	4.14358
86340.163	$H^{13}CN$	J = 1 → 0, F = 2 → 1	-2.80270	14.85302	0.00000	4.14365
86342.251	$H^{13}CN$	J = 1 → 0, F = 0 → 1	-3.50170	2.97026	0.00000	4.14375
86754.288	$H^{13}CO^+$	J = 1 → 0	-2.28080	15.21089	0.00000	4.16353
86846.960	SiO	J = 2 → 1	-2.48320	19.19714	1.44850	6.25203
87090.850	$HN^{13}C$	J = 1 → 0	-2.59520	7.28184	0.00000	4.17968
87284.105	C_2H	N = 1 → 1, J = 3/2 → 1/2, F = 1 → 1	-5.18050	0.10046	0.00150	4.19111
87316.898	C_2H	N = 1 → 1, J = 3/2 → 1/2, F = 2 → 1	-4.18850	0.98557	0.00150	4.19268
87328.585	C_2H	N = 1 → 1, J = 3/2 → 1/2, F = 1 → 0	-4.49110	0.49087	0.00000	4.19109
87401.989	C_2H	N = 1 → 1, J = 1/2 → 1/2, F = 1 → 1	-4.49040	0.49084	0.00150	4.19677
87407.165	C_2H	N = 1 → 1, J = 1/2 → 1/2, F = 0 → 1	-4.88650	0.19715	0.00150	4.19702
87446.470	C_2H	N = 1 → 0, J = 1/2 → 1/2, F = 1 → 0	-5.17890	0.10046	0.00000	4.19674
87924.351	HNCO	$4_{0,4} \rightarrow 3_{0,3}$, F = 3 → 3	-5.41310	0.20803	4.39940	10.54940
88630.416	HCN	J = 1 → 0, F = 1 → 1	-2.99110	8.91247	0.00000	4.25356
88631.848	HCN	J = 1 → 0, F = 2 → 1	-2.76930	14.85197	0.00000	4.25363
88633.936	HCN	J = 1 → 0, F = 0 → 1	-3.46820	2.97073	0.00000	4.25373
89188.525	HCO^+	J = 1 → 0	-2.26080	15.21022	0.00000	4.28035
90663.568	HNC	J = 1 → 0	-2.52180	9.30176	0.00000	4.35114
90979.023	HC_3N	J = 10 → 9	-2.28480	139.25442	13.65650	24.01482
92494.308	^{13}CS	J = 2 → 1	-2.80010	15.33521	1.54270	6.65859
93171.880	N_2H^{+*}	J = 1 → 0, F1 = 1 → 1	-2.78440	37.25038	0.00000	4.47152
93173.700	N_2H^{+*}	J = 1 → 0, F1 = 2 → 1	-2.56250	62.08887	0.00000	4.47161
93176.130	N_2H^{+*}	J = 1 → 0, F1 = 0 → 1	-3.26140	12.41913	0.00000	4.47172
218222.192	H_2CO	$3_{0,3} \rightarrow 2_{0,2}$	-2.76900	16.30796	7.28640	20.95640
219560.354	$C^{18}O$	J = 2 → 1	-4.17940	0.02440	3.66190	15.80580
220398.684	^{13}CO	J = 2 → 1	-4.17490	0.04869	3.67590	15.86618
224714.385	$C^{17}O$	J = 2 → 1	-4.15090	0.02432	3.74790	16.17689

*. N_2H^+ hyperfine structures are blended, so here list 3 most strongest emissions.

- **HNC** and **HN^{13}C** are detected co-spatially at the continuum peak. It has been reported from previous studies that the ratio of HCN/HNC is strongly temperature dependent: high in the warmer region like Orion GMC (Goldsmith et al. 1986a; Schilke et al. 1992) and approximately around unity (Sarrasin et al. 2010) in the cold environment (see discussion in Section 4.4.3).

- **HC$_3$N** is only detected in G 28.34 S and IRDC 18306. It has been found in different types of clouds and is used as a dense gas tracer due to its relatively low optical depth transitions, large dipole moment, and simple linear structure (Bergin et al. 1996).

- **N$_2$H$^+$** is detected in all the four sources. It is a well-known quiescent gas tracer (Caselli et al. 2002a), having previously been detected in both low mass and high mass prestellar cores of dark clouds (e.g., Lee et al. 2001; Pirogov et al. 2003; Fuller et al. 2005; Ragan et al. 2006; Sanhueza et al. 2012; Fontani et al. 2014), and showing anti-correlated spatial distribution with CO. It has multiplet lines at 3 mm, so hyperfine structure fitting is crucial to reveal us the excitation temperature of this species (Table 4.5), and thus indicate the interior kinetic properties of the dark, quiescent regions.

- **^{13}CO**, **C^{18}O** and **C^{17}O** show clear anti-correlation in the spatial distribution with N_2H^+ and NH_2D in G 28.34 S and IRDC 18308, indicating strong depletion in these sources (see discussion in Section 4.4.4). As the second most abundant molecule in the gas phase and possessing a low dipole moment and low critical density, CO can be used to indicate the gas temperature (e.g., Table 4.6).

- **HCO$^+$** and **H^{13}CO$^+$** have strong emission at the continuum peak. However, the line profile of HCO^+ shows an asymmetric non-Gaussian structure, which is different from that of $H^{13}CO^+$. We estimate the shift of $H^{13}CO^+$ in our sources by using $\delta V_{H^{13}CO^+} = (V_{HCO^+} - V_{H^{13}CO^+})/\Delta\upsilon_{H^{13}CO^+}$ Mardones et al. (1997), finding all the $|\delta V_{H^{13}CO^+}| < 0.6$ (Table 4.7), indicative of non-violent dynamics. However, $|\delta V_{H^{13}CO^+}| = 0.51$ in G 28.34 S potentially indicates infall motion. HCO^+ is the typical dense gas tracer produced from CO, and has enhanced abundances around regions with a high ionization fraction and those shocked by outflows (e.g., Codella et al. 2001; Hofner et al. 2001; Rawlings et al. 2000, 2004). To estimate the infall velocity, we need high velocity resolution observations to resolve the red and blue shifted peaks (e.g., Myers et al. 1996).

- **H$_2$CO** is only detected in G 28.34 S. It is an important carbon hydrid which forms CH_3OH and more complex organics later in the gas phase. Sublimation of this species needs a warmer environment, so the detection of this species indicates the host envelope may be in a more evolved phase.

- **SiO** is only detected in G 28.34 S. As a typical shocked gas tracer, its detection indicates an embedded, energetic young outflow(s). However, SiO in G 28.34 S can also come from the strong infrared bright source 40″ south to our source center, or may from G 28.34 P1 which is 1′ north and embeds a jet-like outflow (Wang et al. 2011a). Therefore, the origin of SiO is crucial to diagnose the evolutionary stage of G 28.34 S, and thus needs to be investigated by further kinetic study with higher spatial resolution.

- **C_2H** has multiplet resolved in our data, and it is detected in all of four sources, but with a 5″-10″ shifted from the continuum peaks. It has been predicted by chemical model as residing in the source center in the early stage before being destroyed in the center, and it can be replenished in the outer shells at later stages (Beuther et al. 2008).

- **c-C_3H_2** is well centered at the continuum peak in G 28.34 S and IRDC 18306, and locate in a region surrounding the center of IRDC 18308. This carbon ring was firstly detected in cold dark cloud TMC-1 by Matthews & Irvine (1985). A recent study shows that it traces more external layers than NH_3 (Palau et al. 2014).

- **CH_3C_2H** is only marginally detected in G 28.34 S and IRDC 18306, with the emission shifted 20″ from the continuum peak, so we do not claim this detection. It is considered as a good probe of temperature for early stages of star-forming regions (Bergin et al. 1994).

- **^{13}CS** is detected around the continuum peak of G 28.34 S and IRDC 18306. Owing to its high dipole moment, it is used as a dense gas tracer (e.g., Bronfman et al. 1996). Its detection in both low mass (e.g., Tafalla et al. 2002) and high mass prestellar cores (e.g., Jones et al. 2008) indicates high depletion in the source center (Beuther & Henning 2009).

- **OCS** is only detected in G 28.34 S. This species forms via surface chemistry. It is the only S-bearing molecules that has actually been observed on interstellar ices (Palumbo et al. 1997).

In short, G 28.34 S appears the most chemically evolved in our sample with the sole detections of H_2CO, HC_3N, OCS, strong emission of HNCO, with HCO^+ asymmetric line profile implying infall, and SiO indicating potential protostellar objects embedded. IRDC 18306 is most likely younger than G 28.34 S, but more evolved than the other two cores.

4.4 Analysis and Discussion

4.4.1 Fragmentation

Fig. 4.1 presents the continuum maps from *Herschel* at 70 μm, from ATLASGAL at 870 μm and from SMA at 1.1 mm. Since the maps from SMA with COMP+EXT configuration have filtered out some extended structures, the following calculations are based on the COMP configuration only data.

With an assumption that dust emission is optically thin, and that the dust has the same temperature T_{dust} as the surrounding gas, we estimate the mass of each fragments resolved on the SMA continuum maps as (Hildebrand 1983):

$$M_{fr} = M_{frgas} + M_{frdust} = \frac{S_\nu (R+1) D^2}{B_\nu(T_{dust})\kappa_\nu} \qquad (g) \tag{4.1}$$

where M_{fr} is the total mass of dust and gas in one fragment, D is the source kinematic distance (from the sun), S_ν is the total continuum flux density at frequency ν (Hz) (measured from the region with $> 5\sigma$ rms emission, in units of Jy), R is the isothermal gas to dust mass ratio (taken to be 150, from Draine 2011), $B_\nu(T_{dust})$ is the Planck function for a dust temperature T_{dust}, and $\kappa_\nu = 1.0\ cm^2 g^{-1}$ is the dust absorption coefficient at 1.1 mm (assuming a model of agglomerated grains with thick ice mantles for densities $10^5\ cm^{-3}$, extrapolated from Ossenkopf & Henning 1994).

Assuming that each fragment is spherically symmetric, we then estimate its gas volume number density n_{fr} from its size θ_{fr} (assuming an effective emitting region equal to the projected area showing $> 5\sigma$ rms continuum emission, in units of rad)[7] as:

$$n_{fr} = \frac{6 M_{frgas}}{\pi \mu m_H \theta_{fr}^3} \qquad (cm^{-3}) \tag{4.2}$$

with the mass of an hydrogen atom m_H and the mean molecular weight of the ISM $\mu = 2.33$.

Assuming the fragmentation is governed by Jeans instabilities, the Jeans length and Jeans mass can be estimated as

$$\lambda_J = c_s \left(\frac{\pi}{G\mu m_H n_{fr}}\right)^{1/2} = 0.067\ pc \left(\frac{T_{dust}}{10\,K}\right)^{1/2} \left(\frac{n_{fr}}{10^5\ cm^{-3}}\right)^{-1/2} \tag{4.3}$$

$$M_J = \frac{c_s^3}{6} \left(\frac{\pi^5}{G^3 \mu m_H n_{fr}}\right)^{1/2} = 0.912\ M_\odot \left(\frac{T_{dust}}{10\,K}\right)^{3/2} \left(\frac{n_{fr}}{10^5\ cm^{-3}}\right)^{-1/2} \tag{4.4}$$

[7] A more precise estimation requires 2-D Gaussian fitting, e.g., Zhang et al. (2009); Wang et al. (2011a).

where G is the gravitational constant (6.67×10^{-8} $cm^3 g^{-1} s^{-2}$), and $c_s = [k_B T_{dust}/(\mu m_H)]^{1/2}$ is the speed of sound at temperature T_{dust}.

As described in Table 4.4I, we find the size of fragments are 2–4 times larger than the synthetic beam size, so the filling factor is taken as unity. Moreover, we found the mass of fragments and the average projected separation in between fragments are on average 10–60 times larger than the expected Jeans mass and Jeans length. In particular, fragments in G 28.34 S and IRDC 18306 all have a mass $> 10\,M_\odot$. Since Jeans fragmentation describes the process when the internal pressure is dominated by the thermal motions, the above comparison indicates that non-thermal motions, such as turbulence may play an important role in fragmentation (Wang et al. 2011a, 2014).

To investigate whether non-thermal pressure supports the mass of the fragments, we need to measure the velocity dispersion over the whole clump, which is derived from the linewidth of the dense gas tracer(s). Collated in Table C1, linewidths of all the species are on average 2–3 $km\,s^{-1}$. $H^{13}CO^+$ ($1 \rightarrow 0$) has a high critical density ($n_{crit} > 10^4$ cm^{-3}, Bergin & Tafalla 2007; Csengeri et al. 2011), low E_u/k_B (4 K), and no hyperfine structure. Its velocity dispersion is not impacted by Galactic spiral arms (e.g., the line profiles of CO, $C^{18}O$ and $C^{17}O$ along the line of sight are contributions from various Galactic arms, see Beuther & Sridharan 2007), showing symmetric Gaussian profile, we use this line to measure the observed line of sight velocity dispersion $\sigma_{obs} = \sqrt{\Delta\upsilon/(8\ln 2)}$. Since the structures observed with IRAM 30 m appear more extended than with the SMA, we assume the averaged gas temperature in the whole clump T_g not higher than that in the fragments T_{dust}. Comparing σ_{obs} to the thermal broaden velocity dispersion $\sigma_{th} = \sqrt{8\ln 2 k_B T_g/(\mu m_H)}$, we estimate the non-thermal broaden velocity dispersion $\sigma_{Nth} = \sqrt{\sigma^2_{obs} - \sigma^2_{th}}$, and list them in Table 4.4II. If the real gas temperature is $T_g \leq 10$ K, σ_{obs} throughout the whole source clump (size of $\sim 10^5$ AU) is mainly contributed by non-thermal motions.

Comparing with the large scale filamentary gas distribution at 870 μm, the small scale SMA fragments are well aligned with roughly the same projected separation (Figure 4.1). This feature has been reported from previous observations of other HMSFRs (e.g., the "Nessie" Nebula by Jackson et al. (2010), G 28.34 S P1 by Wang et al. (2011a), G11.11-0.12 by Wang et al. (2014) and NGC 7538 S discussed in Chapter 3). Moreover, theoretical simulations have predicted that isothermal, "cylindrical" gas collapses into a chain of fragments, with equal spatial separation λ_{cl} along the filament under self gravity; the fragments grow due to instability afterwards (Chandrasekhar & Fermi 1953; Nagasawa 1987; Bastien et al. 1991; Inutsuka & Miyama 1992; Fischera & Martin 2012). Without the impact from magnetic field, the critical linear mass density $(M/l)_{crit}$ ($M_\odot pc^{-1}$) represents the mass over which self-gravity overcomes the internal thermal

I. Fragments in each source from SMA observations at 1.1 mm, with the expected Jeans mass and Jeans length

Source	RA J[2000]	Dec J[2000]	I_ν ($\frac{mJy}{beam}$)	S_ν (mJy)	θ_{fr} ($''$)	T (K)	N_{peak} $10^{23}(cm^{-2})$	n_{fr} $10^5(cm^{-3})$	M_{fr} ($M_\odot$)	λ_{fr} (pc)	M_{Jeans} ($M_\odot$)	λ_{Jeans} (pc)
G28	18^h42^m	$-04°04''$				15				0.22		
	A $46^s.426$	$15'.54$	30.0	85.0	9.54		4.49	2.23	65.09		1.12	0.06
	B $46^s.904$	$07'.08$	9.0	48.0	9.34		1.35	1.34	36.75		1.45	0.07
IRDC 18350	18^h55^m	$02°17''$				15				0.15		
	A $29^s.963$	$09'.28$	7.0	16.0	6.19		1.05	1.57	11.72		1.34	0.07
	B $30^s.165$	$07'.76$	5.8	11.0	4.86		0.87	2.23	8.06		1.12	0.06
	C $30^s.534$	$12'.09$	5.3	6.3	4.35		0.79	1.78	4.62		1.25	0.06
IRDC 18306	18^h33^m	$-08°32''$				15				0.18		
	A $31^s.609$	$29'.36$	17.6	36.0	7.15		2.64	2.87	16.88		0.99	0.05
	B $32^s.230$	$29'.58$	10.7	41.0	8.26		1.60	2.12	19.23		1.15	0.06
IRDC 18308	18^h33^m	$-08°$				15				0.12		
	A $35^s.194$	$35''59'.55$	10.3	16.0	5.08		1.54	2.90	11.21		0.98	0.05
	B $34^s.990$	$36''04'.53$	7.3	9.6	4.16		1.09	3.17	6.73		0.94	0.05
	C $35^s.194$	$36''09'.52$	11.9	23.0	5.99		1.78	2.55	16.11		1.05	0.05

λ_{fr} is the mean projected separation of condensations

II. Linewidth of $H^{13}CO^+$ ($1 \rightarrow 0$) in each source from 30 m observations, with the expected critical mass and length from cylindrical fragmentation

Source	$\Delta\upsilon$ (km s^{-1})	σ_{obs} (km s^{-1})	T_g (K)	σ_{th} (km s^{-1})	σ_{Nth} (km s^{-1})	n_c (10^5 cm^{-3})	λ_{cl} (pc)	M_{cl} ($M_\odot$)
G28	3.07 ± 0.06	0.74 ± 0.01	5	0.31	0.67 ± 0.01	3.60	0.49	126.00
			10	0.44	0.60 ± 0.01			
			15	0.54	0.51 ± 0.01			
IRDC 18530	2.01 ± 0.06	0.60 ± 0.01	5	0.31	0.51 ± 0.01	3.28	0.41	69.80
			10	0.44	0.41 ± 0.01			
			15	0.54	0.26 ± 0.02			
IRDC 18306	2.05 ± 0.10	0.61 ± 0.01	5	0.31	0.52 ± 0.02	5.08	0.34	57.70
			10	0.44	0.41 ± 0.02			
			15	0.54	0.27 ± 0.03			
IRDC 18308	2.09 ± 0.09	0.61 ± 0.01	5	0.31	0.53 ± 0.01	1.07	0.74	129.00
			10	0.44	0.42 ± 0.02			
			15	0.54	0.28 ± 0.03			

n_c is measured from ATLASGAL survey at 870 μm

Table 4.4: Parameters of the fragments and two hypotheses of fragmentation. Table I lists the parameters measured from SMA observations at 1.1 mm: the coordinates, specific intensity at continuum peak, total flux density and source size within 5σ rms continuum emission region. H_2 column density at the continuum peak and the average volume density within 5σ rms region are estimated at 15 K. The mass of each fragment and the projected separation in between them are higher than the Jeans mass and Jeans length of the whole clump on the order of 10–60. Table II lists the averaged linewidth of $H^{13}CO^+$ ($1 \rightarrow 0$) in a $40''\times40''$ region (from [$20''$, $20''$] to [-$20''$, -$20''$] offset, corresponding to $\sim 1.5 \times 10^5$ AU) obtained from 30 m observations. The velocity desperation in each source along with the thermal and non-thermal components are estimated at 5 K, 10 K and 15 K. The critical mass and length of cylindrical fragmentation support the observed values in Table I.

and non-thermal pressure. The critical separation λ_{cl} and critical mass of fragment M_{cl} in the large scale clump are given as (Chandrasekhar & Fermi 1953; Nagasawa 1987):

$$(M/l)_{crit} = 2\sigma^2_{obs}/G = 465.02(\frac{\sigma_{obs}}{1\,km\ s^{-1}})^2\,M_\odot pc^{-1} \quad (4.5)$$

$$\lambda_{cl} = 22c_{sc}(4\pi G\mu m_H n_c)^{-1/2} = 1.248\,pc(\frac{\sigma_{obs}}{1\,km\ s^{-1}})(\frac{n_c}{10^5\,cm^{-3}})^{-1/2} \quad (4.6)$$

$$M_{cl} = M_{crit}\lambda_{cl} = 580.381\,M_\odot(\frac{\sigma_{obs}}{1\,km\ s^{-1}})^3(\frac{n_c}{10^5\,cm^{-3}})^{-1/2} \quad (4.7)$$

where $c_{sc} = \sigma_{obs}$ is the velocity dispersion if thermal motions are not sufficient to support the mass (Fiege & Pudritz 2000), and n_c is the average number density in the 40″×40″ region.

We list the critical mass and separation of each source estimated from cylindrical fragmentation in Table 4.4II, and find they are higher than the observed mass and projected separation. That is to say, even without magnetic field taken into consideration, non-thermal motion, such as turbulence is sufficient to support the fragments with mass up to $\sim 100\,M_\odot$.

In short, the mass of the initial fragments resolved from 1.1 mm SMA observation are already high (on average $> 10\,M_\odot$), as predicted by the "core accretion" scenario. Jeans instability alone can not compete against the self-gravity of these fragments, though, the combination of thermal and non-thermal motions can provide the support in opposing the collapse of the fragments.

4.4.2 Molecular column density and abundance

No emission from higher-J molecular transitions are detected in the fragments with the SMA observations, but lower-J transitions of the dense gas tracers are detected in the extended structures with the 30 m line survey. This indicates our sources are in the cold, young evolutionary stage. To probe the chemical properties in the young gas clumps, we need to quantify molecular abundances and excitation conditions in these regions.

Molecular column densities

First, we calculated the molecular column densities averaged from the central 40″×40″ region of each source in reducing noise. In case of large uncertainties brought by the optical depth of certain line, we use different method to correct them.

• N_2H^+, C_2H, HCN and $H^{13}CN$:
These lines have multiplet in their $J = 1 \rightarrow 0$ transitions (multiplet of C_2H is at $N = 1 \rightarrow 0$), so we use the "HFS" method based on the CLASS software package[8] to fit them. The relative intensities between multiplet are converted from the ℓ(300K) value in the "Splatalogue" database.

Four assumptions are made in the "HFS" method in fitting a species: ① All the components of the multiplet have the same excitation temperature. ② The lines and their optical depths have Gaussian profiles. ③ All the multiplets have the same linewidth. ④ The multiplet components do not overlap. With the beam filling factor f, background radiation temperature T_{bg} (assumed to be 2.7 K) and the intensity in unit of temperature $J_\nu(T) = (h\nu/k_B)/[\exp(h\nu/k_BT) - 1]$, this method defines an effective intensity A as:

$$A = f[J_\nu(T_{ex}) - J_\nu(T_{bg})] \qquad (K) \tag{4.8}$$

The output parameters are: the optical depth of the strongest line τ_0, V_{lsr}, the linewidth $\Delta\upsilon$ and the value of effective intensity impacted by the line optical depth $A\tau_0$. Therefore, the excitation temperature of the multiplet T_{ex} and the molecular column density N_T are given as:

$$T_{ex} = \frac{h\nu/k_B}{\ln[\frac{h\nu/k_B}{A\tau_0/(f\tau_0)+J_\nu(T_{bg})} + 1]} \qquad (K) \tag{4.9}$$

$$N_{T,\alpha} = \frac{8\pi\nu}{\ell(T_{ex})\eta c^3}\tau_0\Delta\upsilon \qquad (cm^{-2}) \tag{4.10}$$

We present the fittings in Figure 4.4 and list the T_{ex} in Table 4.5. The linewidth of the strongest components are $\Delta\upsilon \sim 1.7$–3.2 km s^{-1}, consistent with the linewidth of other species, indicating non-thermal motions dominate the velocity dispersion.

Using the above method, we fit N_2H^+ ($J = 1 \rightarrow 0$) and C_2H^+ ($N = 1 \rightarrow 0$) well to the observations, but with some deviation in the lines HCN ($J = 1 \rightarrow 0$) and $H^{13}CN$ ($J = 1 \rightarrow 0$), especially in IRDC 18530, IRDC 18306 and IRDC 18308. According to the fitting, most of T_{ex} are low (< 10 K), and the reasons are multifold:

[8] http://www.iram.fr/IRAMFR/GILDAS/doc/html/class-html/class.html

(1) In the cold gas environment with densities of 10^4–10^5 cm^{-2}, species with high critical densities are sub-thermally excited (e.g., at 10 K, the critical density of N_2H^+ is $\sim 2 \times 10^5$ cm^{-3}, and that of HCN is $\sim 10^6$ cm^{-3}, Gerner et al. 2014), so their T_{ex} is lower than the typical kinetic temperatures of IRDCs (e.g., Sridharan et al. 2005; Vasyunina et al. 2011; Fontani et al. 2012), which is a common feature in both high mass and low mass dark clouds (e.g., Caselli et al. 2002b; Crapsi et al. 2005; Miettinen et al. 2011; Fontani et al. 2012).

(2) To reduce the noise, we extract the average spectra from the the 40″×40″ region, but the gas is not homogeneous as assumed. HCN and $H^{13}CN$ is deficient at the continuum peak of IRDC 18530 and IRDC 18306 (Figure 4.3). In particular, HCN (J = 1 → 0) has an anomalous line profile in IRDC 18306. It has been shown by Afonso et al. (1998) that the intensity ratios between multiplets of HCN are not constant values, and individual hyperfine line may be boosted or suppressed in dark clouds because of non-LTE (Loughnane et al. 2012). Therefore, the low T_{ex} are the averaged excitation temperature derived from the unsatisfactorily fitted spectrum (Figure 4.4C).

(3) "HFS" method has four assumptions. ① -③ are valid if the source is in the ideal LTE condition. However, this is not true for the aforementioned reasons. ④ is not applicable for N_2H^+ because 7 multiplet lines are blended into 3 Gaussian peaks in our observations at a velocity resolution of ~ 0.265 km s^{-1} (Figure 4.4A).

(4) When we estimate T_{ex} according to Eq. 4.10, we assume the filling factor f as unity, because our filamentary sources are more extended than the primary beam, and we could not measure the source size for it is beyond our field of view. However, this assumption brings underestimation of T_{ex} by a factor of 2–3 (if f=0.5).

Although these lines may not be thermalized, we assume all the levels of each molecule can be described by an approximately constant T_{ex}. This so called "CTex method" was introduced by Caselli et al. (2002d) in estimating the column density of N_2H^+ with $T_{ex} \sim 5$ K. Here we follow their approach and use Eq. 4.10 to derive the column densities of the above species[9].

• Molecules with neither hyperfine structure nor rare isotopologues

CO is the most important dense gas tracer because of its low dipole moment and thermalisation near its critical density ($\sim 10^3$ cm^{-3}). Although this species may be highly depleted in the cold IRDCs, estimates of the level of depletion where T_{kin} = 10–15 K and n = 10^4–10^5 cm^{-3} are factors of 20–80 (Fontani et al. 2012), meaning it is still more abundant than the other species

[9] A more precise approach is to use non-LTE radiative transfer code RADEX, but it does not significantly improve out results without knowing the source structure.

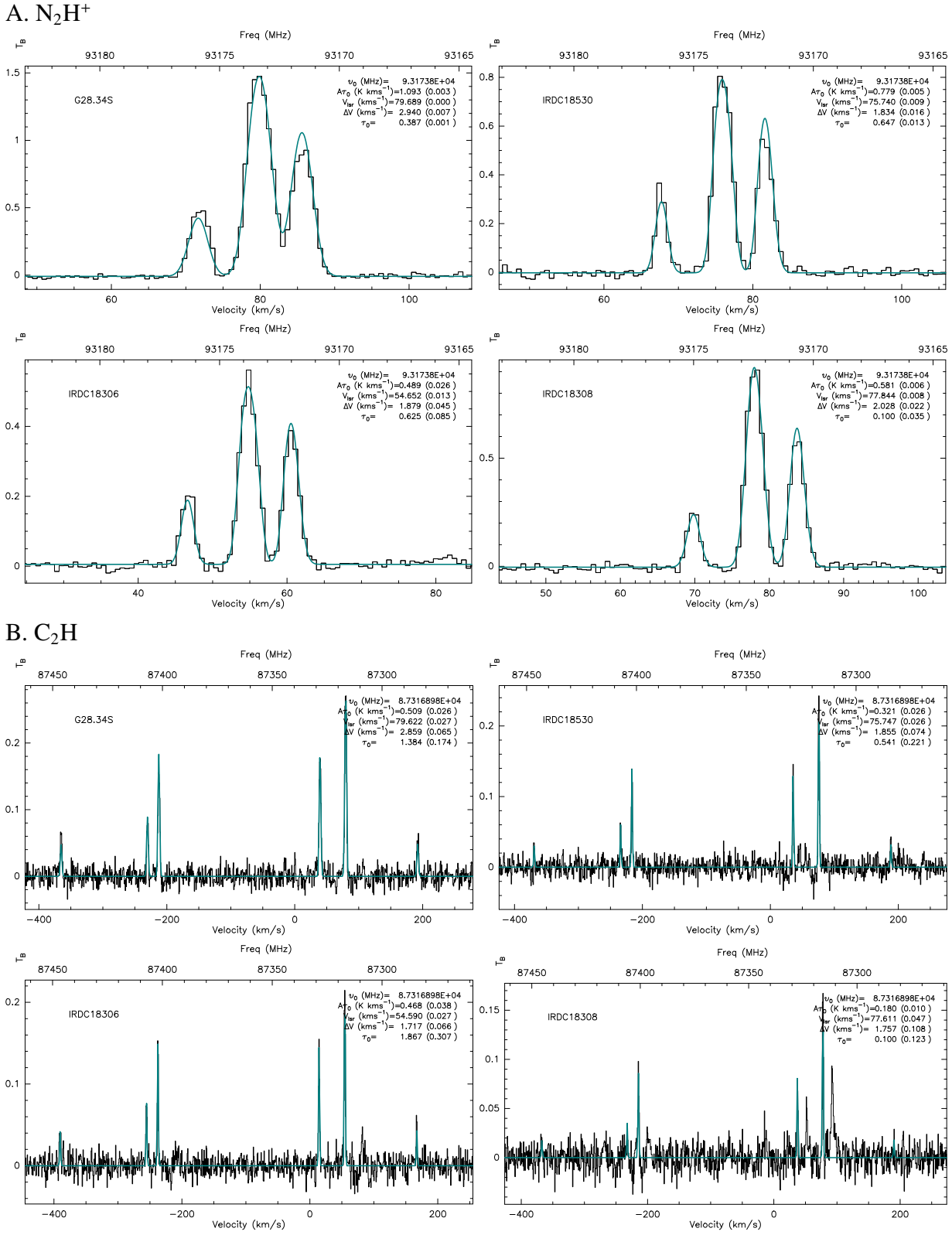

Figure 4.4: Hyperfine structure fittings (green lines) to the observed N_2H^+ (J = 1 → 0), C_2H (N = 1 → 0), HCN (J = 1 → 0) and $H^{13}CN$ (J = 1 → 0) (black histograms) from each IRDC, with the fitting parameters on the right upper corner.

C. HCN

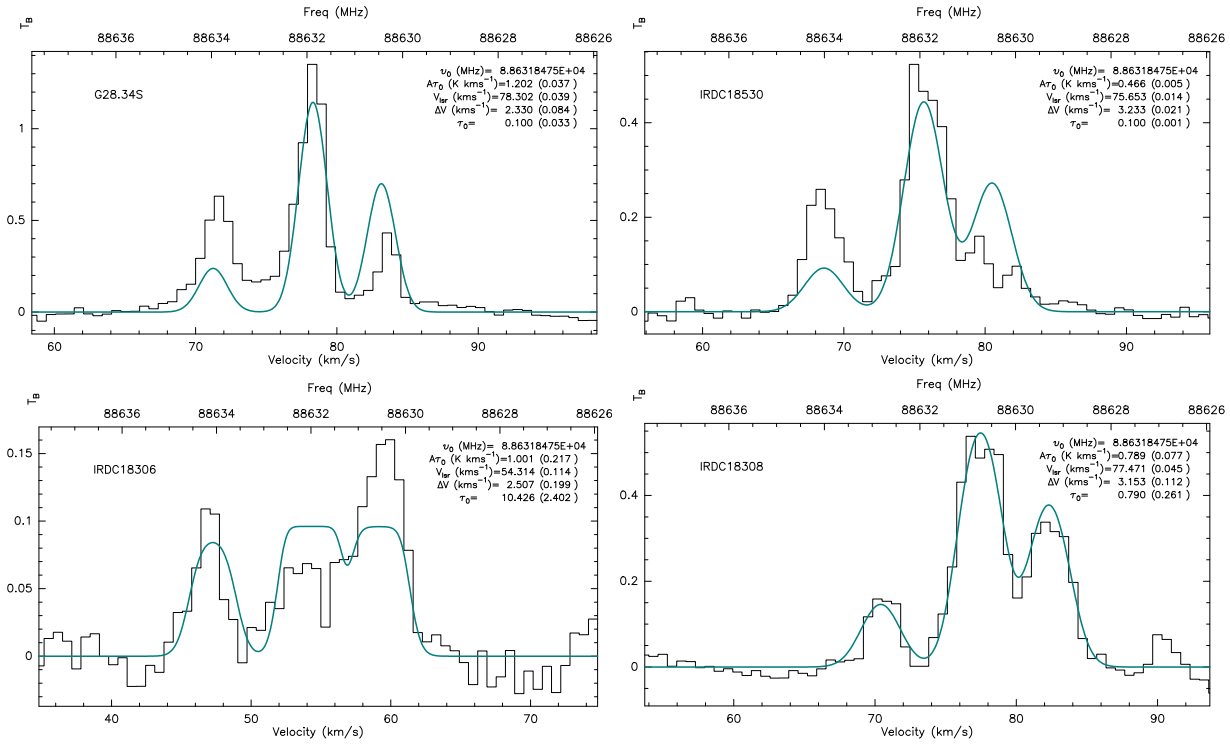

D. $H^{13}CN$

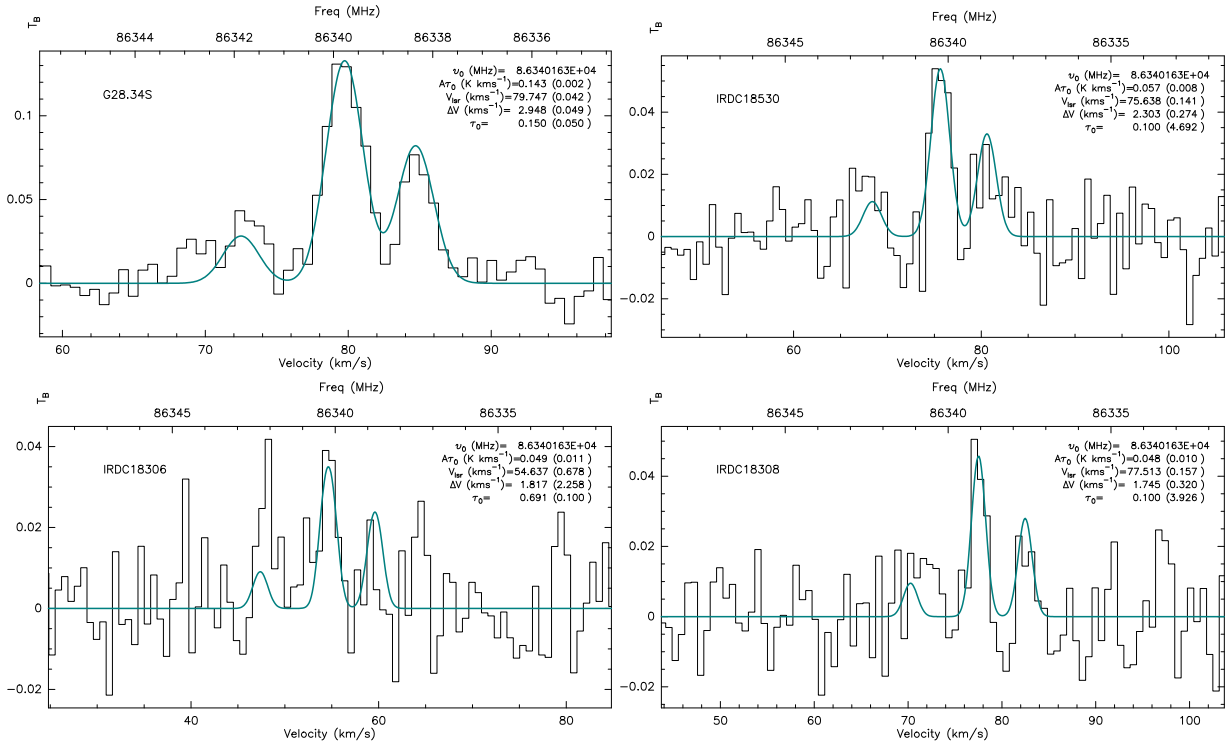

Figure 4.4: (continued)

Table 4.5: T_{ex} derived from hyperfine fittings to N_2H^+, C_2H, HCN and $H^{13}CN$ multiplet in four IRDCs

Species	G 28.34 (K)	IRDC 18530 (K)	IRDC 18306 (K)	IRDC 18308 (K)
N_2H^+ (J = 1 → 0)	5.82 ± 0.04	4.10 ± 0.03	3.62 ± 0.13	8.91 ± 1.49
C_2H (N = 1 → 0)	3.14 ± 0.07	3.39 ± 0.24	3.00 ± 0.06	4.71 ± 1.13
HCN (J = 1 → 0)	15.20 ± 1.62	7.65 ± 0.24	2.82 ± 0.04*	3.76 ± 0.38
$H^{13}CN$ (J = 1 → 0)	4.14 ± 0.88	3.36 ± 0.65*	2.78 ± 0.03*	3.26 ± 0.55*

* Fittings have large deviation from the observation.
** Filling factor f is assumed to be 1.

even taking its depletion into account. Its lower-J transitions are optimally thick, and the ratio between isotopologues have no significant change if without fractional reactions[10], so its T_{ex} can be taken as the T_{kin} of the gas.

^{13}CO (2 → 1), $C^{18}O$ (2 → 1) and $C^{17}O$ (2 → 1) are all detected in our data. Firstly, we use a multi-Gaussian profile to fit their T_{mb} in order to separate the multi-velocity components contributed by Galactic spiral arms. Then, assuming that $C^{17}O$ (2 → 1) is optically thin and that all the lines are in LTE, we use Eq. 2.9 and the "canonical" ratio between isotopes (Eq. 4.12-4.14, Frerking et al. 1982; Wilson & Rood 1994; Giannetti et al. 2014) to correct for the optical depth of ^{13}CO (2 → 1) and $C^{18}O$ (2 → 1). Subsequently, using the following equations, we estimate T_{ex} of each CO isotopologue, and list them in Table 4.6:

$$X^E_{CO} = 9.5 \times 10^{-5} \exp(1.105 - 0.13 D_{GC}) \tag{4.11}$$

$$X^E_{^{13}C} = X^E_{^{12}C}/(7.5 D_{GC} + 7.6) \tag{4.12}$$

$$X^E_{^{18}O} = X^E_{^{16}O}/(58.8 D_{GC} + 37.1) \tag{4.13}$$

$$X^E_{^{17}O} = X^E_{^{16}O}/[3.52 \times (58.8 D_{GC} + 37.1)] \tag{4.14}$$

$$J_\alpha(T_{ex}) = \frac{T_{mb}}{(1 - e^{-\tau_\alpha})} + J_\alpha(T_{bg}) \tag{4.15}$$

where D_{GC} (kpc) is the galactic center distance, and X^E_α is the "canonical" (undepleted) abundance of isotopologue α with respect to H_2.

$C^{18}O$ (1 → 0) is optically thin when its optical depth is measured with $C^{17}O$ (1 → 0)(Table 4.6). Since we did not observe $C^{17}O$ (1 → 0) in IRDC 18530, and the intensity of this line is only ~ 3σ rms in IRDC 18308, we take the optically thin $C^{18}O$ (1 → 0) as a standard to estimate the other chemical parameters afterward. Moreover, as the derived T_{ex} of CO isotopologues are consis-

[10] $^{13}C^+ + ^{12}CO \rightarrow ^{12}C + ^{13}CO + \Delta E$, where $\Delta E/k_B = 35$ K (Watson 1976)

Table 4.6: Optical depth τ and T_{ex} derived for CO ($1 \rightarrow 0$) isotopologues, according to Eq. 2.9, and Eq. 4.12-4.15.

Line	G28		IRDC 18530		IRDC 18306		IRDC 18308	
	τ	T_{ex} (K)	τ	T_{ex} (K)	τ	T_{ex} (K)	τ	T_{ex} (K)
$C^{18}O\,(2 \rightarrow 1)^{*}$	0.25	14	–	–	0.65	8	–	–
$^{13}CO\,(2 \rightarrow 1)^{*}$	2.6	11	–	–	5.8	8	0.9	13
$^{13}CO\,(2 \rightarrow 1)^{**}$	2.8	11	2.9	9	6.6	7	2.1	11

* Derived from $C^{17}O\,(2 \rightarrow 1)$, which is assumed to be optically thin.
** Derived from $C^{18}O\,(2 \rightarrow 1)$, which is assumed to be optically thin.

tent, we assume that species with neither hyperfine structure nor rare isotopologue lines obtained from the 30 m observations are optically thin, and are thermalized at $T_{gas} = T_{dust} = T_{kin} \sim T_{ex,CO}$. Using Eq. 2.7, we derive the column densities of these species.

• HCO^{+}, HNC and ^{13}CO:
^{13}CO ($1 \rightarrow 0$) is optically thick in at least 2 of our sources when measured with $C^{17}O$ ($1 \rightarrow 0$), and the other lines may have the same issue. As we have the rare isotopologues of HCO^{+} ($1 \rightarrow 0$) and HNC ($1 \rightarrow 0$) in our data, we use Eq. 2.9 to obtain their optical depths and correct their column densities, with the assumption that both $H^{13}CO^{+}$ ($1 \rightarrow 0$) and $HN^{13}C$ ($1 \rightarrow 0$) are optically thin.

H_2 column density

Using Eq. 2.10, we derive the column density of H_2 from the 870 μm continuum ($\kappa_{870\,\mu m}$ = 1.8 $cm^2 g^{-1}$), averaged in the same 40″×40″ region. Since the size of the filamentary structure (projected area with $> 10\sigma$ emission) is far larger than the ATLASGAL primary beam (18″), we take the filling factor as unity. At the temperature of $T_{ex,CO} \sim 10$ K, H_2 column density at the continuum peak is by a factor of 10^{23} cm^{-2} (1 g cm^{-2}, Table 4.7), which is consistent with the threshold for high mass star forming clouds proposed by Krumholz & McKee (2008).

Molecular abundance with respect to H_2

Molecular abundances with respect to H_2 are listed in Table C2II. The column densities of N_2H^{+}, C_2H, HCN and $H^{13}CN$ are estimated at their own T_{ex}, which is different from H_2 and introduces a large uncertainty. Previous molecular spectral line observations towards several IRDCs have shown the typical range of T_{kin} = 10–20 K (e.g., Carey et al. 1998; Teyssier et al. 2002; Sridharan et al. 2005; Pillai et al. 2006; Sakai et al. 2008; Devine et al. 2011; Ragan et al. 2011; Zhang & Wang 2011), and spectral energy distributions of clumps within IRDCs indicate a range of dust temperature T_{dust} = 10–50 K (e.g., Henning et al. 2010; Rathborne et al. 2010). Therefore, before

Table 4.7: CO depletion, HNC/HCN ratio, lower limit of ionization and velocity asymmetric degree of $H^{13}CO^+$ in four IRDCs

Source	l (^{o})	b (^{o})	D^a_{GC} (kpc)	$I_{870\,\mu m}$ (Jy/beam)	T_g (K)	N_{H_2} 10^{22} (cm^{-2})	f^b_{CO} ^{13}CO	$C^{18}O$	$X(\frac{HNC}{HCN})^c$	$x(e)^e$ (10^{-7})	$\delta V^f_{H^{13}CO^+}$
G 28.34	28.324	0.067	4.6	0.77 ± 0.10	12	13.23 ± 0.17	15.22 ± 2.19	14.5 ± 7.12	1.35 ± 0.70	3.34	-0.51
IRDC 18530	35.431	0.137	4.5	0.56 ± 0.07	9	17.12 ± 0.21	36.47 ± 5.24	19.54 ± 6.83	1.67 ± 0.69	11.82	-0.19
IRDC 18306	23.296	0.056	3.6	0.48 ± 0.12	8	19.10 ± 0.48	49.81 ± 13.46	21.52 ± 6.57	$--^d$	22.27	0.30
IRDC 18308	23.251	0.017	4.4	0.36 ± 0.07	12	6.12 ± 1.20	19.45 ± 4.31	12.16 ± 4.69	$--^d$	1.68	0.0009

a. Assuming the GC distance of the sun is 8 kpc.
b. Estimated from $C^{18}O$ and optical depth corrected ^{13}CO with Eq. 4.11-4.13.
c. Measured with the optical depth corrected HNC and hyperfine fitted HCN at the same gas temperature $T_{ex,CO}$.
d. The value is not given because of large uncertainties in HCN abundance, see Table C2.
e. Lower limit is measured from Eq. 4.19, with hyperfine fitted N_2H^+, the optical depth corrected ^{13}CO and $H^{13}CO^+$ at the same gas temperature $T_{ex,CO}$.
f. $\delta V_{H^{13}CO^+} = (V_{HCO^+} - V_{H^{13}CO^+})/\Delta\upsilon_{H^{13}CO^+}$, Mardones et al. (1997).

we obtain the precise temperature from the follow-up study, we also estimate the column densities and abundances of N_2H^+, C_2H, HCN and $H^{13}CN$ at the same T_{kin} as the other species, and list the values in Table C2IA and IIA. Comparing the values at these two sets of temperatures, we found the molecular abundances are sensitive to the temperatures in the 5–15 K regime, and 5 K difference in temperature brings the abundance uncertainty to the order of 1–2 magnitudes. In the following analysis, we use the second set of abundances to estimate the other chemical parameters (assuming all line and dust have the same temperature $T_{kin} \sim T_{ex,CO}$).

4.4.3 Chemical similarity and difference between HMSCs and low mass prestellar cores

Similar to the low mass prestellar cores, most strong emission lines in our HMSCs are from N-bearing species, which show spatial anti-correlation with CO isotopologues. Emission from tracers of shock and infall motions (e.g., HCO^+, HNCO, HCN) and carbon ring (e.g., c-C_3H_2) indicate these cold, young clouds are not completely chemically quiescent.

To investigate the chemical difference between HMSCs and low mass prestellar cores qualitatively, we compare the molecular abundances in our sources with previous spectral line studies (e.g., Ohishi et al. 1992; Jørgensen et al. 2004; Tafalla et al. 2006; Padovani et al. 2009; Gerner et al. 2014). On average, CH_3C_2H, HC_3N, HNC, HCN in our sources have lower abundances than the aforementioned studies, probably due to our lower T_{kin} and the possibly overestimated

H_2 column density[11]. Nevertheless, the abundances of C_2H and HCO^+ are comparable to the low mass prestellar cores, and both HNCO and N_2H^+ are more abundant in our sources than the others. In particular, the rare isotopologues such as ^{13}CS, $H^{13}CO^+$, $H^{13}CN$ and the shock tracer SiO are detected above 5σ rms in our sources, indicating our HMSCs are chemically more evolved than the above low mass counterparts, where the detection of these isotopologues were not reported.

On top of that, the typical dense gas tracers HCN and HNC are a pair of isomers, whose abundance ratio are strongly temperature dependent. It has been reported that the HCN/HNC ratio decreases with the increasing temperature, ranging from $\leq$ 1 in the low mass prestellar cores (e.g., Ohishi et al. 1992; Jørgensen et al. 2004; Tafalla et al. 2006; Sarrasin et al. 2010) to the order of unity in dark clouds (e.g., Hirota et al. 1998; Vasyunina et al. 2011), then above 10 in HMPOs (e.g., Blake et al. 1987; Helmich & van Dishoeck 1997), and reaching several tens in warm cores (e.g., Orion GMC, Goldsmith et al. 1986b; Schilke et al. 1992). In our sources, the HCN/HNC ratio is almost unity in G28.34S and IRDC 18530 (Table 4.7), which is consistent with previous result.

4.4.4 CO depletion

The sublimation temperature of CO is around 20 K (Caselli et al. 1999; Fontani et al. 2006; Aikawa et al. 2008), so most CO is frozen out (depleted) onto the grains in the center of cold cloud. In contrast, N-bearing species are more resilient to depletion (e.g., Bergin et al. 2002; Caselli et al. 2002d; Jørgensen et al. 2004). Moreover, since CO destroys N_2H^+ and decreases deuterium fraction, the anti-correlated spatial distribution between N_2H^+, NH_2D and CO in G 28.34 S and IRDC 18308 indicate strong depletion of CO (Figure 4.3).

The depletion factor is defined as the ratio between the expected abundance of a species X_α^E and the observed abundance of that species X_α^O (Lacy et al., 1994),

$$f_\alpha = X_\alpha^E / X_\alpha^O \tag{4.16}$$

Using optically thin line $C^{18}O$ ($2 \rightarrow 1$), we measure the CO depletion factor from $C^{18}O$ and ^{13}CO (with optical depth correction) and list them in Table 4.7. A depletion factor derived from two isotopologues is consistent in G 28.34S and IRDC 18530, but has some difference in IRDC 18306 and 18308, indicating the "canonical" ratio between isotopes may have large

[11]The molecular abundances estimated in IRDC large sample study by Gerner et al. (2014) is on average 1 magnitude higher than ours, because they assume a higher $T_{kin} \sim 15$ K.

uncertainties in these sources. One possibility is fractionation of $^{12}C \Leftrightarrow {}^{13}C$ and of $^{16}O \Leftrightarrow {}^{18}O$ in the low temperature environment (< 10 K). Nevertheless, CO seems to be heavily depleted in our sources, with a depletion factor in the range of 14–50 at < 10 K and n $\sim 10^5$ cm^{-2} gas, which is consistent with the range given by Fontani et al. (2012) from a large sample study.

4.4.5 Ionization

The ionization fraction *x(e)* in the early stage of star formation is an important indicator of the cosmic ray impact in the dense and dark clouds. Based on the assumption that gas is quasi-neutral, *x(e)* can be simply estimated by summing up the abundance of all the molecular ions (e.g., Caselli et al. 2002d; Miettinen et al. 2009). Therefore, the ionization fraction in our sources are dominated by the abundance of N_2H^+, which is on average > 10^{-8}.

In addition, based on the assumption of chemical equilibrium, *x(e)* in dense molecular clouds can also be derived from ion-neutral reaction. Using the same method as described in Miettinen et al. (2011) and the chemical network in their Table 8, considering the reactions between N_2H^+, HCO^+ and CO (without any fractional reactions), we can derive the lower limit of *x(e)* (see also Qi et al. 2003):

$$H_CO^+ + e \xrightarrow{\beta_{11}} CO + H, \qquad \text{where } \beta_{11} = 2.4 \times 10^{-7}(\tfrac{T_{kin}}{300\ K})^{-0.69} \tag{4.17}$$

$$N_2H^+ + CO \xrightarrow{k_{11}} HCO^+ + N_2 \qquad \text{where } k_{15} = 8.8 \times 10^{-10} cm^3 s^{-1} \tag{4.18}$$

$$x(e) \geq \frac{k_{15} X(N_2H^+) X(CO)}{\beta_{11} X(HCO^+)} \tag{4.19}$$

where the parameters β_{11} and k_{15} are adopted from UMIST database (Woodall et al. 2007).

From Table 4.7, we found the lower limit of ionization rate is > 10^{-7} in G 28.34 S and IRDC 18308, while > 10^{-6} in the other two sources. This method has some simplicity, e.g., CO depletion and fractional reaction are not considered, as discussed in (Caselli et al. 1998; Lintott & Rawlings 2006; Miettinen et al. 2011). Nevertheless, these derived rates are consistent with those reported in HMSCs (e.g., Williams et al. 1998; Bergin et al. 1999; Chen et al. 2011; Miettinen et al. 2011) and the modelling result in Gerner et al. (2014), which are higher than the values reported in low mass prestellar objects (e.g., > 10^{-9}, Caselli et al. 2002d), implying larger cosmic ray ionization rates.

4.5 Conclusions

To investigate the initial conditions of high mass star formation, we carried out several observations with the SMA and IRAM 30m, and study the dynamic and chemical properties of four IRDCs (G 28.34S, IRDC 18530, IRDC 18306 and IRDC 18308), which exhibit strong (sub)mm continuum emission toward 70 μm extinction features. At different spatial resolutions and wavelengths, this small sample study of HMSCs illustrates that the cold (T $<$ 15 K), dense ($\sim$ 10^5 cm^{-3}) HMSFRs are not quiescent.

1. At a spatial resolution of 2″ ($\sim$ 10^4 AU at an average distance of 4 kpc), the 1.1 mm SMA observations resolve each source into several fragments, which are well aligned with the filamentary direction and regularly separated. The mass of each fragment is on average $>$ 10 M$_\odot$, exceeding the Jeans mass of the whole clump by a factor of 10–60, supporting the "core accretion" scenario and indicating that thermal pressure does not dominate the fragmentation process.

2. In the 8 GHz SMA observational band at 1.1 mm, higher-J transitions (including dense gas tracers such as $H^{13}CO^+$ (2 $\rightarrow$ 1) are not detected, implying our sources are in the cold and young evolutionary stage when lines with E_u/k_B $>$ 20 K are not excited. However, our line survey at 1 mm & 3 mm shows a number of emission from lower-J transitions. In particular, a $> 5\sigma$ rms detection of SiO in G 28.34 S may be the signature of a potential protostellar object, and the asymmetric HCO^+ line profile in this source probably traces infall motion.

3. Linewidth of all the 30 m detected lines are on average 2–3 km s^{-1}. Using the $H^{13}CO^+$ (1 $\rightarrow$ 0) line, we calculate the velocity dispersion components and the critical mass based on a non-thermal fragmentation scenario ("cylindrical fragmentation"), and propose that the mass of fragments ($>$ 60 M$_\odot$) are supported by non-thermal motions.

4. N_2H^+ (J = 1 $\rightarrow$ 0), C_2H (N = 1 $\rightarrow$ 0), HCN (J = 1 $\rightarrow$ 0) and $H^{13}CN$ (J = 1 $\rightarrow$ 0) have multiplets in our 30 m data. Using a hyperfine structure fitting programme, we estimate their excitation temperature (on average 5–8 K), and conclude that they are sub-thermally excited. Excitation temperature of CO isotopologues are also estimated in this study, which suggests the sources are in the very early cold environment ($\sim$ 10 K).

5. Our sources exhibit similar chemical features as low mass prestellar cores, with a large number of N-bearing species, anti-correlated spatial distributions between N_2H^+, NH_2D and CO, and the existence of carbon rings and molecular ions. We calculate the molecular abundances, HCN/HNC ratio, CO depletion factor and ionization fraction, and found HMSCs are slightly chemically more evolved than low mass prestellar cores.

6. Large scale line survey presents us the chemical uniqueness of these HMSCs, but is not sufficient to probe the chemical complexity of the fragments. The above observations reveal to us non-thermal motions which dominate the fragmentation process, though, without line detection, we do not know the dynamics within the fragments. Further study is expected to uncover the dynamic and chemical features within the fragments of these IRDCs, which can be done with the upcoming 3.4 mm PdBI observations at a spatial resolution of 3″ in Spring 2015[12].

4.6 Appendix

[12]This proposal has been approved (P.I.: S., Feng).

A. Linewidth $\Delta\upsilon$ (km s^{-1}) and integrated intensity $\int T_B(\upsilon)d\upsilon$ (Kkm s^{-1}) in four IRDCs

Species	Freq	G 28.34 S		IRDC 18530		IRDC 18306		IRDC 18308	
	(GHz)	(km s^{-1})	(K km s^{-1})	(km s^{-1})	(K km s^{-1})	(km s^{-1})	(K km s^{-1})	(km s^{-1})	(K km s^{-1})
OCS	85.1391	3.91 ± 0.66	0.26 ± 0.04	−−	−−	−−	≤0.05	−−	≤0.06
c-C_3H_2	85.3389	2.97 ± 0.10	1.51 ± 0.05	−−	−−	1.99 ± 0.12	0.69 ± 0.03	1.76 ± 0.23	0.34 ± 0.04
c − $CH_3C_2H^{(1)}$	85.4557	3.08 ± 0.45	0.31 ± 0.04	−−	−−	2.21 ± 0.42	0.18 ± 0.03	2.81 ± 0.81	0.22 ± 0.06
c − $CH_3C_2H^{(2)}$	85.4573	2.44 ± 0.42	0.26 ± 0.04	−−	−−	1.08 ± 0.55	0.08 ± 0.03	−−	≤0.08
NH_2D	85.9263	6.43 ± 1.09	0.44 ± 0.05	2.86 ± 0.44	0.17 ± 0.02	8.94 ± 1.16	0.32 ± 0.04	7.50 ± 1.57	0.21 ± 0.04
$H^{13}CO^+$	86.7543	3.07 ± 0.06	1.32 ± 0.02	2.01 ± 0.06	0.55 ± 0.02	2.05 ± 0.10	0.50 ± 0.02	2.09 ± 0.09	0.59 ± 0.02
SiO	86.847	4.83 ± 0.39	0.55 ± 0.03	−−	≤0.03	−−	≤0.25	−−	≤0.03
$HN^{13}C$	87.0909	2.99 ± 0.07	1.12 ± 0.02	1.71 ± 0.08	0.47 ± 0.02	2.24 ± 0.10	0.41 ± 0.02	2.08 ± 0.11	0.43 ± 0.02
HNCO	87.9244	2.68 ± 0.09	0.83 ± 0.02	1.76 ± 0.15	0.25 ± 0.02	2.14 ± 0.18	0.25 ± 0.02	2.12 ± 0.36	0.17 ± 0.02
HCO^+	89.1885	2.44 ± 0.08	5.27 ± 0.13	3.74 ± 0.05	4.74 ± 0.05	3.11 ± 0.28	1.72 ± 0.14	3.37 ± 0.06	5.52 ± 0.08
HNC	90.6636	2.59 ± 0.05	5.57 ± 0.08	3.10 ± 0.03	4.01 ± 0.03	2.94 ± 0.12	1.85 ± 0.07	2.83 ± 0.04	3.95 ± 0.05
HC_3N	90.979	3.36 ± 0.16	0.70 ± 0.03	2.22 ± 0.23	0.20 ± 0.02	2.34 ± 0.22	0.25 ± 0.02	3.03 ± 0.87	0.14 ± 0.03
^{13}CS	92.4943	3.06 ± 0.39	0.22 ± 0.02	−−	≤0.03	2.28 ± 0.42	0.11 ± 0.02	−−	≤0.03
H_2CO	218.222	3.73 ± 0.42	0.98 ± 0.09	−−	≤0.15	−−	≤0.15	−−	≤0.14
$C^{18}O$	219.56	3.70 ± 0.07	7.83 ± 0.13	2.42 ± 0.06	3.71 ± 0.08	1.95 ± 0.06	3.75 ± 0.10	1.94 ± 0.07	3.02 ± 0.10
^{13}CO	220.399	4.83 ± 0.20	21.18 ± 0.62	3.78 ± 0.13	16.24 ± 0.47	3.11 ± 0.25	9.79 ± 0.69	2.75 ± 0.13	14.15 ± 0.63
$C^{17}O$	224.714	3.72 ± 0.25	2.35 ± 0.13	−−	−−	2.06 ± 0.12	1.26 ± 0.07	2.61 ± 0.36	0.70 ± 0.09

−−. no observations in our dataset

B. Linewidth $\Delta\upsilon$(km s^{-1}) and integrated intensity $\tau_0\Delta\upsilon$(km s^{-1}) in four IRDCs

Species	Freq	G 28.34 S		IRDC 18530		IRDC 18306		IRDC 18308	
	(GHz)	(km s^{-1})	(K km s^{-1})	(km s^{-1})	(K km s^{-1})	(km s^{-1})	(K km s^{-1})	(km s^{-1})	(K km s^{-1})
N_2H^+,	, 93.1738	2.94 ± 0.00	1.14 ± 0.02	1.83 ± 0.02	1.18 ± 0.03	1.88 ± 0.04	1.17 ± 0.17	2.02 ± 0.02	0.20 ± 0.07
C_2H,	, 87.3169	2.86 ± 0.07	3.95 ± 0.60	1.85 ± 0.07	1.00 ± 0.47	1.72 ± 0.07	3.22 ± 0.67	1.76 ± 0.11	0.18 ± 0.24
HCN,	, 88.6318	2.37 ± 0.05	0.24 ± 0.04	3.20 ± 0.03	0.32 ± 0.02	2.64 ± 0.20	27.50 ± 8.02	3.23 ± 0.16	3.13 ± 1.38
$H^{13}CN$,	, 86.3402	2.95 ± 0.14	0.33 ± 0.54	2.30 ± 0.27	0.23 ± 12.10	1.82 ± 2.26	1.26 ± 1.97	1.74 ± 0.32	0.17 ± 8.13

* Hyperfine structure is not well fitted

Table C1: The intensity integrated over the width of each line, and the optical depth of the main line obtained from the Gaussian/hyperfine structures fitting program based on CLASS. Uncertainties on the measured intensities are typically ≤ 10%. For species which are not detected, an upper limit equal to the 3σ rms is given. For species which are we did not observe, we mark them with "−−". .

I. Molecular Column density [x ± y(z) = (x ± y) × 10^{z}cm^{-2}]

A.

Species	G 28.34 S		IRDC 18530		IRDC 18306		IRDC 18308	
	$T_{ex,\alpha}$ (K)	(12 K)	$T_{ex,\alpha}$ (K)	(9 K)	$T_{ex,\alpha}$ (K)	(8 K)	$T_{ex,\alpha}$ (K)	(12 K)
N_2H^+	1.74 ± 0.05(16)	1.46 ± 0.02(15)	2.26 ± 0.10(17)	2.91 ± 0.08(15)	7.17 ± 1.44(17)	4.18 ± 0.60(15)	5.11 ± 0.51(14)	2.59 ± 0.87(14)
C_2H	4.87 ± 0.84(14)	2.79 ± 0.42(15)	1.32 ± 0.74(14)	4.41 ± 2.05(14)	3.82 ± 0.88(14)	1.17 ± 0.24(15)	3.23 ± 6.60(13)	1.24 ± 1.70(14)
HCN	4.48 ± 0.95(13)	4.26 ± 0.65(13)	7.13 ± 0.10(13)	6.25 ± 0.30(13)	1.78 ± 0.33(17)	5.84 ± 1.71(15)	4.46 ± 0.11(15)	5.62 ± 2.48(14)
$H^{13}CN$	3.24 ± 1.33(14)	6.14 ± 10.20(13)	5.69 ± 132.00(14)	4.68 ± 246.00(13)	9.12 ± 12.90(15)	2.79 ± 4.37(14)	5.01 ± 109.00(14)	3.26 ± 152.00(13)

Column densities in blue are obtained at temperatures list in Table 4.5, under CTEX assumption
Column densities in black are obtained at mean $T_{ex,CO}$, with LTE assumption with LTE assumption

B.

Species	G 28.34 (12 K)	IRDC 18530 (9 K)	IRDC 18306 (8 K)	IRDC 18308 (12 K)
OCS	2.31 ± 0.34(13)	−−	≤ 5.62(12)	≤ 5.32(12)
c-C_3H_2	1.10 ± 0.03(13)	−−	3.61 ± 0.17(12)	2.48 ± 0.32(12)
c − $CH_3C_2H^{(1)}$	5.01 ± 0.69(13)	−−	3.76 ± 0.70(13)	3.52 ± 0.92(13)
c − $CH_3C_2H^{(2)}$	2.23 ± 0.33(13)	−−	6.48 ± 2.08(12)	≤ 7.09(12)
NH_2D	1.42 ± 0.15(13)	6.75 ± 0.83(12)	1.42 ± 0.17(13)	6.89 ± 1.30(12)
$H^{13}CO^+$	4.48 ± 0.08(11)	1.59 ± 0.04(11)	1.36 ± 0.06(11)	2.02 ± 0.07(11)
SiO	1.11 ± 0.07(12)	≤ 5.39(10)	≤ 4.34(11)	≤ 6.00(10)
$HN^{13}C$	2.55 ± 0.05(12)	9.13 ± 0.35(11)	7.45 ± 0.33(11)	9.69 ± 0.45(11)
HNCO	4.42 ± 0.12(14)	1.32 ± 0.09(14)	1.32 ± 0.10(14)	9.16 ± 1.17(13)
HCO^+ *	4.42 ± 0.11(13)	3.82 ± 0.04(13)	2.32 ± 0.18(13)	4.05 ± 0.06(13)
HNC *	6.52 ± 0.09(13)	4.02 ± 0.03(13)	2.49 ± 0.09(13)	3.97 ± 0.05(13)
HC_3N	3.77 ± 0.15(12)	1.58 ± 0.14(12)	2.42 ± 0.20(12)	7.42 ± 1.43(11)
^{13}CS	1.25 ± 0.14(11)	≤ 1.37(10)	4.83 ± 0.85(10)	≤ 1.73(10)
H_2CO	5.66 ± 0.49(12)	≤ 9.15(11)	≤ 9.67(11)	≤ 7.81(11)
$C^{18}O$	4.48 ± 0.07(15)	2.50 ± 0.05(15)	2.78 ± 0.07(15)	1.73 ± 0.06(15)
^{13}CO *	3.41 ± 0.10(16)	3.39 ± 0.10(16)	2.01 ± 0.09(16)	4.61 ± 0.32(16)
$C^{17}O$	3.92 ± 0.22(15)	−−	2.81 ± 0.15(15)	1.17 ± 0.16(15)

Column densities are obtained at mean $T_{ex,CO}$ with LTE assumption.

Table C2: Average column densities and abundances for molecules with respect to H_2 in a square region from [20″, 20″] to [-20″, -20″] of each source observed by IRAM 30 m, listed in the form of x ± y(z) = (x ± y) × 10^{z}. For species which are not detected, an upper limit derived from 3σ rms is given. "−−" mark the species we did not observe in certain source. Column densities of molecules marked with "*" are likely obtained from optically thick lines and for those we did the optical depth correction. The values in red are from optical depth estimation, in black are from $T_{kin} \sim T_{ex,CO}$ under LTE assumption, and the values in blue are from each $T_{ex,\alpha}$ under CTEX assumption. Uncertainties on the measured values are typically ≤ 10%, as determined from T_{rot}, partition function $Q(T_{rot})$, and Gaussian fitting to $\int T_B(\upsilon)d\upsilon$ or hyperfine structure fitting to $\tau_0\Delta\upsilon$.

II. Molecular Abundances with respect to H_2 [x ± y(z) = (x ± y) × 10^z]

A.

Species	G 28.34 S		IRDC 18530		IRDC 18306		IRDC 18308	
	$T_{ex,\alpha}$ (K)	(12 K)	$T_{ex,\alpha}$ (K)	(9 K)	$T_{ex,\alpha}$ (K)	(8 K)	$T_{ex,\alpha}$ (K)	(12 K)
N_2H^+	1.32 ± 1.47(−7)	1.11 ± 0.18(−8)	1.32 ± 1.44(−6)	1.70 ± 0.30(−8)	3.75 ± 4.01(−6)	2.19 ± 1.15(−8)	8.35 ± 9.35(−9)	4.24 ± 2.81(−9)
C_2H	3.68 ± 4.96(−9)	2.11 ± 0.68(−8)	7.72 ± 13.70(−10)	2.58 ± 1.74(−9)	2.00 ± 3.28(−9)	6.13 ± 3.77(−9)	5.27 ± 20.00(−10)	2.03 ± 3.96(−9)
HCN	3.39 ± 4.72(−10)	3.22 ± 1.05(−10)	4.17 ± 4.83(−10)	3.65 ± 0.72(−10)	9.33 ± 14.80(−7)	3.06 ± 2.22(−8)	7.29 ± 8.85(−8)	9.18 ± 7.30(−9)
$H^{13}CN$	2.45 ± 3.98(−9)	4.64 ± 9.55(−10)	3.32 ± 92.10(−9)	2.74 ± 165.00(−10)	4.77 ± 15.40(−8)	1.46 ± 3.54(−9)	8.19 ± 232.00(−9)	5.34 ± 312.00(−10)

Abundances in blue are obtained at temperatures list in Table 4.5, under CTEX assumption
Abundances in black are are obtained at mean $T_{ex,CO}$, with LTE assumption

B.

Species	G 28.34 (12 K)	IRDC 18530 (9 K)	IRDC 18306 (8 K)	IRDC 18308 (12 K)
OCS	1.75 ± 0.55(−10)	−−	≤ 2.94(−11)	≤ 8.70(−11)
c-C_3H_2	8.31 ± 1.53(−11)	−−	1.89 ± 0.75(−11)	4.05 ± 1.64(−11)
c − $CH_3C_2H^{(1)}$	3.79 ± 1.17(−10)	−−	1.97 ± 1.15(−10)	5.75 ± 3.27(−10)
c − $CH_3C_2H^{(2)}$	1.69 ± 0.54(−10)	−−	3.39 ± 2.59(−11)	≤ 1.16(−10)
NH_2D	1.07 ± 0.29(−10)	3.94 ± 1.11(−11)	7.43 ± 3.65(−11)	1.13 ± 0.54(−10)
$H^{13}CO^+$	3.39 ± 0.58(−12)	9.28 ± 1.62(−13)	7.12 ± 2.80(−13)	3.30 ± 0.95(−12)
SiO	8.35 ± 1.82(−12)	≤ 3.15(−13)	≤ 2.27(−12)	≤ 9.81(−13)
$HN^{13}C$	1.93 ± 0.33(−11)	5.33 ± 1.00(−12)	3.90 ± 1.54(−12)	1.58 ± 0.48(−11)
HNCO	3.34 ± 0.61(−9)	7.71 ± 1.72(−10)	6.92 ± 3.02(−10)	1.50 ± 0.60(−9)
HCO^+ *	3.34 ± 0.59(−10)	2.23 ± 0.35(−10)	1.21 ± 0.54(−10)	6.63 ± 1.74(−10)
HNC *	4.58 ± 0.76(−10)	2.18 ± 0.33(−10)	1.56 ± 0.60(−10)	6.49 ± 1.69(−10)
HC_3N	2.85 ± 0.56(−11)	9.25 ± 2.26(−12)	1.26 ± 0.56(−11)	1.21 ± 0.59(−11)
^{13}CS	9.48 ± 2.60(−13)	≤ 7.99(−14)	2.53 ± 1.44(−13)	≤ 2.83(−13)
H_2CO	4.28 ± 1.07(−11)	≤ 5.35(−12)	≤ 5.06(−12)	≤ 1.28(−11)
$C^{18}O$	3.38 ± 0.57(−8)	1.46 ± 0.24(−8)	1.46 ± 0.54(−8)	2.83 ± 0.80(−8)
^{13}CO *	2.58 ± 0.47(−7)	1.98 ± 0.35(−7)	2.41 ± 1.04(−7)	3.28 ± 0.98(−7)
$C^{17}O$	2.96 ± 0.63(−8)	−−	1.47 ± 0.60(−8)	1.91 ± 0.79(−8)

Abundances are obtained at mean T_{ex} of CO isotopologues with LTE assumption.

Table C2: (continued)

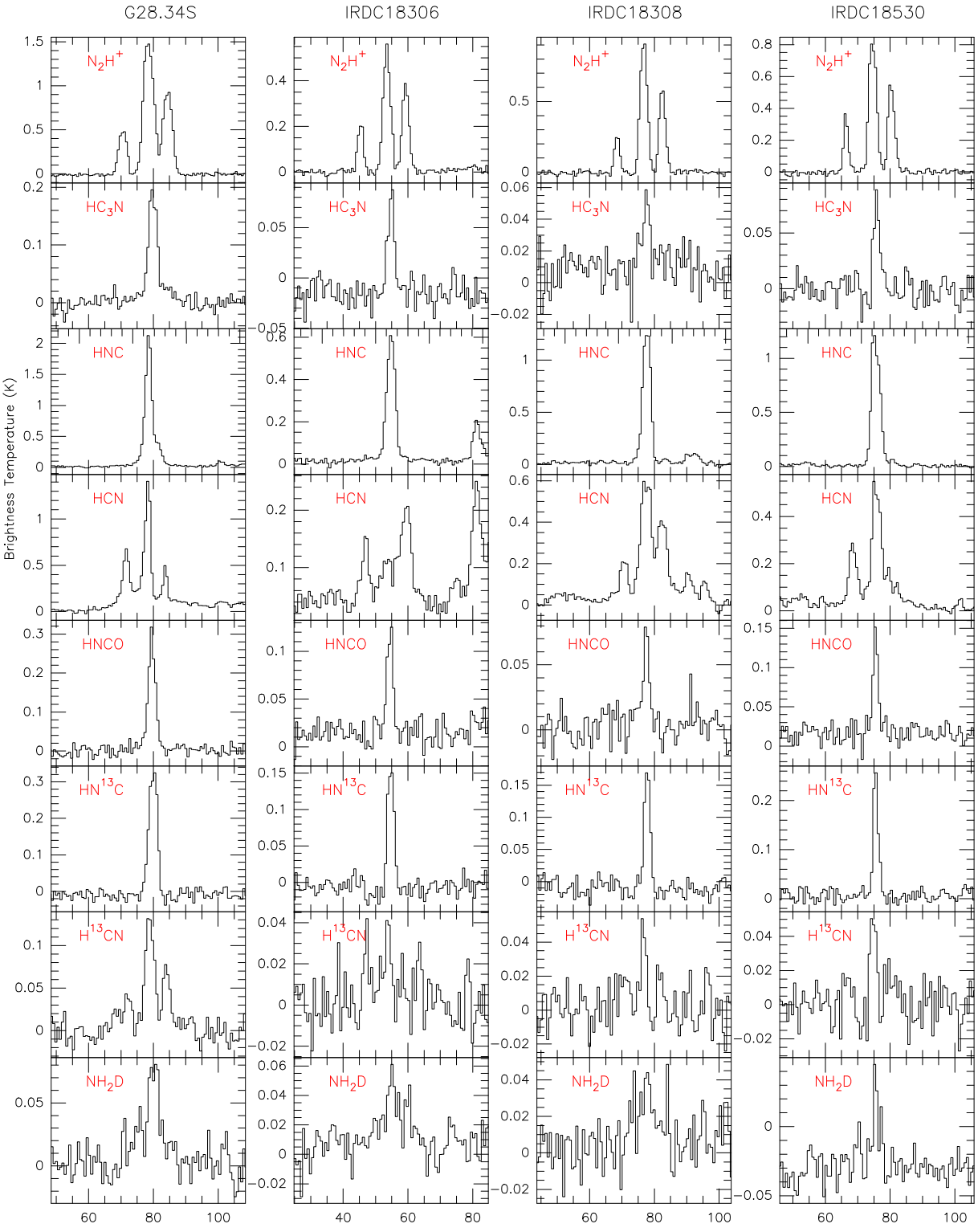

Figure C1: Line profiles of identified species toward each IRDC (transitions are list in Table 4.3). Profiles in blue indicate the lines are obtained from the "extra band", where the rms are higher than the others due to less observation time.

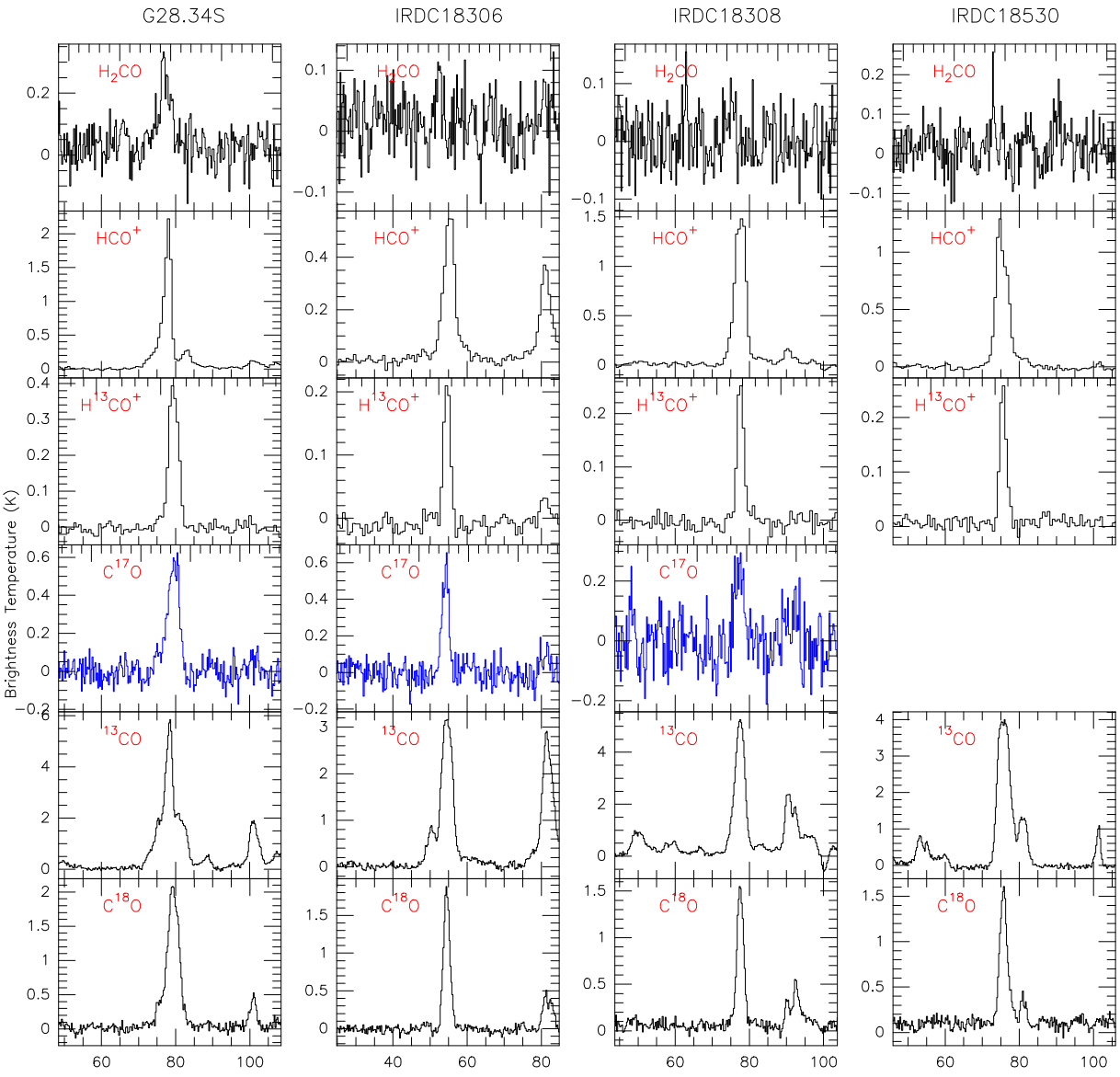

Figure C1: (continued)

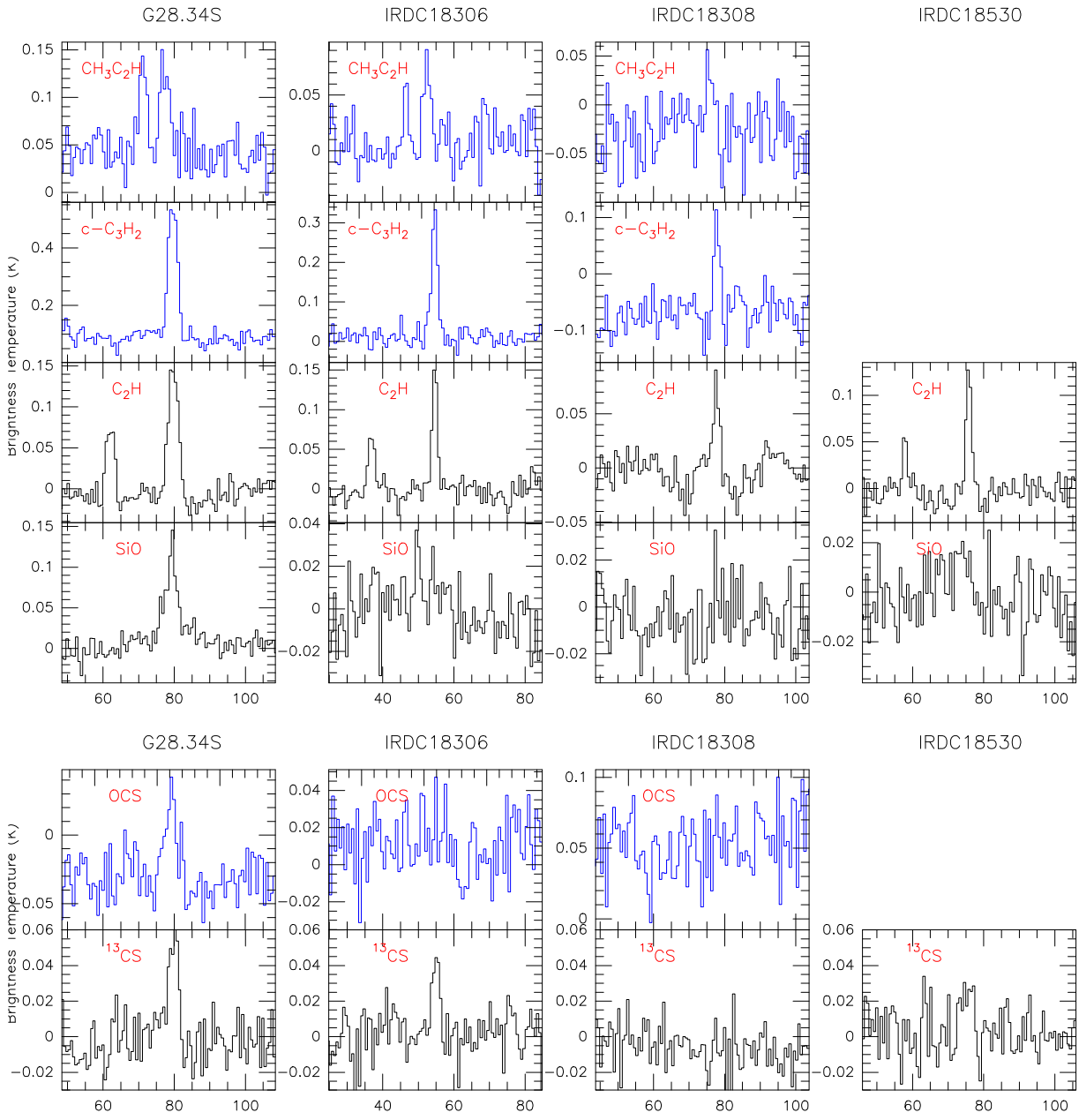

Figure C1: (continued)

5 Remarks and Future Prospects

There are known knowns. There are known unknowns. But there are also unknown unknowns.

– Donald Rumsfeld (2002)

5.1 Summary of the Main Results

With the aim of investigating the dynamic-chemical properties on small scales (< 2 000 AU) of HMSFRs, I analysed the mm wavelength continuum and spectral line features of a series of high mass sources, which are in the evolutionary stages ranging from high mass starless cores (HMSCs: G 28.34 S, IRDC 18530, IRDC 18306, IRDC 18308) to hot molecular cores (HMCs: Orion-KL, NGC 7538 S, NGC 7538 IRS1). Firstly, I took the nearest HMSFR, Orion-KL, as a study template and explored the chemical variations (i.e., variations in molecular complexities, molecular spatial distributions, gas temperatures and densities, molecular abundances) from central condensations to the extended outflow regions, within a field of 2×10^4 AU (Chapter 2). To cover the information from all spatial scales, interferometer and single-dish observations were combined in this study. Then, with a similar analytical approach, I studied the chemical variations at a spatial resolution of $0.4''$ ($\sim$ 1 000 AU) in two neighbouring HMSFRs, which are embedded in the same cloud NGC 7538 at a distance 4 times further than Orion-KL (Chapter 3). On top of that, I compared the observational results with the best fit results from a 1-D physico-chemical model, allowing me to quantitatively draw a general picture of the hierarchical fragmentation in NGC 7538 S. Additionally, hypotheses are suggested to explain the peculiar absorption-mixed-emission spectrum at mm wavelength in the continuum peak of IRS1. As a next step, I targeted four younger sources with both interferometric (SMA, PdBI) and single-dish telescopes (IRAM 30 m), probing the initial chemical and physical conditions in the prestellar cores (Chapter 4).

The main conclusions of the above studies are summarised as follows.

- **Fragmentation:**
  Thanks to the interferometric observations with high spatial resolution, fragmentation is observed in the continuum maps of all the resolved sources in this thesis. In particular, fragments in the HMSCs have on average mass M > 10 $M_{\odot}$, exceeding the Jeans mass of the large-scale clump, indicating that thermal pressure is not dominant in the fragmentation process. This result supports the "core accretion" picture, i.e., the masses of the initial prestellar cores are already high, and high mass stars may be formed in the similar but "scaled-up" approach as low mass stars.

- **Hierarchical fragments in NGC 7538 S:**
  Core collapse and thermal heating follow fragmentation in HMSFRs. In some cases, these processes are not synchronised. In the GMC NGC 7538, an evolutionary sequence does not only propagate on large scale (> 10^5 AU) from the north (IRS1) to the south (S), but also exists in fragments of NGC 7538 S within 5 000 AU separation. Using the PdBI at 1.3 mm (218 GHz) achieving a spatial resolution of < 1 000 AU (0.4″), NGC 7538 S is resolved into at least three condensations along the northeast-southwest direction, exhibiting similar continuum intensities but significantly different molecular line components. The first 1-D gas-grain chemical modelling in this source suggests that the reason for such hierarchic fragmentation is different heating paces from the internal protostars of different condensations, rather than unsynchronised collapse. Although the chemical histories of the fragments are not the same, their chemical ages do not differ much from the modelling, suggesting rapid warm-up processes from one stage to another.

- **Chemical inhomogeneity in the HMC Orion-KL:**
  Chemical variations among fragments may aid in distinguishing evolutionary stages. Even within a source at a certain evolutionary stage, gas temperature and density, molecular distribution and abundances are not homogeneous. At a spatial resolution of 1 200 AU, Orion-KL is resolved into several substructures on the continuum map, including the well-known compact condensations (the Hot Core and mm2), condensations which are previously unresolved (mm3a and mm3b), and structures which are confirmed with > 5σ detections (the southern ridge and the northeast clump). For the first time, I complement the interferometric (SMA) mapping of emission lines with a single-dish (the 30 m) survey at 1 mm (220/230 GHz), and find diversity of molecular species and large abundance variations from the central condensations to the extended outflow regions. While sulfur (S-) bearing molecules, simple organics and CO isotopologues all exhibit extended emission, covering the region from the Hot Core to the cooler southern ridge and outflows, COMs only concentrate in the central high temperature condensations. Moreover, the chemistry within the outflow lobes of Orion-KL does not appear to differ significantly from low mass chemi-

cally active outflows. In particular, tracers like HNCO and $C^{18}O$ have broad line wings in the northeast clump, whereas HNCO, $^{34}SO_2$ and SO have a second component as well as enhanced abundances relative to the high-velocity outflow regions (in the northwest-southeast direction), which may be associated with a strong shock event in the plateau of the low-velocity outflow.

- **A unique spectral feature in NGC 7538 IRS1 :**
  Compared to the hierarchical fragmentation in its neighbouring source, NGC 7538 IRS1 remains unresolved at a spatial resolution of 1 000 AU. Large abundances of COMs (e.g., $CH_3^{13}CN$, NH_2CHO, CH_3OH, $HCOOCH_3$) indicate it is in the HMC phase. The spectrum at its continuum peak is unique: an non-typical absorption feature dominates this 1.3 mm spectrum, while at least three lines from CH_3OH and $HCOOCH_3$ show strong pure emission. I propose several hypotheses for this feature, attempting to interpret this uniqueness by source geometry (e.g., outflow cavity) and/or line excitation states, i.e., non-LTE may be the reason for the primarily absorption lines, while population inversion may indicate a small number of pure emission lines.

- **COMs:**
  As high temperature indicators, rich numbers of COMs are detected in all the HMC/HMPO sources (Orion-KL, NGC 7538 S-MM1, MM2 and IRS1) studied in this thesis. High sensitivity observations allow us to identify and spatially locate several low abundance COMs such as CH_3COCH_3 and CH_3CH_2OH, as well as to tentatively detect long carbon chain molecules C_6H and HC_7N. Instead of a common concentrated emission peak, their spatial distributions are complicated. In Orion-KL, most COMs are segregated by type, peaking at either the Hot Core (e.g., N-bearing species) or the compact ridge (e.g., O-bearing species like $HCOOCH_3$, CH_3OCH_3), indicating distinctive formation paths of N- and O-bearing COMs; while the distributions of the others do not follow this segregation (e.g., CH_3CH_2OH, CH_3OH, CH_3COCH_3), implying connections between the N-/O-bearing forming paths. In NGC 7538 S, most COMs have strong emission in the warmer MM1, except for NH_2CHO. A weak detection in the warmer MM1 and an spatial peak in the colder MM2 suggests NH_2CHO being destroyed in high temperature environments.

Although our 1-D gas-grain model shows large agreement with the observations, current chemical network and the application of that to a computational model has trouble replicating the COM abundances. This processes is hampered by the unclear formation path of COMs, the unknown structure of the source and the limitation of including arbitrary structure beyond spherical symmetry in a 1-D code. Therefore, comprehensive chemical network and more precise modelling fittings require further observations for COMs detection and source structure estimation (e.g., outflow cavity, flatten/multilayer disk structure).

- **The initial chemical conditions derived from four IRDCs:**
  Continuum emission obtained from SMA observations at spatial resolution of $\sim 10^4$ AU reveals that our HMSC sources (four IRDCs) exhibit fragmentation. However, barely any molecular line emission ($> 3\sigma$ rms) is detected among the entire 8 GHz band around 1.1 mm (260/270 GHz), providing no clue on the dynamics of these sources. In particular, the non-detection of $H^{13}CO^+$ ($3 \rightarrow 2$) indicates that the center of these prestellar cores may be in the early, cold, "quiescent" phase, where no warm-up has taken place. At a lower spatial resolution and a larger field (scale of 2 pc), I surveyed these regions with the IRAM 30 m at 1 mm & 3 mm wavelengths, and detected several dense gas infall tracers (e.g., HCO^+ ($1 \rightarrow 0$), $H^{13}CN$ ($1 \rightarrow 0$), HCN ($1 \rightarrow 0$)) and shocked gas tracer (e.g., SiO), which illustrates that these IRDCs are not completely chemically quiescent. Moreover, the IRAM 30 m observations reveal that these regions are characterised by gas phase molecular ions, carbon rings, high depletion of CO, and a rich nitrogen chemistry. In addition, anti-correlated spatial distribution between N_2H^+, NH_2D and CO in G 28.34 S and IRDC 18308 indicates similar chemistry to low mass protostellar regions; and a 6σ detection of SiO in G 28.34 S indicates the existence of a shock trigger in this pre-/protostellar region.

  To follow up the chemical (i.e., the reason for non-detection of $H^{13}CO^+$ ($3 \rightarrow 2$, E_u/k_B = 25 K) but $> 10\sigma$ detection of $H^{13}CO^+$ ($1 \rightarrow 0$, E_u/k_B = 4 K)) and dynamic study in these regions, observations conducted by PdBI at 3.4 mm (88 GHz) achieving a spatial resolution of 5 000 AU (P. I.: S., Feng) are expected in Spring 2015.

5.2 Prospects for the Future Work

From atomic and molecular clouds to main sequence stars, the evolution of gas and dust is a complicated processes, which couples dynamic changes with chemical reactions. On one hand, the current observational results in HMSFRs provide us with the opportunity to investigate the life cycle of the interstellar gas and dust, while on the other hand, they leave us more unsolved mysteries. Currently, we are standing near the entrance of the labyrinth of understanding the chemistry of the Universe, and to pass through it will require great effort.

While not even fully complete, ALMA and NOEMA already, and will continue to, provide us with an unprecedented wealth of molecular data at (sub)mm wavelengths. However, (sum)mm observations are only sensitive to the gas phase lines with strong dipole moments (e.g., CO). To better understand these complicated environments in HMSFRs, the (sub)mm lines must be supplemented through multi-band observations, such as infrared, optical, UV and X-ray. In the

near future, the launch of the 6 m James Webb Space Telescope[1] (JWST, expected late 2018) will be the successor of the Hubble Space Telescope (HST), Spitzer Space Telescope (SST) and Herschel Space Observatory at the infrared wavelength. The Square Kilometer Array[2] (SKA, the initial observations are expected by 2020) will bring us many new insights by collecting data at frequencies of 100 MHz–25 GHz, with maximal baselines extending at least to 3 000 km. To reveal the nature of the chemical-dynamic processes in HMSFRs in the Milky Way and more distant galaxies, collaborations among laboratory studies, chemical models and multi-wavelength observations need to be enhanced.

- Laboratory works: Basic chemical reaction parameters (e.g., collisional cross section and rate for molecular transitions, branching ratio of chemical reactions both in the gas phase and grain surfaces) are vital for both line analysis from observations and systematic error reduction in modelling simulations. Therefore, laboratory studies need high accuracy experiments designed to explore molecular spectroscopy, reactivity (chemical pathways), collisional coefficients calculations, surface chemistry and dust formation/evolution.

- Chemical models: In this thesis and some other current researches, chemical models are based on some assumptions, which may not be true. High spatial resolution observations have already revealed us that the low mass and high mass sources have dramatically inhomogeneous chemistry. This inhomogeneity may come from different conditions, both physical (e.g., large variations in temperature, gas density and dust properties over a small distance, caused by violent processes, such as accretion, outflow) and/or chemical (e.g., warm-up timescale diversity). Moreover, in current gas-grain models, the impacts on the chemistry from the shock is excluded, in addition to neither the grain surface reactions nor the isotopes fractionation mechanisms being accurate. Therefore, a more precise fit demands multidimensional (2-D or 3-D) hydrodynamic simulations including shocks, coupled to an accurate UV radiation transport model, as well as a non-LTE radiation transfer code (e.g., the ARTIST package[3]). Any discrepency which we may see between the observations and the model predictions may indicate missing reactions or poorly known reaction rates in the chemical network.

- Observations: The environment of the ISM is more intricate than that in the laboratory. Chemical simulations have to be improved by including time, location and temperature dependent reactions at different evolutionary stages of star formation. Hence, observations with high sensitivity are essential to provide the input parameters for both the design of laboratory experiments and development of chemical networks.

[1] http://www.jwst.nasa.gov

[2] https://www.skatelescope.org

[3] An undergoing developing package which contains the 3-D non-LTE radiative transfer code LIME and the Monte-Carlo radiative transfer model RADMC-3D, in solving 1-D, 2-D, and 3-D problems.

Until now, three cycles of ALMA operation have brought us advances in several areas (see the "ALMA science highlights" at the website of NRAO[4] and ESO[5]). The future is bright with ALMA, NOEMA, JWST and SKA. Currently, I am interested in constraining the motions of global collapse, by comparing the chemical and kinematic similarities and differences between high mass and low mass star forming regions on similar scales. Below lists several follow-up projects which I am focusing on about this topic.

5.2.1 Feedback processes & shock chemistry

Feedback processes in star forming regions are crucial in connecting all scales of astronomical objects and phenomena, due to their ability to fragment clouds into clusters, cores into binaries, and their abilities to eject gas and dust via protostellar outflows, stellar winds and supernovae explosion during the life cycle of stars. Therefore, understanding the nature of these feedback processes is essential in linking star formation on both local and universal scales (e.g., Krumholz et al. 2014).

Based on the contemporary observations, current studies have collated the possible feedbacks associated with low mass protostellar objects (Fig. 1.2, van Dishoeck et al. 2011), including radiative feedbacks (e.g., thermal heating from the hot core accretion to the inner part of the envelope, and from UV radition along the cavity walls), as well as mechanical feedbacks (e.g., from the embedded accretion disk, from the entrained magneto-centrifugally-driven outflow, from the internal working surfaces within the jet, from the shell shocks and bows shock impacting the envelope and surrounding cloud). These feedback processes should be stronger in high mass protostellar objects, owing to their higher luminosities and shorter evolution timescales in comparison to their low mass counterparts. However, without a sufficiently large and broad observational sample, the role of each feedback process plays in different stages of high mass prestellar objects and protostars will remain an open question.

Protostellar outflow is the dominant feedback mechanism during the period from the birth of the protostar till the beginning of main sequence star contraction. It can not only reduce the radiation pressure by channeling the envelope (Krumholz et al. 2005), but also trigger more nearby star forming processes by sweeping up and heating the surrounding ISM, sputtering mantle/core grains and shaping the parent molecular clouds (e.g., Offner et al. 2013; Bate et al. 2014; Krumholz et al. 2014). Collimated, bipolar protostellar outflows are universally detected from low mass cores (Frank et al. 2014). Similar outflows which are recently observed via CO, HCO^+, hydrides, CS, HCN, CH_3OH, H_2CO, and excited masers (e.g., Beuther et al. 2002; Garay et al. 2007; López-Sepulcre et al. 2009; Sánchez-Monge et al. 2013) indicate their origin from high

[4]https://science.nrao.edu/science/highlights
[5]https://almascience.eso.org/alma-science

mass protostars, particularly those which have mass M > 60 $M_{\odot}$ (e.g., G28.34+0.06 P1, Zhang et al. 2009; Cygnus X N63, Bontemps et al. 2010; Duarte-Cabral et al. 2013; IRDC C1-S, Tan et al. 2013). Although correlations between physical properties (e.g., the outflow power, force and mass loss rate, bolometric luminosity range) all suggest the similar mechanisms between low mass and high mass protostellar outflows (Wu et al. 2005; Arce et al. 2007), no systematic study has been carried to compare their chemical properties.

Associated with the bipolar outflows, large-scale shocks are often produced from high velocity jets and protostellar winds when they impact the envelope cavity walls and surrounding clouds. While the shock dynamics in low mass protostars were previously studied (e.g., magnetic field strength, shock velocity, density, and level of ionization, Draine 1980; Draine et al. 1983; Hollenbach et al. 1989; Hollenbach 1997), their chemical impacts in star forming regions, especially in the HMSFRs, is still unclear. For example, one knows that some endothermic reactions can proceed by gaining the activation energies from shocks (Neufeld & Dalgarno 1989b). Shocks in HMSFRs are expected to be stronger coming from more violent dynamics, but no observation so far has sufficiently quantitatively compared the chemical differences between pre-shock and post-shock regions. Therefore, a comprehensive shock chemistry study needs a large sample of observations at high spatial resolution, with the results being included in the chemical simulations in the future.

5.2.2 Disk chemistry

In the generally accepted scenario of low mass star formation (Section 1.1.2), a cloud collapses in an inside-out fashion, gas is accreted onto the central protostar through a disk-like structure, which reduces the radiative pressure (Nakano 1989; Jijina & Adams 1996; Yorke & Sonnhalter 2002), and may form a planetary system afterward (Alexander et al. 2013; Turner et al. 2014). The protoplanetary disks are ubiquitous around Class II low mass YSOs (namely, "T Tauri" and "Herbig Ae" stars, Dutrey et al. 2007) on the scales of $\sim$ 100–500 AU. Recent studies have reported the Keplerian disks/structures for Class 0 low mass YSOs (e.g., Tobin et al. 2012) and MYSOs up to spectral type B1/B0 (e.g., several MYSOs listed in Cesaroni et al. 2007). However, the presence of these gaseous Keplerian disk is not confirmed by direct observations in type O MYSO so far.

Despite the lack of detections, the existence of accretion disks around MYSOs are indicated from outflow detections (see Section 5.2.1) and magnetohydrodynamics (MHD) simulations (e.g., Yorke & Sonnhalter 2002; Krumholz et al. 2009; Peters et al. 2010; Kuiper et al. 2011; Kuiper & Klessen 2013). Nevertheless, their dynamics are still debated: Are they Keplerian disks or self-gravitating toroids/pseudo-disks (e.g., Cesaroni et al. 2007; Sánchez-Monge et al. 2013), or some multilayer structures where a large scale toroid/pseudo-disk feeds an inner Kep-

lerian disk (e.g., Stahler & Palla 2005; Kuiper et al. 2011). Moreover, even with clear detections by pushing the limit of ALMA (e.g., exhibiting the fine details of disk structure like in low mass HL Tauri[6]), the chemistry of the protoplanetary disks is still poorly understood. The unknown chemistry of MYSO disk candidates challenges the spatial resolution of NOEMA and ALMA[7]. If they are detected, are their resolved dynamics similar to those of low mass protoplanetary disks, will they show similar chemical features, e.g., an obvious snowline[8] which indicates clear chemical anti-correlation between two species (e.g., CO snowline in low mass TW Hya disk, Qi et al. 2013)?

A time promising observational project conducted by the Very Large Array (VLA) at a spatial resolution of 250 AU (P. I.: H., Beuther) will follow up our chemical study in the high mass disk candidate NGC 7538 IRS1. Moreover, a large observational programme is undergoing recently (P. I.: H., Beuther), with the operation of PdBI at a spatial resolution of 0.2-0.35″ ($\leq$ 1000 AU at a distance < 6 kpc). By surveying a sample of 18 HMSFRs at (sub)mm wavelength, complemented by archival data at near- mid-infrared and cm wavelengths, we are aiming to systematically study the fragmentation and disk formation, as well as chemical evolution and inner jet/outflow properties during high mass star formation.

5.2.3 Chemical clocks: deuteration & S-bearing molecules

Searching for the chemical clocks is one of the main goals of astrochemistry. High spatial resolution observations provide us several cases of resolved sources, whose chemical inhomogeneities (Chapter 3) indicate that simultaneous collapsing sources may be in different evolutionary stages despite a small distance separation (< 5 000 AU). To better constrain the source ages from the future observations, both the dynamic timescale and warm-up pace need to be taken into consideration, thus a robust chemical clock is fundamental. However, it not yet clear which line(s) can trace the chemical history during the evolution from a prestellar object to a protostar, how to select the chemical clock and by which means it can quantify the sample. Nevertheless, several candidates are proposed for further consideration.

- **Deuteration:**
  Deuterium is formed at the birth of the Universe with an initial abundance D/H $\sim 1.6 \times 10^{-5}$, and it is destroyed later in the interiors of the stars (Ceccarelli et al. 2014). In some extreme environments (e.g., low temperature, inefficient destroyer such as the free out of CO, cosmic ray ionization), it can be enriched from H_2 or H via the process $H_2/H \rightarrow H_2^+ \rightarrow$

[6]http://www.eso.org/public/news/eso1436

[7]In resolving an outer disk (with typical size 100 AU) in Orion at distance of 450 pc, a spatial resolution of at least 0.2″ is required; in resolving an inner disk (with typical size 5 AU) in the same region, a spatial resolution of at least 0.01″ is required.

[8]The radius where a molecule changes from being primarily in the gas phase to being frozen out as ice.

$H_3^+ \rightarrow H_2D^+/D_2H^+/D_3^+ \rightarrow$ D-bearing species (e.g., Crapsi et al. 2005; Chen et al. 2011), namely, deuteration. Since the deuteration efficiency is strongly temperature dependent (i.e., the lower environment shows higher deuteration, Caselli et al. 2002c; Albertsson et al. 2013), and shows clear correlation with the level of CO depletion (Roueff et al. 2005; Emprechtinger et al. 2009) and gas density (Daniel et al. 2007), observational studies were designed to check the possibility of using deuteration fraction as chemical clock in low mass YSO. Recent systematic studies revealed correlations between N_2H^+ deuteration and CO depletion in several high mass sources at different evolutionary stages (Chen et al. 2011), and proposed the N_2D^+/N_2H^+ column density ratio as an indicator for the evolution of HMSFRs. However, targeting only a single deuterated species, focusing on a limited number of sources is insufficient. The construction of a complete deuterium model requires observations covering a range of molecules in more HMSFRs, spanning the stages from HMSC through HMPO to HMC.

- **S-bearing molecules**
  Previous observations reveal enhanced abundances of S-bearing molecules in shocked regions, motivating their use as shock tracers (Pineau des Forets et al. 1993). Advanced studies indicate S-bearing species can form via both fast gas phase and dust surfaces reactions (Pratap et al. 1997; Bradley 1999). The abundance of these species significantly increase with rising temperature caused by both ice evaporation and shock interaction, hence they are also considered to be good tracers of evolutionary stages of HMSFRs (e.g., Charnley 1997; Hatchell et al. 1998; van der Tak 2004; Wakelam et al. 2004a,b). However, sulfur chemistry has not been widely investigated. For one thing, most of the rate constants for S-bearing reactions were not measured in the laboratory; for another, it is a challenge to identify the key gas phase processes for key S-bearing species in dense clouds because of the sensitivity limit of previous space and ground based telescopes. As a result, despite several attempts to put constraints on the age of the sources through S-bearing abundances (e.g., Buckle & Fuller 2003; Herpin et al. 2009; Dutrey et al. 2011; Druard & Wakelam 2012; Loison et al. 2012), there is neither a well-established database nor a well-described compatible model of sulfur chemistry so far. On top of that, most of the previous observations also pointed to a puzzling behaviour of S-bearing species: Although they appear to be strongly depleted in dense molecular clouds by a factor of 1 000 compared to their estimated cosmic abundance, the depletion of sulfur in the diffuse cloud is negligible (e.g., Spitzer & Fitzpatrick 1993; Sofia et al. 1994; Savage & Sembach 1996). Based on the "zero depletion" feature, these species have been widely used as a proxy for gas density when deriving depletions for some other species in the diffuse cloud. However, a recent calculation argues that the "zero depletion" may come from observational biases (Jenkins 2009), so to re-examine the depletion of S-bearing species in different clouds is essential in the context of investigating the life cycle of molecules in the ISM.

5.2.4 Astrochemistry in the global scale

The detection of COMs in the HMSFRs guides us in the search for the origin of building blocks of life in the Universe. Taking advantage of the improvements in sensitivity and spectral coverage of modern telescopes, the questions we expect to answer are (Herbst 2014; van Dishoeck 2014):

- How are the COMs produced and excited?
- How complex can a stable COM be formed?
- What role does the formation and destruction of the molecules play in the life cycle of stars and planets?
- What are their roles in the evolution of the Universe?
- Most importantly, what is the path from COMs to the prebiotic origin of life?

More surveys need to be performed in regions that are under-represented in observations (e.g., UCHII and PDRs, Pety et al. 2012; Gratier et al. 2013; Guzmán et al. 2012, 2013), at further distance (high redshift galaxies), to hunt for more molecules (e.g., Belloche et al. 2013; Jiménez-Serra et al. 2014; Neill et al. 2014), and to discover new processes and excitations.

As outlined above, astrochemistry is leaving the infancy stage and entering a very bright future, where I am looking forward to dive into even more.

Acknowledgments

Doing a PhD for me is going on a life-changing journey, with a lot of thorny challenges and glory moments. At the terminal point of this journey, with all the works I present in this thesis, I wish to acknowledge those who encouraged me, inspired me and supported me to triumph over the challenges, those who show kindness to me, and those who share part of this journey and friendships with me.

First and foremost, I would like to express my sincere gratitude to Prof. Dr. Henrik Beuther, whom I would rather call as my mentor. In Chinese, a person who does not only teach you some professional skills but also helps your ethical development is respected as a “shifu”, and Henrik is my shifu. He is always available for conversations, providing constructive comments and suggestions on my works, encouraging me and promoting my research independence. Moreover, in the past three years, he helped me overcome the cultural shock, improved my time management skills, and pulled me out of the depression when I was suffering from the loss of my beloved grandparents. He is my role model who introduces me to this fantastic field, helps to boost my self-confidence and inspires my career ambition.

There are two other persons I want to express special gratitude are, Prof. Dr. Thomas Henning and Dr. Qizhou Zhang. I would like to thank Thomas for his expertise and insights into the field of Astronomy, and his suggestions everytime I am lost in the maze of mere details. I would like to thank Qizhou for hosting me during my 2-month visit to Harvard-Smithsonian Center for Astrophysics (CfA). I have greatly benefited from all our conversations, on both astronomy and the non-scientific topics.

Gratitude also goes to Prof. Dr. Cornelis P. Dullemond, for his valuable comments during all of my thesis committee meetings, and his generosity in reviewing my thesis. I would also like to thank Prof. Dr. Mario Trieloff for joining my final examination committee.

I am indebted to my co-authors: Dmitry Semenov, Elisabeth A.C. Mills, Hendrik Linz and Aina Palau, who have significant contributions on my papers; to my colleagues past and present at MPIA: Katharine Johnston, Simon Bihr, Lan Zhang, Guo Chen, Xiangxiang Xue, Veselina Kalinova, Salvatore Cielo, Somayeh Nezami, Yuyen Chang and Tobias Albertsson; to my friends at CfA: Cara Betersby, Linda Watson, Lars Kristensen, Til Birnstiel, Laura Vertatschitsch, and Xing Lv; to my friends Yuan Wang at University of Geneva and Zhiyu Zhang at ESO. All those eye-opening scientific discussions we had illuminated me, and helped to develop me as a professional astronomer; all those mind-blowing non-scientific conversations left me precious memories.

Many thanks to the IMPRS coordinator Christian Fendt, and to all the people in IMPRS especially from the 7th generation. It is very fortunate of me to have you around in the past three years. Those joyful moments we had, during the retreats, from Prague to Sicily, will be engraved in my memory! I am grateful to Simon Bihr, for his help with translating my German Zusammenfassung, and Richard Teague for proof-reading my thesis and giving constructive feedback.

I acknowledge financial support by the European Communitys Seventh Framework Programme [FP7/2007-2013] under grant agreement no. 238258.

The deepest gratitude I owe to my parents. Without their tremendous support and advice, I would not have the courage to face all the challenges since ten years ago when I left my hometown. I appreciate their understanding of the career choice I made, and I am very thankful for their consistent trust and encouragement.

My last gratitude, goes to two most important persons I lost in 2013. This thesis is dedicated to them. Farewell my grandfather and grandmother, thank you for having been in my life. I believe one day I will meet you again, and I believe I can still feel your love from the stars ...

Bibliography

Afonso, J. M., Yun, J. L., & Clemens, D. P. 1998, , 115, 1111

Aikawa, Y., Herbst, E., Roberts, H., & Caselli, P. 2005, , 620, 330

Aikawa, Y., Wakelam, V., Garrod, R. T., & Herbst, E. 2008, , 674, 984

Aikawa, Y., Wakelam, V., Hersant, F., Garrod, R. T., & Herbst, E. 2012, , 760, 40

Akabane, K. & Kuno, N. 2005, , 431, 183

Albertsson, T., Semenov, D. A., Vasyunin, A. I., Henning, T., & Herbst, E. 2013, , 207, 27

Alexander, R., Pascucci, I., Andrews, S., Armitage, P., & Cieza, L. 2013, ArXiv e-prints

Allen, D. A. & Burton, M. G. 1993, , 363, 54

Allen, M. & Robinson, G. W. 1977, , 214, 955

Andersson, M., Askne, J., & Hjalmarson, A. 1984, , 136, 243

André, P. 1995, , 224, 29

André, P., Di Francesco, J., Ward-Thompson, D., et al. 2013, ArXiv e-prints

Anicich, V. G. 1993, Journal of Physical and Chemical Reference Data, 22, 1469

Ao, Y., Henkel, C., Menten, K. M., et al. 2013, , 550, A135

Araya, E., Hofner, P., Kurtz, S., Bronfman, L., & DeDeo, S. 2005, , 157, 279

Arce, H. G., Mardones, D., Corder, S. A., et al. 2013, , 774, 39

Arce, H. G., Shepherd, D., Gueth, F., et al. 2007, Protostars and Planets V, 245

Argon, A. L., Reid, M. J., & Menten, K. M. 2000, , 129, 159

Bachiller, R. & Pérez Gutiérrez, M. 1997, , 487, L93

Bachiller, R., Pérez Gutiérrez, M., Kumar, M. S. N., & Tafalla, M. 2001, , 372, 899

Bacmann, A., Taquet, V., Faure, A., Kahane, C., & Ceccarelli, C. 2012, , 541, L12

Bajaja, E. & van Albada, G. D. 1979, , 75, 251

Ballesteros-Paredes, J., Klessen, R. S., Mac Low, M.-M., & Vazquez-Semadeni, E. 2007, Protostars and Planets V, 63

Bally, J., Cunningham, N. J., Moeckel, N., et al. 2011, , 727, 113

Bally, J. & Zinnecker, H. 2005, , 129, 2281

Balog, Z., Kenyon, S. J., Lada, E. A., et al. 2004, , 128, 2942

Banerjee, R., Vázquez-Semadeni, E., Hennebelle, P., & Klessen, R. S. 2009, , 398, 1082

Barentine, J. C. & Lacy, J. H. 2012, , 757, 111

Bastien, P., Arcoragi, J.-P., Benz, W., Bonnell, I., & Martel, H. 1991, , 378, 255

Bate, M. R., Tricco, T. S., & Price, D. J. 2014, , 437, 77

Becker, R. H., White, R. L., McLean, B. J., Helfand, D. J., & Zoonematkermani, S. 1990, , 358, 485

Beckwith, S., Persson, S. E., Neugebauer, G., & Becklin, E. E. 1978, , 223, 464

Bell, T. A., Cernicharo, J., Viti, S., et al. 2014, , 564, A114

Belloche, A., Garrod, R. T., Müller, H. S. P., et al. 2009, , 499, 215

Belloche, A., Menten, K. M., Comito, C., et al. 2008, , 482, 179

Belloche, A., Müller, H. S. P., Menten, K. M., Schilke, P., & Comito, C. 2013, , 559, A47

Beltrán, M. T., Cesaroni, R., Codella, C., et al. 2006, , 443, 427

Bergin, E. A. 2003, in SFChem 2002: Chemistry as a Diagnostic of Star Formation, ed. C. L. Curry & M. Fich, 63

Bergin, E. A., Alves, J., Huard, T., & Lada, C. J. 2002, , 570, L101

Bergin, E. A., Goldsmith, P. F., Snell, R. L., & Ungerechts, H. 1994, , 431, 674

Bergin, E. A., Hartmann, L. W., Raymond, J. C., & Ballesteros-Paredes, J. 2004, , 612, 921

Bergin, E. A., Phillips, T. G., Comito, C., et al. 2010, , 521, L20

Bergin, E. A., Plume, R., Williams, J. P., & Myers, P. C. 1999, , 512, 724

Bergin, E. A., Snell, R. L., & Goldsmith, P. F. 1996, , 460, 343

Bergin, E. A. & Tafalla, M. 2007, , 45, 339

Beuther, H., Churchwell, E. B., McKee, C. F., & Tan, J. C. 2007, Protostars and Planets V, 165

Beuther, H. & Henning, T. 2009, , 503, 859

Beuther, H., Henning, T., Linz, H., et al. 2010a, , 518, L78

Beuther, H., Kainulainen, J., Henning, T., Plume, R., & Heitsch, F. 2011, , 533, A17

Beuther, H., Linz, H., Bik, A., Goto, M., & Henning, T. 2010b, , 512, A29

Beuther, H., Linz, H., & Henning, T. 2012a, , 543, A88

Beuther, H., Linz, H., & Henning, T. 2013a, , 558, A81

Beuther, H., Linz, H., Tackenberg, J., et al. 2013b, , 553, A115

Beuther, H. & Nissen, H. D. 2008, , 679, L121

Beuther, H., Schilke, P., Menten, K. M., et al. 2002, , 566, 945

Beuther, H., Semenov, D., Henning, T., & Linz, H. 2008, , 675, L33

Beuther, H. & Shepherd, D. 2005, in Cores to Clusters: Star Formation with Next Generation Telescopes, ed. M. S. N. Kumar, M. Tafalla, & P. Caselli, 105–119

Beuther, H. & Sridharan, T. K. 2007, , 668, 348

Beuther, H., Tackenberg, J., Linz, H., et al. 2012b, , 538, A11

Beuther, H., Thorwirth, S., Zhang, Q., et al. 2005a, , 627, 834

Beuther, H., Zhang, Q., Greenhill, L. J., et al. 2004, , 616, L31

Beuther, H., Zhang, Q., Greenhill, L. J., et al. 2005b, , 632, 355

Beuther, H., Zhang, Q., Reid, M. J., et al. 2006, , 636, 323

Bisschop, S. E., Fuchs, G. W., van Dishoeck, E. F., & Linnartz, H. 2007, , 474, 1061

Bisschop, S. E., Schilke, P., Wyrowski, F., et al. 2013, , 552, A122

Blake, G. A., Mundy, L. G., Carlstrom, J. E., et al. 1996, , 472, L49

Blake, G. A., Sutton, E. C., Masson, C. R., & Phillips, T. G. 1987, , 315, 621

Bonnell, I. A., Bate, M. R., Clarke, C. J., & Pringle, J. E. 2001, , 323, 785

Bonnell, I. A., Bate, M. R., & Zinnecker, H. 1998, , 298, 93

Bonnell, I. A., Larson, R. B., & Zinnecker, H. 2007, Protostars and Planets V, 149

Bonnell, I. A., Vine, S. G., & Bate, M. R. 2004, , 349, 735

Bontemps, S., Motte, F., Csengeri, T., & Schneider, N. 2010, , 524, A18

Boucher, D., Burie, J., Bauer, A., Dubrulle, A., & Demaison, J. 1980, Journal of Physical and Chemical Reference Data, 9, 659

Bradley, J. P. 1999, in NATO Advanced Science Institutes (ASI) Series C, Vol. 523, NATO Advanced Science Institutes (ASI) Series C, ed. J. M. Greenberg & A. Li, 485

Bronfman, L., Nyman, L.-A., & May, J. 1996, , 115, 81

Brouillet, N., Despois, D., Baudry, A., et al. 2013, , 550, A46

Buckle, J. V. & Fuller, G. A. 2003, , 399, 567

Butler, M. J. & Tan, J. C. 2009, , 696, 484

Campbell, B. 1984, , 282, L27

Campbell, B. & Thompson, R. I. 1984, , 279, 650

Carey, S. J., Clark, F. O., Egan, M. P., et al. 1998, , 508, 721

Caselli, P., Benson, P. J., Myers, P. C., & Tafalla, M. 2002a, , 572, 238

Caselli, P., Hasegawa, T. I., & Herbst, E. 1993, , 408, 548

Caselli, P., Walmsley, C. M., Tafalla, M., Dore, L., & Myers, P. C. 1999, , 523, L165

Caselli, P., Walmsley, C. M., Terzieva, R., & Herbst, E. 1998, , 499, 234

Caselli, P., Walmsley, C. M., Zucconi, A., et al. 2002b, , 565, 331

Caselli, P., Walmsley, C. M., Zucconi, A., et al. 2002c, , 565, 331

Caselli, P., Walmsley, C. M., Zucconi, A., et al. 2002d, , 565, 344

Ceccarelli, C., Caselli, P., Bockelee-Morvan, D., et al. 2014, ArXiv e-prints

Cesaroni, R. 2005, in IAU Symposium, Vol. 227, Massive Star Birth: A Crossroads of Astrophysics, ed. R. Cesaroni, M. Felli, E. Churchwell, & M. Walmsley, 59–69

Cesaroni, R., Galli, D., Lodato, G., Walmsley, C. M., & Zhang, Q. 2007, Protostars and Planets V, 197

Cesaroni, R., Neri, R., Olmi, L., et al. 2005, , 434, 1039

Chandler, C. J. & Wood, D. O. S. 1997, , 287, 445

Chandrasekhar, S. & Fermi, E. 1953, , 118, 116

Chapman, J. F., Millar, T. J., Wardle, M., Burton, M. G., & Walsh, A. J. 2009, , 394, 221

Charnley, S. B. 1997, , 481, 396

Charnley, S. B., Rodgers, S. D., & Ehrenfreund, P. 2001, , 378, 1024

Charnley, S. B., Tielens, A. G. G. M., & Millar, T. J. 1992, , 399, L71

Charnley, S. B., Tielens, A. G. G. M., & Rodgers, S. D. 1997, , 482, L203

Chen, H.-R., Liu, S.-Y., Su, Y.-N., & Wang, M.-Y. 2011, , 743, 196

Chen, H.-R., Welch, W. J., Wilner, D. J., & Sutton, E. C. 2006, , 639, 975

Chen, L. & Woon, D. E. 2011, J. Phys. Chem. A, 115, 5166

Chernin, L. M., Masson, C. R., & Fuller, G. A. 1994, , 436, 741

Chernin, L. M. & Wright, M. C. H. 1996, , 467, 676

Chin, Y.-N., Henkel, C., Whiteoak, J. B., Langer, N., & Churchwell, E. B. 1996, , 305, 960

Churchwell, E. 2002, , 40, 27

Churchwell, E., Sievers, A., & Thum, C. 2010, , 513, A9

Codella, C., Bachiller, R., Nisini, B., Saraceno, P., & Testi, L. 2001, , 376, 271

Cohen, R. J., Gasiprong, N., Meaburn, J., & Graham, M. F. 2006, , 367, 541

Comito, C., Schilke, P., Phillips, T. G., et al. 2005, , 156, 127

Corder, S. A. 2009, PhD thesis, California Institute of Technology

Cragg, D. M., Johns, K. P., Godfrey, P. D., & Brown, R. D. 1992, , 259, 203

Cragg, D. M., Sobolev, A. M., & Godfrey, P. D. 2005, , 360, 533

Crapsi, A., Caselli, P., Walmsley, C. M., et al. 2005, , 619, 379

Crockett, N. R., Bergin, E. A., Neill, J. L., et al. 2014, , 787, 112

Csengeri, T., Bontemps, S., Schneider, N., Motte, F., & Dib, S. 2011, , 527, A135

Cunningham, A. J., Klein, R. I., Krumholz, M. R., & McKee, C. F. 2011, , 740, 107

Cyganowski, C. J., Brogan, C. L., Hunter, T. R., et al. 2014, , 796, L2

Dalgarno, A. & Black, J. H. 1976, Reports on Progress in Physics, 39, 573

Daniel, F., Cernicharo, J., Roueff, E., Gerin, M., & Dubernet, M. L. 2007, , 667, 980

Daranlot, J., Hincelin, U., Bergeat, A., et al. 2012, Proceedings of the National Academy of Science, 109, 10233

De Buizer, J. M. & Minier, V. 2005, , 628, L151

Demyk, K., Wlodarczak, G., & Carvajal, M. 2008, , 489, 589

Devine, K. E., Chandler, C. J., Brogan, C., et al. 2011, , 733, 44

D'Hendecourt, L. B., Allamandola, L. J., & Greenberg, J. M. 1985, , 152, 130

Di Francesco, J., Johnstone, D., Kirk, H., MacKenzie, T., & Ledwosinska, E. 2008, , 175, 277

Dobbs, C. L., Krumholz, M. R., Ballesteros-Paredes, J., et al. 2013, ArXiv e-prints

Doeleman, S. S., Lonsdale, C. J., & Pelkey, S. 1999, , 510, L55

Doi, T., O'Dell, C. R., & Hartigan, P. 2002, , 124, 445

Dougados, C., Lena, P., Ridgway, S. T., Christou, J. C., & Probst, R. G. 1993, , 406, 112

Downes, D., Genzel, R., Becklin, E. E., & Wynn-Williams, C. G. 1981, , 244, 869

Draine, B. T. 1980, , 241, 1021

Draine, B. T. 2003, , 41, 241

Draine, B. T. 2011, Physics of the Interstellar and Intergalactic Medium

Draine, B. T., Roberge, W. G., & Dalgarno, A. 1983, , 264, 485

Druard, C. & Wakelam, V. 2012, , 426, 354

Duarte-Cabral, A., Bontemps, S., Motte, F., et al. 2013, , 558, A125

Dunham, M. M., Stutz, A. M., Allen, L. E., et al. 2014, ArXiv e-prints

Dutrey, A., Henning, T., Guilloteau, S., et al. 2007, , 464, 615

Dutrey, A., Wakelam, V., Boehler, Y., et al. 2011, , 535, A104

Edgar, R. & Clarke, C. 2003, , 338, 962

Egan, M. P., Shipman, R. F., Price, S. D., et al. 1998, , 494, L199

Ehrenfreund, P. & Charnley, S. B. 2000, , 38, 427

Eisner, J. A., Plambeck, R. L., Carpenter, J. M., et al. 2008, , 683, 304

Ellingsen, S. P. 2006, , 638, 241

Elmegreen, B. G. & Lada, C. J. 1977, , 214, 725

Emprechtinger, M., Caselli, P., Volgenau, N. H., Stutzki, J., & Wiedner, M. C. 2009, , 493, 89

Emprechtinger, M., Lis, D. C., Rolffs, R., et al. 2013, , 765, 61

Erickson, N. R., Goldsmith, P. F., Snell, R. L., et al. 1982, , 261, L103

Esplugues, G. B., Tercero, B., Cernicharo, J., et al. 2013, , 556, A143

Favre, C., Despois, D., Brouillet, N., et al. 2011a, , 532, A32

Favre, C., Wootten, H. A., Remijan, A. J., et al. 2011b, , 739, L12

Fiege, J. D. & Pudritz, R. E. 2000, , 311, 85

Fischera, J. & Martin, P. G. 2012, , 542, A77

Fish, V. L., Muehlbrad, T. C., Pratap, P., et al. 2011, , 729, 14

Fontani, F., Caselli, P., Crapsi, A., et al. 2006, , 460, 709

Fontani, F., Giannetti, A., Beltrán, M. T., et al. 2012, , 423, 2342

Fontani, F., Palau, A., Caselli, P., et al. 2011, , 529, L7

Fontani, F., Sakai, T., Furuya, K., et al. 2014, , 440, 448

Foster, J. B., Jackson, J. M., Barnes, P. J., et al. 2011, , 197, 25

Frank, A., Ray, T. P., Cabrit, S., et al. 2014, ArXiv e-prints

Frerking, M. A., Langer, W. D., & Wilson, R. W. 1982, , 262, 590

Friedel, D. N. & Snyder, L. E. 2008, , 672, 962

Friedel, D. N., Snyder, L. E., Remijan, A. J., & Turner, B. E. 2005, , 632, L95

Friedel, D. N. & Widicus Weaver, S. L. 2011, , 742, 64

Friedel, D. N. & Widicus Weaver, S. L. 2012, , 201, 17

Fuller, G. A., Williams, S. J., & Sridharan, T. K. 2005, , 442, 949

Garay, G., Mardones, D., Bronfman, L., et al. 2007, , 463, 217

Garrod, R. T. 2013, , 765, 60

Garrod, R. T. & Herbst, E. 2006, , 457, 927

Garrod, R. T., Wakelam, V., & Herbst, E. 2007, , 467, 1103

Garrod, R. T., Weaver, S. L. W., & Herbst, E. 2008, , 682, 283

Garrod, R. T. & Widicus Weaver, S. L. 2013, Chemical Reviews, 113, 8939

Gaume, R. A., Goss, W. M., Dickel, H. R., Wilson, T. L., & Johnston, K. J. 1995, , 438, 776

Gaume, R. A., Johnston, K. J., Nguyen, H. A., et al. 1991, , 376, 608

Gaume, R. A., Wilson, T. L., Vrba, F. J., Johnston, K. J., & Schmid-Burgk, J. 1998, , 493, 940

Genzel, R., Reid, M. J., Moran, J. M., & Downes, D. 1981, , 244, 884

Genzel, R. & Stutzki, J. 1989, , 27, 41

Gerner, T., Beuther, H., Semenov, D., et al. 2014, , 563, A97

Giannetti, A., Wyrowski, F., Brand, J., et al. 2014, , 570, A65

Gibb, E. L., Whittet, D. C. B., Boogert, A. C. A., & Tielens, A. G. G. M. 2004, , 151, 35

Girart, J. M., Rao, R., & Estalella, R. 2009, , 694, 56

Giveon, U., Becker, R. H., Helfand, D. J., & White, R. L. 2005, , 129, 348

Goddi, C., Humphreys, E. M. L., Greenhill, L. J., Chandler, C. J., & Matthews, L. D. 2011, , 728, 15

Goldsmith, P. F., Irvine, W. M., Hjalmarson, A., & Ellder, J. 1986a, , 310, 383

Goldsmith, P. F., Irvine, W. M., Hjalmarson, A., & Ellder, J. 1986b, , 310, 383

Goldsmith, P. F. & Langer, W. D. 1999, , 517, 209

Goldsmith, P. F., Snell, R. L., Deguchi, S., Krotkov, R., & Linke, R. A. 1982, , 260, 147

Gómez, L., Rodríguez, L. F., Loinard, L., et al. 2008, , 685, 333

Gómez, L., Rodr´guez, L. F., Loinard, L., et al. 2005, , 635, 1166

Gong, H. & Ostriker, E. C. 2011, , 729, 120

Gratier, P., Pety, J., Guzmán, V., et al. 2013, , 557, A101

Greaves, J. S. & White, G. J. 1991, , 91, 237

Greenhill, L. J., Gezari, D. Y., Danchi, W. C., et al. 2004, , 605, L57

Greenhill, L. J., Gwinn, C. R., Schwartz, C., Moran, J. M., & Diamond, P. J. 1998, , 396, 650

Guélin, M., Brouillet, N., Cernicharo, J., Combes, F., & Wootten, A. 2008, , 313, 45

Guertler, J., Henning, T., Kruegel, E., & Chini, R. 1991, , 252, 801

Guzmán, V., Pety, J., Gratier, P., et al. 2012, , 543, L1

Guzmán, V. V., Goicoechea, J. R., Pety, J., et al. 2013, , 560, A73

Harada, N., Herbst, E., & Wakelam, V. 2010, , 721, 1570

Harada, N., Herbst, E., & Wakelam, V. 2012, , 756, 104

Hartmann, L. 1998, Accretion Processes in Star Formation

Hasegawa, T. I. & Herbst, E. 1993, , 261, 83

Hasegawa, T. I., Herbst, E., & Leung, C. M. 1992, , 82, 167

Hatchell, J., Thompson, M. A., Millar, T. J., & MacDonald, G. H. 1998, , 338, 713

Hatchell, J. & van der Tak, F. F. S. 2003, , 409, 589

Hayashi, C. 1961, , 13, 450

Heiles, C. & Crutcher, R. 2005, in Lecture Notes in Physics, Berlin Springer Verlag, Vol. 664, Cosmic Magnetic Fields, ed. R. Wielebinski & R. Beck, 137

Heitsch, F., Hartmann, L. W., Slyz, A. D., Devriendt, J. E. G., & Burkert, A. 2008, , 674, 316

Helmich, F. P. & van Dishoeck, E. F. 1997, , 124, 205

Henkel, C., Wilson, T. L., & Johnston, K. J. 1984, , 282, L93

Henning, T., Linz, H., Krause, O., et al. 2010, , 518, L95

Henshaw, J. D., Caselli, P., Fontani, F., et al. 2013, , 428, 3425

Herbst, E. 1981, , 289, 656

Herbst, E. 2014, Faraday Discuss., 168, 617

Herbst, E. & Klemperer, W. 1973, , 185, 505

Herbst, E. & van Dishoeck, E. F. 2009, , 47, 427

Herpin, F., Marseille, M., Wakelam, V., Bontemps, S., & Lis, D. C. 2009, , 504, 853

Hildebrand, R. H. 1983, , 24, 267

Hiraoka, K., Sato, T., Sato, S., et al. 2002, , 577, 265

Hirota, T., Ohishi, M., & Yamamoto, S. 2009, , 699, 585

Hirota, T., Yamamoto, S., Mikami, H., & Ohishi, M. 1998, , 503, 717

Ho, P. T. P., Moran, J. M., & Lo, K. Y. 2004, , 616, L1

Hoare, M. G., Purcell, C. R., Churchwell, E. B., et al. 2012, , 124, 939

Hoffman, I. M., Goss, W. M., Palmer, P., & Richards, A. M. S. 2003, , 598, 1061

Hofner, P., Peterson, S., & Cesaroni, R. 1999, , 514, 899

Hofner, P., Wiesemeyer, H., & Henning, T. 2001, , 549, 425

Hollenbach, D. 1997, in IAU Symposium, Vol. 182, Herbig-Haro Flows and the Birth of Stars, ed. B. Reipurth & C. Bertout, 181–198

Hollenbach, D., Kaufman, M. J., Bergin, E. A., & Melnick, G. J. 2009, , 690, 1497

Hollenbach, D. J., Chernoff, D. F., & McKee, C. F. 1989, in ESA Special Publication, Vol. 290, Infrared Spectroscopy in Astronomy, ed. E. Böhm-Vitense, 245–258

Hollis, J. M. 1982, , 260, 159

Hollis, J. M., Jewell, P. R., Lovas, F. J., & Remijan, A. 2004, , 613, L45

Hollis, J. M., Lovas, F. J., & Jewell, P. R. 2000, , 540, L107

Hollis, J. M., Lovas, F. J., Jewell, P. R., & Coudert, L. H. 2002, , 571, L59

Hoq, S., Jackson, J. M., Foster, J. B., et al. 2013, , 777, 157

Hutawarakorn, B. & Cohen, R. J. 2003, , 345, 175

Inutsuka, S.-I. & Miyama, S. M. 1992, , 388, 392

Jackson, J. M., Finn, S. C., Chambers, E. T., Rathborne, J. M., & Simon, R. 2010, , 719, L185

Jackson, J. M., Rathborne, J. M., Foster, J. B., et al. 2013, , 30, 57

Jenkins, E. B. 2009, , 700, 1299

Jeyakumar, S. & Roshi, D. A. 2013, , 434, 2742

Jijina, J. & Adams, F. C. 1996, , 462, 874

Jiménez-Serra, I., testi, L., Caselli, P., & Viti, S. 2014, , 787, L33

Jiménez-Serra, I., Zhang, Q., Viti, S., Martín-Pintado, J., & de Wit, W.-J. 2012, , 753, 34

Johansson, L. E. B., Andersson, C., Ellder, J., et al. 1984, , 130, 227

Johnstone, D. & Bally, J. 1999, , 510, L49

Jones, P. A., Burton, M. G., Cunningham, M. R., et al. 2008, , 386, 117

Jørgensen, J. K., Favre, C., Bisschop, S. E., et al. 2012, , 757, L4

Jørgensen, J. K., Schöier, F. L., & van Dishoeck, E. F. 2004, , 416, 603

Kahane, C., Ceccarelli, C., Faure, A., & Caux, E. 2013, , 763, L38

Kahn, F. D. 1974, , 37, 149

Kalenskii, S. V., Promislov, V. G., Alakoz, A., Winnberg, A. V., & Johansson, L. E. B. 2000, , 354, 1036

Kameya, O., Morita, K.-I., Kawabe, R., & Ishiguro, M. 1990, , 355, 562

Katz, N., Furman, I., Biham, O., Pirronello, V., & Vidali, G. 1999, , 522, 305

Kawabe, R., Suzuki, M., Hirano, N., et al. 1992, , 44, 435

Keto, E. 2003, , 599, 1196

Keto, E. & Wood, K. 2006, , 637, 850

Keto, E., Zhang, Q., & Kurtz, S. 2008, , 672, 423

Kim, K.-T. & Koo, B.-C. 2001, , 549, 979

Knez, C., Lacy, J. H., Evans, II, N. J., van Dishoeck, E. F., & Richter, M. J. 2009, , 696, 471

Kraus, S., Balega, Y., Elitzur, M., et al. 2006, , 455, 521

Krumholz, M. R., Bate, M. R., Arce, H. G., et al. 2014, ArXiv e-prints

Krumholz, M. R. & Bonnell, I. A. 2007, ArXiv e-prints

Krumholz, M. R., Klein, R. I., McKee, C. F., Offner, S. S. R., & Cunningham, A. J. 2009, Science, 323, 754

Krumholz, M. R. & McKee, C. F. 2008, , 451, 1082

Krumholz, M. R., McKee, C. F., & Klein, R. I. 2005, , 618, L33

Kuiper, R., Klahr, H., Beuther, H., & Henning, T. 2011, , 732, 20

Kuiper, R. & Klessen, R. S. 2013, , 555, A7

Kurtz, S. 2005, in IAU Symposium, Vol. 227, Massive Star Birth: A Crossroads of Astrophysics, ed. R. Cesaroni, M. Felli, E. Churchwell, & M. Walmsley, 111–119

Kurtz, S., Cesaroni, R., Churchwell, E., Hofner, P., & Walmsley, C. M. 2000, Protostars and Planets IV, 299

Kurtz, S., Hofner, P., & Álvarez, C. V. 2004, , 155, 149

Kwan, J. & Scoville, N. 1976, , 210, L39

Laas, J. C., Garrod, R. T., Herbst, E., & Widicus Weaver, S. L. 2011, , 728, 71

Lacombe, F., Gendron, E., Rouan, D., et al. 2004, , 417, L5

Lada, C. J. 1991, in NATO Advanced Science Institutes (ASI) Series C, Vol. 342, NATO Advanced Science Institutes (ASI) Series C, ed. C. J. Lada & N. D. Kylafis, 329

Larson, R. B. 1969, , 145, 297

Larson, R. B. 2005, , 359, 211

Lee, C. W. & Cho, S.-H. 2002, Journal of Korean Astronomical Society, 35, 187

Lee, C. W., Myers, P. C., & Tafalla, M. 2001, , 136, 703

Lee, H.-H., Roueff, E., Pineau des Forets, G., et al. 1998, , 334, 1047

Lee, J.-K. & Burton, M. G. 2000, , 315, 11

Lee, T. J. 1972, Nature Physical Science, 237, 99

Leger, A., Jura, M., & Omont, A. 1985, , 144, 147

Lerate, M. R., Yates, J., Viti, S., et al. 2008, , 387, 1660

Lintott, C. J. & Rawlings, J. M. C. 2006, , 448, 425

Linz, H., Krause, O., Beuther, H., et al. 2010, , 518, L123

Lis, D. C., Serabyn, E., Keene, J., et al. 1998, , 509, 299

Liseau, R., Goldsmith, P. F., Larsson, B., et al. 2012, , 541, A73

Liu, S.-Y., Girart, J. M., Remijan, A., & Snyder, L. E. 2002, , 576, 255

Lodders, K. 2003, , 591, 1220

Loison, J.-C., Halvick, P., Bergeat, A., Hickson, K. M., & Wakelam, V. 2012, , 421, 1476

López-Sepulcre, A., Codella, C., Cesaroni, R., Marcelino, N., & Walmsley, C. M. 2009, , 499, 811

Loren, R. B. & Mundy, L. G. 1984, , 286, 232

Loughnane, R. M., Redman, M. P., Thompson, M. A., et al. 2012, , 420, 1367

Lovas, F. J. 2004, Phys. Chem. Ref., 33, 117

Lugo, J., Lizano, S., & Garay, G. 2004, , 614, 807

Mangum, J. G. & Wootten, A. 1993, , 89, 123

Mardones, D., Myers, P. C., Tafalla, M., et al. 1997, , 489, 719

Maret, S., Hily-Blant, P., Pety, J., Bardeau, S., & Reynier, E. 2011, , 526, A47

Markwick, A. J., Millar, T. J., & Charnley, S. B. 2000, , 535, 256

Marti, J., Rodriguez, L. F., & Reipurth, B. 1993, , 416, 208

Martin, A. H. M. 1973, , 163, 141

Martin-Pintado, J., Bachiller, R., & Fuente, A. 1992, , 254, 315

Martin-Pintado, J. & Cernicharo, J. 1987, , 176, L27

Masson, C. R., Claussen, M. J., Lo, K. Y., et al. 1985, , 295, L47

Masson, C. R., Lo, K. Y., Phillips, T. G., et al. 1987, , 319, 446

Matthews, H. E. & Irvine, W. M. 1985, , 298, L61

McCarthy, M. C., Gottlieb, C. A., Gupta, H., & Thaddeus, P. 2006, , 652, L141

McCaughrean, M., Rayner, J., & Zinnecker, H. 1991, , 62, 715

McKee, C. F. & Ostriker, J. P. 1977, , 218, 148

McKee, C. F. & Tan, J. C. 2003, , 585, 850

Meier, D. S. & Turner, J. L. 2005, , 618, 259

Menten, K. M. 1991, , 380, L75

Menten, K. M. & Reid, M. J. 1995, , 445, L157

Menten, K. M., Reid, M. J., Forbrich, J., & Brunthaler, A. 2007, , 474, 515

Menten, K. M., Walmsley, C. M., Henkel, C., et al. 1986, , 169, 271

Miettinen, O., Harju, J., Haikala, L. K., Kainulainen, J., & Johansson, L. E. B. 2009, , 500, 845

Miettinen, O., Hennemann, M., & Linz, H. 2011, , 534, A134

Millar, T. J., Bennett, A., Rawlings, J. M. C., Brown, P. D., & Charnley, S. B. 1991, , 87, 585

Minier, V., Conway, J. E., & Booth, R. S. 2001, , 369, 278

Miotello, A., Bruderer, S., & van Dishoeck, E. F. 2014, ArXiv e-prints

Moscadelli, L., Reid, M. J., Menten, K. M., et al. 2009, , 693, 406

Motte, F., Bontemps, S., Schilke, P., et al. 2007, , 476, 1243

Mueller, K. E., Shirley, Y. L., Evans, II, N. J., & Jacobson, H. R. 2002, , 143, 469

Müller, H. S. P., Schlöder, F., Stutzki, J., & Winnewisser, G. 2005, Journal of Molecular Structure, 742, 215

Mundy, L. G., Scoville, N. Z., Baath, L. B., Masson, C. R., & Woody, D. P. 1986, , 304, L51

Murata, Y., Kawabe, R., Ishiguro, M., et al. 1992, , 44, 381

Myers, P. C., Linke, R. A., & Benson, P. J. 1983, , 264, 517

Myers, P. C., Mardones, D., Tafalla, M., Williams, J. P., & Wilner, D. J. 1996, , 465, L133

Nagasawa, M. 1987, Progress of Theoretical Physics, 77, 635

Nakano, T. 1989, , 345, 464

Naranjo-Romero, R., Zapata, L. A., Vázquez-Semadeni, E., et al. 2012, , 757, 58

Neill, J. L., Bergin, E. A., Lis, D. C., et al. 2014, , 789, 8

Neill, J. L., Steber, A. L., Muckle, M. T., et al. 2011, Journal of Physical Chemistry A, 115, 6472

Neill, J. L., Wang, S., Bergin, E. A., et al. 2013, , 770, 142

Neufeld, D. A. & Dalgarno, A. 1989a, , 340, 869

Neufeld, D. A. & Dalgarno, A. 1989b, , 344, 251

Niederhofer, F., Humphreys, E. M. L., & Goddi, C. 2012, , 548, A69

Nissen, H. D., Cunningham, N. J., Gustafsson, M., et al. 2012, , 540, A119

Nissen, H. D., Gustafsson, M., Lemaire, J. L., et al. 2007, , 466, 949

Norberg, P. & Maeder, A. 2000, , 359, 1025

Norris, R. P. 1984, , 207, 127

Nummelin, A., Bergman, P., Hjalmarson, Å., et al. 2000, , 128, 213

Öberg, K. I., Boogert, A. C. A., Pontoppidan, K. M., et al. 2011, , 740, 109

Öberg, K. I., Bottinelli, S., Jørgensen, J. K., & van Dishoeck, E. F. 2010, , 716, 825

Öberg, K. I., Linnartz, H., Visser, R., & van Dishoeck, E. F. 2009, , 693, 1209

Offner, S. S. R., Clark, P. C., Hennebelle, P., et al. 2013, ArXiv e-prints

Ohishi, M., Irvine, W. M., & Kaifu, N. 1992, in IAU Symposium, Vol. 150, Astrochemistry of Cosmic Phenomena, ed. P. D. Singh, 171

Ojha, D. K., Tamura, M., Nakajima, Y., et al. 2004, , 616, 1042

Olmi, L., Cesaroni, R., & Walmsley, C. M. 1993, in Bulletin of the American Astronomical Society, Vol. 25, American Astronomical Society Meeting Abstracts, 1315

Olofsson, A. O. H., Persson, C. M., Koning, N., et al. 2007, , 476, 791

Osorio, M., Lizano, S., & D'Alessio, P. 1999, , 525, 808

Ossenkopf, V. & Henning, T. 1994, , 291, 943

Padoan, P. & Nordlund, Å. 2002, , 576, 870

Padovani, M., Walmsley, C. M., Tafalla, M., Galli, D., & Müller, H. S. P. 2009, , 505, 1199

Palau, A., Fuente, A., Girart, J. M., et al. 2011, , 743, L32

Palau, A., Rizzo, J. R., Girart, J. M., & Henkel, C. 2014, , 784, L21

Palla, F. & Stahler, S. W. 1993, , 418, 414

Palumbo, M. E., Geballe, T. R., & Tielens, A. G. G. M. 1997, , 479, 839

Patel, N. A., Curiel, S., Sridharan, T. K., et al. 2005, , 437, 109

Peeters, Z., Rodgers, S. D., Charnley, S. B., et al. 2006, , 445, 197

Peng, T.-C., Despois, D., Brouillet, N., et al. 2013, , 554, A78

Peng, T.-C., Despois, D., Brouillet, N., Parise, B., & Baudry, A. 2012a, , 543, A152

Peng, T.-C., Zapata, L. A., Wyrowski, F., Güsten, R., & Menten, K. M. 2012b, , 544, L19

Perault, M., Omont, A., Simon, G., et al. 1996, , 315, L165

Peretto, N., Fuller, G. A., Duarte-Cabral, A., et al. 2013, , 555, A112

Persson, C. M., Olofsson, A. O. H., Koning, N., et al. 2007, , 476, 807

Pestalozzi, M. R., Elitzur, M., & Conway, J. E. 2009, , 501, 999

Pestalozzi, M. R., Elitzur, M., Conway, J. E., & Booth, R. S. 2004, , 603, L113

Pestalozzi, M. R., Minier, V., Motte, F., & Conway, J. E. 2006, , 448, L57

Peters, T., Klessen, R. S., Mac Low, M.-M., & Banerjee, R. 2010, , 725, 134

Pety, J., Gratier, P., Guzmán, V., et al. 2012, , 548, A68

Pickett, H. M., Poynter, R. L., Cohen, E. A., et al. 1998, , 60, 883

Pilbratt, G. L., Riedinger, J. R., Passvogel, T., et al. 2010, , 518, L1

Pillai, T., Kauffmann, J., Wyrowski, F., et al. 2011, , 530, A118

Pillai, T., Wyrowski, F., Carey, S. J., & Menten, K. M. 2006, , 450, 569

Pineau des Forets, G., Roueff, E., Schilke, P., & Flower, D. R. 1993, , 262, 915

Pirogov, L., Zinchenko, I., Caselli, P., Johansson, L. E. B., & Myers, P. C. 2003, , 405, 639

Plambeck, R. L. & Menten, K. M. 1990, , 364, 555

Plambeck, R. L., Wright, M. C. H., Friedel, D. N., et al. 2009, , 704, L25

Plambeck, R. L., Wright, M. C. H., Welch, W. J., et al. 1982, , 259, 617

Plume, R., Bergin, E. A., Phillips, T. G., et al. 2012, , 744, 28

Prasad, S. S. & Huntress, Jr., W. T. 1980, , 239, 151

Pratap, P., Batrla, W., & Snyder, L. E. 1989, , 341, 832

Pratap, P., Dickens, J. E., Snell, R. L., et al. 1997, , 486, 862

Pratap, P., Snyder, L. E., & Batrla, W. 1992, , 387, 241

Puga, E., Marín-Franch, A., Najarro, F., et al. 2010, , 517, A2

Purcell, C. R., Balasubramanyam, R., Burton, M. G., et al. 2006, , 367, 553

Qi, C., Kessler, J. E., Koerner, D. W., Sargent, A. I., & Blake, G. A. 2003, , 597, 986

Qi, C., Öberg, K. I., Wilner, D. J., et al. 2013, Science, 341, 630

Qiu, K. & Zhang, Q. 2009, , 702, L66

Qiu, K., Zhang, Q., & Menten, K. M. 2011, , 728, 6

Ragan, S., Henning, T., Krause, O., et al. 2012a, , 547, A49

Ragan, S. E., Bergin, E. A., & Gutermuth, R. A. 2009, , 698, 324

Ragan, S. E., Bergin, E. A., Plume, R., et al. 2006, , 166, 567

Ragan, S. E., Bergin, E. A., & Wilner, D. 2011, , 736, 163

Ragan, S. E., Heitsch, F., Bergin, E. A., & Wilner, D. 2012b, , 746, 174

Rathborne, J. M., Jackson, J. M., Chambers, E. T., et al. 2010, , 715, 310

Rathborne, J. M., Jackson, J. M., & Simon, R. 2006, , 641, 389

Rawlings, J. M. C., Redman, M. P., Keto, E., & Williams, D. A. 2004, , 351, 1054

Rawlings, J. M. C., Taylor, S. D., & Williams, D. A. 2000, , 313, 461

Reid, M. J., Menten, K. M., Greenhill, L. J., & Chandler, C. J. 2007, , 664, 950

Remijan, A. J., Leigh, D. P., Markwick-Kemper, A. J., & Turner, B. E. 2008, ArXiv e-prints

Rice, C. A. & Maier, J. P. 2013, Journal of Physical Chemistry A, 117, 5559

Richer, J. S., Shepherd, D. S., Cabrit, S., Bachiller, R., & Churchwell, E. 2000, Protostars and Planets IV, 867

Rizzo, J. R., Martín-Pintado, J., & de Vicente, P. 2001, in Highlights of Spanish astrophysics II, ed. J. Zamorano, J. Gorgas, & J. Gallego, 397

Rodríguez, L. F., Poveda, A., Lizano, S., & Allen, C. 2005, , 627, L65

Rohlfs, K. & Wilson, T. L. 2004, Tools of radio astronomy

Roueff, E., Lis, D. C., van der Tak, F. F. S., Gerin, M., & Goldsmith, P. F. 2005, , 438, 585

Russeil, D., Zavagno, A., Motte, F., et al. 2010, , 515, A55

Sakai, T., Sakai, N., Kamegai, K., et al. 2008, , 678, 1049

Sanchez-Monge, A. 2011, PhD thesis, University of Barcelona

Sánchez-Monge, Á., Palau, A., Fontani, F., et al. 2013, , 432, 3288

Sandell, G., Goss, W. M., Wright, M., & Corder, S. 2009, , 699, L31

Sandell, G. & Sievers, A. 2004, , 600, 269

Sandell, G. & Wright, M. 2010, , 715, 919

Sandell, G., Wright, M., & Forster, J. R. 2003, , 590, L45

Sandstrom, K. M., Peek, J. E. G., Bower, G. C., Bolatto, A. D., & Plambeck, R. L. 2007, , 667, 1161

Sanhueza, P., Jackson, J. M., Foster, J. B., et al. 2012, , 756, 60

Sanhueza, P., Jackson, J. M., Foster, J. B., et al. 2013, , 773, 123

Sarrasin, E., Abdallah, D. B., Wernli, M., et al. 2010, , 404, 518

Sault, R. J., Teuben, P. J., & Wright, M. C. H. 1995, in Astronomical Society of the Pacific Conference Series, Vol. 77, Astronomical Data Analysis Software and Systems IV, ed. R. A. Shaw, H. E. Payne, & J. J. E. Hayes, 433

Savage, B. D. & Sembach, K. R. 1996, , 470, 893

Schilke, P., Benford, D. J., Hunter, T. R., Lis, D. C., & Phillips, T. G. 2001, , 132, 281

Schilke, P., Walmsley, C. M., Pineau des Forets, G., & Flower, D. R. 1997, , 321, 293

Schilke, P., Walmsley, C. M., Pineau Des Forets, G., et al. 1992, , 256, 595

Schreyer, K. & Henning, T. 1999, in ASP Conference Series, Vol. 99, The Orion Complex Revisited, 1999

Schuller, F., Menten, K. M., Contreras, Y., et al. 2009, , 504, 415

Scoville, N. Z., Hall, D. N. B., Ridgway, S. T., & Kleinmann, S. G. 1982, , 253, 136

Scoville, N. Z., Sargent, A. I., Sanders, D. B., et al. 1986, , 303, 416

Semenov, D., Hersant, F., Wakelam, V., et al. 2010, , 522, A42

Semenov, D. & Wiebe, D. 2011, , 196, 25

Shalabiea, O. M. & Greenberg, J. M. 1994, , 290, 266

Shu, F. H., Adams, F. C., & Lizano, S. 1987, , 25, 23

Snow, T. P. & McCall, B. J. 2006, , 44, 367

Snyder, L. E., Lovas, F. J., Hollis, J. M., et al. 2005, , 619, 914

Snyder, L. E., Lovas, F. J., Mehringer, D. M., et al. 2002, , 578, 245

Sobolev, A. M., Cragg, D. M., Ellingsen, S. P., et al. 2007, in IAU Symposium, Vol. 242, IAU Symposium, ed. J. M. Chapman & W. A. Baan, 81–88

Sofia, U. J., Cardelli, J. A., & Savage, B. D. 1994, , 430, 650

Sohn, J., Lee, C. W., Park, Y.-S., et al. 2007, , 664, 928

Spitzer, Jr., L. & Fitzpatrick, E. L. 1993, , 409, 299

Sridharan, T. K., Beuther, H., Saito, M., Wyrowski, F., & Schilke, P. 2005, , 634, L57

Sridharan, T. K., Beuther, H., Schilke, P., Menten, K. M., & Wyrowski, F. 2002, , 566, 931

Stahler, S. W. & Palla, F. 2005, The Formation of Stars

Stutz, A., Launhardt, R., Linz, H., et al. 2010, , 518, L87

Sugai, H., Usuda, T., Kataza, H., et al. 1994, , 420, 746

Sutton, E. C., Blake, G. A., Masson, C. R., & Phillips, T. G. 1985, , 58, 341

Sutton, E. C., Peng, R., Danchi, W. C., et al. 1995, , 97, 455

Sutton, E. C. & Sandell, G. 1996, in Amazing Light, ed. R. Y. Chiao, 627–635

Sutton, E. C., Sobolev, A. M., Salii, S. V., et al. 2004, , 609, 231

Tackenberg, J., Beuther, H., Henning, T., et al. 2012, , 540, A113

Tafalla, M. 2011, in Highlights of Spanish Astrophysics VI, ed. M. R. Zapatero Osorio, J. Gorgas, J. Maíz Apellániz, J. R. Pardo, & A. Gil de Paz, 442–453

Tafalla, M., Myers, P. C., Caselli, P., Walmsley, C. M., & Comito, C. 2002, , 569, 815

Tafalla, M., Santiago-García, J., Myers, P. C., et al. 2006, , 455, 577

Tan, J. C., Beltran, M. T., Caselli, P., et al. 2014, ArXiv e-prints

Tan, J. C., Kong, S., Butler, M. J., Caselli, P., & Fontani, F. 2013, , 779, 96

Tan, J. C. & McKee, C. F. 2002, in Astronomical Society of the Pacific Conference Series, Vol. 267, Hot Star Workshop III: The Earliest Phases of Massive Star Birth, ed. P. Crowther, 267

Tang, Y.-W., Ho, P. T. P., Koch, P. M., & Rao, R. 2010, , 717, 1262

Taylor, K. N. R., Storey, J. W. V., Sandell, G., Williams, P. M., & Zealey, W. J. 1984, , 311, 236

Tercero, B., Cernicharo, J., Pardo, J. R., & Goicoechea, J. R. 2010, , 517, A96

Teyssier, D., Hennebelle, P., & Pérault, M. 2002, , 382, 624

Thorwirth, S. 2001, PhD thesis, I. Physikalisches Institut Universität zu Köln Zülpicher Str. 77 50937 Köln Germany

Tideswell, D. M., Fuller, G. A., Millar, T. J., & Markwick, A. J. 2010, , 510, A85

Tielens, A. G. G. M. 2013, Reviews of Modern Physics, 85, 1021

Tielens, A. G. G. M. & Hagen, W. 1982, , 114, 245

Tobin, J. J., Hartmann, L., Chiang, H.-F., et al. 2012, , 492, 83

Turner, B. E. 1989, , 70, 539

Turner, B. E. 1991, , 76, 617

Turner, B. E., Terzieva, R., & Herbst, E. 1999, , 518, 699

Turner, N. J., Fromang, S., Gammie, C., et al. 2014, ArXiv e-prints

Urquhart, J. S., Thompson, M. A., Moore, T. J. T., et al. 2013, , 435, 400

van der Tak, F. F. S. 2004, in IAU Symposium, Vol. 221, Star Formation at High Angular Resolution, ed. M. G. Burton, R. Jayawardhana, & T. L. Bourke, 59

van der Tak, F. F. S. 2005, in IAU Symposium, Vol. 227, Massive Star Birth: A Crossroads of Astrophysics, ed. R. Cesaroni, M. Felli, E. Churchwell, & M. Walmsley, 70–79

van der Tak, F. F. S., Black, J. H., Schöier, F. L., Jansen, D. J., & van Dishoeck, E. F. 2007, , 468, 627

van der Tak, F. F. S., van Dishoeck, E. F., Evans, II, N. J., & Blake, G. A. 2000, , 537, 283

van Dishoeck, E. F. 2009, Astrochemistry of Dense Protostellar and Protoplanetary Environments, ed. H. A. Thronson, M. Stiavelli, & A. Tielens, 187

van Dishoeck, E. F. 2014, Faraday Discuss., 168, 9

van Dishoeck, E. F. & Black, J. H. 1988, , 334, 771

van Dishoeck, E. F., Jonkheid, B., & van Hemert, M. C. 2006, Faraday Discussions, 133, 231

van Dishoeck, E. F., Kristensen, L. E., Benz, A. O., et al. 2011, , 123, 138

Vasyunin, A. I. & Herbst, E. 2013, , 769, 34

Vasyunina, T., Linz, H., Henning, T., et al. 2009, , 499, 149

Vasyunina, T., Linz, H., Henning, T., et al. 2011, , 527, A88

Vázquez-Semadeni, E., Ryu, D., Passot, T., González, R. F., & Gazol, A. 2006, , 643, 245

Viti, S., Codella, C., Benedettini, M., & Bachiller, R. 2004, , 350, 1029

Voronkov, M. A., Brooks, K. J., Sobolev, A. M., et al. 2006, , 373, 411

Wakelam, V., Caselli, P., Ceccarelli, C., Herbst, E., & Castets, A. 2004a, , 422, 159

Wakelam, V., Castets, A., Ceccarelli, C., et al. 2004b, , 413, 609

Wakelam, V., Herbst, E., Loison, J.-C., et al. 2012, , 199, 21

Wang, K., Zhang, Q., Testi, L., et al. 2014, , 439, 3275

Wang, K., Zhang, Q., Wu, Y., & Zhang, H. 2011a, , 735, 64

Wang, K.-S., van der Tak, F. F. S., & Hogerheijde, M. R. 2012, , 543, A22

Wang, S., Bergin, E. A., Crockett, N. R., et al. 2011b, , 527, A95

Wang, Y., Zhang, Q., Pillai, T., Wyrowski, F., & Wu, Y. 2008, , 672, L33

Watanabe, N., Nagaoka, A., Shiraki, T., & Kouchi, A. 2004, , 616, 638

Watson, W. D. 1976, Reviews of Modern Physics, 48, 513

Werner, M. W., Becklin, E. E., Gatley, I., et al. 1979, , 188, 463

Widicus Weaver, S. L. & Friedel, D. N. 2012, , 201, 16

Williams, J. P., Bergin, E. A., Caselli, P., Myers, P. C., & Plume, R. 1998, , 503, 689

Willner, S. P. 1976, , 206, 728

Willner, S. P., Gillett, F. C., Herter, T. L., et al. 1982, , 253, 174

Wilner, D. J., Wright, M. C. H., & Plambeck, R. L. 1994, , 422, 642

Wilson, T. L., Gaume, R. A., Gensheimer, P., & Johnston, K. J. 2000, , 538, 665

Wilson, T. L., Muders, D., Dumke, M., Henkel, C., & Kawamura, J. H. 2011, , 728, 61

Wilson, T. L., Rohlfs, K., & Hüttemeister, S. 2009, Tools of Radio Astronomy (Springer-Verlag)

Wilson, T. L. & Rood, R. 1994, , 32, 191

Wilson, T. L., Walmsley, C. M., Batrla, W., & Mauersberger, R. 1983, , 127, L19

Wilson, T. L., Walmsley, C. M., Jewell, P. R., & Snyder, L. E. 1984, , 134, L7

Wolfire, M. G. & Cassinelli, J. P. 1987, , 319, 850

Wood, D. O. S. & Churchwell, E. 1989, , 69, 831

Woodall, J., Agúndez, M., Markwick-Kemper, A. J., & Millar, T. J. 2007, , 466, 1197

Woody, D. P., Scott, S. L., Scoville, N. Z., et al. 1989, , 337, L41

Woon, D. E. 2002, , 569, 541

Wright, M., Sandell, G., Wilner, D. J., & Plambeck, R. L. 1992, , 393, 225

Wright, M., Zhao, J.-H., Sandell, G., et al. 2012, , 746, 187

Wright, M. C. H. & Plambeck, R. L. 1983, , 267, L115

Wright, M. C. H., Plambeck, R. L., & Wilner, D. J. 1995, Astronomy Data Image Library, 2

Wright, M. C. H., Plambeck, R. L., & Wilner, D. J. 1996, , 469, 216

Wu, Y., Zhu, M., Wei, Y., et al. 2005, , 628, L57

Wynn-Williams, C. G., Becklin, E. E., & Neugebauer, G. 1974, , 187, 473

Wynn-Williams, C. G., Genzel, R., Becklin, E. E., & Downes, D. 1984, , 281, 172

Yorke, H. W. 1986, , 24, 49

Yorke, H. W. & Sonnhalter, C. 2002, , 569, 846

Zapata, L. A., Rodríguez, L. F., Schmid-Burgk, J., et al. 2012, , 754, L17

Zapata, L. A., Schmid-Burgk, J., Ho, P. T. P., Rodríguez, L. F., & Menten, K. M. 2009, , 704, L45

Zapata, L. A., Schmid-Burgk, J., & Menten, K. M. 2011, , 529, A24

Zeng, Q., Mao, P. Q., & Pei, C. C. 2006, Microwave spectrum of astrophysics diagnosis (Chinese edition)

Zhang, Q., Hunter, T. R., Beuther, H., et al. 2007, , 658, 1152

Zhang, Q. & Wang, K. 2011, , 733, 26

Zhang, Q., Wang, Y., Pillai, T., & Rathborne, J. 2009, , 696, 268

Zheng, X.-W., Zhang, Q., Ho, P. T. P., & Pratap, P. 2001, , 550, 301

Zhu, L., Zhao, J.-H., Wright, M. C. H., et al. 2013, , 779, 51

Zinchenko, I., Henkel, C., & Mao, R. Q. 2000, , 361, 1079

Zinnecker, H. & Yorke, H. W. 2007, , 45, 481

Ziurys, L. M. & McGonagle, D. 1993, , 89, 155

Zuckerman, B., Kuiper, T. B. H., & Rodriguez Kuiper, E. N. 1976, , 209, L137